SHEAR STRENGTH BEHAVIOR OF UNSATURATED SOILS DURING STRAIN-SOFTENING

XIUHAN YANG

Thesis submitted to the University of Ottawa
in partial fulfillment of the requirements for the
Doctorate in Philosophy degree in Civil Engineering

Department of Civil Engineering
Faculty of Engineering
University of Ottawa

© Xiuhan Yang, Ottawa, Canada, 2023

ABSTRACT

The shear stress in an unsaturated soil increases rapidly with limited shear strain to a peak value and then drops gradually with a further increase in the shear strain until a residual value is reached. In other words, there is a significant strain-softening behavior under large shear deformation. A variety of geotechnical structures (e.g., slopes, foundations, retaining walls and piles) associated with unsaturated soils typically undergo a large progressive deformation prior to reaching failure conditions due to the influence of environmental factors (e.g., rainfall infiltration and wetting-drying cycles). As a result, the shear strength of soils in sliding zones typically reduces from a peak to a residual value with the progressive development of large shear deformation, while the shear strength of soils in other zones are still at the peak level. In other words, in many scenarios the strain-softening behavior of unsaturated soils can significantly influence the mechanical behavior of geo-structures. Therefore, a thorough understanding of the shear strength behavior of unsaturated soils during strain-softening is required to reliably interpret the mechanical behavior of geo-structures that undergo large shear deformation.

Significant advances have been made during the last thirty years to understand and model the strain-softening behavior of unsaturated soils. Most of these studies however focus on the strain-softening behavior within a relatively small shear deformation due to the limitations of the experimental apparatuses. Only limited experimental studies under large shear deformation were reported based on the modified suction-controlled ring shear apparatus. Therefore, more investigations are still required to provide a comprehensive understanding of the shear strength behavior of unsaturated soils during strain-softening under large shear deformation.

Studies presented in this thesis are directed towards investigating the shear strength behavior of unsaturated soils during strain-softening and its application in geotechnical engineering practice. The following studies have been conducted:

(i) A state-of-the-art review of the strain-softening behavior of unsaturated soils published in the literature during the past three decades is summarized. The physical mechanisms and modelling methods of the strain-softening behavior and the peak, critical and residual shear strength of unsaturated soils are investigated.

(ii) A disturbed state concept model is proposed to predict the variation of shear stress in unsaturated soils during strain-softening process under drained condition. Five sets of experimental data gathered from the literature on unsaturated soils varying from coarse- to

fine-grained soils are used to verify the proposed model. The proposed model can provide reasonable predictions for the strain-softening stress-strain relationships of various types of unsaturated soils. The model is simple in concept and all the required parameters can be obtained from conventional saturated and unsaturated shearing tests and pressure plate tests.

(iii) Two sets of suction-controlled multistage ring shear tests are conducted on unsaturated SP-SM soil and Indian Head till (IHT), respectively. The variation of the shear stress, void ratio, and water content of specimens during shearing (the shear displacement reaches 100 mm) under multi levels of net normal stress and matric suction are described and discussed. The influence of matric suction and net normal stress on the residual shear strength envelops of unsaturated soils are critically discussed.

(iv) A model for predicting the residual shear strength for a wide range of unsaturated soils comprising coarse- to fine-grained soils is developed in terms of two stress state variables (i.e., the net normal stress and matric suction) by using the soil water characteristic curve as a tool. The model is formulated and validated based on experimental data in a series of suction-controlled ring shear tests using the axis-translation technique, including the two sets of tests (SP-SM and IHT) conducted in this research and another three sets of tests (SM, SC-SM and CH) gathered from the literature. The fitting parameters are related to the plasticity index (I_p); thus, only four basic parameters (i.e., c_r', ϕ_r', S_r and I_p) are included in this approach.

(v) A series of slope stability analyses of a landslide in unsaturated condition are conducted using Geoslope software based on the peak and residual shear strength parameters. The analyses results highlight the role of residual shear strength in the slope stability of unsaturated soils.

In summary, the mechanical behavior of unsaturated soils under large shear deformation is comprehensively investigated in this thesis. The experimental results of the suction-controlled ring shear tests reported in this research contribute towards understanding the fundamental shear strength behavior of unsaturated soils during strain-softening under large shear deformation. The models proposed in this research provide simple tools to predict the shear strength of unsaturated soils under different levels of shear deformation.

ACKNOWLEDGEMENTS

The research work presented in this thesis is conducted under the supervision of Prof. Sai K. Vanapalli at the Department of Civil Engineering, University of Ottawa. I would like to express my sincere appreciation to Prof. Vanapalli for his guidance, support, trust, and patience throughout my doctoral study. Prof. Vanapalli provided valuable guidance for me on this research work. He provided several opportunities for training and mentoring to be a good researcher and teacher always keeping my future interests in mind. Prof. Vanapalli is a nice professor, who respected my ideas towards research and as well as life and has encouraged me. He is a role model for me to be a good researcher and teacher.

The financial support received from the China Scholarship Council (CSC) - University of Ottawa joint scholarship is gratefully acknowledged.

I would like to thank Prof. Anand Puppala, Prof. Siva Sivathayalan, Prof. Rozalina Dimitrova and Prof. Julio Angel Infante Sedano, for serving as committee members and providing insightful criticism and comments on the thesis.

Acknowledgements are also extended to my colleagues for their friendship, company, and support; Luc, Jean-Claude, Paula, Zhong, Shunchao, Yunlong, Ping, Huade, Mohammed, Junping, Penghai, Guanlong, Hongyu, Xiaokun, Jiayu, Shilong, Kun, Ende, Le, Mingshu, Mengxi, Xinting, Wenjun, Xingyi, Kenneth, Yu, Junjie, Yao, Aolin, Xinye, Dongliang, Ziwen, Alpesh, Maha, Moussa, and Sada.

I am extremely thankful for my parents who selflessly support my every decision in my life and allowed me, their only child, to study in Canada for more than six years. This thesis would not have been possible without their love and support. I humbly dedicate this thesis to my parents, Hongzhang and Yanhong.

TABLE OF CONTENTS

LIST OF FIGURES

LIST OF TABLES

CHAPTER 1 INTRODUCTION

1.1 Background

Unsaturated soils are widely distributed in the arid and semi-arid regions of world; the natural ground water table in these regions is typically at a greater depth due to significant evaporation of water in comparison to infiltration. The soil between the ground surface and the water table, which is referred to as the vadose zone, is typically in a state of unsaturated condition. The pore-water pressure of the soil in this zone is predominantly negative due to the influence of environmental factors. Most of the geotechnical infrastructures are constructed in this zone. For example, shallow foundations, retaining walls and pipelines are constructed in the unsaturated soil zone which is above the ground water table. Several other infrastructures such as embankments, pavements and man-made slopes are constructed with unsaturated soils. The hydraulic and the mechanical behavior of unsaturated soils are sensitive to the environmental factors, which include the wetting and drying and freezing and thawing cycles and are strongly dependent on the soil water content changes, in the solid, liquid, and vapor phase (Fredlund et al. 2012). Therefore, it is important to understand the behavior of geotechnical infrastructure constructed in or with unsaturated soils taking account of the unsaturated soils behavior.

One of the key factors influencing the design of geotechnical infrastructure is the large shear deformation. Geotechnical engineers are aware of several failures or performance problems that are associated with large shear deformation both in saturated soils (Skempton 1964; Potts et al. 1990; Potts et al. 1997; Leroueil 2001; Gens and Alonso 2006) as well as unsaturated soils (Widger and Fredlund 1979; Kovacevic et al. 2001; Ng et al. 2003; Nyambayo et al. 2004; Take and Bolton 2011; Qi and Vanapalli 2016; Vo et al. 2016; Wang et al. 2018; Al-Khazaali and Vanapalli 2019; Liu and Vanapalli 2019; Postill et al. 2021). The shear strength of unsaturated soils reduces gradually from a peak value (i.e., peak shear strength, PSS) that typically arises after a limited shear deformation to a constant lowest value (i.e., residual shear strength, RSS) after a large shear deformation. The reduction in shear strength with shear deformation is also widely referred to as the strain-softening behavior of soils. For this reason, the geotechnical infrastructure in unsaturated soils typically undergo large progressive shear deformation prior to reaching the failure condition, which can significantly influence the mechanical behaviors of the geotechnical infrastructure. The

progressive failure of an unsaturated soil slope along with its strain-softening behavior is shown in Figure 1.1 to illustrate the residual shear strength of unsaturated soils.

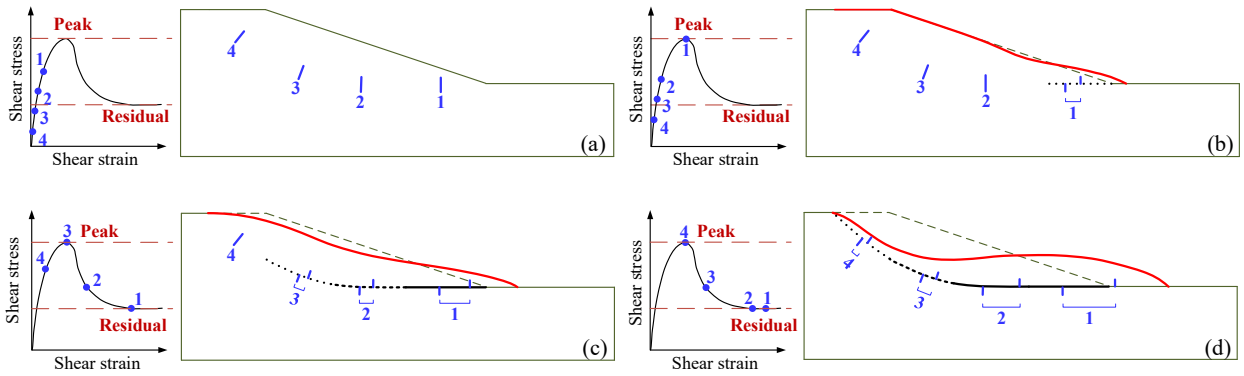

Figure 1.1 Schematic of progressive failure and strain-softening behavior: (a) initial condition; (b) initiation of sliding zone; (c) development of sliding zone; (d) failure condition

In the stable state (Figure 1.1a), the shear deformation is limited, and the shear stress is lower than the peak shear strength. However, soil slopes in natural and compacted unsaturated condition undergo large local shear deformation due to the influence of various environmental factors (e.g., rainfall infiltration, wetting-drying cycles, and variation of ground water table, etc.) and engineering activities (e.g., excavation). As a result, the shear stress increases with increasing shear deformation and the sliding zone arises once the PSS is reached (Point 1 in Figure 1.1b). The shear strength gradually decreases to a residual value in the sliding zones where shear deformation is large (Point 1 in Figure 1.1c), while the shear strength in other zones is still at peak values (Point 3 and Point 4 in Figure 1.1c). The soils in sliding zone cannot provide resistance exceeding their shear strength which has dropped to a post-peak value. Therefore, the extra shear stress will be redistributed into the surrounding zones. Such a behavior contributes to greater shear deformation associated with reduction of shear strength in the surrounding zones. As a result, the sliding zone develops into a larger zone progressively (Figures 1.1b – d). The soil slope reaches the failure condition when the sliding zone goes through the entire slope (Figure 1.1d).

In some scenarios, more than a century is required for reaching failure conditions in unsaturated soils (Postill et al. 2021). During this process, the sliding zone will develop progressively associated with a large shear deformation and the factor of safety of the soil slope decreases

gradually. For this reason, the variation of shear strength within the soil slope with the development of shear deformation should be considered for reliable analysis and design. For example, as shown in Figure 1.1a, the peak shear strength can be used for the entire soil slope; however, as shown in Figure 1.1c, the residual shear strength should be used for Point 1, while the peak shear strength should be used for Point 3 and 4.

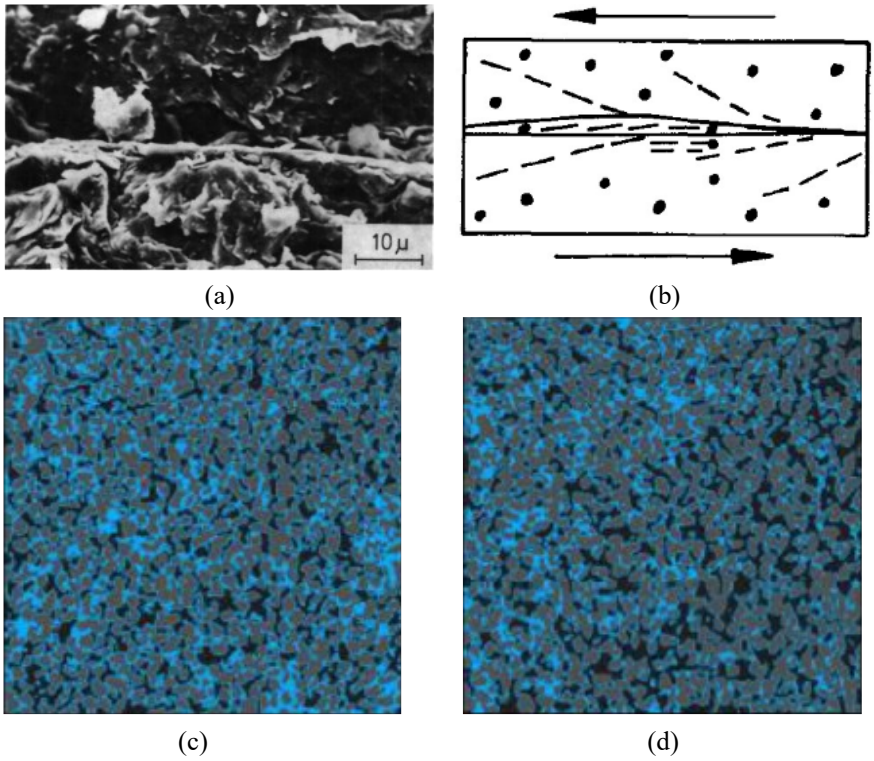

Figure 1.2 Microstructure change of soils associated with the shear strength reduction during shearing: (a) electron micrograph of shear surface of saturated clay in ring shear test (Lupini et al. 1981); (b) diagram of particles reorientation of saturated clay in ring shear test (Lupini et al. 1981); (c) shear band of unsaturated sand at 9% axial strain (around peak state) in triaxial shear test (Kido and Higo 2020); (d) shear band of unsaturated sand at 21% axial strain in triaxial shear test (Kido and Higo 2020)

Figure 1.2a shows the reorientation of platy clay particles in the shear surface of saturated clay sheared to residual condition (Lupini et al. 1981). In unsaturated condition, the clayey soils can also undergo similar microstructure change when they are subjected to large shear deformation. The reorientation of clay particles/aggregates, together with the loss of suction contribution towards shear strength, can lead to a significant reduction in the shear strength of unsaturated

clayey soils from peak to a residual value when they undergo large shear deformation. Several numerical studies on unsaturated clayey soil slopes (Qi and Vanapalli 2016; Postill et al. 2021) have suggested that the factor of safety obtained by considering residual shear strength is significantly lower for unsaturated soils.

In addition, Figure 1.2b shows the loss of water menisci area within the shear band of unsaturated sand under triaxial shearing (Kido and Higo 2020). More water menisci area will be lost with increasing shear deformation until the residual condition is reached. Several suction-controlled ring shear data (Hoyos et al. 2014) suggest unsaturated sandy soils can attain residual condition at a relatively small shear deformation. In other words, unsaturated sandy soils can exhibit a significant reduction in shear strength even under a small shear deformation due to the loss of the contribution of suction. Therefore, the residual shear strength of unsaturated sandy soils should also attract the attention of geotechnical engineers.

During the last three decades, experimental studies were conducted based on conventional (Derbyshire et al. 1994; Dijkstra 1994; Maquaire et al. 2003; Fan et al. 2017; Lian et al. 2020) and suction-controlled ring shear apparatus (Infante Sedano 2006; Velosa 2011; Hossain 2013; Heredia 2015; Romero et al. 2014) to investigate the residual shear strength behavior of unsaturated soils under large shear deformation. These studies are valuable; however, more investigations are required for a comprehensive understanding of the shear strength behavior of unsaturated soils during strain-softening under large shear deformation.

1.2 Objective, novelty, and methodology

The research aims to investigate the shear strength behavior of unsaturated soils during strain-softening and its application in geotechnical engineering practice. For this purpose, four major specific objectives with novelty are addressed in this PhD research program, which are summarized below:

(1) To comprehensively review the studies related to the mechanisms and modelling methods of strain-softening behavior of unsaturated soils

A variety of studies on the shearing behavior of unsaturated soils that exhibit strain-softening behavior have been published in the literature during the past three decades. However, the physical

mechanisms and modelling methods of the strain-softening behavior and different types of shear strengths (i.e., the peak, critical and residual shear strength) of unsaturated soils still need comprehensive discussion and rigorous understanding. The research summarized in this thesis provides a comprehensive review on the studies about the strain-softening behavior of unsaturated soils, which are summarized under several categories as below.

Firstly, various experimental studies related to the strain-softening behavior of unsaturated soils are summarized. The mechanical behavior characteristics and micro-mechanisms of the strain-softening of unsaturated soils under large shear deformation were interpretated. Secondly, the widely used empirical/semi-empirical prediction models from the literature for the peak, critical and residual shear strength of unsaturated soils are comprehensively summarized. The influence of soil fabric and water phase on the shear strength were interpretated. Thirdly, several numerical methods (i.e., conventional plasticity, bounding surface plasticity, disturbed state concept and elasto-viscoplasticity) of modelling the strain-softening behavior of unsaturated soils are discussed highlighting their strengths and limitations.

(2) To develop a simple method for predicting the strain-softening stress-strain relationship of unsaturated soils

The peak and residual shear strength are the upper and lower limits of the shear strength of soils which are derived from the laboratory tests. However, the in-situ shear strength of a soil varies significantly in a non-uniform fashion. Its magnitude is typically somewhere between the peak and the residual shear strength and varies with the shear deformation. Therefore, it is necessary to take account of the influence of shear deformation for the reliable determination of shear strength of soils. Some constitutive models proposed in the literature can capture the strain-softening behavior of unsaturated soils (Alonso et al. 1990; Cui and Delage 1996; Russell and Khalili 2006; Zhou and Sheng 2015; Geiser et al. 1997). These models are however complex and require several parameters that must be determined from cumbersome experimental investigations. Thus, a simple model is proposed in this research for predicting the strain-softening stress-strain relationship of unsaturated soils under triaxial compression loading condition with constant matric suction and net normal stress.

The proposed model is formulated based on the disturbed state concept (DSC). In this model, the evolution of shear band is considered as the disturbance which contributes to the reduction in shear strength after peak state. The predicted stress-strain curve is formulated as a weighted average of a hardening stress-strain curve extending the pre-peak state response which is considered as relatively intact state and a horizontal stress-strain curve extending the critical state response which is considered as the fully adjusted state with an assumed disturbance function as the weight. The mechanical parameters involved in the proposed model are expressed as functions of independent stress state variables (i.e., matric suction and net minor principal stress). The proposed model is validated using several sets of published data on unsaturated soils varying from sand to clay.

(3) To investigate behavior of unsaturated soils under large shear deformation based on suction-controlled ring shear tests

Currently, most of experimental studies on unsaturated soils are based on suction-controlled direct and triaxial shear tests which can only provide a limited shear deformation. There are limited experimental studies available in the literature based on the suction-controlled ring shear tests. The experimental study based on suction-controlled ring shear tests presented in this research can yield first-hand testing data which can contribute to a better understanding of the mechanical behaviors of unsaturated soils under large shear deformation.

The modified suction-controlled ring shear apparatus developed by Infante Sedano et al. (2007) is used to conduct a series of ring shear tests on two unsaturated soils, including a SP-SM soil and an Indian Head till (IHT). Multi matric suction levels are applied for each type of soil by using axis translation technique to study the influence of matric suction on the shearing behavior of unsaturated soils. For each matric suction level, multistage ring shear tests are performed on one unsaturated specimen to obtain the magnitudes of residual shear strength under different net normal stresses. For each stage shearing, the shear displacement reaches 100 mm. During shearing, the shear stress, vertical displacement, and the pore water mass of the specimen are monitored in real time.

(4) To develop a prediction model for the residual shear strength of unsaturated soils

Shear strength of soils is vital to the analysis and design of geotechnical structures. Experimental determination of the shear strength of unsaturated soils is time-consuming, cumbersome, and expansive, which can limit the application of the unsaturated soil mechanics into geotechnical engineering practice. Therefore, a simple prediction model is necessary for determination of the shear strength of unsaturated soils. Currently, a variety of prediction models have been proposed for the peak and critical shear strength of unsaturated soils (e.g., Vanapalli, 2009; Sheng et al. 2011). However, the prediction model for residual shear strength of unsaturated soils is still lacking in the literature. In this research work, a model is proposed for the prediction of the residual shear strength for a wide range of unsaturated soils comprising coarse- to fine-grained soils.

The prediction model is formulated in terms of two independent stress state variables (i.e., the net normal stress and matric suction). A relationship is proposed for the residual shear strength of unsaturated soils based on the observations in a series of suction-controlled ring shear tests using the axis-translation technique. The two sets of tests based on the experimental studies undertaken in this Ph.D. study and another three sets of tests collected from the literature provide a database for the development of the prediction model. The fitting parameters involved in the prediction model are related to the plasticity index of soils to provide a simple and approximate approach for predicting the residual shear strength of a wide range of unsaturated soils.

1.3 Layout

A detailed organization of this thesis is summarized below:

(i) **Chapter 1** presents the background related to the thesis topic and lays out key novel objectives that were addressed in this thesis. In addition, the methodology used is discussed and the layout of the thesis is presented.

(ii) **Chapter 2** presents a comprehensive literature review on the strain-softening behavior of unsaturated soils. The review focus is directed to highlight three aspects: (i) mechanical characteristics and micro-mechanisms, (ii) prediction models for peak, critical and residual shear strength and (iii) numerical methods for modelling strain-softening behavior of unsaturated soils. In addition, the influence of the soil water characteristic curve and the time effects on the strain-softening behavior of unsaturated soils are also discussed.

(iii) **Chapter 3** proposes a model based on the disturbed state concept (DSC) to predict the variation of shear stress in unsaturated soils during the strain-softening process under consolidated drained triaxial compression condition. The formulation of the proposed model and the prediction procedure are described in detail. The validation of the proposed model is presented using five sets of experimental data on unsaturated soils varying from coarse- to fine-grained soils collected from other literature. The prediction errors are evaluated and discussed based on an index of agreement.

(iv) **Chapter 4** presents two sets of suction-controlled ring shear tests that are designed for two different unsaturated soils, including a SP-SM soil and a IHT soil. The modified suction-controlled ring shear apparatus, properties of the investigated materials, and procedures of the designed suction-controlled multistage ring shear tests are succinctly introduced in detail. In addition, several correction methods are described to alleviate the measurement errors due to the limitations of the testing technique.

(v) **Chapter 5** presents the experimental results of the two sets of suction-controlled ring shear tests on the SP-SM and IHT soil. The variations of the shear stress, void ratio, and water ratio of the IHT and SP-SM specimens during shearing stage are described. The shearing behaviors of the investigated unsaturated soils in suction-controlled state under a shear displacement of 100 mm are discussed. The envelopes of the residual shear strength are presented with respect to the net normal stress and matric suction, respectively. The influence of the matric suction and net normal stress on the residual shear strength and the residual friction angle with respect to the net normal stress and the matric suction (i.e., ϕ_r^a and ϕ_r^b) are discussed. In addition, the void ratio, water ratio and degree of saturation of the unsaturated IHT soil sheared to the residual state are discussed.

(vi) **Chapter 6** proposes a model for the prediction of the residual shear strength for a wide range of unsaturated soils comprising coarse- to fine-grained soils. Five sets of experimental data of suction-controlled ring shear tests are presented, including two sets of tests (SP-SM and IHT) from this study and another three sets of tests (SM, SC-SM and CH) collected from the literature. The behaviors of the residual shear strength of unsaturated soils are discussed. The formulation of the proposed model is described in detail based on the observations in the suction-controlled ring shear tests. The validation of the proposed model is presented based on the comparisons between the predicted and experimental results for the five investigated unsaturated soils.

(vii) **Chapter 7** presents a series of slope stability analyses of a reactivated landslide based on the peak and the residual shear strength parameters taking account of saturated and unsaturated conditions. A reactivated landslide reported in the literature is introduced and interpreted extending the mechanics of unsaturated soils. A series of seepage analyses using SEEP/W and slope stability analyses using SLOPE/W are conducted for the reactivated landslide considering the peak and residual shear strength parameters, respectively. The influence on the slope stability of the precipitation and the water level variation of a river at slope toe is investigated. The role of residual shear strength in the slope stability of unsaturated soils is discussed.

(viii) **Chapter 8** provides overall summary of this Ph.D. research as well as suggestions for future research.

1.4 Publications

Journal publications:

1. **Yang, X.**, and Vanapalli, S. K. 2019. Slope stability analyses of outang landslide based on the peak and residual shear strength behavior. *Advanced Engineering Sciences*, 51(4): 55-68. DOI: 10.15961/j.jsuese.201900273.
2. **Yang, X.,** and Vanapalli, S. K. 2021. Model for predicting the variation of shear stress in unsaturated soils during strain-softening. *Canadian Geotechnical Journal*, 58(10): 1513-1526. DOI: 10.1139/cgj-2020-0312.
3. **Yang, X.,** and Vanapalli, S. K. 2022. Mechanisms and modelling methods of strain-softening behavior of unsaturated soils: A state of the art review. *International Journal of Geomechanics*. (Accepted)
4. **Yang, X.,** and Vanapalli, S. K. 2022. Model for the prediction of residual shear strength of unsaturated soils. Under peer review with a Journal.

Conference publications:

5. **Yang, X.,** and Vanapalli, S. K. 2017. Residual shear strength of unsaturated soils. In Proceedings of *the 70th Canadian Geotechnical Conference*, Ottawa, Canada.

6. **Yang, X.,** and Vanapalli, S. K. 2018. Stability analysis of a slope based on the peak and the residual shear strength of unsaturated soils. In Proceedings of *the 7th International Conference on Unsaturated Soils*, Hong Kong, China.
7. **Yang, X.,** and Vanapalli, S. K. 2019. A case study analysis of a landslide considering the residual unsaturated shear strength of soil. In Proceedings of *the 72nd Canadian Geotechnical Conference*, St. John's, Canada.

Chapter publications:

8. **Yang, X.,** and Vanapalli, S. K. 2021. Modeling of unsaturated soils slopes considering the residual shear strength behavior. In *Modeling in Geotechnical Engineering*: 133-149. Academic Press. https://doi.org/10.1016/B978-0-12-821205-9.00001-0.

1.5 References

Al-Khazaali, M., and Vanapalli, S. K. 2019. Axial force–displacement behavior of a buried pipeline in saturated and unsaturated sand. Géotechnique, 69(11): 986-1003.

Alonso, E. E., Gens, A., and Josa, A. 1990. A constitutive model for partially saturated soils. Géotechnique, 40(3): 405-430.

Cui, Y. J., and Delage, P. 1996. Yielding and plastic behavior of an unsaturated compacted silt. Géotechnique, 46(2): 291-311.

Derbyshire, E., Dijkstra, T. A., Smalley, I. J., and Li, Y. 1994. Failure mechanisms in loess and the effects of moisture content changes on remoulded strength. Quaternary International, 24: 5-15.

Dijkstra, T. A., Rogers, C. D. F., Smalley, I. J., Derbyshire, E., Li, Y. J., and Meng, X. M. 1994. The loess of north-central China: geotechnical properties and their relation to slope stability. Engineering Geology, 36(3-4): 153-171.

Fan, X., Xu, Q., Scaringi, G., Li, S., and Peng, D. 2017. A chemo-mechanical insight into the failure mechanism of frequently occurred landslides in the Loess Plateau, Gansu Province, China. Engineering Geology, 228: 337-345.

Fredlund, D. G., Rahardjo, H., and Fredlund, M. D. 2012. Unsaturated Soil Mechanics in Engineering Practice. John Wiley and Sons, Inc., Hoboken, New Jersey, USA.

Geiser, F., Laloui, L., Vulliet, L., and Desai, C. S. 1997. Disturbed state concept for partially saturated soils. In Proceedings of 6th International Symposium on Numerical Models in Geomechanics: 129-133. Rotterdam: Balkema.

Gens, A., and Alonso, E. E. 2006. Aznalcóllar dam failure. Part 2: Stability conditions and failure mechanism. Géotechnique, 56(3): 185-201.

Heredia, J. E. Y. 2015. Thermo-hydro-mechanical behavior of unsaturated clayey soils via thermo/suction-controlled ring shear testing. Ph. D. Thesis, University of Texas at Arlington, Alington, US.

Hossain, J. 2013. Geohazard potential of rainfall induced slope failure on expansive clay. Ph. D. Thesis, University of Texas at Arlington, Arlington, US.

Hoyos, L. R., Velosa, C. L., and Puppala, A. J. 2014. Residual shear strength of unsaturated soils via suction-controlled ring shear testing. Engineering Geology, 172: 1-11.
Infante Sedano, J. A. 2006. A modified ring shear test device for testing hydro-mechanical behavior of saturated soils. Ph.D. thesis, University of Ottawa, Ottawa, Canada.
Infante Sedano, J. A., Vanapalli, S. K. and Garga, V.K. 2007. Modified ring shear apparatus for unsaturated soils testing. Geotechnical Testing Journal, 30(1): 39–47.
Kido, R. and Higo, Y., 2020. Microscopic characteristics of partially saturated dense sand and their link to macroscopic responses under triaxial compression conditions. Acta Geotechnica, 15(11): 3055-3073.
Kovacevic, N., Potts, D. M., and Vaughan, P. R. 2001. Progressive failure in clay embankments due to seasonal climate changes. In International Conference on Soil Mechanics and Geotechnical Engineering: 2127-2130.
Leroueil, S. 2001. Natural slopes and cuts: movement and failure mechanisms. Géotechnique, 51(3): 197-243.
Lian, B., Peng, J., Wang, X. and Huang, Q., 2020. Moisture content effect on the ring shear characteristics of slip zone loess at high shearing rates. Bulletin of Engineering Geology and the Environment, 79(2): 999-1008.
Liu, Y., and Vanapalli, S. K. 2019. Load displacement analysis of a single pile in an unsaturated expansive soil. Computers and Geotechnics, 106: 83-98.
Lupini, J. F., Skinner, A. E., and Vaughan, P. R. 1981. The drained residual strength of cohesive soils. Géotechnique, 31(2): 181-213.
Maquaire, O., Malet, J. P., Remaıtre, A., Locat, J., Klotz, S., and Guillon, J. 2003. Instability conditions of marly hillslopes: towards landsliding or gullying? The case of the Barcelonnette Basin, South East France. Engineering geology, 70(1-2): 109-130.
Ng, C. W. W., Zhan, L. T., Bao, C. G., Fredlund, D. G., and Gong, B. W. 2003. Performance of an unsaturated expansive soil slope subjected to artificial rainfall infiltration. Géotechnique. 53(2): 143-157.
Nyambayo, V. P., Potts, D. M. and Addenbrooke, T. I. 2004. The influence of permeability on the stability of embankments experiencing seasonal cyclic pore water pressure changes. In Advances in geotechnical engineering: proceedings of the Skempton Conference, Imperial College, London, 2: 898-910.
Postill, H., Helm, P. R., Dixon, N., Glendinning, S., Smethurst, J. A., Rouainia, M., Briggs, K. M., El-Hamalawi, A. and Blake, A. P. 2021. Forecasting the long-term deterioration of a cut slope in high-plasticity clay using a numerical model. Engineering Geology, 280: 105912.
Potts, D. M., Dounias, G. T. and Vaughan, P. R. 1990. Finite element analysis of progressive failure of Carsington embankment. Géotechnique, 40(1): 79-102.
Potts, D. M., Kovacevic, N., and Vaughan, P. R. 1997. Delayed collapse of cut slopes in stiff clay. Géotechnique, 47(5): 953-982.
Qi, S., and Vanapalli, S. K. 2016. Influence of swelling behavior on the stability of an infinite unsaturated expansive soil slope. Computers and Geotechnics, 76: 154-169.
Romero, E., Vaunat, J., and Merchán, V. 2014. Suction effects on the residual shear strength of clays. Journal of Geo-Engineering Sciences, 2(1-2): 17-37.
Russell, A. R., and Khalili, N. 2006. A unified bounding surface plasticity model for unsaturated soils. International Journal for Numerical and Analytical Methods in Geomechanics, 30(3): 181-212.

Sheng, D., Zhou, A., and Fredlund, D. G. (2011). Shear strength criteria for unsaturated soils. Geotechnical and Geological Engineering, 29(2): 145-159.
Skempton, A. W. 1964. Long-term stability of clay slopes. Géotechnique, 14(2): 77-102.
Take, W. A., and Bolton, M. D. 2011. Seasonal ratcheting and softening in clay slopes, leading to first-time failure. Géotechnique, 61(9): 757-769.
Vanapalli, S. K. 2009. Shear strength of unsaturated soils and its applications in geotechnical engineering practice. In Keynote Address. In Proceedings of 4th Asia-Pacific Conference on Unsaturated Soils. New Castle, Australia.
Velosa, C. L. 2011. Unsaturated soil behavior under large deformations using a fully servo/suction-controlled ring shear apparatus. Ph. D. Thesis, University of Texas at Arlington, Alington, US.
Vo, T., Taiebat, H., and Russell, A. R. 2016. Interaction of a rotating rigid retaining wall with an unsaturated soil in experiments. Géotechnique, 66(5): 366-377.
Wang, B., Vardon, P. J., and Hicks, M. A. 2018. Rainfall-induced slope collapse with coupled material point method. Engineering Geology, 239: 1-12.
Widger, R. A., and Fredlund, D. G. 1979. Stability of swelling clay embankments. Canadian Geotechnical Journal, 16(1): 140-151.
Zhou, A., and Sheng, D. 2015. An advanced hydro-mechanical constitutive model for unsaturated soils with different initial densities. Computers and Geotechnics, 63: 46-66.

CHAPTER 2 LITERATURE REVIEW[1]

2.1 Introduction

The shear stress increases rapidly with limited shear deformation associated with loading to a peak value and then drops gradually to a constant value with a further increase in the shear deformation. Such a characteristic stress-strain response is referred to as the strain-softening behavior. Unsaturated soils typically exhibit strain-softening behavior during the shearing process, especially under large suction values. A variety of geo-infrastructure (e.g., shallow foundations, retaining walls, pipelines, embankments, natural and manmade slopes) in the arid and semi-arid regions of the world are constructed with unsaturated soils or placed above the groundwater table where the soil is in an unsaturated state. These structures undergo a large progressive deformation prior to reaching failure conditions due to the influence of environmental factors (e.g., rainfall infiltration and wetting-drying cycles) (Widger and Fredlund 1979; Kovacevic et al. 2001; Ng et al. 2003; Take and Bolton 2011; Yerro et al. 2015; Qi and Vanapalli 2016; Vo et al. 2016; Al-Khazaali and Vanapalli 2019; Liu and Vanapalli 2019; Postill et al. 2020). As a result, the shear strength of soils reduces from peak to a post-peak shear strength value and this phenomenon significantly influences the mechanical behavior of those geo-infrastructures. Therefore, a thorough understanding of the strain-softening behavior is required for rational analyses and design of geo-infrastructure.

The mechanical characteristics of the strain-softening behavior of unsaturated soils have been extensively studied based on the experimental results from direct and triaxial shear tests (Cui and Delage 1996; Miao et al. 2002; Toll and Ong 2003; Tarantino and Tombolato 2005; Kayadelen et al. 2007; Estabragh and Javadi 2008; Hossain and Yin 2010a; Zhang et al. 2015; Patil et al. 2017; Liu et al. 2020a). Several researchers have investigated the soil fabric and the water phase changes based on the X-ray micro-CT images on unsaturated sands during the triaxial shearing process (Higo et al. 2011; Higo et al. 2013; Milatz and Grabe 2019; Wang et al. 2019; Kido and Higo 2020). These studies focus on strain-softening behavior of unsaturated soils from peak to critical

[1] The contents presented in this chapter are published as a journal article: **Yang, X.,** and Vanapalli, S. K. 2022. Mechanisms and modelling methods of strain-softening behavior of unsaturated soils: A state of the art review. *International Journal of Geomechanics*. (Accepted)

state that is associated with the dilation. However, relatively small shear deformations were investigated due to the limitations associated with the experimental apparatuses. The shear strength of saturated clays typically decreases after the critical state under large shear deformation due to the reorientation of the platy clay particles (Skempton 1970, 1985). During the last three decades, experimental studies were conducted based on conventional (Derbyshire et al. 1994; Dijkstra 1994; Maquaire et al. 2003; Fan et al. 2017; Lian et al. 2020) and suction-controlled ring shear apparatus (Infante Sedano and Vanapalli 2011; Hoyos et al. 2014; Romero et al. 2014) to investigate the strain-softening behavior of unsaturated soils under large shear deformation. These studies are valuable; however, more investigations are required for a comprehensive understanding of the strain-softening behavior of unsaturated soils.

Experimental studies associated with unsaturated soils are complex, expensive, and time-consuming. Due to this reason, some researchers proposed various prediction models for peak, critical and residual shear strength (PSS, CSS and RSS) of unsaturated soils (for example, Vanapalli et al. 1996; Toll and Ong 2003; Tarantino and Tombolato 2005; Gallipoli et al. 2008; Infante Sedano and Vanapalli 2011; Romero et al. 2014). Several interpretations of these shear strength equations were proposed considering the influence of soil fabric and water phase (for example, Vanapalli et al. 1996; Toll 2000; Karube and Kawai 2001; Gallipoli et al. 2008; Alonso et al. 2010; Infante Sedano and Vanapalli 2011). In addition, several numerical methods were developed for unsaturated soils to reproduce the strain-softening and dilative behavior based on different approaches, for example, the conventional plasticity (Alonso et al. 1990; Cui and Delage 1996), bounding surface plasticity (Russell and Khalili 2006; Yao et al. 2014; Zhou and Sheng 2015), disturbed state concept (Geiser et al. 2000) and elasto-viscoplasticity (Oka et al. 2006; De Gennaro and Pereira 2013; Oka et al. 2019).

A state-of-the-art review of the studies related to the interpretation and modelling of the strain-softening behavior of unsaturated soils over the last three decades however remains outstanding. This chapter provides a comprehensive summary of these studies from the literature.

2.2 Peak, critical, and residual state of saturated soils

The strain-softening of saturated soils can be associated with two key factors: (i) the strain-softening from peak to critical state is associated with the localized dilation inside the shear band;

(ii) the strain-softening from critical to residual state is associated with the reorientation of platy clay particles adjacent to the sliding surface (Bishop et al. 1971; Lupini et al. 1981). Figure 2.1 summarizes the strain-softening behavior of saturated soils (including the peak, critical and residual state) under drained shearing at constant effective normal stress. The behaviors of the saturated soils during strain-softening process are succinctly described in Table 2.1.

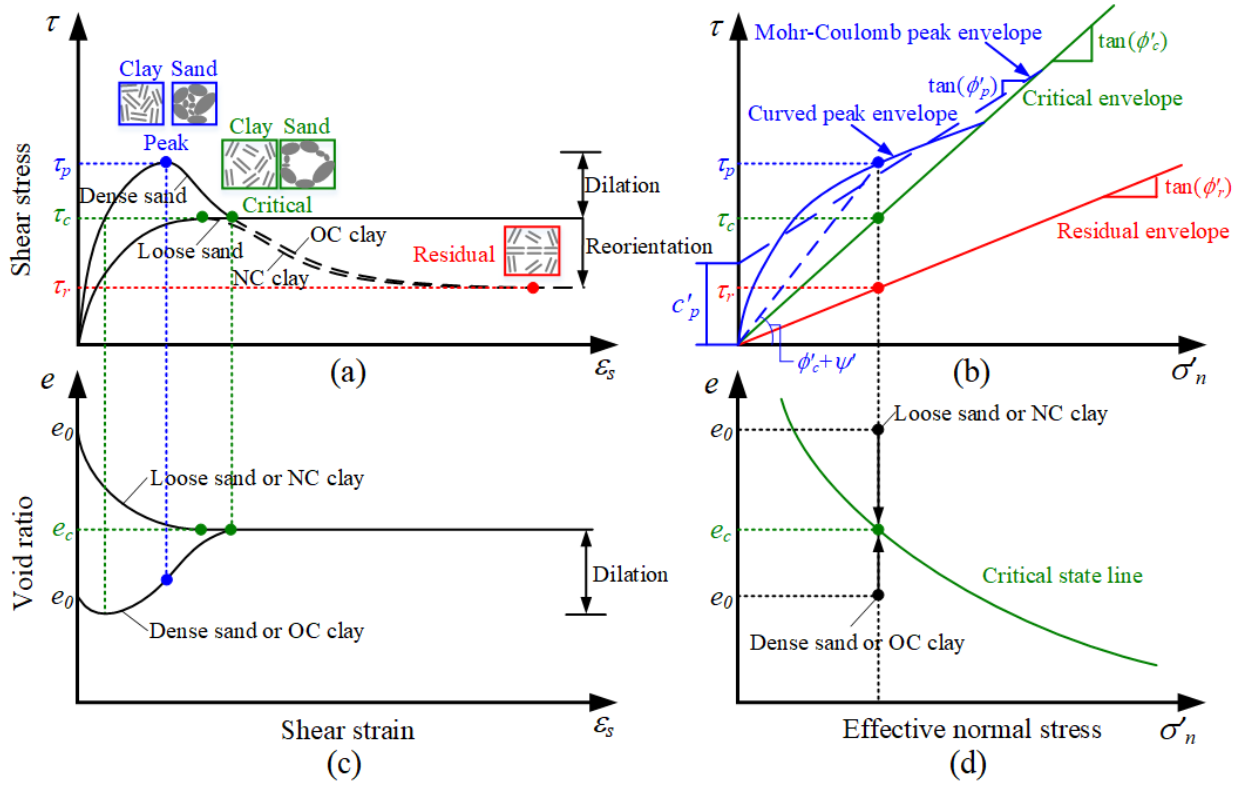

Figure 2.1 Strain-softening behavior of saturated soils: (a) shear stress change with shear strain; (b) shear stress change in $\tau - \sigma'_n$ plane; (c) volume change with shear strain; and (d) volume change in e $- \sigma'_n$ plane (modified after Skempton 1985 and Atkinson 2007)

Roscoe et al. (1958) proposed the concept of critical state of a soil specimen where incremental shear strain would not contribute to any change in void ratio and shear stress (Figures 2.1a and 2.1c). The expected soil behaviors at critical state are summarized in Table 2.1. Soils will ultimately reach a unique condition (i.e., critical state) independent of the initial states of soils provided that the flow of soil particles remains turbulent (Atkinson 2007). Prior to reaching the critical state, the specimens of loose sand and normally consolidated (NC) clay exhibit compressive and strain-hardening behavior. In contrast, the specimens of dense sand and over

consolidated (OC) clay exhibit dilative and strain-softening behavior, with an obvious peak state (Figures 2.1a and 2.1c). The strain-softening behavior of saturated soils from peak to critical state can be interpreted in terms of strain energy and the soil fabric as below.

According to the power assumption in the Camclay model (Schofield and Wroth 1968), the plastic work due to external loading (i.e., $pd\varepsilon_v^p + qd\varepsilon_s^p$, where p and q are deviator and mean stress; $d\varepsilon_v^p$ and $d\varepsilon_s^p$ are plastic volumetric and shear strain) equals the frictional work (i.e., $Mp|d\varepsilon_s^p|$, where M is the critical state frictional constant). This means a dilating specimen ($qd\varepsilon_s^p = Mp|d\varepsilon_s^p| - pd\varepsilon_v^p$, where $d\varepsilon_v^p < 0$) can sustain a deviator stress greater than that at critical state ($qd\varepsilon_s^p = Mp|d\varepsilon_s^p|$). Many studies related to the stress-dilatancy relationship of saturated soils (Rowe 1962; Schofield and Wroth 1968; Roscoe and Burland 1968; Nova and Wood 1979; Bolton 1986; Wood and Belkheir 1994; Li and Dafalias 2000) have highlighted the stress ratio, q/p, is dependent on the critical state friction constant, M, and dilatancy, $d\varepsilon_v^p/d\varepsilon_s^p$. This means, the stress ratio, q/p, can increase with increasing dilatancy, and then decrease with decreasing dilatancy until the critical state is reached. There will be no more dilatancy beyond this state. The PSS, τ_p, depends on the maximum dilatancy that is related to the void ratio at peak state. As a result, there is no well-defined relationship for the τ_p and σ_n' until it reaches the critical state. Atkinson (2007), due to this reason, suggested that the PSS can be described using three different methods: (i) using the Mohr–Coulomb equation with a non-zero cohesion, (ii) using a fitted curved envelope, (iii) using the stress-dilatancy relationship as shown in Figure 2.1b and Table 2.1.

The strain-softening behavior of saturated soils can also be interpreted in terms of the soil fabric based on the movements of soil particles (Figure 2.1a) (Mitchell and Soga 2005; Atkinson 2007), the evolution of shear bands (Andò et al. 2012; Higo et al. 2013; Takano et al. 2015) and the change in the loading transmission mode (Oda and Kazama 1998; Mitchell and Soga 2005; Rechenmacher et al. 2010). These details are also summarized in Table 2.1.

Table 2.1 Characteristics of the strain-softening behavior of saturated soils under drained condition

		Pre-peak state	Peak state	Post-peak state	Critical state	Residual state (clayey soils)
Shear strength behavior	—	The shear stress increases and exceeds the critical shear strength due to a lower void ratio in comparison to critical state.	(i) $\tau_p = c'_p + \sigma'_n \tan\phi'_p$; (ii) Fitting a curved line between τ_p and σ_n'; (iii) $\tau_p = f(\sigma'_n, \phi'_c, \psi')$;	The shear stress decreases gradually due to a looser structure of the soil particles inside the shear band.	$\tau_c = \sigma'_n \tan\phi'_c$	$\tau_r = \sigma'_n \tan\phi'_r$
Deformation behavior	Volumetric strain behavior	The dilation zones are disorganized over the specimen.	The dilation zones are disorganized over the specimen.	Localized dilation zones concentrate in the localized shear strain band.	The dilation is localized in a well-formed shear band.	No obvious volume change happens after critical state.
	Shear strain behavior	More shear strain will accumulate in the dilation zones that are weaker than surrounding zones. At low deformation, several shear zones are distributed over the specimen. Around peak, shear strain localizes in a wide banded area.	The shear strain is localized in a wide banded area. The magnitude of shear strain is on the order of 1%	The shear strain become more localized due to more significant localized dilation inside the shear band. Thus, the wide localized banded area progressively thins to a narrower band.	The shear strain is localized in a well-formed shear band. The magnitude of shear strain is on the order of 10%	The shear deformation is along a polished sliding surface. The magnitude of shear displacement exceeds 100 mm typically.
Mechanism	Specimen state	Relatively homogeneous elastoplastic solid	Relatively homogeneous elastoplastic solid	—	Soils inside the shear band is turbulent flow of viscous fluid, and soils on its two opposite sides act as rigid bodies.	The specimen is separated into two blocks along a polished sliding surface.
	Particle scale behavior	The soil particles are interlocked together and cannot slip easily to fall into the neighboring voids. Instead, they roll up over each other, which results in the dilation.	The soil particles are interlocked together.	Inside the shear band, due to localized large shear strain, soil particles keep rolling, the interlocking is destroyed, and large voids are generated, which results in the significant localized dilation inside the shear band.	Inside the shear band, the original interlocking structure is destroyed, and the soil particles move randomly.	The particles near the sliding surface are reoriented and become parallel to each other.
	Loading transmission (Granular material)	The major principal stress is transmitted through soil columns parallel to its direction.	The columns start buckling.	The buckling of columns gradually concentrates to the shear band.	The buckling columns keep collapsing and forming continuously.	—
	Source of shear resistance	Interparticle friction and interlocking	Interparticle friction and interlocking	—	Interparticle friction and the rotational resistance between particles inside and outside shear band	The friction between the reoriented particles along sliding surface

Note: τ_p, τ_c and τ_r = peak, critical and residual shear stress; ϕ_p', ϕ_c' and ϕ_r' = peak, critical and residual effective friction angle; c_p' = effective peak cohesion; ψ' = dilation angle of saturated soils.

In an ideal case, the soil can ultimately reach the critical state where it continues to deform under constant stress and constant volume as defined by Roscoe (1958). In practice applications, however, the shearing behavior of clays is much more complex (Skempton 1970). As shown by a continuous line with dashes in Figure 2.1a, after the critical state, the shear strength of clays typically exhibits a further decrease and reaches to a lower and constant value under large deformation (i.e., RSS).

Lupini et al. (1981) explained the residual state based on the proportions of particles with different shapes and the coefficient of interparticle friction. For the soils that mainly consist of platy particles with low interparticle friction, the platy particles can gradually reorient under large shear deformation contributing to a significant decrease in shear strength, as described in Table 2.1. There is no preferred particle orientation for the soils that predominantly consist of round particles or platy particles with high interparticle friction. The shear strength of such soils will not decrease after the critical state is reached; in other words, the RSS is equal to the critical value. The residual friction angle, $\phi'_r = \arctan(\tau_r/\sigma_n')$, is widely used to describe the RSS behavior. However, various research studies (Bishop et al. 1971; Lupini et al. 1981; Skempton 1985; Stark and Eid 1994; Mesri and Shahien 2003) showed that the relationship between the RSS and effective normal stress is nonlinear. Stark and Eid (1994) suggested that the higher effective normal stress can compress the initial edge-to-face interactions to form a face-to-face interaction and increases the contact area at residual state, which contributes to the nonlinearity of RSS envelope. In addition, for clayey soils, the RSS is sensitive to many factors which include particle shape, grading, mineralogy, and pore water chemistry (Lupini et al. 1981). Some researchers have suggested relationships between the RSS and soil index properties (e.g., clay fraction, Atterberg limits), which are extensively reviewed in the literature (Lupini et al. 1981; Stark and Eid 1994; Hayden et al. 2018).

2.3 Interpretation of strain-softening behavior of unsaturated soils

2.3.1 Strain-softening behavior associated with dilation

During the last three decades, several investigations were undertaken to study the strain-softening behavior of unsaturated soils using different experimental techniques, which include the unsaturated consolidated drained direct shear tests (Zhan and Ng 2006; Hossain and Yin 2010a; Kim et al. 2010; Schnellmann et al. 2013; Monghassem et al. 2021), triaxial shear tests (Cui and Delage 1996; Rampino et al. 2000; Miao et al. 2002; Cunningham et al. 2003; Rahardjo et al. 2004;

Geiser et al. 2006; Kayadelen et al. 2007; Thu et al. 2007; Estabragh and Javadi 2008; Nicotera et al. 2015; Zhang et al. 2015; Ma et al. 2016; Patil et al. 2017; Liu et al. 2020a; Yang et al. 2021; Liu et al. 2021; Cai et al. 2022) and unsaturated constant water content direct shear tests (Tarantino and Tombolato 2005) and triaxial shear tests with suction measurements (Ng and Chiu 2003; Toll and Ong 2003; Jotisankasa et al. 2009; Fern et al. 2016; Kim et al. 2016; Rasool and Aziz 2020; Kouzegaran et al. 2021; Shire and Standing 2021). These experimental studies have shown the strain-softening behaviors of unsaturated and saturated soils are similar. However, the matric suction can have a significant influence on certain characteristics of strain-softening behavior of unsaturated soils.

Several experimental studies (Cui and Delage 1996; Cunningham et al. 2003; Rahardjo et al. 2004; Jotisankasa et al. 2009; Patil et al. 2017) have shown that the strain-softening behavior of unsaturated soils is associated with the generation of shear band. As the suction increases, the failure mode of unsaturated specimens changes progressively from barreling without a shear band, to barreling with a shear band, and finally non-barreling with a shear band (Jotisankasa et al. 2009; Patil et al. 2017). The general evolution pattern of the shear band of unsaturated soil specimens is similar to saturated soil specimens as summarized in Table 2.1 (Higo et al. 2013; Li et al. 2015; Kido and Higo 2019; Milatz et al. 2021).

The microstructure of soil particles and the change of water phase within the shear band of unsaturated sands associated with the dilation were investigated using X-ray micro-CT and trinarized CT images (Higo et al. 2011; Higo et al. 2013; Khaddour 2015; Kido and Higo 2019; Milatz and Grabe 2019; Wang et al. 2019; Kido and Higo 2020). Figure 2.2 presents a typical example of the CT images of an unsaturated sand specimen during drained triaxial compression test. The strain-softening of unsaturated soils can be attributed to the change in the soil fabric inside the shear band consistent with the saturated soils. In addition, they can also be associated to the change in water phase within the shear band.

The experimental studies about the soil fabric (Higo et al. 2011; Higo et al. 2013) suggest that the changes of the soil fabric within the shear band in unsaturated soils is similar to saturated soils (see Table 2.1 for more details). The strain-softening process of unsaturated soils is strongly related to

its dilation behavior and soil fabric which can be explained using Figure 2.3; Table 2.1 summarizes some succinct details.

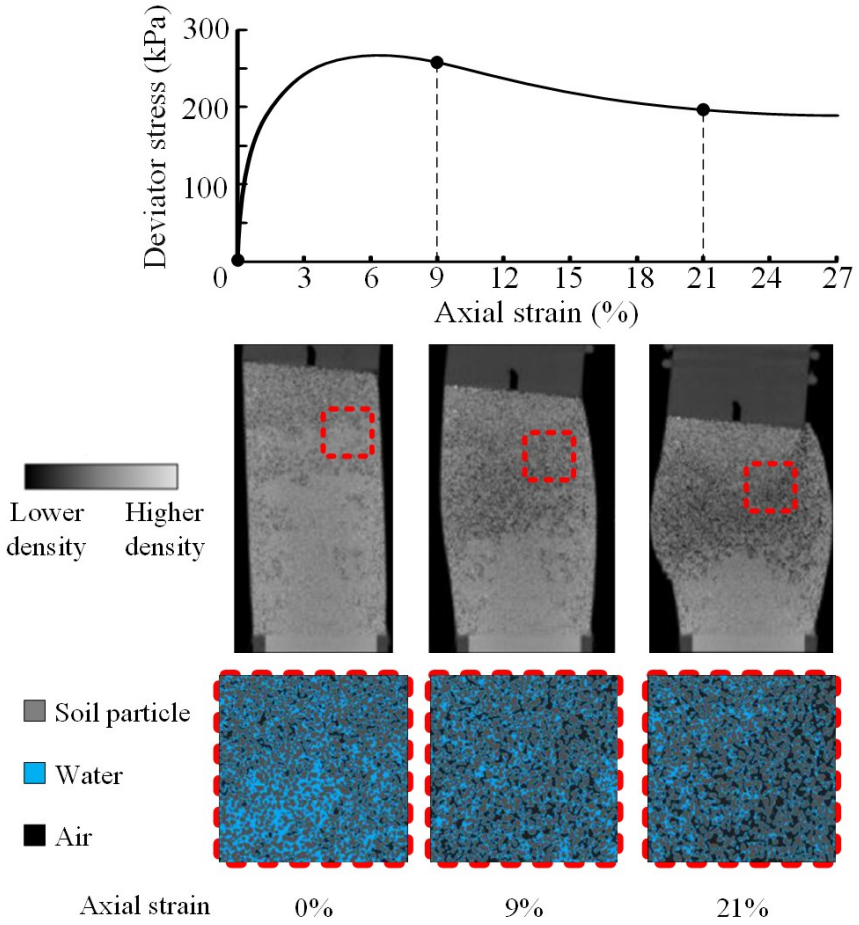

Figure 2.2 CT images and local trinarized images of unsaturated sands under drained triaxial compression test (modified after Kido and Higo 2020)

The experimental studies about the water phase (Khaddour 2015; Kido and Higo 2019; Milatz and Grabe 2019; Wang et al. 2019; Kido and Higo 2020) showed that the local degree of saturation within the shear band decreases significantly during shearing (Figure 2.2). A large number of water menisci exist until the peak state; however, the water menisci within the shear band decrease as shearing progresses. The local degree of saturation and the number of water menisci within the shear band are lower than the corresponding values outside the shear band. This may be attributed to the lower water retention capability inside the shear band caused by the large voids that are typically generated within the shear band during shearing due to localized dilation. When the

matric suction is constant, the pore water will be drained out from those large voids (Figures 2.3B′ - 2.3D′). In addition, as shown in Figure 2.3D′, some water menisci inside the shear band will rupture due to the continuous movement and rotation of soil particles and the water will flow away from the shear band (Khaddour 2015). As summarized in Vanapalli et al. (1996), matric suction influence is transmitted to the soil particles through the water menisci area in contact with the soil particles or aggregates. The local loss of water menisci area can reduce the contribution of matric suction towards shear strength as shearing progresses, which contributes to the strain-softening behavior of unsaturated soils.

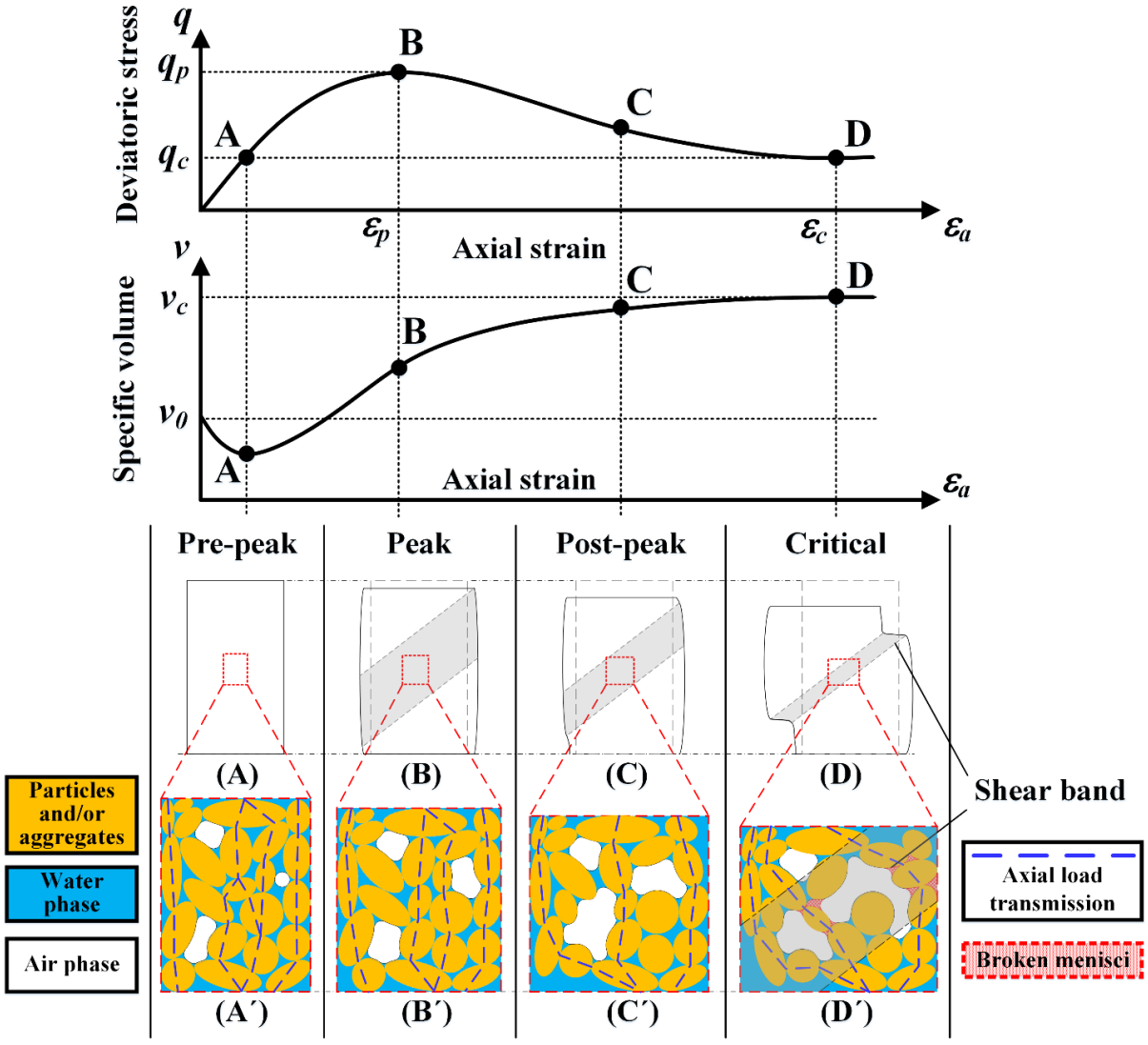

Figure 2.3 Interpretation of strain-softening behavior of unsaturated soils associated with dilation: (A–D) specimen state; (A′–D′) particle scale behavior

In summary, the strain-softening of unsaturated soils associated with the dilation can be explained by the destruction of the original structure of soil particles and the local loss of water menisci area inside the shear band. This background can be extended to explain the influence of matric suction on the strain-softening behavior of unsaturated soils, which is succinctly summarized below:

(1) Influence of suction on dilatancy behavior of unsaturated soils:

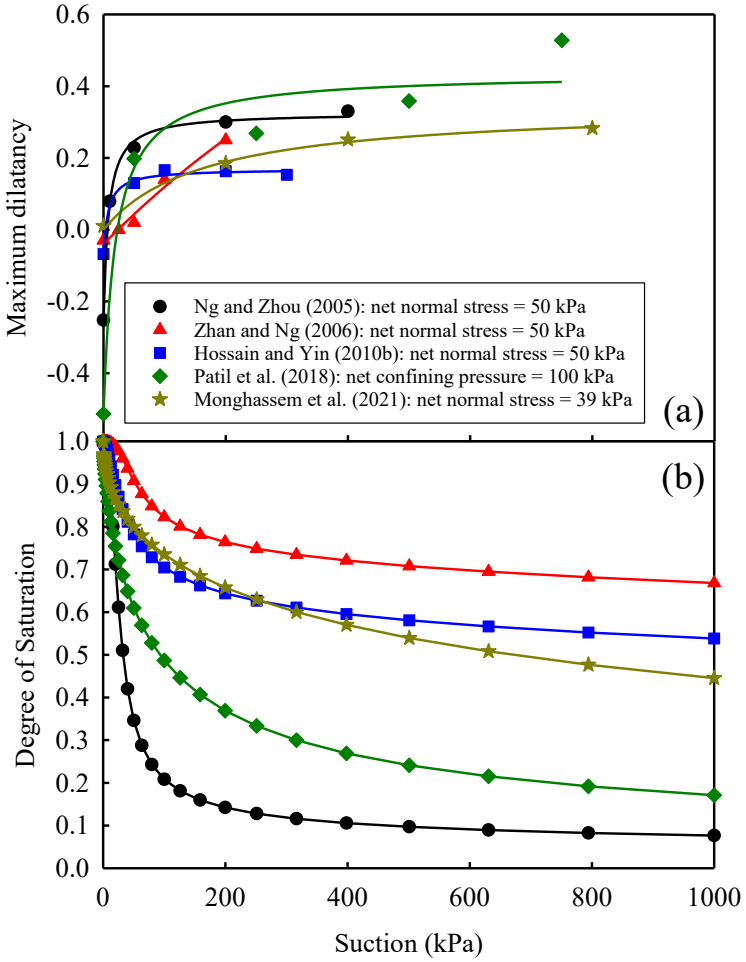

Figure 2.4 Influence of suction on the dilatancy of unsaturated soils in CD triaxial shear tests: (a) variation of maximum dilatancy with suction (positive value of the maximum dilatancy represents dilation); (b) Soil-Water Characteristic Curves

Many experimental studies (Cui and Delage 1996; Ng and Chiu 2003; Ng and Zhou 2005; Zhan and Ng 2006; Zhao and Zhang 2014; Hossain and Yin 2010b; Fern et al. 2016; Patil et al. 2018; Monghassem et al. 2021; Cai et al. 2022) have shown that the suction can enhance the dilatancy of unsaturated specimens. Figure 2.4 summarizes the variations of maximum dilatancy with

suction for several unsaturated soils under constant net normal stress in suction-controlled direct shear tests or under constant net confining pressure in suction-controlled triaxial shear tests. The collected unsaturated soils include compacted completely decomposed granite (Ng and Zhou 2005; Hossain and Yin 2010b), compacted expansive clay (Zhan and Ng 2006), compacted SM (Patil et al. 2018), and CL adobe (Monghassem et al. 2021). The osmotic technique was used for controlling suction by Monghassem et al. (2021), while the axis-translation technique was used in other four tests. As a reference, the corresponding Soil-Water Characteristic Curves (SWCC) of these soils are also presented in Figure 2.4. All the five experimental results show a significant increase in the dilatancy of unsaturated soils with increasing suction within the studied suction range (0 – 1000 kPa). However, the relationships between the maximum dilatancy and suction are nonlinear. The rate at which the maximum dilatancy increases with suction is greater in the lower suction range and decreases gradually with increasing suction. This nonlinear trend is consistent with the SWCC behavior, where the decrease in degree of saturation is significant in the lower suction range compared to the higher suction range. In addition to the magnitude of suction, several studies (Goh et al. 2014; Chen et al. 2018; Liu et al. 2020b) also show the influence of the suction history (i.e., drying-wetting cycles) on the dilatancy behavior of unsaturated soils.

The suction-induced enhancement in dilatancy can be attributed to several possible reasons. It is reasonable to suggest that the soil particles are strongly bonded together due to suction working as inter-particle force through the liquid bridges (Kido and Higo 2020). In other words, this can contribute to a stronger interlocking among soil particles; as a result, soil particles cannot slip easily and tend to roll over each other during shearing (Zhao and Zhang 2014). In addition, the suction-induced soil fabric change can also influence the dilatancy of unsaturated soils. Ng and Zhou (2005) attributed the suction-induced enhancement in dilatancy to the lower void ratio of specimens under higher suction. Alonso et al. (2007) indicated the enhanced dilatancy of unsaturated granular aggregates due to suction can be attributed to the generation of stronger particles at lower relative humidity. Some studies on fine-grained soils (Hoyos et al. 2014; Zhao and Zhang 2014) indicated that the suction-induced stiffening of the aggregations associated with fine grains can contribute to significant dilation in soil. Recently, the experimental results (Ng et al. 2020a) showed, at a given void ratio, recompacted loess with more uniform distribution of voids exhibited higher dilation than intact loess with larger number of large voids. This means the

increase in dilatancy associated with an increase in suction can be attributed to the distribution between micro- and macro-porosity.

(2) Influence of suction on shear strength behavior of unsaturated soils:

Early research studies (Bishop 1959; Escario and Saez 1986; Gan et al. 1988; Vanapalli et al. 1996) highlighted the contribution of matric suction towards to an increase in the PSS of unsaturated soils in the low suction range irrespective of the type of soil. In simple terms, matric suction can be assumed to pull the soil particles together that contributes to a greater contact pressure between the soil particles with air-water interphase. At peak state, the greater contact pressure enhances the frictional resistance and interlocking among soil particles; there is significant resistance against slipping. Several researchers (Toll 1990; Rampino et al. 2000; Toll and Ong 2003; Tarantino and Tombolato 2005; Estabragh and Javadi 2008; Patil et al. 2017; Monghassem et al. 2021; Cai et al. 2022) based on extensive experimental studies have shown the matric suction can also contribute to an increase in the CSS of unsaturated soils. This phenomenon can be associated with the water menisci that are available within the shear band even at critical state (Figures 2.2 and 2.3D′), which can contribute to a greater contact pressure between the soil particles that offers rotational resistance amongst the soil particles.

Some research studies (Cui and Delage 1996; Zhan and Ng 2006; Estabragh and Javadi 2008; Hossain and Yin 2010a; Patil et al. 2017; Monghassem et al. 2021) suggested that the matric suction enhances the brittleness of the soil specimen (i.e., the difference between PSS and CSS). The increased tendency of dilation associated with higher matric suction contributes to the development of larger voids and greater rotations of soil particles within the shear band during shearing. This means there will be a greater decrease in the local degree of saturation and the number of water menisci within the shear band due to shearing of specimen with higher matric suction. In other words, the specimen with higher matric suction exhibits a greater reduction in density, grain contacts and water menisci area within the shear band during shearing. Due to this reason, there will be a more pronounced reduction from PSS to CSS for specimens with higher matric suction that is subjected to shear.

(3) Influence of suction on microstructure of unsaturated soils:

The matric suction can influence the soil fabric which in turn can influence the mechanical behavior of unsaturated soils. Some studies (Delage et al. 1996; Romero et al. 1999; Vanapalli et al. 1999) suggested that the aggregation of soil particles can be formed in unsaturated fine-grained soils compacted at dry side of optimum. In unsaturated condition, this aggregated fabric can be maintained during shearing because matric suction provides the requisite shear strength to the aggregates. Due to this reason, the aggregates can act as large individual particles during shearing. Critical state is reached within the macrostructure of the soil; however, the same is not true for the microstructure of individual aggregates (Toll 1990; Wheeler and Sivakumar 1995; Toll and Ong 2003). The higher matric suction typically results in stiffer aggregates; hence the soil behavior is similar to a coarse-grained soil. In other words, dilatancy behavior of the soil enhances the brittle nature as stiffer aggregates are formed due to the influence of higher matric suction.

2.3.2 Strain-softening behavior under large deformation

Most of current experimental studies on the strain-softening behavior of unsaturated soils are performed using modified suction-controlled direct shear or triaxial shear testing apparatuses, which can only provide information of limited shear deformation. In these studies, the strain-softening behavior of unsaturated soils from peak to critical state have been well investigated. However, studies related to the residual state behavior of unsaturated soils under larger shear deformation are rather limited. Romero et al. (2014) attributed the lack of relevant studies to two factors; namely: (i) extending an assumption that the water menisci across the sliding surface are broken at residual state and the suction cannot contribute to RSS; and (ii) the difficulty associated with developing a closed suction control system by modifying ring shear cells for extending the axis translation technique.

Despite the difficulties associated with experimental procedures, there has been significant progress over the last three decades based on the contributions of several investigators for better understanding the residual state behavior of unsaturated soils. For example, some researchers studied the RSS of unsaturated loess with different water contents using conventional ring shear tests (Derbyshire et al. 1994; Dijkstra 1994). This approach was also extended by other researchers for other soils (Maquaire et al. 2003; Fan et al. 2017; Hu et al. 2018; Lian et al. 2020; Chen et al. 2021; Kang et al. 2022). The focus of all these studies was directed towards understanding the influence of water content (or degree of saturation) on the RSS of unsaturated soils. Despite these

studies based on conventional ring shear or reversal direct shear tests, understanding of the residual state behavior of unsaturated soils still is limited. This may be attributed to the lack of understanding of the independent contribution of suction in these tests.

For this reason, several modified suction-controlled ring shear apparatuses have been developed during the last fifteen years extending the axis translation technique (Infante Sedano et al. 2007; Hoyos et al. 2011) and the vapor equilibrium technique (Merchán et al. 2011). Using these apparatuses, several researchers during the last decade have investigated the residual state behavior of unsaturated soils both in the low (Infante Sedano and Vanapalli 2011; Hoyos et al. 2014; Heredia 2015) and high (Vaunat et al. 2006; Vaunat et al. 2007; Merchán et al. 2008; Romero et al. 2014) suction range. All these experimental studies highlighted the contribution of suction to the RSS even at relatively large displacements (i.e., greater than 100 mm).

Research studies related to the influence of suction on soil fabric and water phase under relatively large shear deformation are still limited. However, some indirect information about the soil fabric can be derived from the available literature. Romero et al. (2014) performed a series of ring shear tests on four different clays under high total suction (> 10 MPa) and suggested that the RSS increase was entirely due to an increase in the residual friction angle associated with the total suction. This phenomenon was attributed to the aggregated structure that was reinforced by observations of the pore size distribution of a clay sample that presented two dominant pore modes after being sheared to residual state (Merchán et al. 2008). This explanation provides credence to the aggregated structure associated with drying that can be maintained during the residual state under high total suction. The strain-softening under large deformation may be associated with reorientation of the stiff aggregates. Therefore, an increase in the residual friction angle with imposed total suction can be attributed to the enhancement of the size, stiffness, and surface roughness of these aggregates due to the contribution arising from total suction.

The experimental results of SM specimens sheared under relatively low matric suction (0 – 100 kPa) reported by Hoyos et al. (2014) were consistent with Romero et al. (2014) results on clay specimens. The residual friction angle with respect to net normal stress increased with increasing matric suction, which may indicate the influence of the imposed matric suction on the fabric of the unsaturated SM specimen even after being sheared to residual state. In addition, the SEM

micrographs of the unsaturated SM specimen near the sliding surface (Figures 2.5a and 2.5b) showed the particles after shearing under large deformation were more angular in shape and exhibited a wider range of sizes (Velosa 2011), which may indicate the crushing of sand particles under large shear deformation.

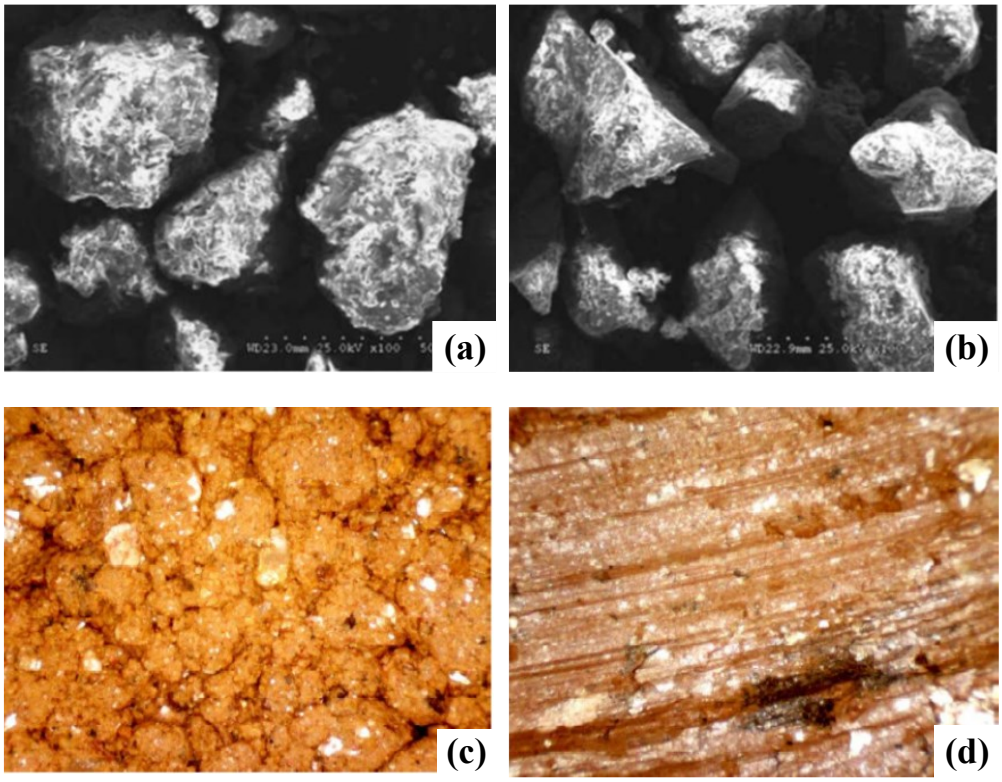

Figure 2.5 Images of unsaturated soils before and after suction-controlled ring shear tests (modified after Velosa 2011): (a) SEM micrographs of SM specimen before shearing; (b) SEM micrographs of SM specimen after shearing; (c) digital images of SC-SM specimen before shearing; (d) digital images of SC-SM specimen after shearing

However, Hoyos et al. (2014) and Infante Sedano and Vanapalli (2011) suggested that the residual friction angle with respect to net normal stress was constant with increasing matric suction, based on the experimental results of SC-SM specimens (sheared under 0 – 100 kPa matric suction) and glacial till specimens (sheared under 0 – 400 kPa suction). These results suggest the imposed matric suction cannot influence the fabric of the tested materials when it is sheared to the residual state. This deduction may be reinforced by the digital images of the SC-SM specimen near the

sliding surface (Figures 2.5c and 2.5d), characterized by a polished and bright sliding surface, clearly indicating a reorientation of platy clayey minerals along the surface.

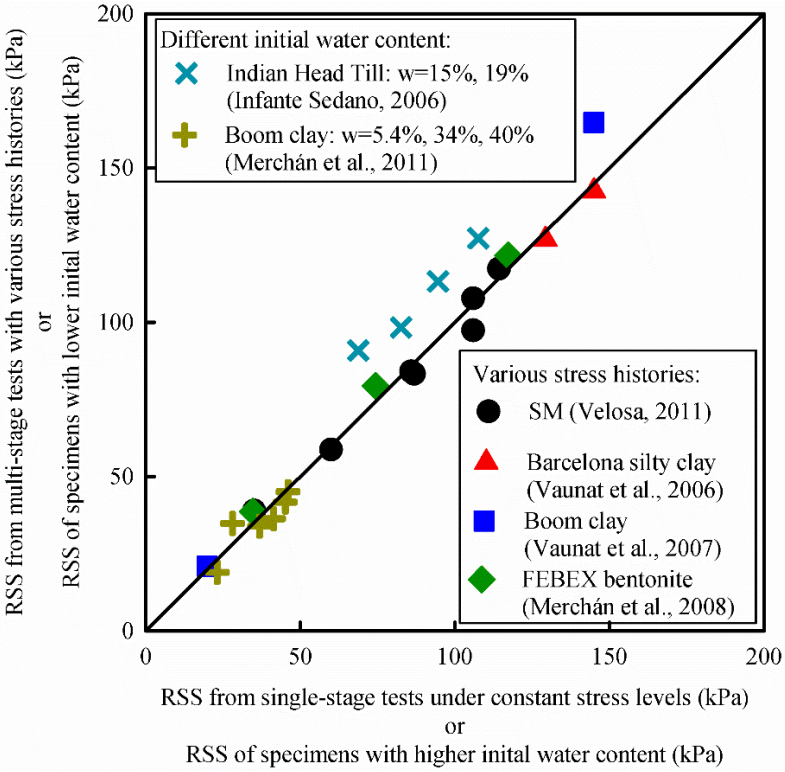

Figure 2.6 Influence of history specific structure on the RSS of unsaturated soils

Figure 2.6 provides comparison between the values of RSS of the unsaturated specimens that were sheared under the same normal stress and suction level but prepared at different initial water contents that contributes to different soil structures or prepared with different stress histories. The summarized results of RSS of unsaturated soils suggest that they are not influenced by the initial water contents and stress histories for identical stress levels at residual state. This finding can be reinforced by the observation of the SWCC of the unsaturated specimens that have been sheared using the ring shear apparatus (Infante Sedano and Vanapalli 2011). The experimental results showed a unique SWCC behavior irrespective of the specimen's initial compaction water content (i.e., dry or wet of optimum condition) and the stress path experienced by the specimens (i.e., constant loading condition or constant volume condition). This means any history specific (i.e., compaction water content, initial stresses, volume changes) structure of the soil can be erased if shear deformations are large enough.

In summary, suction is shown to have a significant influence on the residual state behavior of unsaturated soils even if the shear displacement has reached 100 mm. However, the micro-mechanism is still unclear, which may be attributed to many factors including the soil physical properties, suction level, state of pore water and others. The experimental research about the residual state behavior of unsaturated soils under large shear deformation are still far from conclusive. Due to this reason, more experimental data and further studies are required for better understanding of the shear strength behavior of unsaturated soils under large shear deformation.

2.4 Prediction models for PSS, CSS and RSS of unsaturated soils

2.4.1 PSS and CSS prediction model

Fredlund et al. (1978) extended the Mohr-Coulomb shear strength criterion of saturated soils in terms of two independent stress variables, (σ_n - u_a) and (u_a - u_w), to interpret the shear strength behavior of unsaturated soils, using the equation given below:

$$\tau = c'' + (\sigma_n - u_a)\tan\phi^a + (u_a - u_w)\tan\phi^b \tag{2.1}$$

where τ is shear strength; (σ_n - u_a) is net normal stress; (u_a - u_w) is matric suction; c'' is cohesion intercept of shear strength envelopes in τ – (σ_n - u_a) – (u_a - u_w) space; ϕ^a is friction angle with respect to net normal stress; ϕ^b is friction angle with respect to matric suction.

This equation can also be written in the q – (p - u_a) – (u_a - u_w) space as suggested by Toll (1990):

$$q = m'' + (p - u_a)M^a + (u_a - u_w)M^b \tag{2.2}$$

where q is deviator stress; (p - u_a) is net mean stress; m'' is intercept of shear strength envelopes in q – (p - u_a) – (u_a - u_w) space; M^a is stress ratio with respect to net mean stress; M^b is stress ratio with respect to matric suction.

Bishop (1959) suggested interpreting the shear strength of unsaturated soils using the equation below:

$$\tau = c' + [(\sigma_n - u_a) + \chi(u_a - u_w)]\tan\phi' \tag{2.3}$$

where c' is effective cohesion of saturated soils; ϕ' is effective internal friction angle of saturated soils; χ is a material parameter that is often assumed to be a function of degree of saturation, S, or suction.

Equation 2.3 can also be written in a form consistent with Equation 2.1 assuming $\tan\phi^a = \tan\phi'$ and $\tan\phi^b = \chi\tan\phi'$. Therefore, in terms of estimating the magnitude of shear strength, Equation 2.3 can be considered as a special case of Equation 2.1.

As shown in Equations 2.1 – 2.3, the shear strength of unsaturated soils consists of three parts, namely; the cohesion, the shear strength due to net normal stress and the shear strength due to suction. Among the three shear strength parameters (c'', ϕ^a, and ϕ^b), c'' is typically assumed to be constant and $\tan\phi^b$ decreases nonlinearly with respect to suction. However, the patterns of $\tan\phi^a$ variation with respect to suction reported in the literature are not consistent (Figure 2.7). The published experimental data from the literature have shown that $\tan\phi^a$ may be a constant value with respect to suction for several investigated soils (Gan et al. 1988; Vanapalli et al. 1996; Rampino et al. 2000; Wang et al. 2002; Tarantino and Tombolato 2005), or it may increase with suction (Escario and Saez 1986; Toll 1990; Wheeler and Sivakumar 1995; Sivakumar et al. 2010), or it may decrease with suction (Delage and Graham 1995; Maatouk et al. 1995; Estabragh and Javadi 2008). However, the comprehensive understanding of the mechanism associated with the variation in $\tan\phi^a$ with respect to suction is still not clear, despite some possible explanations (Toll 2000; Toll and Ong 2003; Gallipoli et al. 2008). Conclusions of Delage and Graham (1995) that more research is required to investigate the influence of various parameters, such as the soil type, grain size distribution, plasticity and initial density for better understanding the variation of $\tan\phi^a$ with respect to suction should receive attention, which is still valid after twenty-five years.

For this reason, the existing shear strength prediction models can be divided into two groups based on how they describe the variation of $\tan\phi^a$; namely, (i) $\tan\phi^a$ equal to $\tan\phi'$, (ii) $\tan\phi^a$ varying with suction. In addition, these models can be formulated in terms of two independent stress state variables (σ_n - u_a) and (u_a - u_w) or three variables (σ_n - u_a), (u_a - u_w) and S (Tarantino 2011). For the models that are based on two independent stress state variables (σ_n - u_a) and (u_a - u_w), no other material parameter is required; therefore, they are simple and can be easily embodied into a constitutive model. For those based on three variables, despite an additional parameter, S,

contained in the models, they can consider the influence of water menisci area, volume change and soil fabric and other parameters. The parameter, *S*, however, is not an independent variable, since there is a relationship between *S* and suction, which is referred to as SWCC. For this reason, the SWCC equations (for example, van Genuchten 1980; Fredlund and Xing 1994) need to be introduced as a tool to calculate *S*. A variety of prediction models for PSS and CSS of unsaturated soils have been proposed in the literature, which have been well summarized and evaluated in previous review studies (Vanapalli 2009; Sheng et al. 2011). Therefore, in this study, only widely used prediction models for PSS and CSS of unsaturated soils are summarized (Table 2.2) to discuss the typical methods of incorporating the influence of the soil fabric and water phase on the shear strength in the prediction models of $\tan\phi^a$ and $\tan\phi^b$.

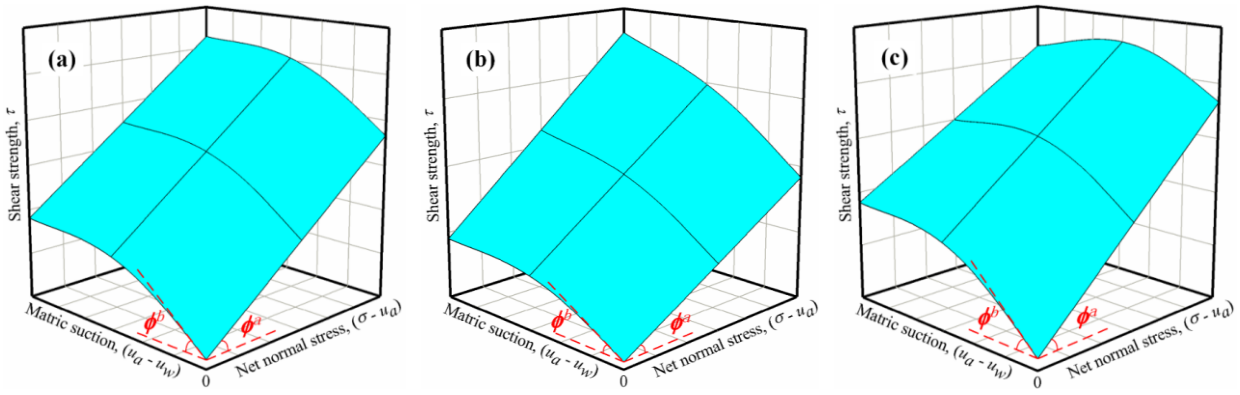

Figure 2.7 Different shapes of shear strength surfaces of unsaturated soils: (a) shear strength surface with constant ϕ^a; (b) shear strength surface with increasing ϕ^a; (c) shear strength surface with decreasing ϕ^a (modified after Delage 2002)

Table 2.2 Commonly used models for prediction of the peak shear strength and critical shear strength

Model		c'' or m''	$\tan\phi^a$ or M^a	$\tan\phi^b$ or M^b	Fitting parameters
Models with constant $\tan\phi^a$	Fredlund et al. (1978); Alonso et al. (1990)	c' or 0	$\tan\phi'$ or M'_c	$\tan\phi^b$ or kM'_c M'_c: slope of CSS envelope of saturated soils in $q - p'$ space	ϕ^b or k
	Wheeler and Sivakumar (1995)	0	M'_c	$(u_a - u_w)M^b = \mu(u_a - u_w)$	$\mu(u_a - u_w)$: nonlinear function obtained from experiments
	Khalili and Khabbaz (1998)	c'	$\tan\phi'$	$\left[\frac{(u_a - u_w)}{(u_a - u_w)_b}\right]^k tan\phi'$, $(u_a - u_w)_b$: air entry value	k
	Öberg and Sällfors (1997); Jommi (2000)	c' or 0	$\tan\phi'$ or M'_c	$S\tan\phi'$ or SM'_c	-
	Vanapalli et al. (1996): first approach	c'	$\tan\phi'$	$(S)^\kappa \tan\phi'$	κ
	Vanapalli et al. (1996): second approach; Lu et al. (2010); Kim et al. (2016); Patil et al. (2017)	c' or 0	$\tan\phi'$ or M'_c	$\frac{S - S_r}{1 - S_r} tan\phi'$ or $\frac{S - S_r}{1 - S_r} M'_c$ S_r: degree of saturation at residual state on SWCC	-
	Karube and Kawai (2001)	0	M'_c	$\frac{S - S_0}{1 - S_0} M'_c$ S_0: the ratio of the volume of adsorbed water to the total void volume	-
	Tarantino and Tombolato (2005); Alonso et al. (2010)	c' or 0	$\tan\phi'$ or M'_c	$\frac{S - \xi_m}{1 - \xi_m}\tan\phi'$ or $\frac{S - \xi_m}{1 - \xi_m} M'_c$ ξ_m: the ratio of the volume of intra-aggregate pores to the total void volume	-
Models with varying $\tan\phi^a$ with suction	Sun et al. (2000)	0	$M'_c + k\frac{a(u_a - u_w)}{a + (u_a - u_w)}$	$\frac{a}{a + (u_a - u_w)} M^a$	k, a
	Toll and Ong (2003)	0	$\left[K - (K-1)\left(\frac{S - S_{r2}}{S_{r1} - S_{r2}}\right)^{k_1}\right] M'_c$	$(\frac{S - S_{r2}}{S_{r1} - S_{r2}})^{k_2} M'_c$	K; k_1; k_2; S_{r1}; S_{r2}
	Murray (2002)	0	$\begin{cases} M^a = M^t > M'_c, (u_a - u_w) > 0 \\ M^a = M'_c, (u_a - u_w) = 0 \end{cases}$	$\frac{e(S-1)}{1+e} M^t + \Lambda$	M^t, Λ
	Hossain and Yin (2010a)	c'	$\tan(\phi' + \psi_s)$	$S^\kappa \tan(\phi' + \psi_s)$ ψ_s: dilation angle of unsaturated soils which is function of suction	κ, ψ_s
	Maatouk et al. (1995)	0	$M'_c - b_2(u_a - u_w)$	b_1	b_1, b_2
	Gallipoli et al. (2008)	0	$M'_c \frac{M^a}{M'_c}(\xi)$	$SM'_c \frac{M^a}{M'_c}(\xi)$, ξ: a bonding variable	$\frac{M^a}{M'_c}(\xi)$: a function obtained from experiments

2.4.1.1 Models with constant $\tan\phi^a$

Fredlund et al. (1978) and Alonso et al. (1990) have made a simple assumption for interpreting the shear strength of unsaturated soils (Table 2.2). In both of these widely used approaches for the shear strength, c'' and $\tan\phi^a$ (or M^a) are assumed to be constants, which are equal to the corresponding saturated shear strength parameters, and $\tan\phi^b$ is assumed to be a constant which is independent on other parameters.

There are experimental data (Escario and Saez 1986; Gan et al. 1988; Toll 1990; Wheeler and Sivakumar 1995; Vanapalli et al. 1996; Rampino et al. 2000) evidence showing $\tan\phi^b$ decreases with respect to suction rather than being a constant. Thus, some researchers (Wheeler and Sivakumar 1995; Khalili and Khabbaz 1998; Rampino et al. 2000; Miao et al. 2002; Wang et al. 2002; Chiu and Ng 2003) expressed the shear strength due to suction as a nonlinear function of suction to describe the reduction in the contribution of suction towards shear strength.

Vanapalli et al. (1996) suggested the matric suction acts on the soil particles or aggregates through the area of water (i.e., water menisci area in contact with the soil particles or aggregates); for this reason, the contribution of matric suction to the shear strength of unsaturated soils is reduced due to the decrease in the water area under higher matric suction. This philosophy is widely used in the literature for the explanation of the variation of $\tan\phi^b$. Thus, the Mohr-Coulomb failure criterion can be extended based on this concept along with force equilibrium analysis in an unsaturated soil element as shown in Figure 2.8a.

$$\tau = c' + (\sigma_n - u_a)\tan\phi' + (u_a - u_w)\frac{A_w}{A}\tan\phi' \tag{2.4}$$

where A_w is the cross-sectional area of water phase in unsaturated soil mass; A is the cross-sectional area of unsaturated soil mass.

Comparing Equations 2.3 and 2.4, the proportion of water area, A_w/A, provides a physical explanation for the material parameter, χ, proposed by Bishop (1959). A_w/A can be considered as an area degree of saturation; however, it is generally related to the volumetric degree of saturation due to the difficulties in its measurement. Some researchers (Öberg and Sällfors 1997; Jommi 2000) directly used the degree of saturation, S, to replace A_w/A for simplification. However, the

experimental results (Öberg and Sällfors 1997) did not exhibit a unique linear relationship between S and A_w/A. Vanapalli et al. (1996) related A_w/A to $(S)^{\kappa}$ to obtain a better correlation between predicted and experimental shear strength data. Subsequent studies (for example, Vanapalli and Fredlund 2000; Tang 2019) built some empirical relationships between the fitting parameter, κ, and the physical properties of soils to predict the shear strength of unsaturated soils conveniently.

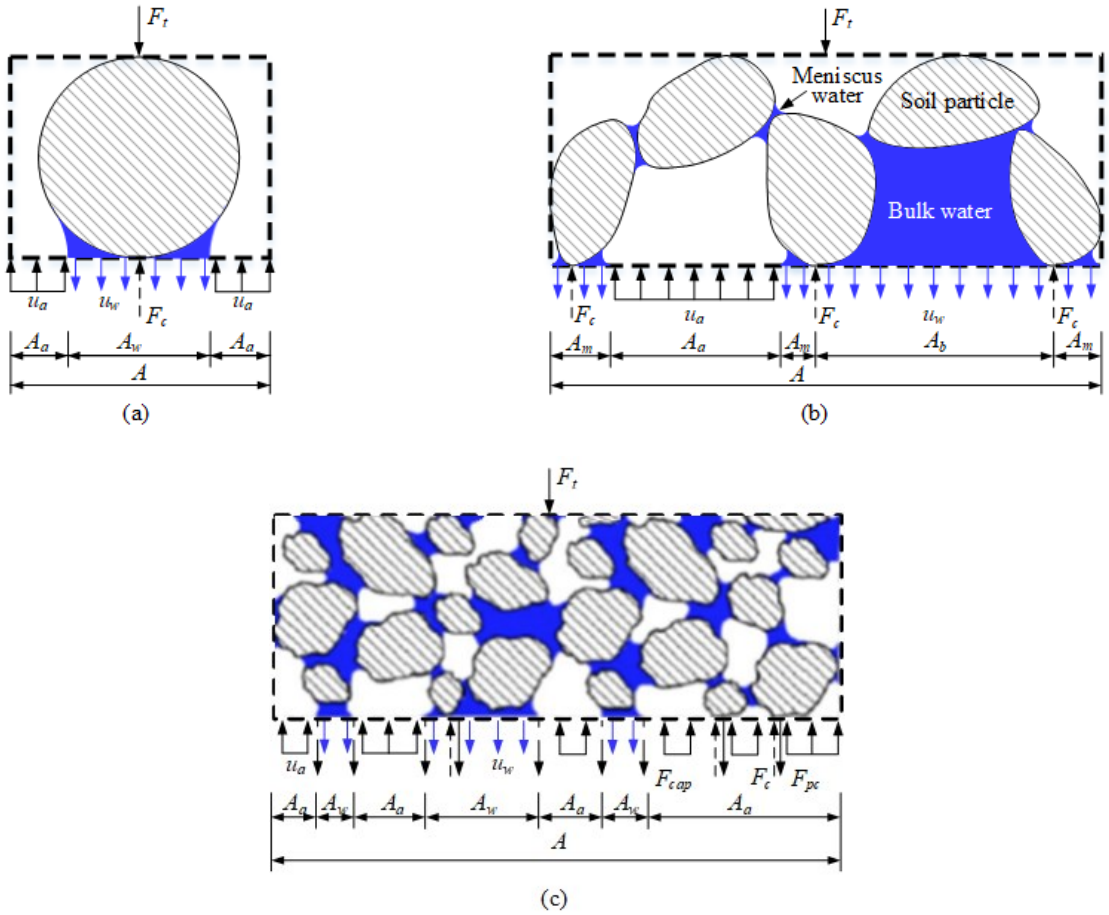

Figure 2.8 Force equilibrium in unsaturated soils: (a) only considering soil particle and water meniscus; (b) considering difference between bulk and meniscus water (modified after Karube and Kawai 2001); (c) considering all known physical forces (modified after Lu 2008)

Some researchers (Vanapalli et al. 1996; Karube and Kawai 2001; Tarantino and Tombolato 2005; Alonso et al. 2010) recognized a part of pore water (e.g., the adsorbed water) has a different mechanical action with the free capillary water existing as water menisci among soil particles or aggregates. Thus, Equation 2.4 should be revised as:

$$\tau = c' + (\sigma_n - u_a)\tan\phi' + (u_a - u_w)\frac{A_w - A'}{A - A'}\tan\phi' \quad (2.5)$$

where A' is the area of water that has different mechanical action with free capillary water.

A couple of different approaches were proposed to interpret Equation 2.5. For example, Vanapalli et al. (1996) provided conceptual evidence to show the shear strength behavior of unsaturated soils in the residual zone ($S < S_r$) where the vapor flow is predominant is different with that in transition zone ($S > S_r$) where the liquid flow prevails. Extending this philosophy, Vanapalli et al. (1996) proposed the second shear strength prediction model using the residual degree of saturation, S_r, to represent A'/A (Table 2.2). In addition to that, Karube and Kawai (2001) suggested the adsorbed water has a minor influence on the mechanical behavior of unsaturated soils. Thus, the adsorbed water degree of saturation, S_0 (i.e., the volume of adsorbed water over the total void volume), was used to represent A'/A (Table 2.2). Other researchers (Tarantino and Tombolato 2005; Alonso et al. 2010) suggested that the water in the intra-aggregates pores has a limited influence on the mechanical behavior of the unsaturated soils with a double porosity structure due to aggregation. Therefore, a microstructural state variable, ξ_m (i.e., the volume of intra-aggregate pores over the total void volume), was used to represent A'/A (Table 2.2).

In addition, Karube and Kawai (2001) also suggested that the influence of capillary water on mechanical behavior of unsaturated soils should be separated into two different categories: namely, bulk water and meniscus water. The suction stress induced by bulk water (Figure 2.8b) can be transmitted through the soil skeleton similar to the effective stress in saturated soils; thus, it can be considered as a part of skeleton stress. The suction stress induced by meniscus water (Figure 2.8b) works at the contact points between particles to stiffen the soil skeleton but does not contribute to equilibrium with the external applied force. In other words, Equation 2.5 should be rewritten as:

$$\tau = c' + \left[(\sigma_n - u_a) + (u_a - u_w)\frac{A_b}{A - A_0}\right]\tan\phi' + (u_a - u_w)\frac{A_m}{A - A_0}\tan\phi' \quad (2.6)$$

where A_b, A_m and A_0 are the cross-sectional areas of bulk water, meniscus water and adsorbed water, respectively.

Lu and Likos (2006) conducted the force equilibrium analysis on an air-water-solid representative elementary volume (REV) (Figure 2.8c) taking account of all known physical forces, including the interparticle physico-chemical forces, surface tension, and pore-water pressure in terms of matric suction. Thus, a more general equation for shear strength of unsaturated soils can be expressed as:

$$\tau = c' + (\sigma_n - u_a)\tan\phi' + \left[\frac{F_{pc}}{A} + \frac{F_{cap}}{A} + \frac{A_w}{A}(u_a - u_w)\right]\tan\phi' \tag{2.7}$$

where F_{pc} is the interparticle physico-chemical force; F_{cap} is the capillary force due to surface tension.

2.4.1.2 Models with varying tanϕ^a with suction

The assumption, tanϕ^a = tanϕ', has been widely used in the literature; however, some experimental results (Escario and Saez 1986; Toll 1990; Wheeler and Sivakumar 1995; Sivakumar et al. 2010; Zhao and Zhang 2014) suggested an increase in tanϕ^a with increasing suction for the shear strength envelopes of unsaturated soils. Toll (2000) studies suggest that an increase in tanϕ^a at critical state is associated with an increase in the critical void ratio, which is not consistent with the expectation that tanϕ^a would decrease due to an increase in the critical void ratio. In addition, some experimental results (Sivakumar et al. 2010; Mendes and Toll 2016) showed that the critical state behavior of unsaturated compacted fine-grained soils is influenced by the stress history. This is not consistent with the saturated soils for which the critical state behavior is unique and is independent of the stress history.

The above phenomena were explained based on the fabric aggregation of unsaturated compacted fine-grained soils (Toll 1990, 2000). The double porosity structure influences both the variation of tanϕ^b with suction due to the existing states of pore water (Tarantino and Tombolato 2005; Alonso et al. 2010), and the variation of tanϕ^a with suction due to the change in granularity and rigidness of the aggregates (Toll 1990, 2000). As discussed in previous section, the aggregates will be retained during shearing in the unsaturated soil specimen and act as large individual particles; thus, higher matric suction can contribute to a more granular structure which in turn results in greater values of tanϕ^a.

Based on this philosophy, some research studies (Zhan and Ng 2006; Hossain and Yin 2010a) suggested ϕ^a should be considered as the sum of saturated effective friction angle, ϕ', and the dilation angle, ψ_s, which can increase with suction, for interpreting the PSS (Table 2.2). In addition, Sun et al. (2000) suggested a simplified assumption that M^a for CSS increases hyperbolically with suction (Table 2.2). However, some experimental results (Toll 1990; Zhao and Zhang 2014) showed that M^a increases nonlinearly with degree of saturation and that the nonlinear relationship can be related to the SWCC. For this reason, Toll and Ong (2003) defined M^a and M^b as power functions of a normalized degree of saturation (Table 2.2). Murray (2002) reanalyzed the experimental data provided by Wheeler and Sivakumar (1995) and Toll (1990) and suggested a constant M^a value that is greater than M'_c in unsaturated state. Based on his investigation studies, Murray (2002) also suggested that the fabric aggregation of unsaturated soils can contribute to a M^a greater than M'_c, but the contribution is independent on the suction level (Table 2.2).

Experimental results of several other investigations (Delage et al. 1987; Maatouk et al. 1995; Estabragh and Javadi 2008) showed that in the $q - (p - u_a)$ space, the slopes of CSS envelopes decrease with increasing suction. The envelopes converge towards a point corresponding to a certain net mean stress, beyond which the suction has no influence on the shear strength.

The mechanism associated with the decrease in $\tan\phi^a$ is still unclear. Delage et al. (1987) suggested such a behavior for an unsaturated silt that they tested may be due to the high friction angle and low degree of saturation. Toll and Ong (2003) proposed a unified explanation for the increase and decrease in $\tan\phi^a$ based on the aggregation fabric of compacted unsaturated fine-grained soils. It is suggested that at intermediate values of suction the aggregates are held by the suction and can contribute to a high $\tan\phi^a$. However, as the suction increases, the aggregates can desaturate and break down; due to this reason, there can be a decrease in $\tan\phi^a$. Therefore, $\tan\phi^a$ increases with suction when the pore water is drained out from inter-aggregate pores and decreases with suction when the pore water is drained out from intra-aggregate pores. Some prediction models that can consider the decrease in $\tan\phi^a$ (e.g., Maatouk et al. 1995; Gallipoli et al. 2008) are also summarized in Table 2.2.

2.4.1.3 Comparisons for models with varying $\tan\phi^a$

Three prediction models (Equations 2.8 – 2.10) with varying $\tan\phi^a$ for CSS of unsaturated soils in Table 2.2 are selected for providing a comparison study. Equation 2.8 is proposed by Sun et al. (2000) based on the concept of Bishop stress by assuming the suction stress as a hyperbolic function of suction:

$$q=\left[\left(p-u_a\right)+\frac{a\left(u_a-u_w\right)}{a+\left(u_a-u_w\right)}\right]\left[M_c'+k\frac{a\left(u_a-u_w\right)}{a+\left(u_a-u_w\right)}\right] \tag{2.8}$$

where M_c' is critical stress ratio of saturated soils; k and a are material parameters.

Equation 2.9 is proposed by Toll and Ong (2003) based on the two stress state variables:

$$q=\left(p-u_a\right)M^a+\left(u_a-u_w\right)M^b \tag{2.9a}$$

$$M^a=\left[K-\left(K-1\right)\left(\frac{S-S_{r2}}{S_{r1}-S_{r2}}\right)^{k_1}\right]M_c' \tag{2.9b}$$

$$M^b=\left(\frac{S-S_{r2}}{S_{r1}-S_{r2}}\right)^{k_2}M_c' \tag{2.9c}$$

where S is degree of saturation; S_{r1} and S_{r2} are degree of saturation at two reference states; in this study, S_{r1} is assumed to be 1 for simplification; k_1, k_2 and K are material parameters.

Gallipoli et al. (2008) proposed Equation 2.10a based on the average skeleton stress to predict CSS of unsaturated soils. In Equation 2.10a, the ratio of M^a to M_c' was related to ξ; however, no specific equation was proposed for the relationship between M^a/M_c' and ξ. Therefore, in this study, a linear function (Equation 2.10b) is assumed for the relationship between M^a/M_c' and ξ. Gallipoli et al. (2008) defined ξ as $f(u_a - u_w)(1 - S)$ and Lashkari and Kadivar (2016) suggested ξ can be estimated by using Equation 2.10c. Therefore, the prediction model proposed by Gallipoli et al. (2008) can be modified as:

$$q = \left[\left(p - u_a\right) + S\left(u_a - u_w\right)\right]\frac{M^a}{M_c'}\left(\xi\right)M_c' \tag{2.10a}$$

$$\frac{M^a}{M_c'}\left(\xi\right) = 1 + k_1\xi \tag{2.10b}$$

$$\xi = f\left(u_a - u_w\right)\left(1 - S\right) \approx \left(1 + \frac{\left(u_a - u_w\right)^{0.75}}{250 + 2\left(u_a - u_w\right)^{0.75}}\right)\left(1 - S\right) \tag{2.10c}$$

where $M^a/M_c'(\xi)$ is ratio between M^a and M_c' that is function of ξ; ξ is bonding parameter; k_1 is material parameter.

Three sets of experimental data of CSS of unsaturated soils (Wheeler and Sivakumar 1995; Hossain and Yin 2010a; Estabragh and Javadi 2008) are selected for the evaluation of the selected prediction models. The experimental data reported by Wheeler and Sivakumar (1995) is obtained from a series of suction-controlled triaxial shear tests on kaolin specimens. The experimental results showed an increase in M^a of CSS envelopes with increasing suction. The experimental data reported by Hossain and Yin (2010a) is obtained from a series of suction-controlled direct shear tests on compacted completely decomposed granite (CDG) specimens. The experimental results showed an increase in $\tan\phi^a$ of CSS envelopes with increasing suction. For predicting the direct shear test results, Equations 2.8 – 2.10 should be modified by replacing $(p - u_a)$ with $(\sigma_n - u_a)$ and by replacing M^a, M^b and M_c' with $\tan\phi^a$, $\tan\phi^b$ and $\tan\phi'$. The experimental data reported by Estabragh and Javadi (2008) is obtained from a series of suction-controlled triaxial shear tests on ML specimens. The experimental results showed a decrease in M^a of CSS envelopes with increasing suction. More details about the three materials and corresponding testing procedures can be found in the source papers.

Figures 2.9 – 2.11 show the comparisons between the experimental results and the predicted results of the three selected prediction models. The predicted results of M^a and M^b (or $\tan\phi^a$ and $\tan\phi^b$) are presented in Figures 2.9a, 2.10a and 2.11a; in addition, the predicted results of critical deviatoric stress (or critical shear stress) are presented in Figures 2.9b, 2.10b and 2.11b. M^a is determined from the slope of CSS envelopes with respect to net mean stress at a specific suction in the $q - (p$

– u_a) space. Then, M^b can be defined as $M^b = [q – (p – u_a) M^a]/(u_a – u_w)$. The material parameters of Equations 2.8 and 2.10 can be determined by best-fitting the values of CSS under different (p – u_a) and (u_a – u_w). As for the determination of material parameters in Equation 2.9, Equation 2.9c is used to best-fit the values of M^b under different suctions to get S_{r2} and k_2 and then Equation 2.9b with fixed S_{r2} is used to best-fit the values of M^a under different suctions to get K and k_1. All the material parameters in Equations 2.8 – 2.10 for the three sets of experimental data are summarized in Table 2.3.

Table 2.3 Material parameters in Equations 2.8 – 2.10

Equation	Material parameters	Kaolin (Wheeler and Sivakumar 1995)	Completely decomposed granite (Hossain and Yin 2010a)	ML (Estabragh and Javadi 2008)	SM (Hoyos et al. 2014)	SC-SM (Hoyos et al. 2014)
2.8	k	0.00054	0.0024	-0.0012	0.005	0.0015
	a	251.88	157.76	36405	305.28	176.91
2.9	S_{r2}	0.42	0.38	0.35	0	0
	k_1	7.65	0.3	0.066	1.687	20
	k_2	0.65	0.74	0.076	0.065	-0.067
	K	1.16	2.86	0	1.83	1.12
2.10	k_1	-0.016	0.41	-0.043	1.409	0.595

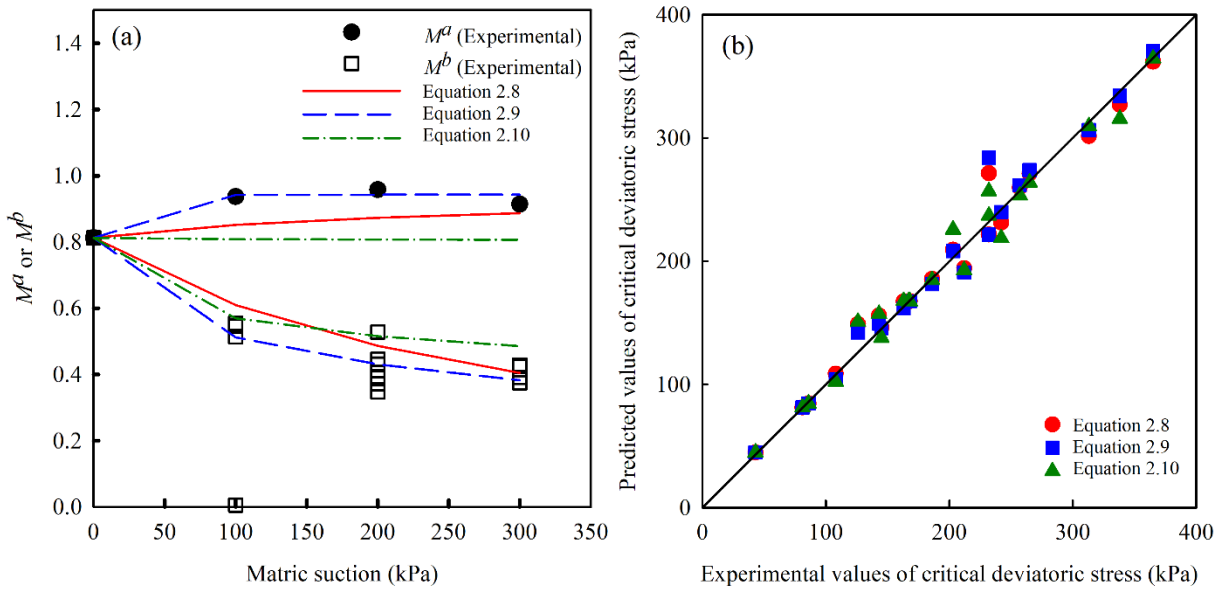

Figure 2.9 Predictions of suction-controlled triaxial shear test data on kaolin (modified after Wheeler and Sivakumar 1995): (a) predicted results of M^a and M^b; (b) predicted results of critical deviatoric stress

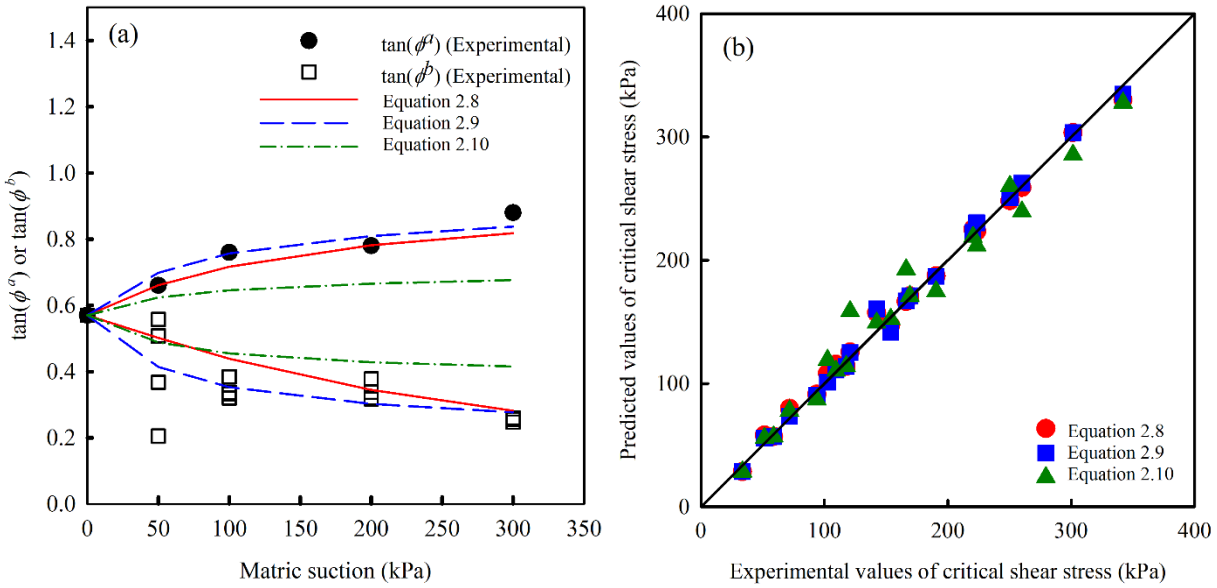

Figure 2.10 Predictions of suction-controlled direct shear test data on completely decomposed granite (modified after Hossain and Yin 2010a): (a) predicted results of tan(ϕ^a) and tan(ϕ^b); (b) predicted results of critical shear stress

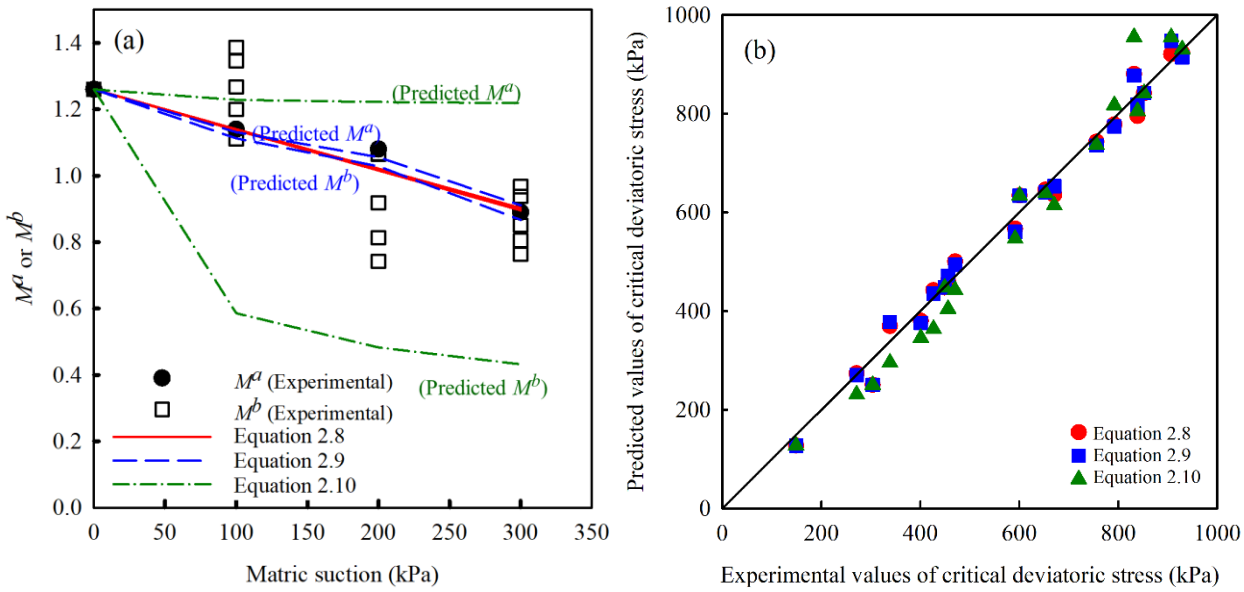

Figure 2.11 Predictions of suction-controlled triaxial shear test data on ML (modified after Estabragh and Javadi 2008): (a) predicted results of M^a and M^b; (b) predicted results of critical deviatoric stress

It can be found that all the three prediction models (Equations 2.8 – 2.10) can predict well the magnitudes of critical deviatoric/shear stress of the three unsaturated soils (Figures 2.9b, 2.10b

and 2.11b). However, Equations 2.8 and 2.10 under predict M^a and over predict M^b for the kaolin (Figure 2.9a) and CDG (Figure 2.10a). Equation 2.10 significantly over predicts M^a and under predicts M^b of the ML (Figure 2.11a). Equation 2.10 does not capture well the variations of M^a and M^b with suction for the three unsaturated soils. This may indicate that the assumed linear relationship between M^a/M_c' and ξ (Equation 2.10b) in this study is not suitable for unsaturated soils. Equation 2.9 provides good predictions of M^a and M^b for all the three unsaturated soils (Figures 2.9a, 2.10a and 2.11a). This can be attributed to that Equation 2.9 was formulated based on the two stress state variables, which makes it more flexible to predict M^a and M^b separately.

2.4.2 RSS prediction model

Research studies on RSS prediction model are limited in comparison to the studies on PSS and CSS. Infante Sedano and Vanapalli (2011) proposed an RSS prediction model for unsaturated soils (Equation 2.11) by modifying the first approach proposed by Vanapalli et al. (1996) based on the experimental data from the suction-controlled ring shear tests under low suction condition.

$$\tau_r = c_r' + (\sigma_n - u_a)\tan\phi_r' + (u_a - u_w)S^{\kappa_r}\tan\phi_r' \tag{2.11}$$

where c_r' and ϕ_r' are saturated RSS parameters; κ_r is a fitting parameter for residual shear strength of unsaturated soils; S is degree of saturation determined using the apparent SWCC (i.e., the SWCC that is obtained using the sheared specimen under large deformation).

In addition, some experimental results (Vaunat et al. 2006; Vaunat et al. 2007; Merchán 2008) showed that suction can still contribute to the RSS even when it is greater than 100 MPa. In the τ – σ_n space, RSS envelopes displayed null cohesion intercept and increasing friction angle with increasing total suction due to the aggregated structure. For this reason, Romero et al. (2014) proposed an RSS prediction model based on the experimental data from suction-controlled ring shear tests under high suction condition.

$$\tau_r = \sigma_n(\tan\phi_r' + aS\Psi_s) \tag{2.12}$$

where Ψ_s is the total suction; a is a fitting parameter.

Figure 2.12 shows the experimental results of RSS due to suction (i.e., $\tau_r - c_r' - (\sigma_n - u_a)\tan\phi_r'$) reported by Infante Sedano and Vanapalli (2011) and the predicted results of several models in Table 2.2 proposed for PSS and CSS of unsaturated soils. Infante Sedano and Vanapalli (2011) conducted a series of suction-controlled ring shear tests under a fixed net normal stress of 150 kPa on the Indian Head till specimens. The variation of $\tan\phi_r^a$ with suction was not studied based on this set of data. For this reason, only models with constant $\tan\phi^a$ in Table 2.2 were used to predict the variations of RSS due to suction with suction. In addition, the predicted results of Equation 2.11 are also presented in Figure 2.12 for comparison. The fitting parameters in the selected models were obtained by best-fitting the experimental results. The microstructural state variable, ξ_m, in the model proposed by Tarantino and Tombolato (2005) was not provided in the source paper; therefore, it is also obtained by best-fitting the experimental results.

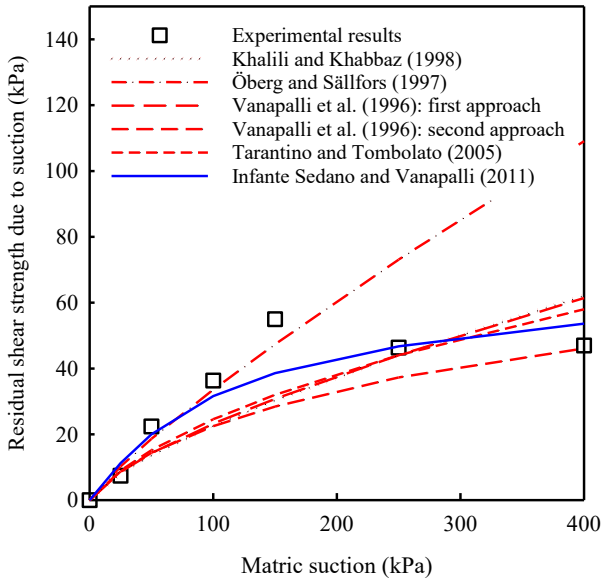

Figure 2.12 Predictions of suction-controlled ring shear test data on Indian Head till (modified after Infante Sedano and Vanapalli 2011)

It can be found that the Öberg and Sällfors (1997) model significantly over predicts the RSS due to suction when suction is higher than 150 kPa. Vanapalli et al. (1996) second approach under predicts the RSS due to suction when suction is lower than 400 kPa. The other selected models (Khalili and Khabbaz 1998; Vanapalli et al. 1996 first approach; Tarantino and Tombolato 2005) under predict the RSS due to suction when suction is less than 300 kPa and over predict it when suction exceeds 300 kPa. This means the RSS envelopes with respect to matric suction flattens

more at higher matric suction than the PSS and CSS envelopes. This is because, at residual state, the contribution of matric suction to shear strength (i.e., S^{κ_r} in Equation 2.11) is lower than that at peak state (i.e., S^{κ} in the first approach of Vanapalli et al. 1996) due to the breakage of water menisci and decrease in local degree of saturation inside the shear band. For this reason, Infante Sedano and Vanapalli (2011) suggested κ_r in Equation 2.11 should have a higher value than κ used in Vanapalli et al. (1996) first model. Equation 2.11 provided a good fit between the experimental data and the predicted RSS due to suction. However, this approach still has a limitation because it did not consider the variation of $\tan\phi_r^a$ with suction and it requires costly facilities and complex operations to generate the apparent SWCC from sheared specimens.

Figures 2.13 and 2.14 show the experimental results (Hoyos et al. 2014) of suction-controlled ring shear tests on unsaturated SM and SC-SM specimens, respectively, and corresponding predicted results of several models proposed for PSS and CSS of unsaturated soils. These two sets of experimental data show $\tan\phi_r^a$ varies with suction (Figures 2.13a and 2.14a). Thus, the models with varying $\tan\phi^a$ for PSS and CSS (Equations 2.8 – 2.10) are used for comparison study. The material parameters are obtained by best-fitting the experimental results and summarized in Table 2.3. It can be found the prediction results of Equations 2.8 – 2.10 on the magnitudes of RSS are not good for SM (Figure 2.13b), but they are reasonably good for SC-SM (Figure 2.14b). The experimental results show $\tan\phi_r^a$ increases with suction and then decreases after suction exceeds a specific value (Figures 2.13a and 2.14a). This tendency cannot be well captured by the three selected models for PSS and CSS (Equations 2.8 – 2.10). In addition, Equations 2.9 and 2.10 under predict the $\tan\phi_r^b$ of SM and Equations 2.8 and 2.10 under predict the $\tan\phi_r^b$ of SC-SM.

From the comparisons shown in Figures 2.12 – 2.14, it can be suggested that the existing prediction models for PSS and CSS of unsaturated soils cannot be used for predicting the RSS of unsaturated soils. Therefore, it is necessary to develop models for the prediction of RSS of unsaturated soils. However, to the authors best knowledge, such studies are still limited (Infante Sedano and Vanapalli 2011; Romero et al. 2014).

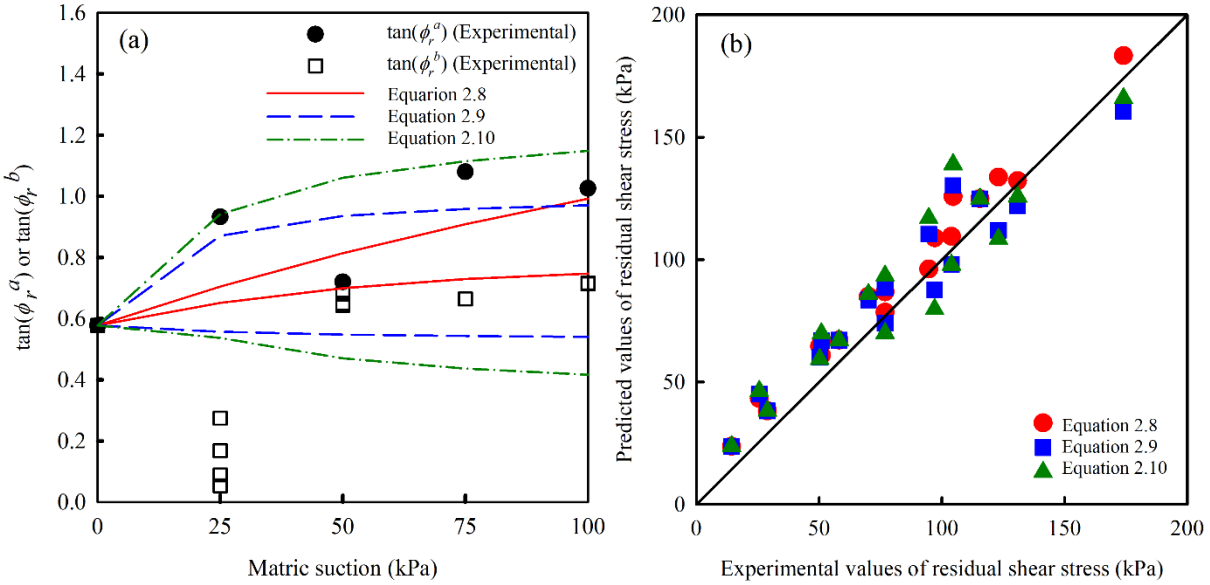

Figure 2.13 Predictions of suction-controlled ring shear test data on SM (modified after Hoyos et al. 2014): (a) predicted results of tan(ϕ_r^a) and tan(ϕ_r^b); (b) predicted results of residual shear stress

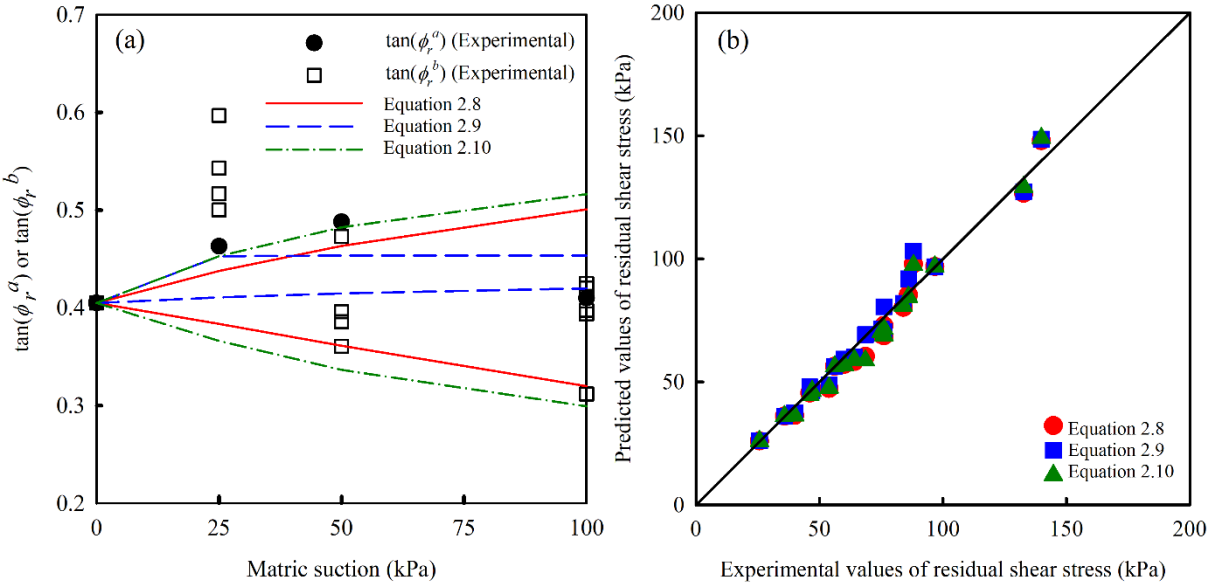

Figure 2.14 Predictions of suction-controlled ring shear test data on SC-SM (modified after Hoyos et al. 2014): (a) predicted results of tan(ϕ_r^a) and tan(ϕ_r^b); (b) predicted results of residual shear stress

2.5 Numerical methods of modelling strain-softening behavior of unsaturated soils

A variety of elastoplastic constitutive models have been developed for modelling the complex behaviors of unsaturated soils, that have been well summarized and evaluated by some previous review studies (e.g., Gens et al. 2006; Sheng 2011; D'Onza et al. 2011). Instead of a comprehensive review of existing constitutive models for unsaturated soils, this section devotes its main attention to the introduction of three commonly used numerical methods of modelling the strain-softening behavior of unsaturated soils. Several typical constitutive models were selected (Table 2.4) as examples to illustrate the formulation of constitutive models that can reproduce the strain-softening behavior of unsaturated soils based on conventional plasticity (CP), bounding surface plasticity (BSP) and disturbed state concept (DSC) approach, respectively.

2.5.1 Conventional plasticity

Alonso et al. (1990) extended the classic Modified Cam-clay (MCC) model and formulated an elastoplastic model (BBM) for unsaturated soils (Table 2.4). This model has been validated for explaining the wetting-collapse and other behaviors of unsaturated soils. Several other similar and improved models were subsequently proposed by other researchers (e.g., Wheeler and Sivakumar 1995; Cui and Delage 1996). The Cam-clay-type models that were formulated based on the conventional plasticity can capture the strain-softening behavior of unsaturated soils for certain scenarios. For example, Figure 2.15 shows the evolution of the ellipse yield surface of BBM under a drained triaxial compression test on a heavily overconsolidated unsaturated soil specimen. The shear stress is increased elastically until the initial yield surface can be reached at the supercritical side (A–B). Once yielding, the hardening parameter, $(p - u_a)_0$ decreases associated with dilation, which results in the shrinkage of yield surface (B–C). Therefore, the stress-strain curve exhibits strain-softening behavior.

Table 2.4 Commonly used methods of modelling the strain-softening behavior of unsaturated soils

Model type	Unsaturated constitutive models	Reference saturated constitutive models	Key points about the formulation of the constitutive models
Conventional plasticity	Barcelona Basic Model (BBM) (Alonso et al. 1990)	Modified Camclay (Roscoe and Burland 1968)	(1) The net normal stress, $(p - u_a)$, and matric suction, $(u_a - u_w)$, were treated as two independent stress state variables. (2) The apparent cohesion of critical state line (CSL) in $q - (p - u_a)$ plane and the slope of the normal compression line (NCL) in $v - \ln(p - u_a)$ plane were assumed to be functions of suction. (3) The two-dimensional ellipse yield surface of modified Camclay model was extended in a three-dimensional space (i.e., $q - (p - u_a) - (u_a - u_w)$) by defining the load-collapse (LC) and suction increase (SI) yield loci. (4) Two hardening parameters were related to specific volume, v, by using the assumed linear relationships between v and $\ln(p - u_a)$ and $\ln(u_a - u_w)$ for loading and unloading path.
	Wheeler and Sivakumar (1995)	—	(1) The original BBM was modified. (2) The parameters related to the CSL and NCL were assumed as functions of suction and were suggested to be obtained by best fitting the experimental results.
	Cui and Delage (1996)	—	(1) The original BBM was modified. (2) An ellipse yield surface inclined along the K_0 line in constant suction planes was used.
	Chiu and Ng (2003)	—	(1) The net normal stress, $(p - u_a)$, and matric suction, $(u_a - u_w)$, were treated as two independent stress state variables. (2) The parameters related to the CSL and NCL were assumed as functions of suction. (3) A two-dimensional right-angled triangle yield surface was extended in a three-dimensional space (i.e., $q - (p - u_a) - (u_a - u_w)$) by using similar approach with BBM. (4) A state-dependent stress–dilatancy relationship, that can consider the influence of suction and density, was proposed for unsaturated soils and used as flow rule.
Bounding surface plasticity	Russell and Khalili (2006)	Russell and Khalili (2004)	(1) The effective mean stress, $(p - u_w)$, in original saturated model was substituted with the Bishop's effective stress, $p' = (p - u_a) + \chi (u_a - u_w)$. (2) The NCL and CSL of unsaturated soils undergo a suction-dependent shift along κ line in comparison to the lines of saturated soils in $v - \ln(p')$ plane. (3) The hardening law for the bounding surface was derived from NCL as a function of the plastic volumetric change and suction. The hardening law for the loading surface in original saturated model was retained with updating some parameters as functions of suction obtained from Step (2).
	Morvan et al. (2010)	Bardet (1986)	(1) The effective mean stress, $(p - u_w)$, in original saturated model was substituted with the Bishop's effective stress, $p' = (p - u_a) + \chi (u_a - u_w)$. (2) The apparent cohesion of CSL in $q - p'$ plane and the slope of CSL in $e - \log(p')$ plane were assumed to be functions of suction. (3) The hardening law of bounding surface was assumed to be a function of plastic volumetric strain and suction. The hardening law for the loading surface in original saturated model was retained with updating some parameters as functions of suction obtained from Step (2).

Table 2.4 Commonly used methods of modelling the strain-softening behavior of unsaturated soils (continue)

Model type	Unsaturated constitutive models	Reference saturated constitutive models	Key points about the formulation of the constitutive models
Bounding surface plasticity	Fern et al. (2016)	Nor-sand model (Jefferies 1993)	(1) The effective mean stress, $(p - u_w)$, in original saturated model was substituted with the Bishop's effective stress, $p' = (p - u_a) + \chi (u_a - u_w)$. (2) The loading and bounding surfaces in original saturated model were retained. (3) The hardening law for the bounding surface that is related to the maximum dilatancy rate (D_{max}) was modified by updating the prediction model of D_{max} to consider the effects of degree of saturation. The hardening law for the loading surface in original saturated model was also modified.
	Yao et al. (2014)	Unified hardening model (Yao et al. 2009)	(1) The net normal stress and matric suction were treated as two independent stress state variables. (2) The apparent cohesion of CSL in $q - (p - u_a)$ space and the slope of the NCL in $v - \ln(p - u_a)$ space were assumed to be functions of suction, which were same with BBM. (3) The loading surface and bounding surface were built using the same yield functions as that of BBM. (4) The hardening parameter for the bounding surface was related to the plastic volumetric strain. The hardening parameter for the loading surface is related to a unified hardening parameter which depends on the relationship between the loading and bounding surface.
	Zhou and Sheng (2015)	—	(1) The Bishop's effective stress (p') and effective degree of saturation (S_e) were treated as two independent stress variables. (2) The slope of the NCL in $v - \ln p'$ space was assumed to be a function of S_e. (3) The bounding surface was built by extending the MCC ellipse yield surface in a three-dimensional space (i.e., $q - p' - S_e$) using the LC curve. The loading surface was built using the same yield function as that of bounding surface. (4) The hardening laws for loading and bounding surfaces were formulated using the similar approach with Yao et al. (2014).
Disturbed state concept	Geiser et al. (2000)	DSC-HISS model (Desai 2000)	(1) The HISS model in the original saturated model was extended for unsaturated soils by assuming some material parameters as functions of matric suction. This extended HISS model for unsaturated soils (HISS-δ_{1unsat}) was used to describe the RI state. (2) The saturated state was used as the FA state, which was described by HISS-δ_{1unsat} with $(u_a - u_w) = 0$. (3) Some parameters of the disturbance function in the original saturated model were assumed as functions of matric suction.
	Hamid and Miller (2008)	DSC-HISS model (Desai 2000)	(1) An elastoplastic model for unsaturated soil-steel interface was developed as RI state constitutive model analogous to the extended HISS model by Geiser et al. (2000). (2) At FA state, the shear stress is assumed to be constant at zero. (3) The disturbance function in the original saturated model was modified as a piecewise function with some parameters assumed as functions of suction.

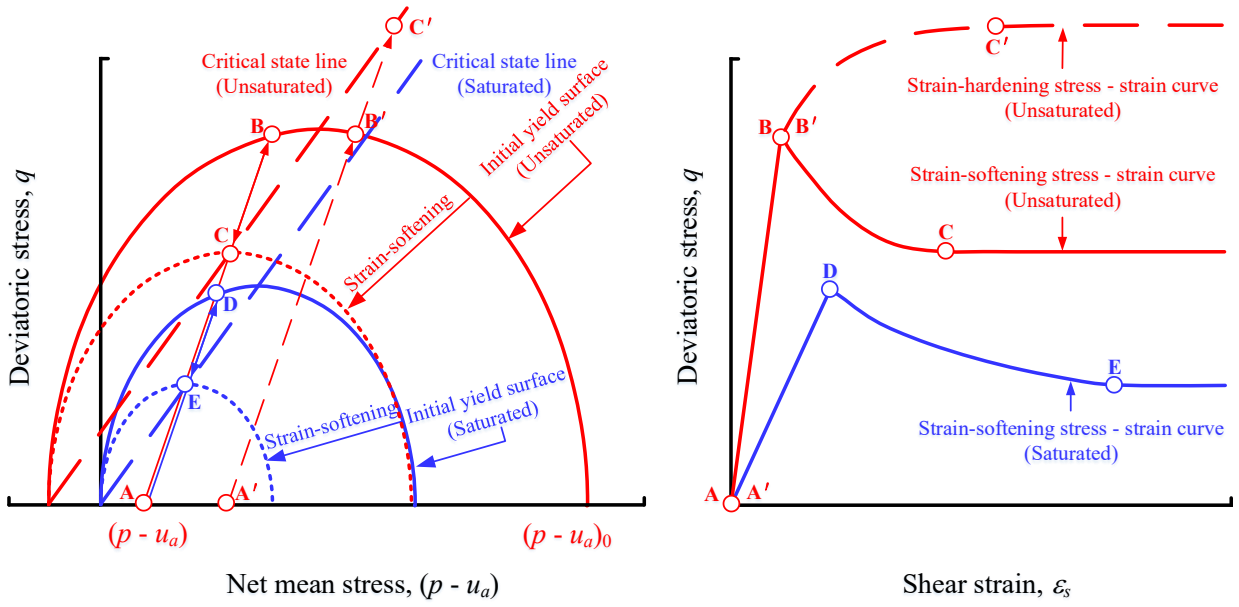

Figure 2.15 Diagram for strain-softening constitutive model of unsaturated soils based on conventional plasticity

Due to the inherent shortcomings of MCC, the Cam-clay-type models have some limitations despite having capabilities for modeling the key features of the typical behaviors of unsaturated soils for various types of loading and drainage condition scenarios (Rampino et al. 2000; Romero et al. 2019). For example, the Cam-clay-type models cannot reproduce the strain-softening stress-strain curve when the overconsolidation ratio is not large enough (i.e., the stress path A'–B'–C' intersects the initial yield surface at the right of CSL as shown in Figure 2.15). This limitation is also shown in Figure 2.16a which shows the experimental results of suction-controlled triaxial shear tests on unsaturated SM specimens and corresponding predictions results of BBM (solid lines). It can be found that the strain-softening behavior of the experimental stress-strain curves cannot be reproduced despite good predictions for the initial part of stress-strain curve and for the ultimate deviatoric stress. Another limitation is the Cam-clay-type models will overestimate the PSS when the overconsolidation ratio is large enough to reproduce the strain-softening behavior. The overestimation can be attributed to the assumed shape of the elliptical yield surface. This can be overcome by changing the shape of the yield surface on the dry side of the critical state, for example, introducing the Hvorslev surface for unsaturated soils (Tsiampousi et al. 2013). In addition, in Cam-clay-type models, only elastic strain happens prior to reaching the initial yield surface (A-B in Figure 2.15) and, as a result, there is a sharp transition at the peak point of the

stress-strain relationship between the elastic and plastic states (Point B in Figure 2.15). This limitation is also shown in Figures 2.16b and 2.16c where the stress-strain curves (solid lines) predicted by a conventional plasticity model (Solowski and Sloan 2015) exhibit sharp transition at the peak point.

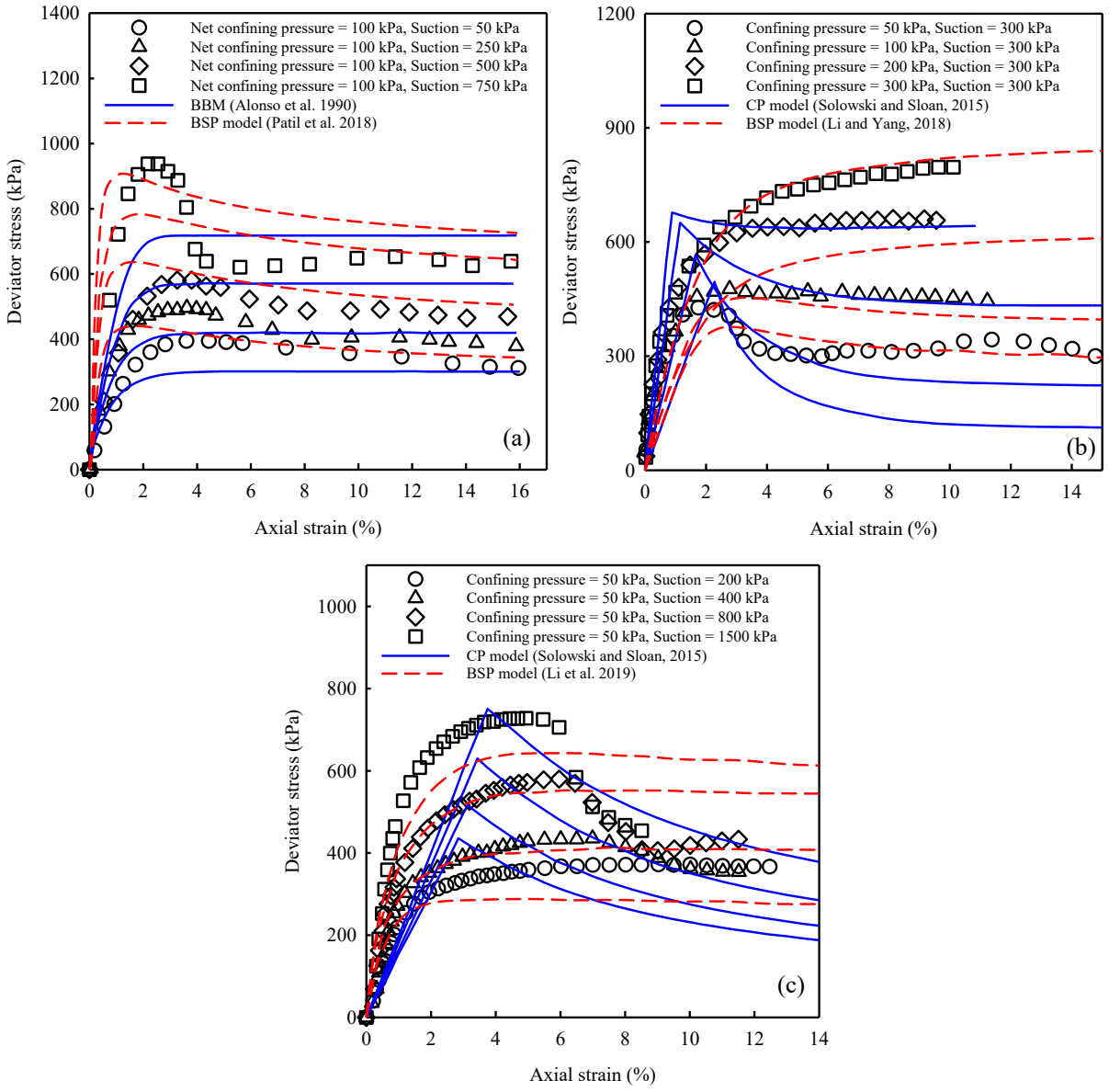

Figure 2.16 Comparisons between prediction results of conventional plasticity model and bounding surface plasticity model: (a) stress-strain curves of SM (experimental data from Patil et al. 2018); (b) stress-strain curves of ML (experimental data from Estabragh and Javadi 2008); (c) stress-strain curves of Jossigny silt (experimental data from Cui and Delage 1996)

These limitations of the Cam-clay-type models can be improved to some extent in the constitutive models considering a state-dependent dilatancy for unsaturated soils (e.g., Chávez and Alonso 2003; Chiu and Ng 2003; Lashkari and Kadivar 2016; Musso et al. 2020; Ng et al. 2020b). In Cam-clay-type models, the stress-dilatancy relationship does not consider the influence of density. This means, during the plastic deformation, no more plastic volumetric strain will happen ($d\varepsilon_v^p = 0$) once the stress ratio reaches CSL. In other words, the stress path cannot exceed the CSL during plastic deformation. However, if a state parameter (e.g., $\psi = e - e_{cr}$ where, e is current void ratio and e_{cr} is critical state void ratio corresponding to the current effective mean stress) is considered in the stress-dilatancy relationship, $d\varepsilon_v^p$ will not be equal to zero when the stress ratio reaches CSL, but the void ratio does not reach CSL. Due to this reason, the stress ratio can continue increasing and reach to a peak value higher than CSS. By using this method, even in some scenarios where the stress path intersects the initial yield surface at the right of CSL, the strain-softening behavior can also be reproduced, and the predicted stress-strain curve can be smooth at the peak point.

2.5.2 Bounding surface plasticity

The bounding surface plasticity (BSP) is an advanced plasticity model that can overcome the limitations of the models based on conventional plasticity. It was originally introduced by Dafalias and Popov (1975). In BSP, a loading surface, passing through a current stress point, is assumed to expand or shrink within the bounding surface that can expand or shrink during the loading process. The hardening and softening behaviors of soils can be simulated by the expansion and shrinkage of the loading surface. The sizes of the two surfaces are controlled by their respective hardening parameters. The hardening parameter of the bounding surface can be related to the plastic strain or plastic work using the conventional plasticity approach. The hardening parameter of the loading surface, however, depends on the relative position between the loading and bounding surfaces. The relationship between the two surfaces can be described by a mapping rule.

A variety of BSP models have been developed for unsaturated soils due to the powerful ability of modelling various complex behaviors of unsaturated soils. Some BSP models for unsaturated soils (Rampino et al. 2000; Russell and Khalili 2006; Morvan et al. 2010; Fern et al. 2016; Lai et al. 2016; Patil et al. 2018) were formulated by extending the existing BSP models for saturated soils. For this purpose, the effective stress in the original saturated BSP model was replaced by the

Bishop's stress or net stress and several equations of saturated BSP models (e.g., equations for CSL, NCL and stress-dilatancy relationship, etc.) were modified to take into account of the influence of suction or degree of saturation. In addition, some other BSP models for unsaturated soils were formulated by: (i) building three-dimensional loading and bounding surface along similar logics with BBM based on two independent constitutive variables, for example, the net stress and matric suction (Yao et al. 2014; Romero et al. 2019; Luo et al. 2020; Zhao et al. 2021), the Bishop's stress and effective degree of saturation (Zhou and Sheng 2015), the Bishop's stress and degree of saturation (Li and Yang 2018), the Bishop's stress and suction (Li et al. 2019), or the Bishop's stress and bonding parameter (Han et al. 2021); (ii) assuming the mapping rule to describe the relationship between the loading and bounding surface and assuming proper hardening laws and flow rules for loading and bounding surface, respectively. The BSP approach was also applied to model the behaviors of unsaturated interfaces (Zhou et al. 2020). The formulation of several BSP models for unsaturated soils are succinctly summarized in Table 2.4.

Figure 2.17 shows the evolution of the ellipse loading and bounding surfaces of the unified hardening (UH) model proposed by Yao et al. (2014) for overconsolidated unsaturated soils based on drained triaxial compression test results. In this figure, points A – D are the current stress points on the loading surfaces and points A′ – D′ are the image points on the bounding surfaces that can be determined using the radial mapping rule. The hardening parameter of bounding surface, $(\bar{p}-u_a)_0$, is related to the plastic volumetric strain, ε_v^p, and the hardening parameter of loading surface, $(p-u_a)_0$, depends on ε_v^p and an overconsolidation parameter, $R=\left[(p-u_a)+p_s\right]/\left[(\bar{p}-u_a)+p_s\right]$. The initial state is represented by point A which is achieved after unloading from point A′. As the stress state moves along the stress path (A-B), both loading and bounding surfaces expand ($d(p-u_a)_0>0$ and $d(\bar{p}-u_a)_0>0$) until the characteristic state is reached at point B where $q_B = M_c(p_B - u_a)$. At this point, $d\varepsilon_v^p$ turns from compression to dilation and, as a result, $d(\bar{p}-u_a)_0$ turns from positive to negative value. After this point (B-C), the bounding surface begins to shrink ($d(\bar{p}-u_a)_0<0$) and the loading surface remains expanding ($d(p-u_a)_0>0$). When point C is reached, the stress state falls on the peak state line, whose slope is a function of R, and, as a result, $d(p-u_a)_0$ turns from positive to negative value. After this point (C-D), both the loading and bounding surfaces shrink ($d(p-u_a)_0<0$ and $d(\bar{p}-u_a)_0<0$), which

means the soil exhibits softening behavior, until the critical state is reached at point D, where the loading and bounding surfaces coincide. Figure 2.17 also presents the diagram of the stress-strain relationships simulated by CP and BSP for comparison. The discussions summarized suggest that BSP approach can overcome several of the limitations of the conventional Cam-clay-type models.

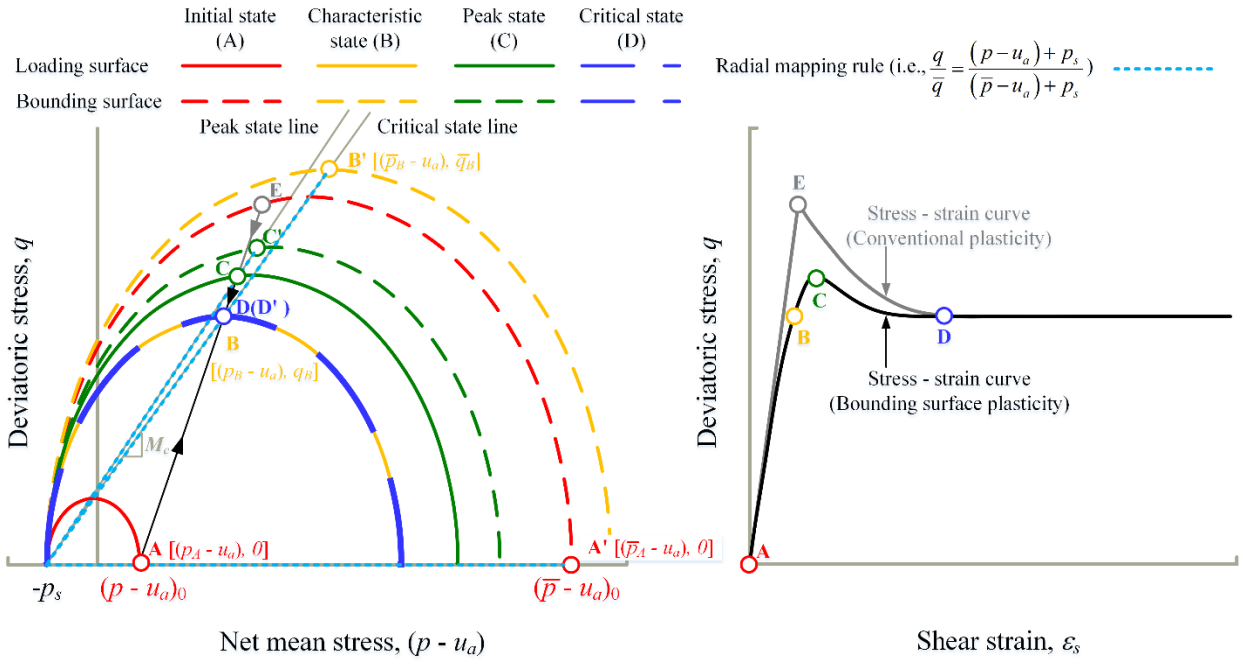

Figure 2.17 Diagram for strain-softening constitutive model of unsaturated soils based on bounding surface plasticity

Figure 2.16 compares the predicted results of CP models (solid lines) and the BSP models (dash lines) for three sets of experimental data (Patil et al. 2018; Estabragh and Javadi 2008; Cui and Delage 1996) of unsaturated soils which exhibit the strain-softening behavior. All the predicted results are collected from the corresponding source paper indicated in Figure 2.16. From these comparisons, it can be found that BSP models can overcome the limitations of CP models discussed in the previous section. Therefore, BSP model is a promising approach for modelling the strain-softening behavior of unsaturated soils. However, BSP models require more parameters in comparison with the CP models due to the introduction of the bounding surface. BSP models are complex due to involving advanced soil plasticity concepts, which limits their application in conventional engineering practice. Despite its limitations, the CP model is a relatively simpler approach that have been widely used in engineering practice.

2.5.3 Disturbed state concept

The disturbed state concept (DSC) that was originally introduced by Desai (1974) has been used as a tool in several constitutive models for modelling the strain-softening behavior of unsaturated soils. In DSC, the deforming soil is considered to transform gradually from a relative intact (RI) state to a fully adjusted (FA) state associated with microstructural changes during deformation. The RI state is defined as the initial condition where the soil is not influenced by the disturbance and the FA state is the final condition where the soil is fully disturbed. At any intermediate stage during the deforming process, the soil is assumed to be a combined random mixture of RI and FA states. Thus, the apparent response of the soil can be expressed as a weighted average of the responses at RI and FA states with a disturbance function as the weight (Desai 2000):

$$\sigma_{ij}^{a} = (1-D)\sigma_{ij}^{RI} + D\sigma_{ij}^{FA} \tag{2.13a}$$

$$D = D_u\left[1-\left\{1+\left(\frac{\xi_D}{h}\right)^{w}\right\}^{-s}\right] \tag{2.13b}$$

$$D = D_u\left[1-\exp\left(-A\xi_D^{Z}\right)\right] \tag{2.13c}$$

where σ_{ij}^{a} is the apparent stress tensor; σ_{ij}^{RI} is the stress tensor in the RI part; σ_{ij}^{FA} is the stress tensor in the FA part; D is the disturbance function, which represents the degree of disturbance occurring in the soil, varying between 0 when the entire soil is in RI state and 1 when the entire soil reaches FA state; D_u is the ultimate value of D in practice, which is less than 1 since FA can only be attained in an idealized condition; $\xi_D = \int (dE_{ij}^{p} dE_{ij}^{p})^{1/2}$ is the deviatoric plastic strain trajectory; E_{ij}^{p} is the deviatoric part of the plastic strain tensor; h, w, s and A, Z are material parameters in the disturbance function.

In order to formulate the DSC model, the two reference (RI and FA) states and corresponding constitutive models should be defined firstly. The constitutive models for RI and FA states can be assumed as any commonly used constitutive models for simplicity and reliability. For instance, in the DSC-HISS model (Desai 2000), the pre-peak state simulated by an elastoplastic model based

on conventional plasticity is selected as the RI state and the critical state simulated by a critical state model is selected as the FA state. Then, D is defined as a functional relationship of various internal variables (e.g., plastic strain) that can reflect the influence of microstructural changes resulting in the disturbance. For this purpose, two types of functions (i.e., Equations 2.13b and 2.13c) have been suggested by Desai (2000). The DSC model can be formulated by substituting the constitutive models for RI and FA states and the disturbance function into Equation 2.13a. Two DSC-based constitutive models (Geiser et al. 2000; Hamid and Miller 2008) for unsaturated soils and interfaces are summarized in Table 2.4. More recently, the DSC approach was used by Yang and Vanapalli (2020) to develop a model for the prediction of the strain-softening stress-strain relationship for a wide range of unsaturated soils.

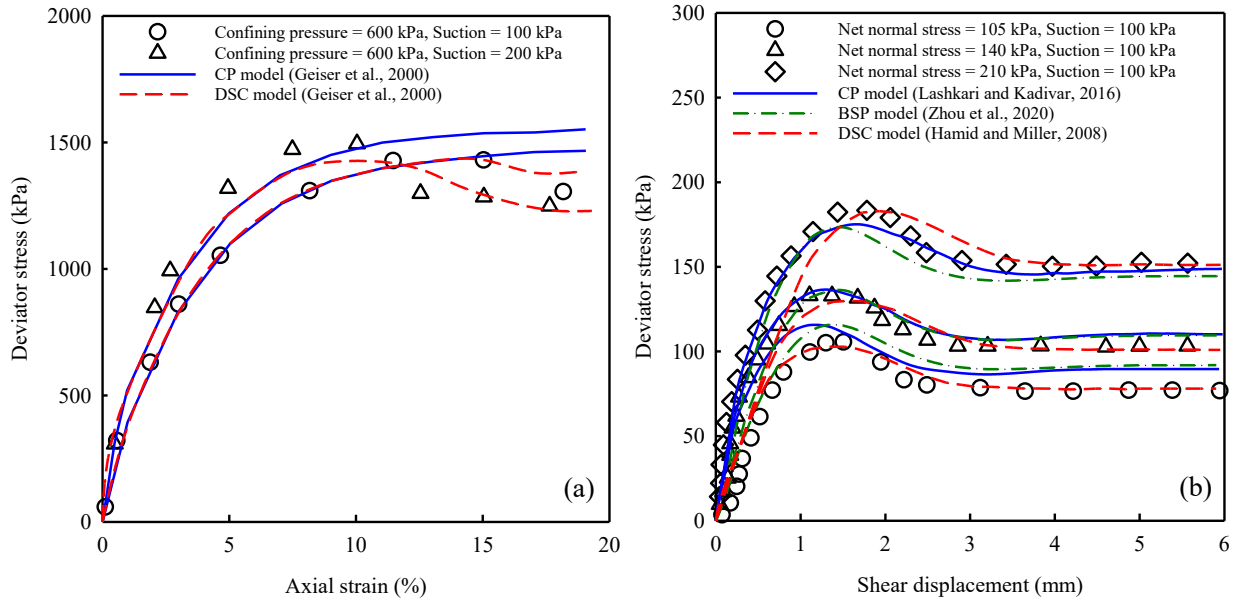

Figure 2.18 Comparisons between prediction results of conventional plasticity model and disturbed state concept model: (a) stress-strain curves of Sion silt (experimental data from Geiser et al. 2000); (b) stress-strain curves of rough soil–steel interface (experimental data from Hamid and Miller 2008)

Geiser (2000) developed a CP model for unsaturated soils (HISS-δ_{1unsat}) and then extended this model with DSC to formulate a DSC model (DSC- HISS-δ_{1unsat}). The details of the formulation of the two models are summarized in Table 2.4. Figure 2.18a compares the prediction results of HISS-δ_{1unsat} model (solid lines) and DSC-HISS-δ_{1unsat} model (dash lines) for experimental data of

suction-controlled triaxial shear tests on unsaturated silt specimens reported by Geiser (2000). It can be found, despite good predictions for the pre-peak part of the stress-strain curves, the CP model cannot reproduce the strain-softening behavior of unsaturated soils. This can be improved by introducing the DSC.

Figure 2.18b compares the prediction results of a CP model with state-dependent dilatancy, a BSP model, and a DSC model for the experimental data of suction-controlled direct shear tests on unsaturated rough soil–steel interfaces reported by Hamid and Miller (2008). All the prediction results were collected from the corresponding source paper indicated in Figure 2.18b. It can be found the prediction results of these three models are consistent and fit the experimental results well. This means the DSC model can provide good predictions similar to the BSP model. In addition, as discussed in previous section, the application of the state-dependent dilatancy in the CP model can improve the limitations of the Cam-clay-type models.

In summary, both the BSP and DSC approach can overcome the limitations of the models based on CP. However, the DSC approach is simpler in concept since it does not require the use of advanced soil plasticity concepts. In addition, the DSC approach can be combined conveniently with various commonly used constitutive models to reproduce complex soil behaviors. The flexibility of the DSC approach has encouraged various researchers to develop DSC-based constitutive models for saturated soils (Desai 2016) and unsaturated soils (Yang and Vanapalli 2020). However, on the other hand, the DSC models are formulated based on the assumptions of responses at RI and FA states and the disturbance function. This means, to a certain extent, the DSC models cannot provide a comprehensive physical interpretation of the material response despite being capable of reproducing various material responses mathematically.

2.6 SWCC and strain-softening behavior of unsaturated soils

In the prediction models of shear strength and constitutive models of unsaturated soils, the suction and the degree of saturation are typically included as variables to capture the hydraulic-mechanical behaviors of soils in unsaturated condition. However, the suction and the degree of saturation are not independent variables. The relationship between the suction and the degree of saturation is termed as Soil-Water Characteristic Curve (SWCC).

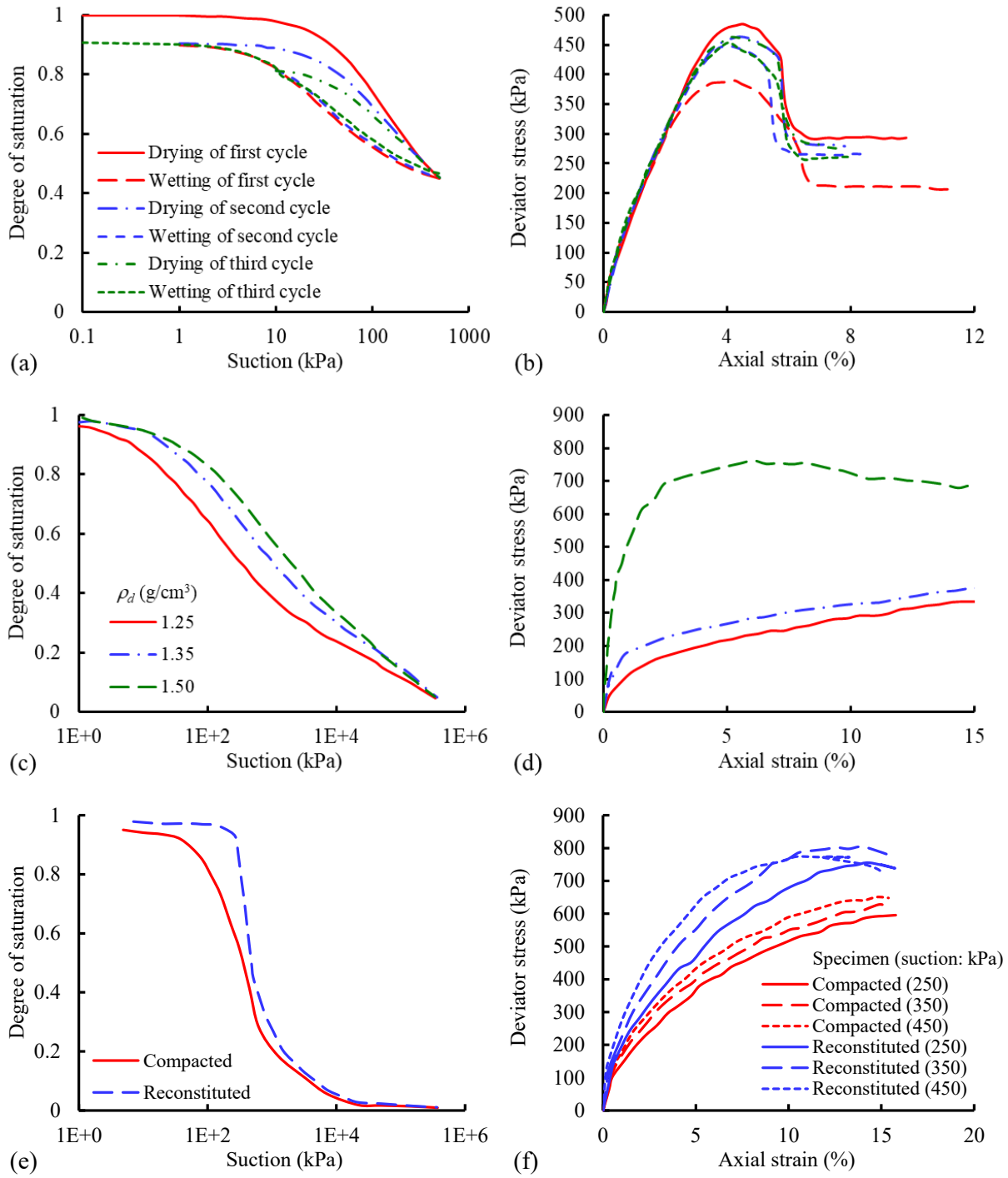

Figure 2.19 Influence of different factors on SWCC and corresponding stress-strain curve of unsaturated soils: (a), (b) influence of hydraulic hysteresis (modified after Goh et al. 2014); (c), (d) influence of dry density (modified after Zhang et al. 2020); (e), (f) influence of soil fabric (modified after Gao et al. 2016)

A unique SWCC is typically used in the interpretation and prediction of various properties of unsaturated soils. However, the SWCC is not unique and is influenced by many factors, such as the hydraulic hysteresis, the variation of dry density and the soil fabric. Accordingly, the strain-softening behavior of unsaturated soils will also be influenced by the hydraulic hysteresis (Goh et al. 2014; Pineda et al. 2014; Chen et al. 2018; Liu et al. 2020b), the variation of dry density (Gao et al. 2019; Zhang et al. 2020), the soil fabric (Zhan and Ng 2006; Gao et al. 2016; Mendes and Toll 2016; Ng et al. 2020). Figure 2.19 illustrates the influence of different factors on SWCC and corresponding stress-strain curves of unsaturated soils. Goh et al. (2014) measured the drying and wetting paths of SWCC and corresponding drained stress-strain curves (at matric suction of 300 kPa and net confining pressure of 50 kPa) of clayey sand specimens undergoing different drying-wetting cycles. It was found the subsequent-cycles drying and wetting paths was enclosed by the first-cycle drying and wetting paths (Figure 2.19a). Accordingly, the stress-strain curves corresponding to the drying and wetting paths of different drying-wetting cycles exhibit different strain-softening behaviors that are consistent with the SWCCs (Figure 2.19b). Zhang et al. (2020) measured the SWCC and corresponding drained stress-strain curves (at matric suction of 800 kPa and net confining pressure of 100 kPa) of expansive soil specimens with different dry densities. The experimental results show, at a given suction, the degree of saturation increases with an increase in the dry density (Figure 2.19c) and the stress-strain curve transfers from the strain-hardening to the strain-softening (Figure 2.19d). Gao et al. (2016) measured the SWCC and corresponding drained stress-strain curves (at matric suction of 250, 350 and 450 kPa and net confining pressure of 200 kPa) of compacted and reconstituted specimens of a clayey silt. The experimental results (Figures 2.19e and 2.19f) show, at a given suction, the reconstituted specimen (exhibiting a unimodal pore-size distribution) has a higher degree of saturation and exhibit strain-softening, while the compacted specimen (exhibiting a bimodal pore-size distribution) has a lower degree of saturation and exhibit strain-hardening.

A variety of models have been proposed for fitting the SWCC (e.g., Van Genuchten 1980; Fredlund and Xing 1994), which were well reviewed by Leong and Rahardjo (1997). Several models of SWCC that can take account of the influence of void ratio and the hydraulic hysteresis were developed, which were reviewed by Sheng (2011). In recent years, more models that can take account of the influence of void ratio and the hydraulic hysteresis (Gallipoli 2012; Zhou et al. 2012a; Han et al. 2021; Mahmoodabadi and Bryson 2021) were developed. These models

formulate the main drying/wetting curve equations, and the scanning curve equation based the incremental relationship between the degree of saturation and suction and void ratio (or volumetric strain). In addition, Rahardjo et al. (2018) formulated a model based on the incremental relationship between the degree of saturation and suction and net mean stress. Salager et al. (2013) developed a SWCC model using the theory of elastoplasticity and assuming the air-entry value as a function of void ratio. In addition to the models considering the effects of current void ratio, several simple models (Zhou et al. 2012b; Wijaya and Leong 2017; Tao et al. 2018) were developed to capture the effects of initial void ratio.

Due to the influence of the fabric of soil particles, the same unsaturated soils can exhibit a unimodal (e.g., reconstituted specimens and specimens compacted at the wet side of optimum) or bimodal (e.g., specimens compacted at the dry side of optimum) pore-size distribution, which can have an influence on the strain-softening behavior of unsaturated soils (Figure 2.19f). The bimodal pore-size distribution is usually associated with a bimodal SWCC according to the capillary theory. For this reason, the bimodal SWCC model should be taken account to capture the influence of soil fabric on strain-softening behavior. Wijaya and Leong (2016) and Li and Vanapalli (2021) have reviewed several commonly used bimodal SWCC models. The bimodal SWCC models can be categorized into three approaches: (i) the piecewise approach (i.e., two separate unimodal models corresponding to the macropores and micropores are combined by using an arbitrarily determined merging point), (ii) the fraction of total volume approach (i.e., the unimodal models for all components of the soil corresponding to the pore series are summed with the respective volumetric percentages as weights), and (iii) the unique parameter approach (all or some parameters of the bimodal model have physical meaning and can be determined graphically from SWCC). In addition, several models (Chen et al. 2019; Qian et al. 2022) that can take account of the influence of void ratio and bimodal behavior were also developed.

2.7 Time-dependency of strain-softening behaviors of unsaturated soils

The research summarized above mainly focus on the strain-softening behaviors of unsaturated soils without taking account of the influence of time (i.e., independent of time condition). However, in some scenarios (e.g., the embankment under traffic loads, the landslide, geo-structures under earthquake loading, etc.), the time effects can have a significant influence on the behavior of unsaturated soils (e.g., creep, stress relaxation and strain rate effect, etc.) (Augustesen et al. 2004).

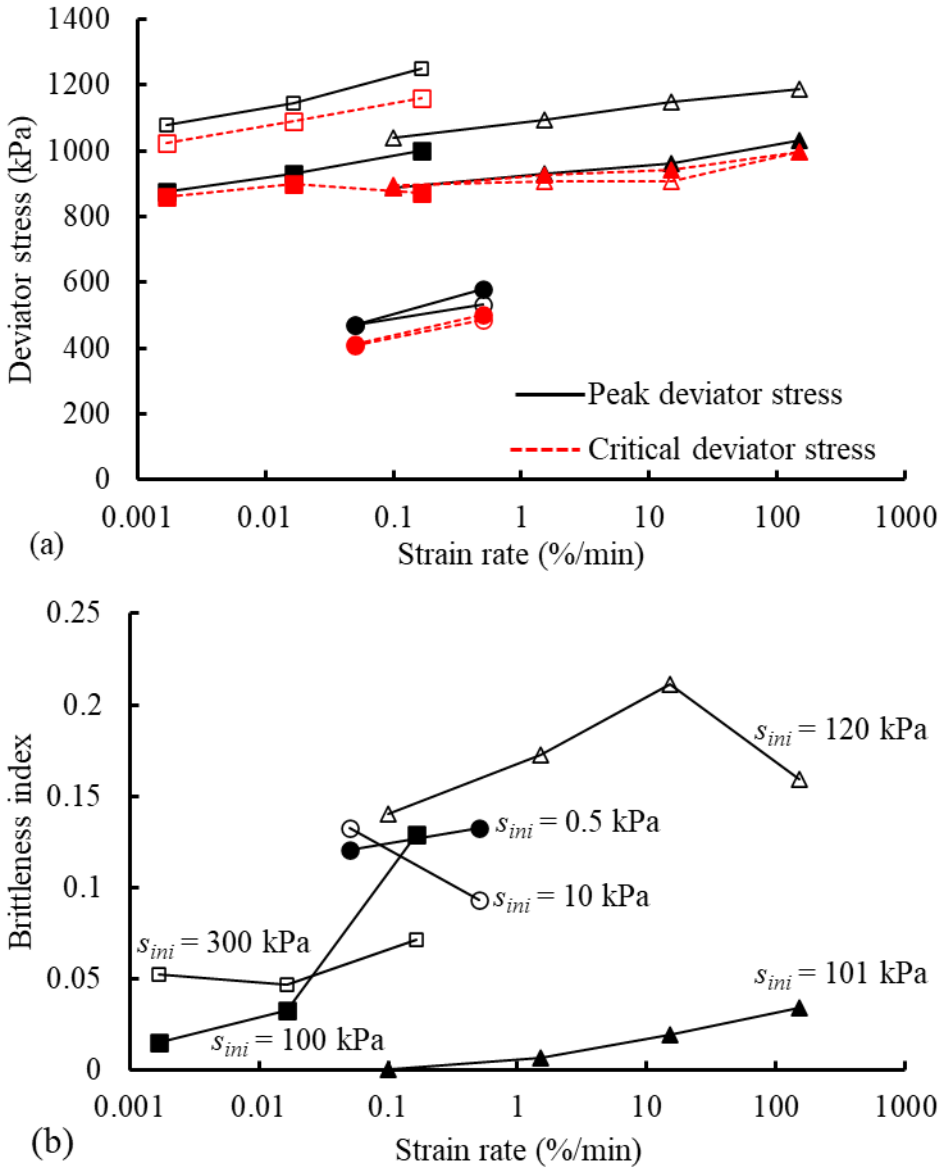

Zhang et al. (2014): CD, NCP = 50 kPa, s_{ini} = 0.5 kPa	Note:
Zhang et al. (2014): CD, NCP = 50 kPa, s_{ini} = 10 kPa	CD = drained condion;
Mun et al. (2016): UU, TCP = 207 kPa, s_{ini} = 101 kPa	UU = Unconsolidated undrained condtion;
Mun et al. (2016): UU, TCP= 207 kPa, s_{ini} = 120 kPa	CW = Constant water content condition;
Wu et al. (2020): CW, NCP = 400 kPa, s_{ini} = 100 kPa	NCP = Net confining pressure;
Wu et al. (2020): CW, NCP = 400 kPa, s_{ini} = 300 kPa	TCP = Total confining pressure;
	s_{ini} = initial suction.

Figure 2.20 Effects of strain rate on the strain-softening behaviors of unsaturated soils: (a) peak and critical deviator stress; (b) brittleness index

For unsaturated soils, the rate-dependency of the shearing behavior has been investigated in several experimental studies (Oka et al. 2010; Zhang et al. 2014; Mun et al. 2016; Toyota et al. 2019; Wu et al. 2020; Hu et al. 2020). Figure 2.20 summarizes the relationships between peak deviator stress (q_p), critical deviator stress (q_c) and brittleness index ($(q_p - q_c)/q_p$) and the strain rate that were obtained in different triaxial shearing tests on unsaturated granular (Zhang et al. 2014), silty (Wu et al. 2020) and clayey soils (Mun et al. 2016). Figure 2.20a shows the higher strain rate can contribute to larger peak and critical deviator stress in the three sets of tests (Zhang et al. 2014; Wu et al. 2020; Mun et al. 2016). However, some other studies (Oka et al. 2010; Toyota et al. 2019) also showed a decrease in the peak deviator stress with increasing strain rate. Figure 2.20b shows the strain rate can enhance the brittleness of the unsaturated specimens in the three sets of tests (Zhang et al. 2014; Wu et al. 2020; Mun et al. 2016). In addition, the effects of strain rate on the brittleness are different under different initial suctions.

The rate-dependency of the peak and critical deviator stress and brittleness is strongly related to the rate-dependency of the volumetric change, suction and degree of saturation during shearing of unsaturated soils. Most of studies (Oka et al. 2010; Zhang et al. 2014; Mun et al. 2016; Toyota et al. 2019; Wu et al. 2020; Hu et al. 2020) showed that the specimen under higher strain rate exhibits more dilatancy instead of compression than that under lower strain rate. In addition, Wu et al. (2000) showed the suction at critical state increases and degree of saturation at critical state decrease as the strain rate rises. The rate-dependency of shearing behavior of unsaturated soils can be attributed to the viscoelastic property of the pore fluids and the loading time that influences the rearrangement of soil structure, the transfer of pore water, the dissolution of pore air, the drainage of pore fluids and the crushing of coarse grains, etc. (Oka et al. 2010; Zhang et al. 2014; Wu et al. 2020).

In summary, the strain rate can have a significant influence on the strain-softening behavior of unsaturated soils. However, the experimental studies on the rate-dependency of strain-softening behavior of unsaturated soils are limited and far from conclusive.

Different classes of constitutive models have been developed for the saturated soils to capture the time-dependent viscous phenomena based on the empirical, rheological, and elasto-viscoplastic approach (Liingaard et al. 2004). However, most of the constitutive models for unsaturated soils

were formulated based on the rate-independent theory (Khalili et al. 2022). Ehlers et al. (2004) and Oka et al. (2006) were pioneers in the development of the elasto-viscoplastic models for capturing the time-dependent behaviors of unsaturated soils based on the overstress theory (Perzyna 1966). Shahbodagh (2011) and Oka et al. (2019) extended the Oka et al. (2006) model for dynamic analysis of unsaturated soils taking account of nonlinear kinematic hardening rule and structural degradation of the soil skeleton. Lazari et al. (2015) developed a local and non-local elasto-viscoplastic model for multiphase geomaterials under quasi-static loading. The overstress theory was extended according to non-local approach (Lazari et al. 2015) for handling weakly rate-sensitive materials (e.g., granular materials). Collin et al. (2008) and Thanh et al. (2019) extended the BBM model (Alonso et al. 1990) using overstress theory to capture the viscoplastic behavior of oil reservoir chalks (considering oil-water suction) and unsaturated soils, respectively. In addition to the overstress-type models, some elasto-viscoplastic models were formulated based on other approaches. Mac et al. (2019) formulated an elasto-viscoplastic model by extending a bounding surface plasticity model of unsaturated soils. The hardening parameter representing the size of the bounding surface is defined as a function of viscoplastic strain, viscoplastic strain rate, and suction. De Gennaro and Pereira (2013) formulated an elasto-viscoplastic models for unsaturated soils based on the concept of timelines (Bjerrum 1967). Due to the secondary compression, there is not a single stress-strain curve in one-dimensional compression of clay, but a family of curves (i.e., timelines) each of which is corresponding to different strain rate. The concept of timelines can be extended to unsaturated soils, and it can be incorporated into the existing elasto-plastic models of unsaturated soils (e.g., BBM) to capture the time-dependent behaviors of unsaturated soils (De Gennaro and Pereira 2013).

2.8 Discussion

The residual state behavior of unsaturated soils is important in the rational analysis and design of geo-structures undergoing large shear deformation. However, most of current studies on the strain-softening behavior of unsaturated soils are based on the suction-controlled direct or triaxial shear tests which can only provide limited shear deformation. The studies on the strain-softening behavior of unsaturated soils under large shear deformation are still limited. As is well known, the studies on the behavior of unsaturated soils under large shear deformation must be conducted based on suction-controlled ring shear apparatus. However, despite some progress in the last fifteen years

in the design of suction-controlled ring shear apparatus (Infante Sedano et al. 2007; Hoyos et al. 2011; Merchán et al. 2011), there are still several problems (e.g., the extrusion of soils during shearing, sliding between the top platen and the specimen, etc.) influencing the reliability of the measured results. Therefore, the development of a reliable suction-controlled ring shear apparatus will be a key for obtaining reliable and reproducible studies on the strain-softening behavior of unsaturated soils under large shear deformation. In addition, due to the lack of experimental data, the studies on the prediction of the RSS of unsaturated soils and the numerical modeling of the reduction in shear strength of unsaturated soils under large deformation are also limited. These studies will be meaningful for the design and analysis of geo-structures in unsaturated soils that undergo large shear deformation, for example, the progressive failure of unsaturated soil slopes. For this purpose, the DSC model that not only overcomes the limitations of CP models but also is simpler than the BSP models may be a promising approach for modelling the strain-softening behavior of unsaturated soils under large shear deformation. In addition, the elasto-viscoplastic models can be used as tools for capturing the time-dependency of the strain-softening behavior of unsaturated soils.

2.9 Summary

The studies related to the strain-softening behavior of unsaturated soils are summarized in this chapter under three categories: (i) mechanical characteristics and micro-mechanisms, (ii) prediction models for shear strength and (iii) numerical methods for modelling strain-softening behavior of unsaturated soils. In addition, the influence of SWCC and time effects on the strain-softening behavior of unsaturated soils are discussed.

A variety of experimental studies (including unsaturated direct and triaxial shear tests and X-ray micro-CT images) are summarized to interpret the strain-softening behavior of unsaturated soils from peak to critical state that is typically associated with the localized dilation inside the shear band. The strain-softening of unsaturated soils associated with the dilation can be attributed to two key factors: (i) the destruction of the original structure of soil particles inside the shear band due to the rolling of soil particles, which is similar to the behavior of saturated soils, and (ii) the local loss of water menisci area within the shear band caused by the rupture of the water menisci and the lower water retention capability due to the generation of the large voids.

Several experimental studies based on the conventional and suction-controlled ring shear apparatuses are summarized to interpret the strain-softening behavior of unsaturated soils under large shear deformation. These studies highlighted the contribution of suction to the residual shear strength (RSS) even when the shear displacement have exceeded 100 mm. However, research on the microstructure of unsaturated soils that is subjected to large shear deformation is limited despite some indirect information derived from the mechanical behavior. The experimental results show inconsistent behavior with respect to the microstructure of unsaturated soils sheared to residual state, which may be attributed to many factors such as the soil physical properties, suction level, state of pore water and others. On the other hand, a consensus was reached from these studies that the RSS of unsaturated soils is independent of the history specific structure caused by various factors, e.g., the initial water content, the suction history, and the pre-shearing history.

Various prediction models for peak and critical shear strength (PSS and CSS) are summarized to discuss the typical methods of incorporating the influence of the soil fabric and water phase on the shear strength in the prediction models of $\tan\phi^a$ and $\tan\phi^b$. These models are divided into two groups: (i) $\tan\phi^a$ equal to $\tan\phi'$, and (ii) $\tan\phi^a$ varying with suction. In these models, $\tan\phi^b$ typically decreases nonlinearly with respect to suction which can be interpreted in terms of the area of free capillary water existing as water menisci among soil particles or aggregates. However, $\tan\phi^a$ can be constant, increase or decrease with suction. Some possible interpretations for the variation of $\tan\phi^a$ are also summarized in terms of the aggregation fabric of unsaturated fine-grained soils. However, there is still a lack of a unified interpretation approach that can be extended for the different patterns of $\tan\phi^a$ variation of a wide range of unsaturated soils. Three prediction models for CSS of unsaturated soils that considers the variation of $\tan\phi^a$ with suction were compared and discussed. All of them can predict the magnitudes of CSS well; however, the model based on two stress state variables is more flexible that can provide a better prediction for the variations of $\tan\phi^a$ and $\tan\phi^b$ with suction.

Two prediction models for the RSS of unsaturated soils are summarized that can be used for low and high suction range, respectively. The prediction results of the models proposed for PSS and CSS of unsaturated soils were compared with the experimental data of RSS of unsaturated soils reported by Infante Sedano and Vanapalli (2011) and Hoyos et al. (2014). The comparisons show

that the models proposed for PSS and CSS of unsaturated soils are not suitable for the prediction of RSS of unsaturated soils. Due to these reasons, there is a need for more studies on the RSS prediction model of unsaturated soils.

Three numerical methods (i.e., conventional plasticity (CP), bounding surface plasticity (BSP) and disturbed state concept (DSC) approach) of modelling the strain-softening behavior of unsaturated soils are discussed. The conventional Cam-clay-type models are widely used in engineering practice and can capture the main features of the behaviors observed in unsaturated soils. However, they are limited in reproducing the strain-softening behavior; for example, the strain-softening behavior cannot be reproduced when the stress path intersects the initial yield surface at the right of CSL, only elastic strain is considered prior to yielding and there is a sharp transition at the peak point of the stress-strain relationship between the elastic and plastic states. The limitations of the CP approach can be overcome by introducing the BSP approach. The BSP models are powerful for simulating various behaviors of unsaturated soils; however, they are complex as they are based on advanced soil plasticity concepts that typically require more parameters due to introduction of the bounding surface. The DSC approach can also be extended to overcome several of the limitations of the CP models; additionally, it does not require advanced soil plasticity concepts and is based on simpler concepts in comparison to BSP. For this reason, it can be a promising approach for modelling the strain-softening behavior of unsaturated soils. However, the DSC models can offer a good performance from the perspective of mathematics but may not be able to provide a comprehensive physical interpretation of the material response because it is formulated based on the assumptions of RI and FA states and disturbance function.

A unique SWCC is typically used in conventional analysis approach to capture the hydraulic-mechanical behaviors of unsaturated soils. However, the SWCC is not unique for a given soil due to the influence of various factors (e.g., the hydraulic hysteresis, the variation of dry density, the soil fabric, etc.); accordingly, the strain-softening behavior of unsaturated soils will also be influenced by these factors. For this reason, the SWCC models that can take account of the influence of the hydraulic hysteresis, void ratio and bimodal pore-size distribution are discussed.

The strain-softening behavior of unsaturated soils exhibit significant rate-dependency. This can be attributed to the viscoelastic property of the pore fluids and the loading time that influences the

rearrangement of soil structure, the transfer of pore water, the dissolution of pore air, the drainage of pore fluids and the crushing of coarse grains, etc. However, the experimental studies on the rate-dependency of strain-softening behavior of unsaturated soils are limited and far from conclusive. The elasto-viscoplastic behavior of unsaturated soils can be taken into account extending numerical modelling techniques for capturing the time-dependency of the strain-softening behavior of unsaturated soils.

2.10 References

Al-Khazaali, M., and Vanapalli, S. K. 2019. Axial force–displacement behaviour of a buried pipeline in saturated and unsaturated sand. Géotechnique, 69(11): 986-1003.

Alonso, E. E., Gens, A., and Josa, A. 1990. A Constitutive model for partially saturated soils. Géotechnique, 40(3): 405-30.

Alonso, E. E., Iturralde, E. F. O., and Romero, E. E. 2007. Dilatancy of coarse granular aggregates. In Experimental unsaturated soil mechanics, 119-135. Springer, Berlin, Heidelberg.

Alonso, E. E., Pereira, J. M., Vaunat, J., and Olivella, S. 2010. A microstructurally based effective stress for unsaturated soils. Géotechnique, 60(12): 913-25.

Andò, E., Hall, S. A., Viggiani, G., Desrues, J., and Bésuelle, P. 2012. Grain-scale experimental investigation of localised deformation in sand: a discrete particle tracking approach. Acta Geotechnica, 7(1): 1-3.

Atkinson, J. 2007. The mechanics of soils and foundations, 2nd edition. London: Taylor and Francis.

Augustesen, A., Liingaard, M., and Lade, P. V. 2004. Evaluation of time-dependent behavior of soils. International Journal of Geomechanics, 4(3): 137-156.

Bardet, J. P. 1986. Bounding surface plasticity model for sands. Journal of Engineering Mechanics, 112(11): 1198-217.

Bishop, A. W. 1959. The principle of effective stress. Teknisk Ukeblad, 39: 859-63.

Bishop, A. W., Green, G. E., Garga, V. K., Andresen, A., and Brown, J. D. 1971. A new ring shear apparatus and its application to the measurement of residual strength. Géotechnique, 21(4): 273-328.

Bjerrum, L. 1967. Engineering geology of Norwegian normally-consolidated marine clays as related to settlements of buildings. Geotechnique, 17(2): 83-118.

Bolton, M. D. 1986. The strength and dilatancy of sands. Géotechnique, 36(1): 65-78.

Cai, G., Han, B., Asreazad, S., Liu, C., Zhou, A., Li, J., and Zhao, C. 2022. Experimental study on critical state behavior of unsaturated silty sand under constant matric suctions. Géotechnique, 1-67.

Chávez, C., and Alonso, E. E. 2003. A constitutive model for crushed granular aggregates which includes suction effects. Soils and foundations, 43(4) : 215-227.

Chen, R., Xu, T., Lei, W., Zhao, Y., and Qiao, J. 2018. Impact of multiple drying–wetting cycles on shear behaviour of an unsaturated compacted clay. Environmental Earth Sciences, 77(19): 1-9.

Chen, R. P., Liu, P., Liu, X. M., Wang, P. F., and Kang, X. 2019. Pore-scale model for estimating the bimodal soil–water characteristic curve and hydraulic conductivity of compacted soils with different initial densities. Engineering Geology, 260: 105199.

Chen, W., Song, B., Wu, W., Sun, Y., and Song, Y. 2021. Direct and reversal shear behaviors of three kinds of slip zone soil in the Northwest of China. Bulletin of Engineering Geology and the Environment, 80(5): 3939-3952.

Chiu, C. F., and Ng, C. W. 2003. A state-dependent elasto-plastic model for saturated and unsaturated soils. Géotechnique, 53(9): 809-29.

Collin, F., Gennaro, V. D., Delage, P., and Priol, G. 2008. An elasto-viscoplastic model for chalk including suction effects. In 1st European Conference on Unsaturated Soils. Taylor & Francis, London, United Kingdom.

Cui, Y. J., and Delage, P. 1996. Yielding and plastic behaviour of an unsaturated compacted silt. Géotechnique, 46(2): 291-311.

Cunningham, M. R., Ridley, A. M., Dineen, K., and Burland, J. B. 2003. The mechanical behaviour of a reconstituted unsaturated silty clay. Géotechnique, 53(2): 183-194.

Dafalias, Y. F, and Popov, E. P. 1975. A model of nonlinearly hardening materials for complex loading. Acta Mechanica, 21(3): 173-92.

De Gennaro, V., and Pereira, J. M. 2013. A viscoplastic constitutive model for unsaturated geomaterials. Computers and Geotechnics, 54: 143-151.

Delage, P., Suraj de Silva, G. R., and De Laure, E. 1987. Un nouvel appareil triaxial pour les sols non-satures. In Proceedings of 9th European Conference on Soil Mechanics and Foundation Engineering, 25–28. Rotterdam: Balkema.

Delage, P., and Graham, J. 1995. Mechanical behavior of unsaturated soils: understanding the behavior of unsaturated soils requires reliable concept models. In Proceedings of 1st International Conference on Unsaturated Soils, 1223-56. Rotterdam: Balkema.

Delage, P., Audiguier, M., Cui, Y. J., and Howat, M. D. 1996. Microstructure of a compacted silt. Canadian Geotechnical Journal, 33(1): 150-8.

Delage, P. 2002. Experimental unsaturated soil mechanics. In Proceedings of 3rd International Conference on Unsaturated Soils, 973-96. Rotterdam: Balkema.

Derbyshire, E., Dijkstra, T. A., Smalley, I. J., and Li, Y. 1994. Failure mechanisms in loess and the effects of moisture content changes on remoulded strength. Quaternary International, 24: 5-15.

Desai, C. S. 1974. A consistent finite element technique for work-softening behavior. In Proceedings of the International Conference on Computational Methods in Nonlinear Mechanics. Austin, TX: University of Texas.

Desai, C. S. 2016. Disturbed state concept as unified constitutive modeling approach. Journal of Rock Mechanics and Geotechnical Engineering, 8(3): 277-93.

Desai, C. S. 2000. Mechanics of materials and interfaces: the disturbed state concept. Boca Raton: CRC press.

Dijkstra, T. A., Rogers, C. D., Smalley, I. J., Derbyshire, E., Li, Y. J., and Meng, X. M. 1994. The loess of north-central China: geotechnical properties and their relation to slope stability. Engineering Geology, 36(3-4): 153-71.

D'Onza, F., Gallipoli, D., Wheeler, S., Casini, F., Vaunat, J., Khalili, N., Laloui, L., Mancuso, C., Mašín, D., Nuth, M. and Pereira, J.M. 2011. Benchmark of constitutive models for unsaturated soils. Géotechnique, 61(4): 283-302.

Ehlers, W., Graf, T., and Ammann, M. 2004. Deformation and localization analysis of partially saturated soil. Computer methods in applied mechanics and engineering, 193(27-29): 2885-2910.
Escario, V., and Saez, J. 1986. The shear strength of partly saturated soils. Géotechnique, 36(3): 453-6.
Estabragh, A. R., and Javadi, A. A. 2008. Critical state for overconsolidated unsaturated silty soil. Canadian Geotechnical Journal, 45(3): 408-20.
Fan, X., Xu, Q., Scaringi, G., Li, S., and Peng, D. 2017. A chemo-mechanical insight into the failure mechanism of frequently occurred landslides in the Loess Plateau, Gansu Province, China. Engineering Geology, 228: 337-45.
Fern, E. J., Robert, D. J., and Soga, K. 2016. Modeling the stress-dilatancy relationship of unsaturated silica sand in triaxial compression tests. Journal of Geotechnical and Geoenvironmental Engineering, 142(11): 04016055.
Fredlund, D. G., Morgenstern, N. R., and Widger, R. A. 1978. The shear strength of unsaturated soils. Canadian Geotechnical Journal, 15(3): 313-21.
Fredlund, D. G., and Xing, A. 1994. Equations for the soil-water characteristic curve. Canadian Geotechnical Journal, 31(4): 521-32.
Gallipoli, D., Gens, A., Chen, G., and D'Onza, F. 2008. Modelling unsaturated soil behaviour during normal consolidation and at critical state. Computers and Geotechnics, 35(6): 825-34.
Gallipoli, D. 2012. A hysteretic soil-water retention model accounting for cyclic variations of suction and void ratio. Geotechnique, 62(7): 605-616.
Gan, J. K., Fredlund, D. G., and Rahardjo, H. 1988. Determination of the shear strength parameters of an unsaturated soil using the direct shear test. Canadian Geotechnical Journal, 25(3): 500-10.
Gao, Y., Sun, D. A., and Zhou, A. 2016. Hydromechanical behaviour of unsaturated soil with different specimen preparations. Canadian Geotechnical Journal, 53(6): 909-917.
Gao, Y., Sun, D. A., Zhu, Z., and Xu, Y. 2019. Hydromechanical behavior of unsaturated soil with different initial densities over a wide suction range. Acta Geotechnica, 14(2): 417-428.
Geiser, F., Laloui, L., and Vulliet, L. 2000. Modelling the behaviour of unsaturated silt. Experimental evidence and theoretical approaches in unsaturated soils, 163-184. CRC Press.
Geiser, F., Laloui, L., and Vulliet, L. 2006. Elasto-plasticity of unsaturated soils: laboratory test results on a remoulded silt. Soils and Foundations, 46(5): 545-56.
Gens, A., Sánchez, M., and Sheng, D. 2006. On constitutive modelling of unsaturated soils. Acta Geotechnica, 1(3): 137-147.
Goh, S. G., Rahardjo, H., and Leong, E. C. 2014. Shear strength of unsaturated soils under multiple drying-wetting cycles. Journal of Geotechnical and Geoenvironmental Engineering, 140(2): 06013001.
Hamid, T. B., and Miller, G. A. 2008. A constitutive model for unsaturated soil interfaces. International Journal for Numerical and Analytical Methods in Geomechanics, 32(13): 1693-714.
Han, B., Cai, G., Zhou, A., Li, J., and Zhao, C. 2021. A bounding surface model for unsaturated soils considering the microscopic pore structure and interparticle bonding effect due to water menisci. Acta Geotechnica, 16(5): 1331-1354.
Hayden, C. P., Purchase-Sanborn, K., and Dewoolkar, M. 2018. Comparison of site-specific and empirical correlations for drained residual shear strength. Géotechnique, 68(12): 1099-108.

Heredia, J. E. Y. 2015. Thermo-hydro-mechanical behavior of unsaturated clayey soils via thermo/suction-controlled ring shear testing. Ph.D. dissertation, Arlington, US: University of Texas.

Higo, Y., Oka, F., Kimoto, S., Sanagawa, T., and Matsushima, Y. 2011. Study of strain localization and microstructural changes in partially saturated sand during triaxial tests using microfocus X-ray CT. Soils and Foundations, 51(1): 95-111.

Higo, Y., Oka, F., Sato, T., Matsushima, Y., and Kimoto, S. 2013. Investigation of localized deformation in partially saturated sand under triaxial compression using microfocus X-ray CT with digital image correlation. Soils and Foundations, 53(2): 181-98.

Hossain, M. A., and Yin, J. H. 2010a. Behavior of a compacted completely decomposed granite soil from suction controlled direct shear tests. Journal of Geotechnical and Geoenvironmental Engineering, 136(1): 189-98.

Hossain, M. A., and Yin, J. H. 2010b. Shear strength and dilative characteristics of an unsaturated compacted completely decomposed granite soil. Canadian Geotechnical Journal, 47(10): 1112-1126.

Hoyos, L. R., Velosa, C. L., and Puppala, A. J. 2011. A servo/suction-controlled ring shear apparatus for unsaturated soils: Development, performance, and preliminary results. Geotechnical Testing Journal, 34(5): 413-23.

Hoyos, L. R., Velosa, C. L., and Puppala, A. J. 2014. Residual shear strength of unsaturated soils via suction-controlled ring shear testing. Engineering Geology, 172: 1-11.

Hu, W., Scaringi, G., Xu, Q., Van Asch, T. W., Huang, R., and Han, W. 2018. Suction and rate-dependent behaviour of a shear-zone soil from a landslide in a gently-inclined mudstone-sandstone sequence in the Sichuan basin, China. Engineering Geology, 237: 1-11.

Hu, T., Liu, D., and Chang, J. 2020. Experimental study on strain rate effect of strength characteristics of unsaturated silty clay. Case Studies in Construction Materials, 12, e00332.

Infante Sedano, J. A., Vanapalli, S. K., and Garga, V. K. 2007. Modified ring shear apparatus for unsaturated soils testing. Geotechnical Testing Journal, 30(1): 39-47.

Infante Sedano, J. A., and Vanapalli, S. 2011. Experimental investigation of the relationship between the critical state shear strength of unsaturated soils and the soil-water characteristic curve. International Journal of Geotechnical Engineering, 5(1): 1-8.

Jefferies, M. G. 1993. Nor-Sand: a simle critical state model for sand. Géotechnique, 43(1): 91-103.

Jommi, C. 2000. Remarks on the constitutive modelling of unsaturated soils. In Experimental Evidence and Theoretical Approaches in Unsaturated Soils, edited by Tarantino, A., and Mancuso, C., 139-53. Rotterdam: Balkema.

Jotisankasa, A., Coop, M., and Ridley, A. 2009. The mechanical behaviour of an unsaturated compacted silty clay. Géotechnique, 59(5): 415-28.

Kang, X., Wang, S., and Yu, Z. 2022. Effects of Soil–Water Interaction on the Mechanical Behaviors of Shear-Zone Soils. International Journal of Geomechanics, 22(10): 06022028.

Karube, D., and Kawai, K. 2001. The role of pore water in the mechanical behavior of unsaturated soils. Geotechnical and Geological Engineering, 19(3-4): 211-41.

Kayadelen, C., Tekinsoy, M. A., and Taşkıran, T. 2007. Influence of matric suction on shear strength behavior of a residual clayey soil. Environmental Geology, 53(4): 891.

Khaddour, G. 2015. Multi-scale charaterisation of the hydro-mechecanical behaviour of unsaturated sand: water retention and triaxial responses. Ph.D. dissertation, Grenoble, France: Université Grenoble Alpes.

Khalili, N., and Khabbaz, M. H. 1998. A unique relationship for χ for the determination of the shear strength of unsaturated soils. Géotechnique, 48(5): 681-7.
Khalili, N., Romero, E., and Marinho, F. A. 2022. State of the Art Report. Advances in Unsaturated Soil Mechanics: Constitutive modelling, experimental investigation, and field instrumentation. Proceedings of the 20th ICSMGE, Sydney.
Kido, R., and Higo, Y. 2019. Distribution changes of grain contacts and menisci in shear band during triaxial compression test for unsaturated sand. Japanese Geotechnical Society Special Publication, 7(2): 627-35.
Kido, R., and Higo, Y. 2020. Microscopic characteristics of partially saturated dense sand and their link to macroscopic responses under triaxial compression conditions. Acta Geotechnica, 15(11): 3055-73.
Kim, B. S., Shibuya, S., Park, S. W., and Kato, S. 2010. Application of suction stress for estimating unsaturated shear strength of soils using direct shear testing under low confining pressure. Canadian Geotechnical Journal, 47(9): 955-70.
Kim, B. S., Park, S. W., Takeshita, Y., and Kato, S. 2016. Effect of suction stress on critical state of compacted silty soils under low confining pressure. International Journal of Geomechanics, 16(6): D4016010.
Kouzegaran, S., Shahnazari, H., and Jafarian, Y. 2021. The unsaturated shear strength of calcareous soil in comparison with silicate soil. Marine Georesources & Geotechnology, 39(2): 200-218.
Kovacevic, N., Potts, D. M., Vaughan, P. R. 2001. Progressive failure in clay embankments due to seasonal climate changes. In Proceedings of 15th International Conference on Soil Mechanics and Geotechnical Engineering, 2127-30. Lisse: Balkema.
Lai, B. T., Wong, H., Fabbri, A., and Branque, D. 2016. A new constitutive model of unsaturated soils using bounding surface plasticity (BSP) and a non-associative flow rule. Innovative Infrastructure Solutions, 1(1): 3.
Lashkari, A., and Kadivar, M. 2016. A constitutive model for unsaturated soil–structure interfaces. International Journal for Numerical and Analytical Methods in Geomechanics, 40(2): 207-234.
Lazari, M., Sanavia, L., and Schrefler, B. A. 2015. Local and non-local elasto-viscoplasticity in strain localization analysis of multiphase geomaterials. International Journal for Numerical and Analytical methods in Geomechanics, 39(14): 1570-1592.
Leong, E. C., and Rahardjo, H. 1997. Review of soil-water characteristic curve equations. Journal of geotechnical and geoenvironmental engineering, 123(12): 1106-1117.
Li, X. S., and Dafalias, Y. F. 2000. Dilatancy for cohesionless soils. Géotechnique, 50(4): 449-60.
Li, L., Zhang, X., Chen, G., and Lytton, R. 2015. Measuring unsaturated soil deformations during triaxial testing using a photogrammetry-based method. Canadian Geotechnical Journal, 53(3): 472-489.
Li, W., and Yang, Q. 2018. Hydromechanical constitutive model for unsaturated soils with different overconsolidation ratios. International Journal of Geomechanics, 18(2): 04017142.
Li, J., Yin, Z. Y., Cui, Y. J., Liu, K., and Yin, J. H. 2019. An elasto-plastic model of unsaturated soil with an explicit degree of saturation-dependent CSL. Engineering Geology, 260, 105240.
Li, Y., and Vanapalli, S. K. 2021. A novel modeling method for the bimodal soil-water characteristic curve. Computers and Geotechnics, 138: 104318.
Lian, B., Peng, J., Wang, X., and Huang, Q. 2020. Moisture content effect on the ring shear characteristics of slip zone loess at high shearing rates. Bulletin of Engineering Geology and the Environment, 79(2): 999-1008.

Liingaard, M., Augustesen, A., and Lade, P. V. 2004. Characterization of models for time-dependent behavior of soils. International Journal of Geomechanics, 4(3): 157-177.
Liu, Y., and Vanapalli, S. K. 2019. Load displacement analysis of a single pile in an unsaturated expansive soil. Computers and Geotechnics, 106: 83-98.
Liu, K., Yin, J. H., Chen, W. B., Feng, W. Q., and Zhou, C. 2020a. The stress–strain behaviour and critical state parameters of an unsaturated granular fill material under different suctions. Acta Geotech, 15: 3383–3398.
Liu, P., Chen, R. P., Wu, K., and Kang, X. 2020b. Effects of drying-wetting cycles on the mechanical behavior of reconstituted granite-residual soils. Journal of Materials in Civil Engineering, 32(8): 04020199.
Liu, K., Yin, Z. Y., Chen, W. B., Feng, W. Q., and Yin, J. H. 2021. Nonlinear Model for the Stress–Strain–Strength Behavior of Unsaturated Granular Materials. International Journal of Geomechanics, 21(7): 04021103.
Lu, N., and Likos, W. J. 2006. Suction stress characteristic curve for unsaturated soil. Journal of Geotechnical and Geoenvironmental Engineering, 132(2): 131-42.
Lu, N. 2008. Is matric suction a stress variable? Journal of Geotechnical and Geoenvironmental Engineering, 134(7): 899-905.
Lu, N., Godt, J. W., and Wu, D. T. 2010. A closed-form equation for effective stress in unsaturated soil. Water Resources Research, 46(5): W05515.
Luo, T., Chen, D., Yao, Y. P., and Zhou, A. N. 2020. An advanced UH model for unsaturated soils. Acta Geotechnica, 15(1): 145-164.
Lupini, J. F., Skinner, A. E., and Vaughan, P. R. 1981. The drained residual strength of cohesive soils. Géotechnique, 31(2): 181-213.
Ma, T., Wei, C., Wei, H., and Li, W. 2016. Hydraulic and mechanical behavior of unsaturated silt: Experimental and theoretical characterization. International Journal of Geomechanics, 16(6): D4015007.
Maatouk, A., Leroueil, S., and La Rochelle, P. 1995. Yielding and critical state of a collapsible unsaturated silty soil. Géotechnique, 45(3): 465-77.
Mac, T. N., Shahbodagh, B., and Khalili, N. 2019. A fully coupled flow-deformation model for time-dependent analysis of unsaturated soils. Japanese Geotechnical Society Special Publication, 7(2): 587-594.
Mahmoodabadi, M., and Bryson, L. S. 2021. Constitutive Model for describing the fully coupled hydromechanical behavior of unsaturated soils. International Journal of Geomechanics, 21(4): 04021027.
Maquaire, O., Malet, J. P., Remaıtre, A., Locat, J., Klotz, S., and Guillon, J. 2003. Instability conditions of marly hillslopes: towards landsliding or gullying? The case of the Barcelonnette Basin, South East France. Engineering Geology, 70(1-2): 109-30.
Mendes, J., and Toll, D. G. 2016. Influence of initial water content on the mechanical behavior of unsaturated sandy clay soil. International Journal of Geomechanics, 16(6): D4016005.
Merchán, V., Vaunat, J., Romero, E., and Meca, T. 2008. Experimental Study of the Influence of Drying on the Residual Friction Angle of Clays. In Proceedings of the 1st European Conference on Unsaturated Soils, 423-8. London: CRC Press, Taylor & Francis Group.
Merchán, V., Romero, E., and Vaunat, J. 2011. An adapted ring shear apparatus for testing partly saturated soils in the high suction range. Geotechnical Testing Journal, 34(5): 433-44.
Mesri, G., and Shahien, M. 2003. Residual shear strength mobilized in first-time slope failures. Journal of Geotechnical and Geoenvironmental Engineering, 129(1): 12-31.

Miao, L., Liu, S., and Lai, Y. 2002. Research of soil–water characteristics and shear strength features of Nanyang expansive soil. Engineering Geology, 65(4): 261-7.
Milatz, M., and Grabe, J. 2019. Microscopic investigation of the hydro-mechanical behavior of unsaturated granular media with X-ray CT. Japanese Geotechnical Society Special Publication, 7(2): 615-26.
Milatz, M., Hüsener, N., Ando, E., Viggiani, G., and Grabe, J. 2021. Quantitative 3D imaging of partially saturated granular materials under uniaxial compression. Acta Geotechnica, 16(11): 3573-3600.
Mitchell, J. K., and Soga, K. 2005. Fundamentals of soil behavior, 3rd edition. New York: John Wiley and Sons.
Monghassem, M., Ajdari, M., Binesh, S. M., and Vahedifard, F. 2021. Effects of Suction and Drying–Wetting Cycles on Shearing Response of Adobe. Journal of Materials in Civil Engineering, 33(7): 04021173.
Morvan, M., Wong, H., and Branque, D. 2010. An unsaturated soil model with minimal number of parameters based on bounding surface plasticity. International Journal for Numerical and Analytical Methods in Geomechanics, 34(14): 1512-37.
Mun, W., Teixeira, T., Balci, M. C., Svoboda, J., and McCartney, J. S. 2016. Rate effects on the undrained shear strength of compacted clay. Soils and Foundations, 56(4), 719-731.
Murray, E. J. 2002. An equation of state for unsaturated soils. Canadian Geotechnical Journal, 39(1): 125-40.
Musso, G., Azizi, A., and Jommi, C. 2020. A microstructure-based elastoplastic model to describe the behaviour of a compacted clayey silt in isotropic and triaxial compression. Canadian Geotechnical Journal, 57(7): 1025-1043.
Ng, C. W., and Chiu, A. C. 2003. Laboratory study of loose saturated and unsaturated decomposed granitic soil. Journal of Geotechnical and Geoenvironmental Engineering, 129(6): 550-9.
Ng, C. W., Zhan, L. T., Bao, C. G., Fredlund, D. G., Gong, B. W. 2003. Performance of an unsaturated expansive soil slope subjected to artificial rainfall infiltration. Géotechnique, 53(2): 143-57.
Ng, C. W. W., and Zhou, R. Z. B. 2005. Effects of soil suction on dilatancy of an unsaturated soil. In Proceedings of the 16th International Conference on Soil Mechanics and Geotechnical Engineering, 559-562. IOS Press.
Ng, C. W. W., Sadeghi, H., Jafarzadeh, F., Sadeghi, M., Zhou, C., and Baghbanrezvan, S. 2020a. Effect of microstructure on shear strength and dilatancy of unsaturated loess at high suctions. Canadian Geotechnical Journal, 57(2): 221-235.
Ng, C. W. W., Zhou, C., and Chiu, C. F. 2020b. Constitutive modelling of state-dependent behaviour of unsaturated soils: an overview. Acta Geotechnica, 15(10): 2705-2725.
Nicotera, M. V., Papa, R., and Urciuoli, G. 2015. The hydro-mechanical behaviour of unsaturated pyroclastic soils: An experimental investigation. Engineering Geology, 195: 70-84.
Nova, R., and Wood, D. M. 1979. A constitutive model for sand in triaxial compression. International Journal for Numerical and Analytical Methods in Geomechanics, 3(3): 255-78.
Öberg, A. L., and Sällfors, G. 1997. Determination of shear strength parameters of unsaturated silts and sands based on the water retention curve. Geotechnical Testing Journal, 20(1): 40-8.
Oda, M., and Kazama, H. 1998. Microstructure of shear bands and its relation to the mechanisms of dilatancy and failure of dense granular soils. Géotechnique, 48(4): 465-81.

Oka, F., Kodaka, T., Suzuki, H., Kim, Y. S., Nishimatsu, N., and Kimoto, S. 2010. Experimental study on the behavior of unsaturated compacted silt under triaxial compression. Soils and foundations, 50(1): 27-44.

Oka, F., Kodaka, T., Kimoto, S., Kim, Y. S., and Yamasaki, N. 2006. An elasto-viscoplastic model and multiphase coupled FE analysis for unsaturated soil. Proceedings of the fourth international conference on unsaturated soils, Geotechnical Special Publication (ASCE), 147(2): 2039–2050.

Oka, F., Shahbodagh, B., and Kimoto, S. 2019. A computational model for dynamic strain localization in unsaturated elasto‐viscoplastic soils. International Journal for Numerical and Analytical Methods in Geomechanics, 43(1): 138-165.

Patil, U. D., Puppala, A. J., Hoyos, L. R., and Pedarla, A. 2017. Modeling critical-state shear strength behavior of compacted silty sand via suction-controlled triaxial testing. Engineering Geology, 231: 21-33.

Patil, U. D., Hoyos, L. R., Puppala, A. J., and Bheemasetti, T. V. 2018. Modeling stress–dilatancy behavior of compacted silty sand under suction-controlled axisymmetric shearing. Geotechnical and Geological Engineering, 36(6), 3961-3977.

Perzyna, P., 1966. Fundamental problems in viscoplasticity. Advances in Applied Mechanics, 9: 243–377.

Pineda, J. A., Romero, E., De Gracia, M., and Sheng, D. 2014. Shear strength degradation in claystones due to environmental effects. Géotechnique, 64(6): 493-501.

Postill, H., Dixon, N., Fowmes, G., El-Hamalawi, A., and Take, W. A. 2020. Modelling seasonal ratcheting and progressive failure in clay slopes: a validation. Canadian Geotechnical Journal, 57(9): 1265-79.

Qi, S., and Vanapalli, S. K. 2016. Influence of swelling behavior on the stability of an infinite unsaturated expansive soil slope. Computers and Geotechnics, 76: 154-69.

Qian, J., Lin, Z., and Shi, Z. 2022. Experimental and modeling study of water-retention behavior of fine-grained soils with dual-porosity structures. Acta Geotechnica, 1-14.

Rahardjo, H., Heng, O. B., and Choon, L. E. 2004. Shear strength of a compacted residual soil from consolidated drained and constant water content triaxial tests. Canadian Geotechnical Journal, 41(3): 421-36.

Rahardjo, H., Thang, N. C., Kim, Y., and Leong, E. C. 2018. Unsaturated elasto-plastic constitutive equations for compacted kaolin under consolidated drained and shearing-infiltration conditions. Soils and foundations, 58(3): 534-546.

Rampino, C., Mancuso, C., and Vinale, F. 2000. Experimental behaviour and modelling of an unsaturated compacted soil. Canadian Geotechnical Journal, 37(4): 748-63.

Rasool, A. M., and Aziz, M. 2020. Advanced Triaxial Tests on Partially Saturated Soils Under Unconfined Conditions. International Journal of Civil Engineering, 18: 1139–1156.

Rechenmacher, A., Abedi, S., and Chupin, O. 2010. Evolution of force chains in shear bands in sands. Géotechnique, 60(5): 343-51.

Romero, E., Gens, A., and Lloret, A. 1999. Water permeability, water retention and microstructure of unsaturated compacted Boom clay. Engineering Geology, 54(1-2): 117-27.

Romero, E., Vaunat, J., and Merchán, V. 2014. Suction effects on the residual shear strength of clays. Journal of Geo-Engineering Sciences, 2(1-2): 17-37.

Romero, E., Sánchez, M., Gai, X., Barrera, M., and Lloret, A. 2019. Mechanical behavior of an unsaturated clayey silt: an experimental and constitutive modelling study. Canadian Geotechnical Journal, 56(10): 1461-74.

Roscoe, K. H., Schofield, A., and Wroth, A. P. 1958. On the yielding of soils. Géotechnique, 8(1): 22-53.
Roscoe, K. H., and Burland, J. B. 1968. On the generalized stress-strain behavior of 'wet' clay. In Engineering plasticity, edited by Heyman, J., and Leckie, F. A., 535–609. Camridge: Camridge University Press.
Rowe, P. W. 1962. The stress-dilatancy relation for static equilibrium of an assembly of particles in contact. In Proceedings of the Royal Society of London, Series A, Mathematical and Physical Sciences, 269(1339): 500-27. London: Royal Society.
Russell, A. R., and Khalili, N. 2004. A bounding surface plasticity model for sands exhibiting particle crushing. Canadian Geotechnical Journal, 41(6): 1179-92.
Russell, A. R., and Khalili, N. 2006. A unified bounding surface plasticity model for unsaturated soils. International Journal for Numerical and Analytical Methods in Geomechanics, 30(3): 181-212.
Salager, S., Nuth, M., Ferrari, A., and Laloui, L. 2013. Investigation into water retention behaviour of deformable soils. Canadian Geotechnical Journal, 50(2): 200-208.
Schnellmann, R., Rahardjo, H., and Schneider, H. R. 2013. Unsaturated shear strength of a silty sand. Engineering Geology, 162: 88-96.
Schofield, A., and Wroth, P. 1968. Critical state soil mechanics. London: McGraw-Hill.
Shahbodagh B. Large deformation dynamic analysis method for partially saturated elasto - viscoplastic soils. Ph.D. thesis, Kyoto University, 2011.
Sheng, D. 2011. Review of fundamental principles in modelling unsaturated soil behaviour. Computers and Geotechnics, 38(6): 757-776.
Sheng, D., Zhou, A., and Fredlund, D. G. 2011. Shear strength criteria for unsaturated soils. Geotechnical and Geological Engineering, 29(2): 145-159.
Shire, T., and Standing, J. 2021. Strength and stiffness properties of an unsaturated clayey silt: experimental study at high degrees of saturation. International Journal of Geomechanics, 21(7): 04021094.
Sivakumar, V., Sivakumar, R., Boyd, J., and Mackinnon, P. 2010. Mechanical behaviour of unsaturated kaolin (with isotropic and anisotropic stress history). Part 2: performance under shear loading. Géotechnique, 60(8): 595-609.
Skempton, A. W. 1970. First-time slides in over-consolidated clays. Géotechnique, 20 (3): 320-4.
Skempton, A. W. 1985. Residual strength of clays in landslides, folded strata and the laboratory. Géotechnique, 35(1): 3-18.
Solowski, W. T., and Sloan, S. W. 2015. Equivalent stress approach in creation of elastoplastic constitutive models for unsaturated soils. International Journal of Geomechanics, 15(2): 04014041.
Stark, T. D., and Eid, H. T. 1994. Drained residual strength of cohesive soils. Journal of Geotechnical Engineering, 120(5): 856-71.
Sun, D. A., Matsuoka, H., Yao, Y., and Ichihara, W. 2000. An elasto-plastic model for unsaturated soil in three-dimensional stresses. Soils and Foundations, 40(3): 17-28.
Takano, D., Lenoir, N., Otani, J., and Hall, S. A. 2015. Localised deformation in a wide-grained sand under triaxial compression revealed by X-ray tomography and digital image correlation. Soils and Foundations, 55(4): 906-15.
Take, W. A., and Bolton, M. D. 2011. Seasonal ratcheting and softening in clay slopes, leading to first-time failure. Géotechnique, 61(9): 757-69.

Tang, C. T., Borden, R. H., and Gabr, M. A. 2019. Model applicability for prediction of residual soil apparent cohesion. Transportation Geotechnics, 19: 44-53.
Tao, G., Chen, Y., Kong, L., Xiao, H., Chen, Q., and Xia, Y. 2018. A simple fractal-based model for soil-water characteristic curves incorporating effects of initial void ratios. Energies, 11(6): 1419.
Tarantino, A., and Tombolato, S. 2005. Coupling of hydraulic and mechanical behaviour in unsaturated compacted clay. Géotechnique, 55(4): 307-17.
Tarantino, A. 2011. Unsaturated soils: compacted versus reconstituted states. In Proceedings of 5th International Conference on Unsaturated Soil, 113-36.
Thanh, D. T., Long, N. T. and Thang, L. T. (2019). Analysis the effects of the degree of saturation on the slopes stability using modelling and numerical simulation. International Journal of GEOMATE, 17(63): 119-125.
Thu, T. M., Rahardjo, H., and Leong, E. C. 2007. Critical state behavior of a compacted silt specimen. Soils and Foundations, 47(4): 749-55.
Toll, D. G. 1990. A framework for unsaturated soil behaviour. Géotechnique, 40(1): 31-44.
Toll, D. G. 2000. The influence of fabric on the shear behavior of unsaturated compacted soils. In Advances in unsaturated geotechnics, 222-34. Reston: American Society of Civil Engineers.
Toll, D. G., and Ong, B. H. 2003. Critical-state parameters for an unsaturated residual sandy clay. Géotechnique, 53(1): 93-103.
Toyota, H., Takada, S., and Susami, A. 2019. Rate dependence on mechanical properties of unsaturated cohesive soil with stress-induced anisotropy. Soils and Foundations, 59(4): 1013-1023.
Tsiampousi, A., Zdravković, L., and Potts, D. M. 2013. A new Hvorslev surface for critical state type unsaturated and saturated constitutive models. Computers and Geotechnics, 48: 156-66.
Van Genuchten, M. T. 1980. A closed‐form equation for predicting the hydraulic conductivity of unsaturated soils. Soil Science Society of America Journal, 44(5): 892-8.
Vanapalli, S. K., Fredlund, D. G., Pufahl, D. E., and Clifton, A. W. 1996. Model for the prediction of shear strength with respect to soil suction. Canadian Geotechnical Journal, 33(3): 379-92.
Vanapalli, S. K., Fredlund, D. G., Pufahl, D. E. 1999. The influence of soil structure and stress history on the soil–water characteristics of a compacted till. Géotechnique, 49(2): 143-59.
Vanapalli, S. K., and Fredlund, D. G. 2000. Comparison of different procedures to predict unsaturated soil shear strength. In Advances in Unsaturated Geotechnics, edited by Shackelford, C. D., 195–209. New York: ASCE.
Vanapalli, S. K. 2009. Shear strength of unsaturated soils and its applications in geotechnical engineering practice. In Proceeding of 4th Asia-Pacific Conference on Unsaturated Soils, 579-598. New Castle, Australia.
Vaunat, J., Amador, C., Romero, E., and Djeren-Maigre, I. 2006. Residual strength of a low plasticity clay at high suctions. In Proceedings of 4th International Conference on Unsaturated Soils, 1279-89.
Vaunat, J., Merchán, V., Romero, E., and Pineda, J. 2007. Residual strength of clays at high suctions. In Theoretical and Numerical Unsaturated Soil Mechancs, 151–63. Berlin: Springer.
Velosa, C. L. 2011. Unsaturated soil behavior under large deformations using a fully servo/suction-controlled ring shear apparatus. Ph.D. dissertation, Arlington, US: University of Texas.
Vo, T., Taiebat, H., and Russell, A. R. 2016. Interaction of a rotating rigid retaining wall with an unsaturated soil in experiments. Géotechnique, 66(5): 366-77.

Wang, Q., Pufahl, D. E., and Fredlund, D. G. 2002. A study of critical state on an unsaturated silty soil. Canadian Geotechnical Journal, 39(1): 213-8.
Wang, J. P., Andò, E., Charrier, P., Salager, S., Lambert, P., and François, B. 2019. Micro-scale investigation of unsaturated sand in mini-triaxial shearing using X-ray CT. Géotechnique Letters, 9(4): 269-77.
Wheeler, S. J., and Sivakumar, V. 1995. An elasto-plastic critical state framework for unsaturated soil. Géotechnique, 45(1): 35-53.
Widger, R. A., and Fredlund, D. G. 1979. Stability of swelling clay embankments. Canadian Geotechnical Journal, 16(1): 140-51.
Wijaya, M., and Leong, E. C. 2016. Equation for unimodal and bimodal soil–water characteristic curves. Soils and Foundations, 56(2): 291-300.
Wijaya, M., and Leong, E. C. 2017. Modelling the effect of density on the unimodal soil-water characteristic curve. Géotechnique, 67(7): 637-645.
Wood, D. M., and Belkheir, K. 1994. Strain softening and state parameter for sand modelling. Géotechnique, 44(2): 335-9.
Wu, S., Zhou, A., Shen, S. L., and Kodikara, J. 2020. Influence of different strain rates on hydro-mechanical behaviour of reconstituted unsaturated soil. Acta Geotechnica, 15(12): 3415-3431.
Yang, J., Ishikawa, T., Lin, T., Tokoro, T., Nakamura, T., and Momoya, Y. 2021. Influence of aging on hydro-mechanical behavior of unsaturated ballast. Transportation Geotechnics, 27: 100480.
Yang, X., and Vanapalli, S. K. 2020. Model for predicting the variation of shear stress in unsaturated soils during strain-softening. Canadian Geotechnical Journal.
Yao, Y. P., Hou, W., and Zhou, A.N. 2009. UH model: three-dimensional unified hardening model for overconsolidated clays. Géotechnique, 59(5): 451-69.
Yao, Y. P., Niu, L., and Cui, W. J. 2014. Unified hardening (UH) model for overconsolidated unsaturated soils. Canadian Geotechnical Journal, 51(7): 810-21.
Yerro, A., Alonso, E. E., and Pinyol, N. M. 2015. The material point method for unsaturated soils. Géotechnique, 65(3): 201-17.
Zhan, T. L., and Ng, C. W. 2006. Shear strength characteristics of an unsaturated expansive clay. Canadian Geotechnical Journal, 43(7): 751-63.
Zhang, Y., Ishikawa, T., Tokoro, T., and Nishimura, T. 2014. Influences of degree of saturation and strain rate on strength characteristics of unsaturated granular subbase course material. Transportation Geotechnics, 1(2), 74-89.
Zhang, J., Sun, D. A., Zhou, A., and Jiang, T. 2015. Hydromechanical behaviour of expansive soils with different suctions and suction histories. Canadian Geotechnical Journal, 53(1): 1-3.
Zhang, J., Niu, G., Li, X., and Sun, D. A. 2020. Hydro-mechanical behavior of expansive soils with different dry densities over a wide suction range. Acta Geotechnica, 15(1): 265-278.
Zhao, H. F., and Zhang, L. M. 2014. Effect of coarse content on shear behavior of unsaturated coarse granular soils. Canadian Geotechnical Journal, 51(12): 1371-83.
Zhao, N. F., Ye, W. M., Wang, Q., Chen, B., and Cui, Y. G. 2021. A bounding surface model for unsaturated compacted bentonite. European Journal of Environmental and Civil Engineering, 25(14): 2692-2706.
Zhou, A. N., Sheng, D., Sloan, S. W., and Gens, A. 2012a. Interpretation of unsaturated soil behaviour in the stress–saturation space, I: volume change and water retention behaviour. Computers and Geotechnics, 43: 178-187.

Zhou, A. N., Sheng, D., and Carter, J. P. 2012b. Modelling the effect of initial density on soil-water characteristic curves. Géotechnique, 62(8): 669-680.
Zhou, A., and Sheng, D. 2015. An advanced hydro-mechanical constitutive model for unsaturated soils with different initial densities. Computers and Geotechnics, 63: 46-66.
Zhou, C., Tai, P., and Yin, J. H. 2020. A bounding surface model for saturated and unsaturated soil‐structure interfaces. International Journal for Numerical and Analytical Methods in Geomechanics, 44(18): 2412-2429.

CHAPTER 3 MODEL FOR PREDICTING THE VARIATION OF SHEAR STRESS IN UNSATURATED SOILS DURING STRAIN-SOFTENING[2]

3.1 Introduction

The shear stress increases rapidly during the initial stage of shearing in both saturated and unsaturated soils. However, in several scenarios, shear stress drops gradually from peak to a critical value after a relatively large shear deformation, which is referred to as strain-softening. Such a behavior is well recognized in the progressive failure of slopes in saturated soils (Skempton 1964; Potts et al. 1997; Locat et al. 2011). In such slopes, the local shear strength is reduced due to large local deformation. As a result, soil slopes typically undergo progressive shear failure prior to reaching failure condition. The behavior of slopes in unsaturated soils is also similar to saturated soils. The large local deformation in unsaturated soil slopes can be triggered by several environmental factors; for example, the rainfall infiltration (Widger and Fredlund 1979; Lee et al. 2008), and the wetting-drying cycles (Take and Bolton 2011; Postill et al. 2019). Rigorous analyses of such failures should be undertaken by taking account of the variation of shear stress in unsaturated soils due to large deformation within the slope (Wang et al. 2018; Qi and Vanapalli 2016; Postill et al. 2019).

During the last twenty-five years, several investigators studied the strain-softening behavior of unsaturated soils from laboratory investigations (e.g., Cui and Delage 1996; Miao et al. 2002; Rahardjo et al. 2004; Kayadelen et al. 2007; Estabragh and Javadi 2008; Patil 2014; Zhang et al. 2016). Typical characteristics of strain-softening behavior of unsaturated soils are well known from experimental studies. For example, the matric suction as an independent stress state variable contributes to both the peak and critical shear strength of unsaturated soils. However, its contribution to critical shear strength is lower in comparison to that of the peak shear strength,

[2] The contents presented in this chapter are published as a journal article: **Yang, X.,** and Vanapalli, S. K. 2021. Model for predicting the variation of shear stress in unsaturated soils during strain-softening. *Canadian Geotechnical Journal*, 58(10): 1513-1526. DOI: 10.1139/cgj-2020-0312.

which results in an increase in soil brittleness with increasing matric suction. In other words, matric suction plays a significant role in the rational interpretation of the strain-softening mechanism of unsaturated soils.

Investigations related to the strain-softening behavior of unsaturated soils are however limited because experimental studies are complex, expensive, and time-consuming. Several elastoplastic constitutive models have been developed that are capable to reproduce the strain-softening behavior of unsaturated soils based on numerical techniques. Alonso et al. (1990) extended the classic Cam-clay model to formulate an elastoplastic model (BBM), which is widely used for capturing the behavior of unsaturated soils for different scenarios. This model was subsequently modified by some researchers (e.g., Wheeler and Sivakumar 1995; Cui and Delage 1996). In addition to the models based on conventional plasticity, some other constitutive models were developed based on the bounding surface plasticity (BSP) (Russell and Khalili 2006; Yao et al. 2014; Zhou and Sheng 2015). Furthermore, Geiser et al. (1997) extended the disturbed state concept (DSC) based model, which provides a novel approach to model the strain-softening behavior of unsaturated soils. These advanced elastoplastic models are promising for modeling the strain-softening behavior of unsaturated soils. However, they are complex and require comprehensive tools that can be explained only with advanced soil plasticity concepts. Due to this reason, their application in conventional engineering practice is limited.

In this chapter, a simple DSC-based model is developed to predict the variation of shear stress during strain-softening process for a wide range of unsaturated soils under consolidated drained triaxial compression condition. The relative intact state (i.e., pre-peak state) is described using a hyperbolic stress-strain relationship. The fully adjusted state (i.e., critical state) is described using a linear stress-strain relationship. The variation of degree of strain-softening with axial strain is described using a disturbance function. In addition to the parameters that are derived from conventional saturated triaxial drained tests and the soil-water characteristic curve (SWCC), a total of seven fitting parameters that are derived from limited number of unsaturated triaxial drained tests are required to capture the influence of matric suction. In this chapter, the formulation of the model and the procedure to determine model parameters are described. In addition, the proposed model was validated by comparing the predicted and experimental results of stress-strain relationships of several unsaturated soils varying from coarse- to fine-grained soils. Finally, a

comprehensive error analysis is undertaken based on an index of agreement that supports the proposed model with the validity guidelines.

3.2 Background

3.2.1 Disturbed state concept

The disturbed state concept (DSC) for soils was originally introduced into the literature by Desai (1974). Typically, under an applied load, the soil gradually deforms simultaneously undergoing microstructural changes and reaches a 'disturbed' state. Consequently, the deforming soil transforms gradually from a relative intact (RI) state to a fully adjusted (FA) state. The soil can be considered to be in a combined random mixture of elements in RI and FA states at any intermediate stage during the soil disturbance process.

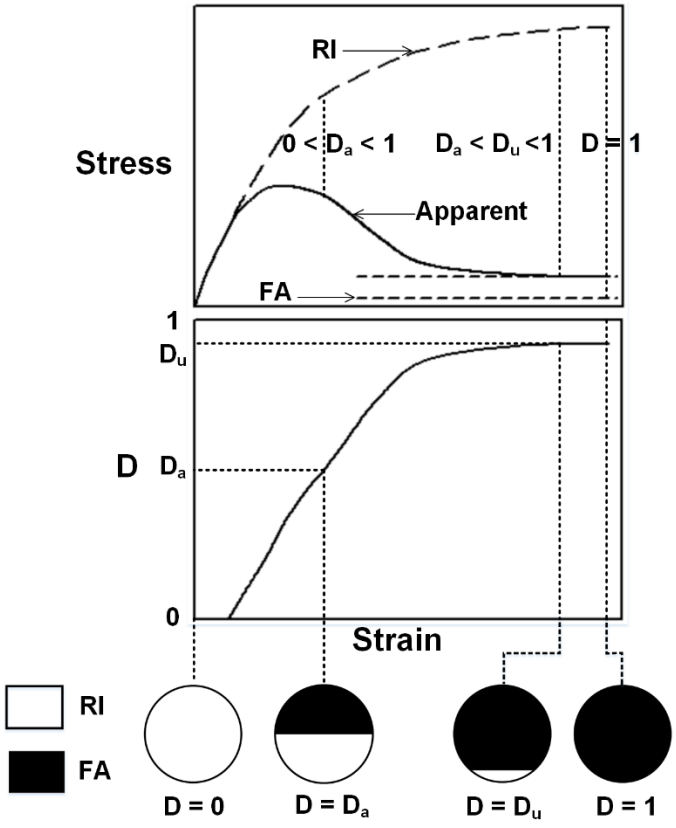

Figure 3.1 Schematic of the DSC

The two reference states (RI and FA) should be selected depending on the definition and stage of soil disturbance. The RI state is defined as the initial condition where the soil is not influenced by

the disturbance. The FA state is defined as the final condition where the soil is fully disturbed. Once the reference states and corresponding constitutive models have been determined, the apparent response of a material element with unit thickness can be expressed as a weighted average of the responses at RI and FA states (Figure 3.1) as discussed in Desai (2000):

$$\sigma^a = \sigma^{RI}\frac{A^T - A^{FA}}{A^T} + \sigma^{FA}\frac{A^{FA}}{A^T} = (1-D)\sigma^{RI} + D\sigma^{FA} \tag{3.1}$$

where σ^a is the apparent stress; σ^{RI} is the stress in the RI part; σ^{FA} is the stress in the FA part; A^T is the total area of the material element; A^{FA} is the area of the FA part; $D = A^{FA}/A^T$ is the disturbance function.

The disturbance function D is defined as the ratio of the volume of the FA parts to the total volume of the material element, which represents the degree of disturbance occurring in the soil. As shown in Figure 3.1, the entire element is initially in the RI state without any disturbance, which means D is equal to zero. As the deformation progresses, there is an increase in the percentage of FA state in the soil element; as a result, D increases gradually from an initial value of zero. The FA state will finally be attained in the entire soil element and at this stage, D reaches a value equal one. Desai (2000) suggested the disturbance function D can be determined by two different approaches.

In the first approach, D is determined from the measured apparent responses and responses in reference states from laboratory test results using the equation:

$$D = \frac{\sigma^{RI} - \sigma^a}{\sigma^{RI} - \sigma^{FA}} \tag{3.2}$$

In the second approach, D can be defined as a functional relationship of various internal variables that reflect the influence of microstructural changes resulting in the disturbance. As suggested by Desai (2000), the function that relates the D and the internal variables can be expressed as:

$$D = D_u\left[1 - \left\{1 + \left(\frac{\xi_D}{h}\right)^w\right\}^{-s}\right] \tag{3.3a}$$

where $\xi_D = \int (dE_{ij}^p dE_{ij}^p)^{1/2}$ is the deviatoric plastic strain trajectory; E_{ij}^p is the deviatoric part of the plastic strain tensor; h, w, s are parameters in the disturbance function; D_u is the ultimate value of D in practice (Figure 3.1), which is less than 1 since FA can only be attained in an idealized condition.

A simpler function form of D was also suggested by Desai (2000), which is given as:

$$D = D_u \left[1 - \exp\left(-A\xi_D^Z\right)\right] \tag{3.3b}$$

where A and Z are parameters in the disturbance function.

3.2.2 DSC models for saturated and unsaturated soils

The DSC can be conveniently accommodated into the constitutive models. The flexibility of the DSC has encouraged various researchers to develop DSC-based constitutive models. Table 3.1 summarizes several widely used DSC-based models for the strain-softening behavior of both saturated and unsaturated materials.

A commonly used model is the disturbed state concept-hierarchical single surface (DSC-HISS) model for saturated soils and soil-interfaces (Desai 2000). These types of models perform well for modelling the strain-softening and dilatancy behavior of saturated soils and for soil-interfaces. However, a large number of parameters are required to use them. For this reason, Hu and Pu (2004) proposed another type of DSC-based model for soil-structure interface to limit the use of various parameters. In this model, an elastoplastic constitutive model was developed for RI state, extending the assumption that the stress-strain relationship is hyperbolic.

Geiser et al. (1997) extended the HISS-model (Desai 2000) for the unsaturated soils by taking account of the variation of soil parameters with respect to suction. A DSC-based model was developed for the strain-softening behavior of unsaturated soils by using the pre-peak behavior as RI state and saturated behavior as FA state. The extended HISS-model was used to describe the RI and FA behavior. Additionally, Equation 3.3b is used as the disturbance function, but the fitting parameters A and Z are expressed as functions of suction, while D_u is considered independent of suction. In addition, Hamid and Miller (2008) proposed a DSC-based model for unsaturated soil-

steel interfaces. An elastoplastic model was developed as the RI constitutive model that is analogous to the HISS model for unsaturated soils (Geiser et al. 1997). The shear stress at FA state is assumed constant at zero despite shear strain. In addition, Equation 3.3b was modified to describe the disturbance.

Table 3.1 DSC-based models for the strain-softening behavior of saturated and unsaturated materials

Condition	Literature	RI state	FA state	*D*
Saturated	Desai and Ma (1992)	Pre-peak behavior described by elastoplastic model (HISS)	Critical state behavior	Equation 3.3b
	Armaleh and Desai (1994)	Pre-peak behavior described by elastoplastic model (HISS)	Critical state behavior	Equation 3.3b
	Seo et al. (2004)	Elastic-perfectly plastic behavior	Critical state behavior	Equation 3.3b
	Hu and Pu (2004)	Elastoplastic behavior described by a model derived from a hyperbolic stress-strain relationship	Critical state behavior	Equation 3.3b
	Veiskarami et al. (2012)	Nonlinear elastic behavior described by hyperbolic equation	Hardening elastoplastic behavior	Equation 3.3b
Unsaturated	Geiser et al. (1997)	Pre-peak behavior described by extended HISS for unsaturated soils	Saturated behavior	Equation 3.3b, A and Z vary with suction
	Hamid and Miller (2008)	Pre-peak behavior described by modified unsaturated extended HISS	Shear stress is constant at zero	A piecewise function modified from Equation 3.3b
	Haeri et al. (2016)	Hyperbolic stress-strain response	Saturated behavior	Equation 3.3b, A and Z are fitting parameters

Haeri et al. (2016) also proposed a DSC-based model to describe the stress-strain relationship of unsaturated collapsible soils. This model used a hyperbolic relationship as the RI behavior and the saturated stress-strain relationship as the FA behavior. However, the FA state behavior were determined from experimental results instead of being predicted using a constitutive model. In addition, four of five required parameters must be determined by fitting a specific experimental stress-strain relationship. Therefore, the proposed model can be used as a tool to back-predict the stress-strain relationship from which the model parameters were determined. However, this model is limited for prediction of the stress-strain response of unsaturated collapsible soils under various loading conditions.

3.3 DSC-based model for strain-softening stress-strain relationships of unsaturated soils

3.3.1 Reference states

The focus of the present investigation is directed towards developing a model for predicting the variation of shear stress during strain-softening process for various types of unsaturated soils. The general equation of the DSC-based model, Equation 3.1, can be rewritten as below for predicting the results of unsaturated soils performed under consolidated drained triaxial compression loading conditions:

$$q^a = (1-D)q^{RI} + Dq^{FA} \tag{3.4}$$

where $q^a = \sigma_1 - \sigma_3$ is the apparent deviatoric stress; σ_1 is the major principal stress; σ_3 is the minor principal stress; q^{RI} and q^{FA} are the deviatoric stress sustained by the RI and FA part, respectively.

As discussed, the selection of RI and FA state has to be based on the definition of disturbance. Therefore, the disturbance associated with the strain-softening behavior of unsaturated soils should be well understood. Some researchers (Atkinson 2007; Mitchell and Soga 2005) have attributed the strain-softening behavior of dry and saturated soils to the generation of a localized strain zone (i.e., shear band). This is because the original structure of soil particles will be destroyed inside the shear band associated with the generation of large voids due to soil particles rolling over each other. The axial load is transferred by the rotation resistance between the soil particles inside and outside shear band, which results in the reduction in shear strength.

The generation and development of the shear band can also be considered as disturbance that arises in unsaturated soils. Firstly, Higo et al. (2011) has found the microstructure in shear band of unsaturated sand is similar with that of dry and saturated sand. This means the soil particle structure was also destroyed in the shear band of unsaturated soils, which can contribute to the reduction in shear strength of unsaturated soils under large deformation. In addition, as the matric suction transmits to soil particles through the water menisci (Vanapalli et al. 1996), the decrease in its area can be an additional factor that contributes to the reduction in shear strength of unsaturated soils. More recently, Kido and Higo (2019) based on their studies from CT images suggest that there is

a decrease in the local degree of saturation and the number of water menisci (i.e., wetted contact area) in the shear band of unsaturated soils.

The evolution of the shear band during triaxial compression has been studied experimentally using X-ray micro computed tomography (micro-CT) and digital image correlation (DIC) for dry (Hall et al. 2010; Andò et al. 2012; Takano et al. 2015) and unsaturated sands (Higo et al. 2011; Higo et al. 2013). These studies suggest that the exact axial strain where the shear band is initialized is difficult to be reliably determined. For this reason, in this research, the onset of shear band is assumed to be at the peak state. In other words, the pre-peak state can be assumed as the RI state where the disturbance does not happen yet. This is because, prior to peak state, the rotation and volumetric strain are still disorganized in the specimen, which is the main cause of the strain-softening behavior as discussed in the earlier paragraphs. During this stage, the localizations of displacement and shear strain are still not obvious despite having been initialized. In addition, their initializations are close to peak state in spite of being prior to the peak state. This means the assumption does not contribute to a significant error. As for the evolution of shear band at post-peak state, these studies suggest the shear band that develops progressively after peak state is well defined at critical state where the shear strength is constant. In other words, the specimen will be fully disturbed at critical state. Thus, FA state can be assumed at the critical state, where the shear band has been formed clearly in the test specimen.

3.3.2 Models for reference states

Suitable models should be selected that are consistent with the introduced RI and FA states definitions to calculate q^{RI} and q^{FA} in Equation 3.4. The stress-strain relationship at RI state (i.e., pre-peak state) can be described by a hardening response extending the pre-peak curve. Consistent with the approaches of Hu and Pu (2004), Veiskarami et al. (2012) and Haeri et al. (2016), a nonlinear hardening stress-strain relationship for the RI state can be modelled with the aid of a hyperbolic equation that was originally suggested by Duncan and Chang (1970) in terms of axial strain, which is shown below:

$$q^{RI} = \frac{\varepsilon_a}{\frac{1}{E_i} + \frac{1}{q_{ult}}\varepsilon_a} \tag{3.5}$$

where ε_a is the axial strain; E_i is the initial tangent modulus (i.e., the initial slope of the stress-strain curve); q_{ult} is the ultimate deviatoric stress of the hardening stress-strain curve extending the pre-peak curve (i.e., the asymptotic value of the deviatoric stress when ε_a is infinity).

Additionally, the critical state was used as the FA state in this research, where the deviatoric stress will not change with the shear strain. Therefore, the stress-strain curve at FA state should be a horizontal line with respect to the variation in the axial strain. The stress-strain relationship at FA state can be described as follows:

$$q^{FA} = q_c \tag{3.6}$$

where q_c is the critical deviatoric stress.

3.3.3 Disturbance function

In this research, Equation 3.3a is used as the disturbance function. Since the models for RI and FA state have been expressed as the functions of axial strain, ε_a, Equation 3.3a should also be rewritten in terms of ε_a. Since the critical state is selected as the FA state in this research, which typically reaches at the end of triaxial tests, D_u can be assumed equal to unity. In addition, an assumption $s = 1$ was introduced to simplify the parameters. As a result, the disturbance function D can be defined using Equation 3.3a in terms of only two parameters; namely, h and w as below:

$$D = 1 - \left[1 + \left(\frac{\varepsilon_a}{h}\right)^w\right]^{-1} \tag{3.7}$$

In Equation 3.7, the values of h and w are mathematical parameters that cannot be predicted in terms of stress state variables. Therefore, some reasonable relationships should be built between h and w and the mechanical properties of unsaturated soils such that they can be predicted in terms of stress state variables.

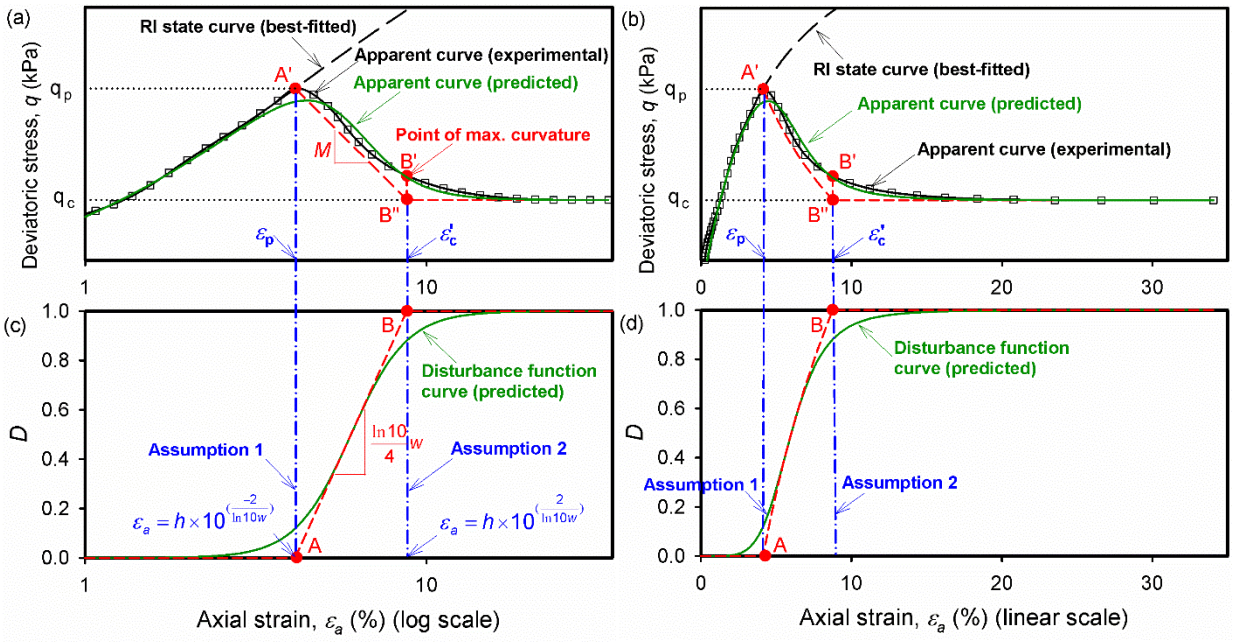

Figure 3.2 Definition of model parameters related to softening: (a) stress-strain curve on a semi-logarithmic scale; (b) stress-strain curve on a linear scale; (c) disturbance function curve on a semi-logarithmic scale; (d) disturbance function curve on a linear scale

Figure 3.2a summarizes an apparent shear stress-shear strain curve (continuous line with open squares) obtained from a consolidated drained triaxial compression test on a semi-logarithmic scale. The RI state curve of the apparent stress-strain curve was obtained by best fitting its pre-peak part, which is also shown in Figure 3.2a (continuous line with long dashes). Figure 3.2c summarizes a disturbance function curve (solid line) predicted by Equation 3.7 as a semi-logarithmic relationship. As a comparison, the same stress-strain curve and disturbance function curve were also plotted on a linear scale in Figures 2b and 2d, respectively.

It can be found that the D – log(ε_a) curve is a S-shape curve, which is similar to a unimodal soil water characteristic curve (SWCC). Therefore, a similar method of analysis can be used as for a SWCC (Vanapalli et al. 1998). Firstly, a tangent line (line shown with short dashes in Figure 3.2c) can be plotted through the inflection point of the D – log(ε_a) curve with a slope of (ln10/4)w. Then, two horizontal lines can be plotted at D = 0 and D = 1, respectively. Thus, two intersection points (A and B in Figure 3.2c) can be found between the tangent line and the two horizontal lines.

As shown in Figure 3.2c, D is low and close to zero prior to Point A. Increase in axial strain cannot result in a remarkable deviation of predicted apparent stress-strain curve from the RI state curve. After Point A, D will increase much more significantly; as a result, the predicted apparent shear stress-shear strain curve will begin to deviate from the RI state curve. This means Point A can approximate the point where softening begins. After Point B, D is high and close to unity. The increase in axial strain will not cause significant decrease in predicted deviatoric stress. In other words, after Point B, the predicted apparent stress-strain curve will be approximately equal to the FA state curve. Most of softening should have occurred prior to Point B. This means Point B can approximate the point where most of the softening ends.

Therefore, two assumptions were made in this research about the positions of A and B as below:

(1) Point A corresponds to the peak point (A') on the apparent stress-strain curve measured in experiment. Thus, $h\times10^{(\frac{-2}{\ln10w})}=\varepsilon_p$ where ε_p is the axial strain at peak point.

(2) Point B corresponds to the point of maximum curvature (B') on the apparent stress-strain curve measured in experiment. Thus, $h\times10^{(\frac{2}{\ln10w})}=\varepsilon_c'$ where ε'_c is the axial strain at the post-peak point of maximum curvature.

Since the pre-peak state is used as the RI state, the peak point of the apparent stress-strain curve should be also on the RI state curve. Thus, the (ε_p, q_p) should satisfy Equation 3.5. Equation 3.8 can be obtained by combining the Equation 3.5 and the first assumption as summarized below:

$$h\times10^{(\frac{-2}{\ln10w})}=\varepsilon_p=\frac{q_p q_{ult}}{E_i(q_{ult}-q_p)} \tag{3.8}$$

where ε_p is the axial strain at peak point of apparent stress-strain curve; q_p is the peak deviatoric stress.

In addition, as shown in Figure 3.2a, a post-peak modulus, M, is defined to describe the rate of softening after peak state. Firstly, a vertical line is plotted through the post-peak point of maximum curvature (B'). The critical state part is then extended horizontally. Finally, an intersection point (B'') can be determined. The magnitude of the slope of the line A' B'' is defined as the post-peak

modulus, M, in this research. Equation 3.9 can be obtained by combining the definition of M and the two assumptions:

$$M = \frac{q_p - q_c}{\log \varepsilon_c' - \log \varepsilon_p} = \frac{\ln 10}{4} w(q_p - q_c) \tag{3.9}$$

where M is the post-peak modulus; ε'_c is the axial strain at the post-peak point of maximum curvature of apparent stress-strain curve.

By using Equations 3.8 and 3.9, h and w can be related to the mechanical properties of the material (i.e., E_i, M, q_p, q_{ult} and q_c). Thus, the disturbance function Equation 3.7 can be rewritten as below:

$$D = 1 - \left[1 + \left(\varepsilon_a \frac{E_i (q_{ult} - q_p)}{q_p q_{ult}} 10^{\frac{q_c - q_p}{2M}} \right)^{\frac{4M}{\ln 10 (q_p - q_c)}} \right]^{-1} \tag{3.10}$$

According to the definition, M and $(q_p - q_c)$ should equal zero when there is no softening; however, Equation 3.10 will offer no solution. Therefore, M and $(q_p - q_c)$ are assumed equal one for soils that exhibit hardening behavior.

In Figures 3.2a and 3.2b, the predicted stress-strain curve (solid line) is presented for comparison purposes. The five mechanical parameters in Equation 3.10 (E_i, M, q_p, q_{ult} and q_c) were directly determined from the experimental apparent stress-strain curve. The predicted stress-strain curve closely matches with the experimental results. This suggests the assumptions made in this research to determine h and w are reasonable. However, the peak point of the predicted stress-strain curve is not exactly at the position of Point A' (ε_p, q_p). This is because, in assumption (1), D is considered as zero before Point A (line with short dashes in Figures 3.2c and 3.2d), which is not consistent with its real values (solid line in Figures 3.2c and 3.2d).

3.3.4 Formulation of model

A DSC-based model for predicting the stress-strain relationship of unsaturated soils associated with strain-softening subjected to consolidated drained triaxial compression loading conditions is formulated by combining the Equations 3.4, 3.5, 3.6 and 3.10 as below:

$$q^a = (1-D)\times\frac{\varepsilon_a}{\frac{1}{E_i}+\frac{1}{q_{ult}}\varepsilon_a}+D\times q_c,\quad D=1-\left[1+\left(\varepsilon_a\frac{E_i(q_{ult}-q_p)}{q_p q_{ult}}10^{\frac{q_c-q_p}{2M}}\right)^{\frac{4M}{\ln 10(q_p-q_c)}}\right]^{-1} \tag{3.11}$$

Five mechanical parameters; namely, E_i, M, q_p, q_{ult} and q_c are included in this equation to model the strain-softening relationship. As discussed earlier, the matric suction has a significant influence on the shearing behavior of unsaturated soils. For this reason, all the five parameters were expressed as functions of matric suction, $(u_a - u_w)$, to consider its influence on the stress-strain relationship. The variations of those parameters with matric suction are described below.

(1) Initial tangent modulus E_i

Duncan and Chang (1970) suggested a linear relationship between $\log(E_i/p_a)$ and $\log(\sigma'_3/p_a)$ as shown in Equation 3.12 within the framework of saturated soil mechanics.

$$\log\left(\frac{E_i}{p_a}\right)=\log K_E+n_E\log\left(\frac{\sigma_3'}{p_a}\right) \tag{3.12}$$

where σ'_3 is the effective minor principal stress; p_a is the atmospheric pressure which is always 101.3 *kPa*; K_E and n_E are initial tangent modulus parameters of the saturated soil.

Hoyos et al. (2015) studied the influence of matric suction on E_i of unsaturated soils using suction-controlled resonant column tests. The experimental results suggest independent contributions of $(\sigma_3 - u_a)$ and $(u_a - u_w)$ to E_i, which are consistent with the independent two-stress state variables framework proposed by Fredlund and Morgenstern (1977). Along similar lines as Fredlund et al. (1978), who extended the Mohr-Coulomb failure criterion for interpreting the shear strength of unsaturated soils, Hoyos et al. (2015) extended the Equation 3.12 for interpreting the stiffness of unsaturated soils. However, as suggested by Vanapalli et al. (1996), the mechanical behavior of unsaturated soil is influenced not only by the matric suction but also by the water menisci area. For this reason, the contribution of matric suction towards peak shear strength was considered and related to the degree of saturation of the soil. Analogous with this approach, Equation 3.12 was modified in this research to consider the influence of matric suction and degree of saturation. In

addition, the contribution of net minor principal stress is assumed as a linear function of matric suction. Therefore, the prediction model for E_i of unsaturated soils was expressed as Equation 3.13.

$$\log(\frac{E_i}{p_a}) = \log K_E + \left[n_E + \alpha_E(u_a - u_w)\right]\log(\frac{\sigma_3 - u_a}{p_a}) + \beta_E \log[(\frac{u_a - u_w}{p_a}) \times (\frac{S - S_r}{1 - S_r}) + 1] \quad (3.13)$$

where ($\sigma_3 - u_a$) is the net minor principal stress; ($u_a - u_w$) is matric suction; S is the degree of saturation; S_r is the residual degree of saturation; α_E and β_E are fitting parameters for the initial tangent modulus of unsaturated soils.

(2) Post-peak modulus M

Analogous to the approach of predicting E_i, Equation 3.14 is proposed for predicting M taking account of independent contribution from net minor principal stress and matric suction.

$$\log(\frac{M}{p_a}) = \log K_M + \left[n_M + \alpha_M(u_a - u_w)\right]\log(\frac{\sigma_3 - u_a}{p_a}) + \beta_M \log[(\frac{u_a - u_w}{p_a}) \times (\frac{S - S_r}{1 - S_r}) + 1] \quad (3.14)$$

where K_M and n_M are post-peak modulus parameters of the saturated soil; α_M and β_M are fitting parameters for the post-peak modulus of unsaturated soils.

(3)Ultimate deviatoric stress q_{ult} and peak deviatoric stress q_p

The q_{ult} of a hardening response of saturated soils is the asymptotic value of the deviatoric stress when ε_a is infinity, which in reality cannot be reached. The saturated soil specimen typically fails when the deviatoric stress exceeds a specific value q_f. Therefore, q_{ult} is commonly estimated by amplifying q_f using R_f as an amplification factor (i.e., $q_{ult} = R_f \times q_f$) (Duncan and Chang 1970).

An approach with a similar philosophy used for saturated soils can be extended for unsaturated soils. The specimen can be considered to fail when the peak state is reached since it typically would not be exhibiting a hardening response with an increase in the axial strain. Therefore, the peak deviatoric stress of unsaturated soils can be used as q_f. The peak shear strength of unsaturated soils can be predicted using Vanapalli et al. (1996) equation, which was modified to predict q_p in terms of ($\sigma_3 - u_a$) and ($u_a - u_w$) as below:

$$q_p = m_p + (p - u_a)M_p + (u_a - u_w)M_p S^{\kappa_p}$$
$$= \frac{3}{3 - M_p}[m_p + (\sigma_3 - u_a)M_p + (u_a - u_w)M_p S^{\kappa_p}] \quad (3.15)$$

$$q_{ult} = \frac{3R_f}{3 - M_p}[m_p + (\sigma_3 - u_a)M_p + (u_a - u_w)M_p S^{\kappa_p}] \quad (3.16)$$

where $(p - u_a) = (\sigma_1 + 2\sigma_3)/3 - u_a$ is the net mean stress; m_p and M_p are peak shear strength parameters of the saturated soil, i.e., the intercept and slope of saturated peak failure envelope in the $q - p'$ space; κ_p is the fitting parameter for peak shear strength of unsaturated soils; R_f is the failure ratio.

(4) Critical deviatoric stress q_c

The critical deviatoric stress of unsaturated soils can also be described extending Mohr-Coulomb criterion using Equation 3.15, given below:

$$q_c = \frac{3}{3 - M_c}[m_c + (\sigma_3 - u_a)M_c + (u_a - u_w)M_c S^{\kappa_c}] \quad (3.17)$$

where m_c and M_c are critical shear strength parameters of the saturated soil, i.e., the intercept and slope of saturated critical failure envelope in the $q - p'$ space; κ_c is the fitting parameter for critical shear strength of unsaturated soils.

Eventually, the DSC-based model for the strain-softening stress-strain relationship of unsaturated soils under consolidated drained triaxial compression condition can be expressed as Equation 3.11 with five parameters (E_i, M, q_p, q_{ult} and q_c). These five parameters can be predicted using Equations 3.13 through 3.17 based on the net minor principal stress and matric suction.

3.4 Prediction procedure and verification

3.4.1 Prediction procedure

Figure 3.3 summarizes the procedures for predicting the stress-strain relationship of unsaturated soils under consolidated drained triaxial compression condition using the proposed model. The procedural steps are summarized below:

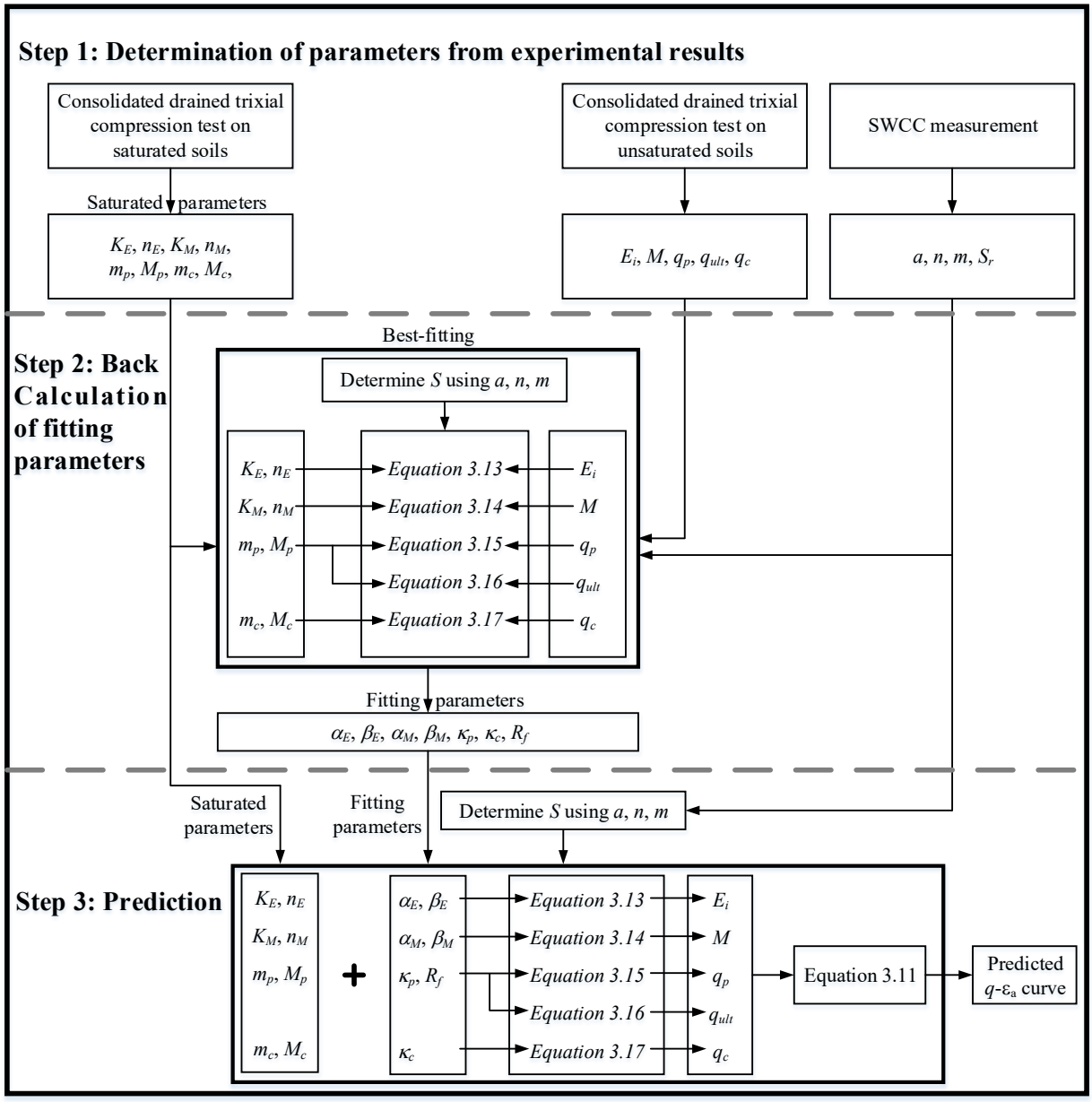

Figure 3.3 Flowchart for predicting the stress-strain relationship of unsaturated soils under consolidated drained triaxial compression loading

(1) Determine parameters from the experimental results

Firstly, saturated soil parameters (i.e., K_E, n_E, K_M, n_M, m_p, M_p, m_c and M_c) should be determined by using the experimental results of consolidated drained triaxial compression tests of saturated soils under different confining pressures. Once a series of $q - \varepsilon_a$ curves can be obtained, the pre-peak part of those curves can be replotted on the $\varepsilon_a/q - \varepsilon_a$ coordinate system as shown in Figure 3.4a. Afterwards, a linear relationship can be fitted to the part at relatively large axial strain of the pre-peak curve. According to Equation 3.5, the intercept of the fitted line will be $1/E_i$ and the slope will be $1/q_{ult}$. During this process, only the part at relatively large axial strain (e.g., ε_a > 1% in Figure 3.4a) are used for fitting, which is similar to Duncan and Chang (1970). This is because experimental data at small axial strain does not typically exhibit a well-defined linear relationship (Figure 3.4a).

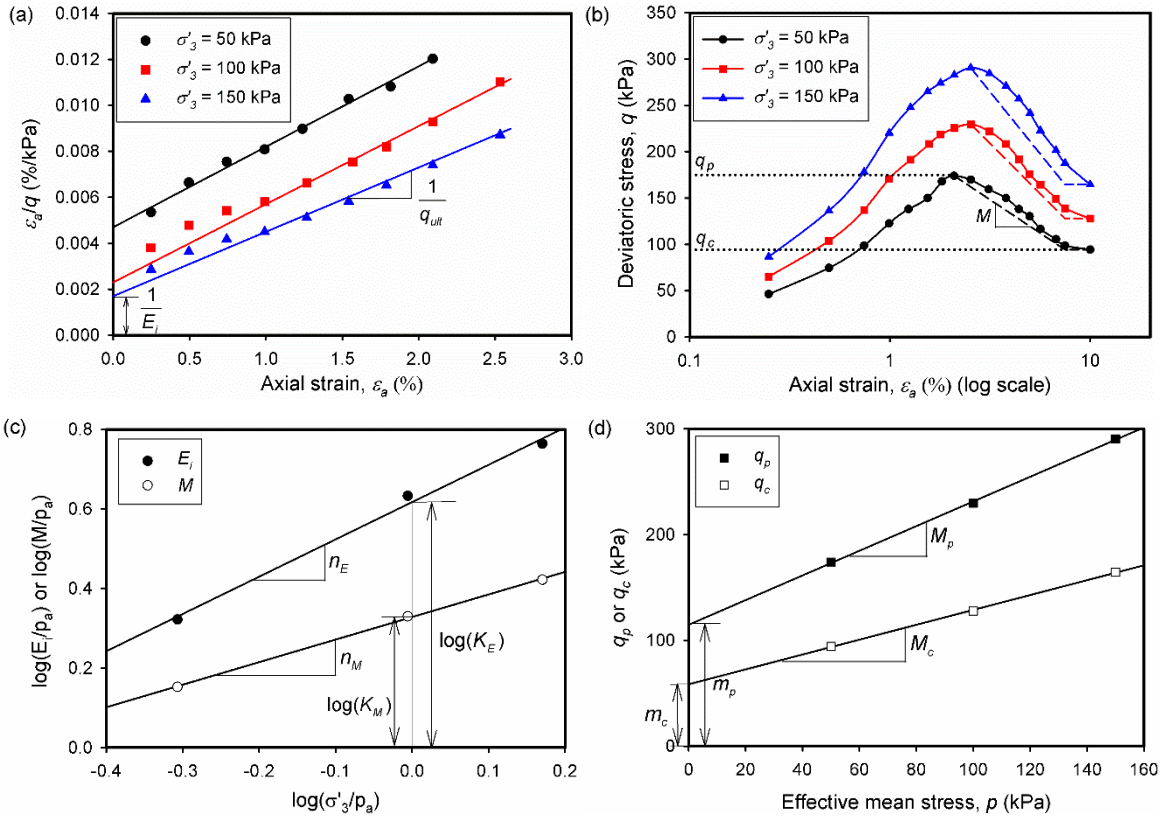

Figure 3.4 Determination of saturated parameters from experimental results (data from Miao et al. 2002): (a) E_i and q_{ult}; (b) q_p, q_c and M; (c) n_E, K_E and n_M, K_M; (d) m_p, M_p and m_c, M_c

The peak and critical deviatoric stress, q_p and q_c, can be determined from the $q - \varepsilon_a$ curves of triaxial tests. q_c is the ultimate constant deviatoric stress and q_p is the maximum deviatoric stress. However, well-defined constant deviatoric stress conditions may not be observed from the stress-strain curves of some triaxial tests at the end of the tests. Therefore, in this research, the maximum deviatoric stress is also used as q_c for hardening materials. The minimum deviatoric stress after peak state is used as q_c for softening material.

In order to determine the post-peak modulus, M, the $q - \varepsilon_a$ curves can be replotted as $q - \log(\varepsilon_a)$ relationship as shown in Figure 3.4b. The point of maximum curvature is typically found on the post-peak stress-strain curve in $q - \log(\varepsilon_a)$ space. An intersection point can be determined between the vertical line passing through the point of maximum curvature and the horizontal line plotted along the critical state. M is the slope of the line connecting the peak point and the intersection point in $q - \log(\varepsilon_a)$ space (Figure 3.4b).

The values of E_i, M, q_p, q_{ult} and q_c are determined under different values of σ'_3 from triaxial tests performed on saturated soil specimens. A linear relationship can then be fitted between $\log(M/p_a)$ and $\log(\sigma'_3/p_a)$ ($\log(E_i/p_a)$ and $\log(\sigma'_3/p_a)$). The intercept and slope of the fitted line will be $\log(K_M)$ and n_M ($\log(K_E)$ and n_E), respectively (Figure 3.4c). The peak and critical failure envelope can be plotted in the $q - p'$ space. The intercept and slope of the critical (peak) failure envelope will be m_c and M_c (m_p and M_p) (Figure 3.4d).

Secondly, a series of the values of E_i, M, q_p, q_{ult} and q_c under different $(\sigma_3 - u_a)$ and $(u_a - u_w)$ are required for determination of the fitting parameters in Equations 3.13 through 3.17. They should be determined by using the experimental results of consolidated drained triaxial compression tests of unsaturated soils. The same procedure for determination of the values of E_i, M, q_p, q_{ult} and q_c for saturated soils can also be followed for unsaturated soils.

Thirdly, the SWCC parameters (i.e., a, n and m) should be determined by fitting the experimental results of SWCC using the equation proposed by Fredlund and Xing (1994). The residual degree of saturation, S_r, can be determined following the procedure proposed by Vanapalli et al. (1998) using the best fit SWCC.

(2) Back-calculate the fitting parameters

In the last step, a series of values of E_i, M, q_p, q_{ult} and q_c for unsaturated soils for different $(\sigma_3 - u_a)$ and $(u_a - u_w)$ are determined. The relationships between each of them (i.e., E_i, M, q_p, q_{ult} and q_c) and $(\sigma_3 - u_a)$ and $(u_a - u_w)$ can be best-fitted using Equations 3.13 through 3.17 along with the saturated soil parameters determined in Step (1) to estimate the required fitting parameters (i.e., α_E, β_E, α_M, β_M, κ_p, κ_c and R_f).

(3) Predict the stress-strain relationship of unsaturated soils

After obtaining the required saturated soil and the SWCC parameters as summarized in Step 1 and fitting parameters as detailed in Step 2, the gathered information is substituted into Equations 3.13 through 3.17 to predict the values of E_i, M, q_p, q_{ult} and q_c under different combinations of independent stress state variables, $(\sigma_3 - u_a)$ and $(u_a - u_w)$. The soil can be considered to exhibit strain-hardening behavior when the values of M are less than 1; for this reason, the value of M is assumed equal one. Then, the values of E_i, M, q_p, q_{ult} and q_c can be substituted into Equation 3.11 to predict the shear stress-shear strain relationship.

3.4.2 Validation

Five sets of consolidated drained triaxial tests data performed on unsaturated soils ranging from coarse- to fine-grained soils (Table 3.2) gathered from literature were used to verify the prediction ability of the proposed model. For each set of data, the saturated soil parameters and SWCC parameters were compiled by following prediction procedure in Step (1). For ML (Estabragh and Javadi 2008), the SWCC information is not available in this study. However, a series of values of degree of saturation were presented when the specimens reached the equilibrium state under different suctions, which were used to determine the SWCC parameters. For each set of data, the fitting parameters were back calculated by using only a portion of the experiments on unsaturated soils (Table 3.2) following prediction procedure in Step (2). Experimental data over a wide range of suction were used for obtaining the reasonable fitting parameters. All the parameters determined for the investigated experimental studies are summarized in Table 3.3.

Table 3.2 Properties of the studied soils and loading conditions of studied triaxial tests

	SM (Patil 2014)	CL (Rahardjo et al. 2004)	ML (Estabragh and Javadi 2008)	Expansive clay (Miao et al. 2002)	Residual clayey soil (Kayadelen et al. 2007)
Sand (%)	55	34	5	-	4
Silt (%)	37	24	90	-	28.8
Clay (%)	8	42	5	24.8	67.2
Optimum Moisture Content (%)	12.2	14.2	14.5	21.4	-
Maximum Dry Density (g/cm^3)	1.87	1.86	1.74	1.63	-
Liquid Limit (%)	-	36.4	29	58.3	77
Plastic Limit (%)	-	21.6	10	26.5	32
Plasticity Index	-	14.8	19	31.8	45
Initial water content of specimens (%)	14.2	15.6	10	17	-
Specimen preparation technique	Static compaction (1600 kPa final vertical stress)	Static compaction	Static compaction (1600 kPa final vertical stress)	Static compaction	Undisturbed samples
Saturated tests	σ'_3 = 100, 200, 300 kPa	σ'_3 = 50, 100, 150 kPa	σ'_3 = 50, 100, 200, 300, 400 kPa	σ'_3 = 50, 100, 150 kPa	σ'_3 = 50, 150, 200 kPa
Unsaturated tests for back prediction	$(u_a - u_w)$ = 250, 750 kPa	$(u_a - u_w)$ = 100, 290 kPa	$(u_a - u_w)$ = 100, 300 kPa	$(u_a - u_w)$ = 80, 200 kPa	$(u_a - u_w)$ = 100, 400 kPa
Unsaturated tests for prediction	$(u_a - u_w)$ = 50, 500 kPa	$(u_a - u_w)$ = 50, 150 kPa	$(u_a - u_w)$ = 200 kPa	$(u_a - u_w)$ = 50, 120 kPa	$(u_a - u_w)$ = 50, 200 kPa

For each set of data, the proposed model with corresponding parameters in Table 3.3 was used to back-predict the experiments that were used for finding the fitting parameters. Figure 3.5 presents the typical comparisons between the back-predicted and experimental results. Then, the proposed model with these parameters was used to predict the reminder of experiments that were not used for finding the fitting parameters. Figure 3.6 presents the typical comparisons between the predicted and experimental results.

Figure 3.7 provides comparisons between the experimental and predicted values of E_i, M, q_p, q_{ult}, q_c and ε_p for all the five sets of stress-strain curves. The predicted values of E_i, M, q_{ult} and q_c were calculated using Equations 3.13, 3.14, 3.16 and 3.17, respectively. However, as discussed earlier, the peak point of the predicted stress-strain curve is not exactly at the position defined by the values of ε_p and q_p calculated using Equations 3.8 and 3.15 (see Figure 3.2). For this reason, the predicted

values of ε_p and q_p were determined from the predicted stress-strain curves shown in Figures 3.5 and 3.6. In addition, it is difficult to determine the axial strain at failure for a hardening stress-strain curve. Thus, only the values of ε_p of strain-softening stress-strain curves were included in Figure 3.7c. The comparisons suggest that M, q_p, q_{ult}, q_c and ε_p have been predicted reasonably ($R^2 \geq 0.9$). However, significant errors can be observed in the prediction of E_i. Such a behavior can be attributed to the irregular variations of the pre-peak parts of some stress-strain curves with stress state variables. The irregularity could not be reduced despite using a part of pre-peak stress-strain curve at relatively large axial strain to do fitting.

Table 3.3 Summary of various parameters for experimental studies investigated

		SM	CL	ML	Expansive clay	Residual clayey soil
Saturated soil parameters	K_E	1.58	1.19	1.55	4.14	1.04
	n_E	0.92	1.18	0.26	0.94	0.86
	K_M	0.01	0.01	0.01	2.13	1.78
	n_M	0	0	0	0.57	0.65
	m_p	0	0	45.84	82.7	35.47
	M_p	1.4	1.23	1.18	0.84	0.84
	m_c	0	0	45.84	47.44	11.79
	M_c	1.4	1.23	1.18	0.57	0.77
Fitting parameters	α_E	-0.0006	-0.0085	-0.0015	-0.0042	-0.0005
	β_E	3.16	0.76	4.65	0.48	0.18
	α_M	0.0009	-0.0497	-0.0088	-0.0011	-0.0003
	β_M	10.1	-5.81	8.72	0.37	0.83
	κ_p	0.71	0.54	1.23	1.25	2.03
	κ_c	1.24	1.27	1.45	-0.67	2.76
	R_f	1.26	1.23	1.09	1.34	1.29
SWCC parameters	a	20.7	109.24	13.13	324.01	9.23
	n	0.95	3.53	0.91	1.17	0.6
	m	1.1	0.74	0.93	1.12	0.31
	S_r	0.125	0.126	0.178	0.107	0.147

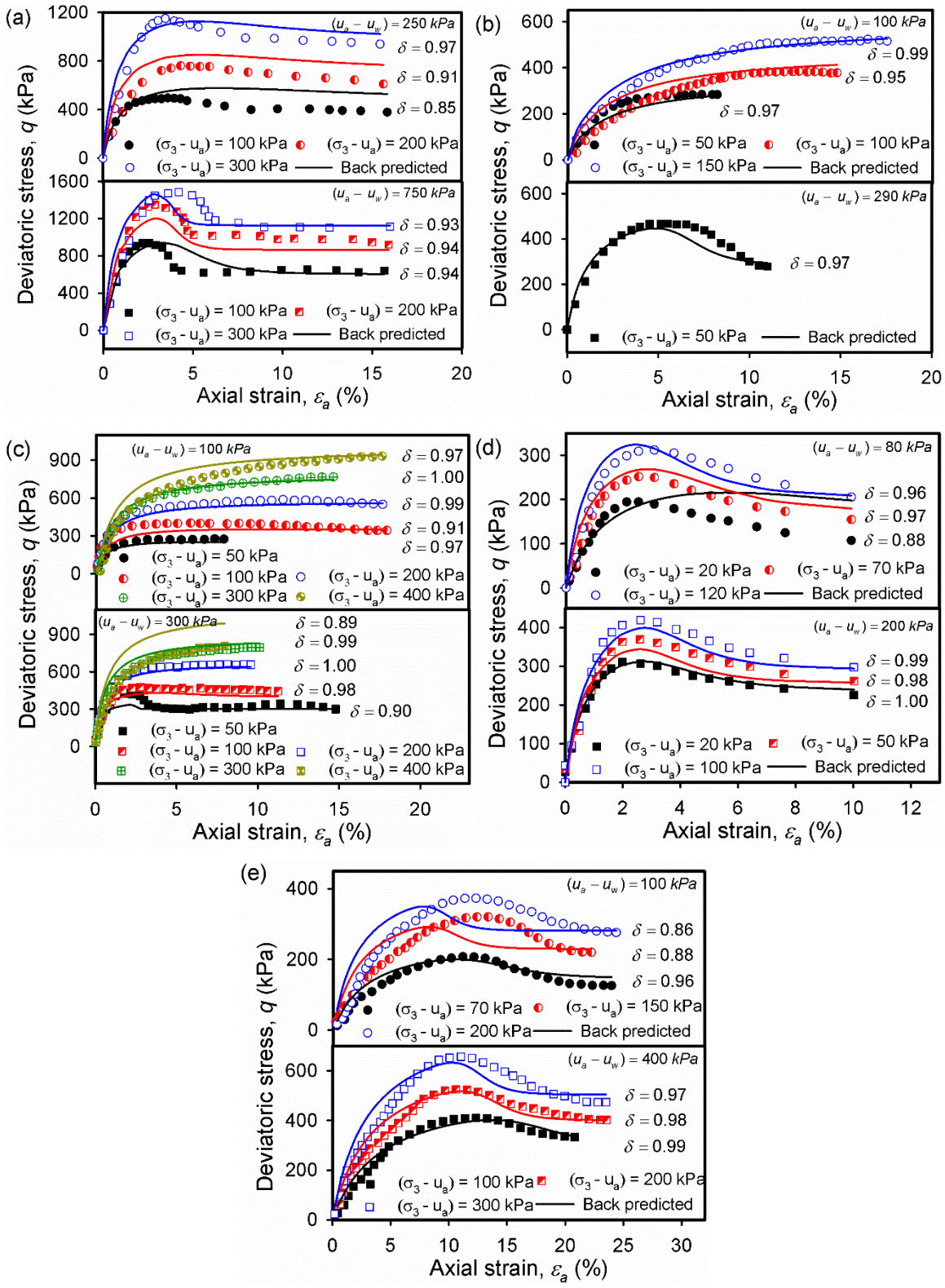

Figure 3.5 Comparisons between the back-predicted and experimental results: (a) SM; (b) CL; (c) ML; (d) expansive clay; (e) residual clayey soil

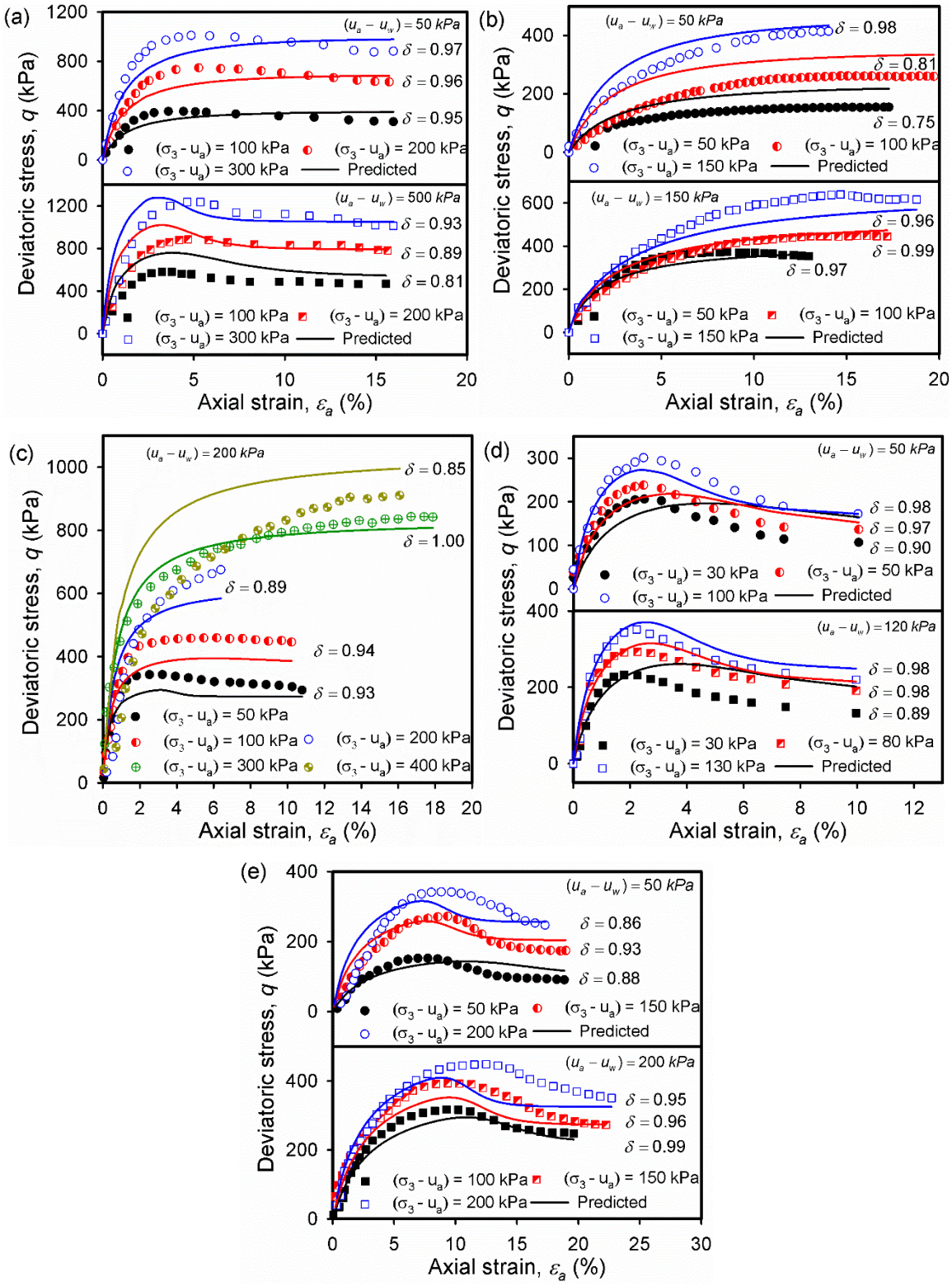

Figure 3.6 Comparisons between the predicted and experimental results: (a) SM; (b) CL; (c) ML; (d) expansive clay; (e) residual clayey soil

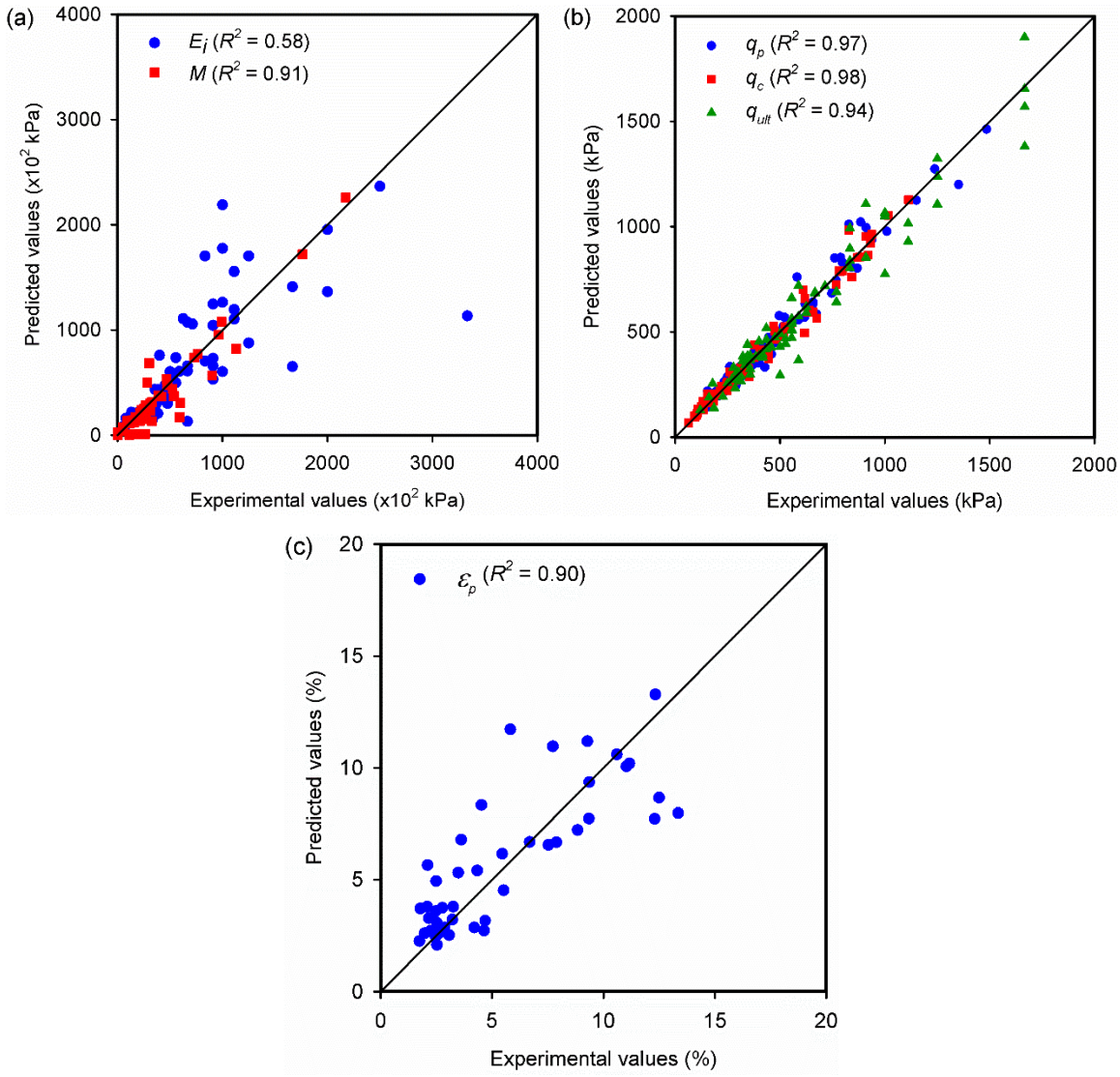

Figure 3.7 Comparisons between experimental and predicted values of mechanical properties: (a) E_i and M; (b) q_p, q_c and q_{ult}; (c) ε_p

3.5 Discussion

The index of agreement (δ) (Willmott 1981) was calculated for each of the curves summarized in Figures 3.5 and 3.6 to describe the degree to which the experimental data is estimated from the predicted data to evaluate the accuracy of the prediction quantitatively. This value varies between 0 and 1; a value of 1 indicates a perfect agreement between predicted and experimental curves. δ can be expressed as

$$\delta = 1 - \left[\frac{\sum_{i=1}^{N} (X_{Ei} - X_{Pi})^2}{\sum_{i=1}^{N} (|X_{Pi} - \overline{X_E}| + |X_{Ei} - \overline{X_E}|)^2} \right] \tag{3.18}$$

where X_{Ei} is the experimental values of the deviatoric stress derived from a stress-strain curve; X_{Pi} is the predicted values of the deviatoric stress for a stress-strain curve; $\overline{X_E}$ is the mean of the experimental deviatoric stress values of a stress-strain curve; N is the number of experimental and predicted values of a stress-strain curve.

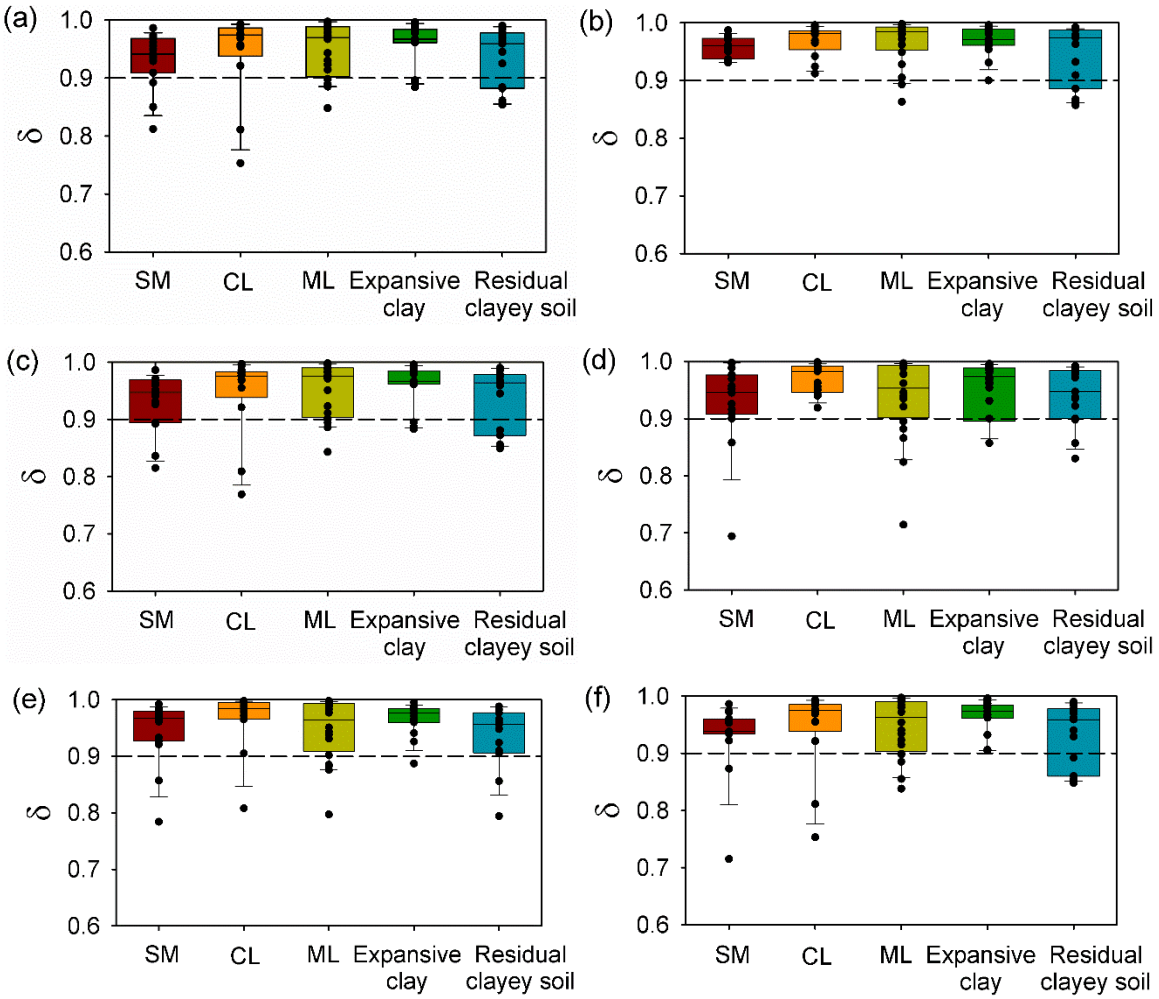

Figure 3.8 Box plots of the values of δ: (a) δ of predicted stress-strain curves; (b) q_p is replaced with experimental data; (c) q_c is replaced with experimental data; (d) q_{ult} is replaced with experimental data; (e) E_i is replaced with experimental data; (f) M is replaced with experimental data. The box plots show medians, interquartile ranges, and outliers

The δ values of the stress-strain curves of five different types of unsaturated soils shown in Figures 3.5 and 3.6 are summarized in Figure 3.8a. The predictions are considered to be satisfactory if the value of δ is greater than 0.9. In Figure 3.8a, three quarters of δ values for each set of soil data were greater than 0.9. This suggests the prediction model performed well for most of stress-strain relationships used in this research.

However, there are some outliers for each set of soil data with values less than 0.9. The influence of the prediction accuracy of the five mechanical parameters (E_i, M, q_p, q_{ult} and q_c) calculated using Equations 3.13 through 3.17 on prediction errors of the stress-strain relationships was further studied to analyze the reasons associated with prediction errors. For this reason, δ values were recalculated for five different cases where the predicted values of one of the mechanical parameters (E_i, M, q_p, q_{ult} and q_c) were replaced with the experimental data, while the other four parameters were still predicted at the same time. The results were summarized in Figures 3.8b through 3.8f, respectively. For example, the experimental data of peak deviatoric stress were used as the q_p in Equation 3.11, while E_i, M, q_{ult} and q_c were predicted using the proposed equations. Based on these values, a series of new predicted stress-strain curves were generated and their δ values are summarized in Figure 3.8b.

Comparisons between Figures 3.8a and 3.8b suggest that the predictions for SM, CL, ML and expansive clay can be improved significantly, if the predicted values of q_p were replaced with the experimental data. Some stress-strain curves in Figure 3.9 are summarized with q_p replaced using the experimental data. A better agreement can be observed between those curves and experimental results. This means the error in prediction using the proposed model is sensitive to the degree of accuracy of predicting peak deviatoric stress, q_p. On the other hand, the accuracy of predictions for these soils would not be influenced significantly, if the experimental data were substituted for the predicted values of q_c (Figure 3.8c), q_{ult} (Figure 3.8d), E_i (Figure 3.8e) and M (Figure 3.8f) respectively. In spite of a relatively large error in predicting E_i (shown in Figure 3.7a), the prediction of stress-strain relationships is not sensitive to the values of E_i; thus, the error in predicting E_i cannot cause a significant error in predicting the stress-strain relationships.

The predictions for the residual clayey soil however were not improved, irrespective of the mechanical parameter that was replaced with the experimental data. Such a behavior can be

attributed to the obvious irregularity of the pre-peak part of the experimental stress-strain relationships. It can be found from Figures 3.5e and 3.6e, for the residual clayey soil under a constant net minor principal stress, some pre-peak stress-strain curves under different matric suctions almost overlap within small axial strain range (axial strain < 5%), which is clearly unreasonable. Therefore, for some pre-peak stress-strain curves of this soil, only the part close to peak state were used to determine the E_i and q_{ult}. This causes a lower accuracy of predictions for this residual clayey soil within the small axial strain range compared with other four soils.

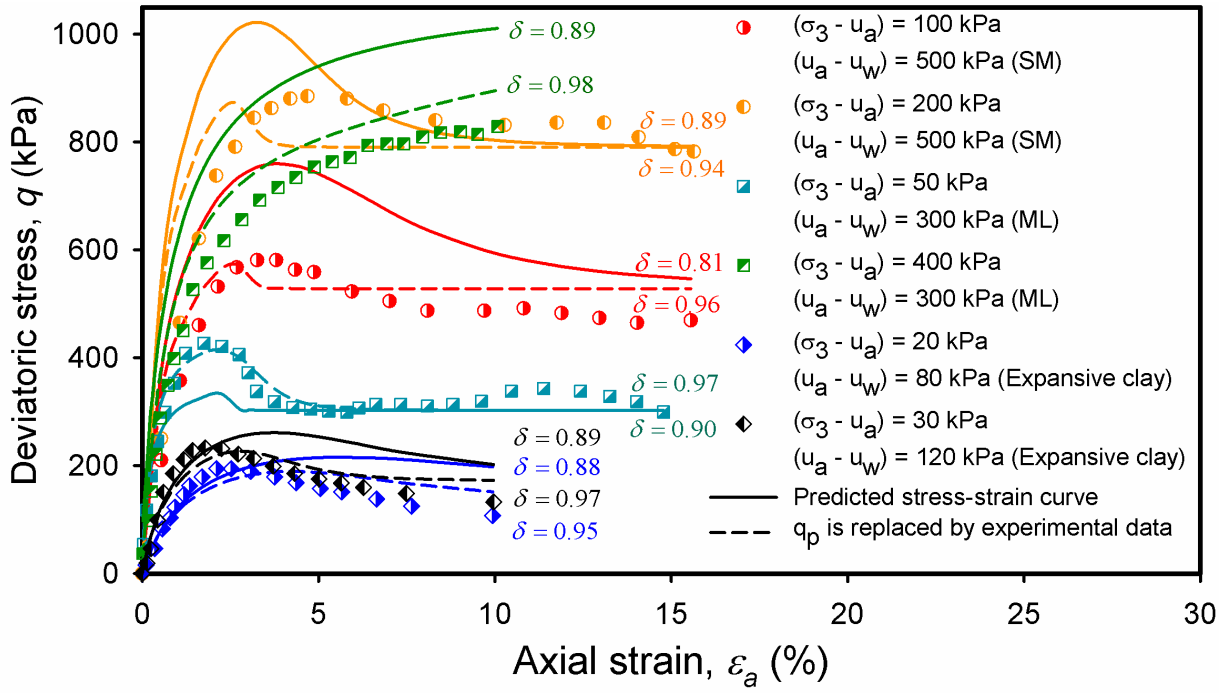

Figure 3.9 Comparisons between predicted stress-strain curves and predicted curves with q_p replaced using experimental data

The proposed model can be used for predicting the strain-softening stress-strain relationships of various types of unsaturated soils ranging from the coarse- to fine-grained soils. In addition, the model is simple in concept since it does not require the use of advanced soil plasticity concepts. All the required parameters in this model (Table 3.3) can be obtained from conventional saturated and unsaturated triaxial shearing tests and pressure plate tests. However, the volume change behavior of the soils was not considered in this model. In some stress paths (e.g., the undrained shearing condition), the values of u_a and u_w are influenced by volume change behavior which cannot be predicted using this model. For this reason, this model can only be used for the stress

paths where the values of (u_a – u_w) and (σ_3 – u_a) are known. However, this model can be incorporated into an elastoplastic constitutive model of unsaturated soils. One possible approach is to use the proposed model as a shear strength criterion to describe the variation of shear strength with deformation along similar lines as Qi and Vanapalli (2016). In this way, this model can be extended for any stress paths and implemented in solutions of the boundary value problems.

3.6 Summary

In this chapter, a disturbed state concept (DSC) based model is proposed to predict the variation of shear stress during strain-softening process for a wide range of unsaturated soils taking account of the influence of stress state variables; namely, net minor principal stress and matric suction. The strain-softening behavior of both saturated and unsaturated soils can be associated with the development of shear band, which can be considered as the disturbance leading to the strain-softening behavior. Based on this concept, the pre-peak state where no obvious shear band generates is selected as the relative intact (RI) state and the critical state where a shear band fully generates is selected as the fully adjusted (FA) state.

The RI state behavior can be described by a hardening response extending the pre-peak stress-strain curve, which is predicted using a hyperbolic model with two parameters (i.e., initial tangent modulus, E_i and ultimate deviatoric stress, q_{ult}). The FA state behavior is predicted using a linear model with one parameter (i.e., critical deviatoric stress, q_c). A S-shape curve on a semi-logarithmic plot (disturbance – logarithm of axial strain) is used as the disturbance function curve (Figure 3.2c). Another two parameters (i.e., post-peak modulus, M and peak deviatoric stress, q_p) are introduced to formulate the disturbance function with five parameters (i.e., E_i, M, q_p, q_{ult} and q_c) based on two assumptions: (i) the point on the disturbance function curve where softening initiates corresponds to the peak point on the measured apparent stress-strain curve; (ii) the point on the disturbance function curve where most of softening ends corresponds to the post-peak point with maximum curvature on the measured apparent stress-strain curve.

The five mechanical parameters discussed above can be expressed as functions (Equations 3.13 through 3.17) of independent stress state variables, (u_a – u_w) and (σ_3 – u_a) along with saturated soil parameters, SWCC and seven fitting parameters (i.e., α_E, β_E, α_M, β_M, κ_p, κ_c and R_f). Finally, a DSC

model (Equation 3.11) is proposed for predicting the strain-softening stress-strain relationships for unsaturated soils combining the RI state model, FA state model and disturbance function.

A three-step procedure is described for predicting a stress-strain relationship of unsaturated soils using the proposed model, that includes: (i) determination of the saturated soil parameters (i.e., K_E, n_E, K_M, n_M, m_p, M_p, m_c and M_c) and SWCC parameters (a, n, m and S_r) from conventional laboratory tests; (ii) determination of the fitting parameters (i.e., α_E, β_E, α_M, β_M, κ_p, κ_c and R_f) by back-calculating a few typical experimental results of unsaturated soil specimens; (iii) prediction of the stress-strain relationship under any combination of ($u_a - u_w$) and ($\sigma_3 - u_a$) based on the saturated soil parameters, fitting parameters and the SWCC.

Validations of the proposed model using five sets of experimental data for SM, CL, ML, expansive clay, and residual clayey soil suggest a satisfactory agreement between the experimental and predicted results. Comprehensive error analysis based on the index of agreement (δ) suggests that the error in predicting the stress-strain relationship using the proposed model is sensitive to the degree of accuracy of predicting peak deviatoric stress.

3.7 References

Alonso, E.E., Gens, A., and Josa, A. 1990. A constitutive model for partially saturated soils. Géotechnique, 40(3): 405–430.

Andò, E., Hall, S.A., Viggiani, G., Desrues, J., and Bésuelle, P. 2012. Grain-scale experimental investigation of localised deformation in sand: a discrete particle tracking approach. Acta Geotechnica, 7(1): 1-13.

Armaleh, S.H., and Desai, CS. 1994. Modelling and testing of a cohesionless material using the disturbed state concept. Journal of the Mechanical Behavior of Materials, 5(3): 279–296.

Atkinson, J. 2007. The mechanics of soils and foundations (2nd edition). London, UK: Taylor and Francis.

Cui, Y.J., and Delage, P. 1996. Yielding and plastic behaviour of an unsaturated compacted silt. Géotechnique, 46(2): 291–311.

Desai, C.S. 1974. A consistent finite element technique for work-softening behaviour. In Proceedings of the International Conference on Computational Methods in Nonlinear Mechanics. Austin, Texas, USA.

Desai, C.S. 2000. Mechanics of materials and interfaces: the disturbed state concept. Boca Raton, USA: CRC press.

Desai, C.S., and Ma, Y. 1992. Modelling of joints and interfaces using the disturbed-state concept. International Journal for Numerical and Analytical Methods in Geomechanics, 16(9): 623–653.

Duncan, J.M., and Chang, C.Y. 1970. Nonlinear analysis of stress and strain in soils. Journal of Soil Mechanics & Foundations Division, 96(5): 1629–1653.
Estabragh, A.R., and Javadi, A.A. 2008. Critical state for overconsolidated unsaturated silty soil. Canadian Geotechnical Journal, 45(3): 408–420.
Fredlund, D.G., and Morgenstern, N.R. 1977. Stress state variables for unsaturated soils. Journal of the Geotechnical Engineering Division. ASCE, 103(GT5): 447-466.
Fredlund, D.G., Morgenstern, N.R., and Widger, R.A. 1978. The shear strength of unsaturated soils. Canadian Geotechnical Journal, 15(3): 313–321.
Fredlund, D.G., and Xing, A. 1994. Equations for the soil-water characteristic curve. Canadian Geotechnical Journal, 31(4): 521–532.
Geiser, F., Laloui, L., Vulliet, L., and Desai, C.S. 1997. Disturbed state concept for partially saturated soils. In Proceedings of the 6th International Symposium on Numerical Models in Geomechanics. Balkema, Rotterdam, Netherlands.
Haeri, S.M., Khosravi, A., Garakani, A.A., and Ghazizadeh, S. 2016. Effect of soil structure and disturbance on hydromechanical behaviour of collapsible loessial soils. International Journal of Geomechanics, 17(1): 04016021.
Hall, S.A., Bornert, M., Desrues, J., Pannier, Y., Lenoir, N., Viggiani, G., and Bésuelle, P. 2010. Discrete and continuum analysis of localised deformation in sand using X-ray CT and volumetric digital image correlation. Géotechnique, 60(5): 315–322.
Hamid, T.B., and Miller, G.A. 2008. A constitutive model for unsaturated soil interfaces. International Journal for Numerical and Analytical Methods in Geomechanics, 32(13): 1693–1714.
Higo, Y., Oka, F., Kimoto, S., Sanagawa, T., and Matsushima, Y. 2011. Study of strain localization and microstructural changes in partially saturated sand during triaxial tests using microfocus X-ray CT. Soils and foundations, 51(1): 95-111.
Higo, Y., Oka, F., Sato, T., Matsushima, Y., and Kimoto, S. 2013. Investigation of localized deformation in partially saturated sand under triaxial compression using microfocus X-ray CT with digital image correlation. Soils and Foundations, 53(2): 181-198.
Hoyos, L.R., Suescún-Florez, E.A., and Puppala, A.J. 2015. Stiffness of intermediate unsaturated soil from simultaneous suction-controlled resonant column and bender element testing. Engineering Geology, 188(7): 10–28.
Hu, L., and Pu, J. 2004. Testing and modeling of soil-structure interface. Journal of Geotechnical and Geoenvironmental Engineering, 130(8): 851–860.
Kayadelen, C., Tekinsoy, M.A., and Taşkıran, T. 2007. Influence of matric suction on shear strength behaviour of a residual clayey soil. Engineering Geology, 53(4): 891–901.
Kido, R., and Higo, Y. 2019. Distribution changes of grain contacts and menisci in shear band during triaxial compression test for unsaturated sand. Japanese Geotechnical Society Special Publication, 7(2): 627-635.
Lee, Y.S., Cheuk, C.Y., and Bolton, M.D. 2008. Instability caused by a seepage impediment in layered fill slopes. Canadian Geotechnical Journal, 45(10): 1410-1425.
Locat, A., Leroueil, S., Bernander, S., Demers, D., Jostad, H.P., and Ouehb, L. 2011. Progressive failures in eastern Canadian and Scandinavian sensitive clays. Canadian Geotechnical Journal, 48(11): 1696-1712.
Miao, L., Liu, S., and Lai, Y. 2002. Research of soil–water characteristics and shear strength features of Nanyang expansive soil. Engineering Geology, 65(4): 261–267.

Mitchell, J.K., and Soga, K. 2005. Fundamentals of soil behavior (3rd edition). New York, USA: John Wiley & Sons.

Patil, U.D. 2014. *Response of unsaturated silty sand over a wider range of suction states using a novel double-walled triaxial testing system*. Ph. D. Thesis, University of Texas at Arlington, Arlington, USA.

Postill, H., Dixon, N., Fowmes, G., El-Hamalawi, A., and Take, W.A. 2019. Modelling seasonal ratcheting and progressive failure in clay slopes: A validation. Canadian Geotechnical Journal.

Potts, D.M., Kovacevic, N., and Vaughan, P.R. 1997. Delayed collapse of cut slopes in stiff clay. Géotechnique, 47(5): 953–982.

Qi, S., and Vanapalli, S.K. 2016. Influence of swelling behaviour on the stability of an infinite unsaturated expansive soil slope. Computers and Geotechnics, 76: 154–169.

Rahardjo, H., Heng, O.B., and Choon, L.E. 2004. Shear strength of a compacted residual soil from consolidated drained and constant water content triaxial tests. Canadian Geotechnical Journal, 41(3): 421-436.

Russell, A. R., and Khalili, N. 2006. A unified bounding surface plasticity model for unsaturated soils. International Journal for Numerical and Analytical Methods in Geomechanics, 30(3): 181-212.

Seo, M.W., Park, I.J., and Park, J.B. 2004. Development of displacement-softening model for interface shear behaviour between geosynthetics. Soils and Foundations, 44(6): 27–38.

Skempton, A.W. 1964. Long-term stability of clay slopes. Géotechnique, 14(2): 77-102.

Takano, D., Lenoir, N., Otani, J., and Hall, S.A. 2015. Localized deformation in a wide-grained sand under triaxial compression revealed by X-ray tomography and digital image correlation. Soils and Foundations, 55(4): 906-915.

Take, W.A., and Bolton, M.D. 2011. Seasonal ratcheting and softening in clay slopes, leading to first-time failure. Géotechnique, 61(9): 757-769.

Vanapalli, S.K., Fredlund, D.G., Pufahl, D.E., and Clifton, A.W. 1996. Model for the prediction of shear strength with respect to soil suction. Canadian Geotechnical Journal, 33(3): 379–392.

Vanapalli, S.K., Sillers, W.S., and Fredlund, M.D. 1998. The meaning and relevance of residual state to unsaturated soils. In Proceedings of the 51st Canadian Geotechnical Conference, Edmonton, Alberta, Canada, 1: 101–108.

Veiskarami, M., Ghorbani, A., and Alavipour, M. 2012. Development of a constitutive model for rockfills and similar granular materials based on the disturbed state concept. Frontiers of Structural and Civil Engineering, 6(4): 365–378.

Wang, B., Vardon, P.J., and Hicks, M.A. 2018. Rainfall-induced slope collapse with coupled material point method. Engineering Geology, 239: 1-12.

Wheeler, S.J., and Sivakumar, V. (1995). An elasto-plastic critical state framework for unsaturated soil. Géotechnique, 45(1): 35-53.

Widger, R.A., and Fredlund, D.G. 1979. Stability of swelling clay embankments. Canadian Geotechnical Journal, 16(1): 140–151.

Willmott, C.J. 1981. On the validation of models. Physical Geography, 2(2): 184–194.

Yao, Y.P., Niu, L., and Cui, W.J. 2014. Unified hardening (UH) model for overconsolidated unsaturated soils. Canadian Geotechnical Journal, 51(7): 810-821.

Zhang, J., Sun, D.A., Zhou, A., and Jiang, T. 2016. Hydromechanical behaviour of expansive soils with different suctions and suction histories. Canadian Geotechnical Journal, 53(1): 1–13.

Zhou, A., and Sheng, D. 2015. An advanced hydro-mechanical constitutive model for unsaturated soils with different initial densities. Computers and Geotechnics, 63: 46-66.

CHAPTER 4 SUCTION-CONTROLLED RING SHEAR EXPERIMENTS ON UNSATURATED SOILS

4.1 Introduction

The shear strength is a key property required in the analysis and design of the geo-structures (e.g., foundations, retaining walls, natural and manmade slopes, etc.) associated with soils that are in a state of unsaturated condition. The shear strength of the unsaturated soils has been widely studied based on the direct shear tests (Vanapalli et al. 1996; Tarantino and Tombolato 2005; Hossain and Yin 2010) or triaxial shear tests (Toll 1990; Wheeler and Sivakumar 1995; Cui and Delage 1996; Estabragh and Javadi 2008; Patil et al. 2017; Cai et al. 2022) using relatively small size unsaturated soil specimens. However, the direct and triaxial shear testing apparatus can only provide limited shear deformation. Several studies (Derbyshire et al. 1994; Dijkstra 1994; Infante Sedano and Vanapalli 2011; Hoyos et al. 2014; Romero et al. 2014) have shown the shear strength of unsaturated soils reduces to a residual value under large shear deformation. Such a reduction in shear strength of unsaturated soils under large shear deformation can have a significant influence on the mechanical behaviors and factor of safety of the geo-structures in unsaturated soils (Take and Bolton 2011; Qi and Vanapalli 2016; Postill et al. 2020).

Research studies on the residual shear strength of soils are based on the ring shear testing apparatus which can theoretically provide unlimited shear deformation. Since the 1990s, some researchers (Derbyshire et al. 1994; Dijkstra 1994) have made efforts to study the residual shear strength of unsaturated soils in constant water content state using the conventional ring shear apparatus. This method was also used by other researchers (Maquaire et al. 2003; Fan et al. 2017; Lian et al. 2020) due to its simplification and convenience. However, the independent contribution of suction to the residual shear strength of unsaturated soils is still unclear despite these valuable studies. For this reason, several suction-controlled ring shear apparatuses have been developed during the last fifteen years using the axis translation technique (Infante Sedano et al. 2007; Hoyos et al. 2011) and the vapor equilibrium technique (Merchán et al. 2011).

In this chapter, the modified suction-controlled ring shear apparatus based on the axis translation technique developed by Infante Sedano et al. (2007) is introduced briefly. Three suction-controlled

ring shear cells were specially fabricated for this study extending this design philosophy. A series of suction-controlled ring shear tests were conducted for testing two different unsaturated soils, that include a poorly graded sand with silt (SP-SM) and the Indian Head till (IHT). The properties of the test materials and the procedures of suction-controlled multistage ring shear tests are described in the later sections that follow. The modified suction-controlled ring shear apparatus still has several limitations (e.g., the extrusion of soils during shearing, the evaporation of water, etc.) which can result in the errors in the measurements of the shear stress, volume change and water content of the specimens. Therefore, several correction methods were introduced for rational and reasonable interpretation of the measured results.

4.2 Modified ring shear apparatus

The modified suction-controlled ring shear apparatus developed by Infante Sedano et al. (2007) was used in this research to measure the residual shear strength of unsaturated soils. As shown in Figure 4.1, the apparatus consists of four key parts: the loading system, ring shear cell, flushing system and data acquisition system.

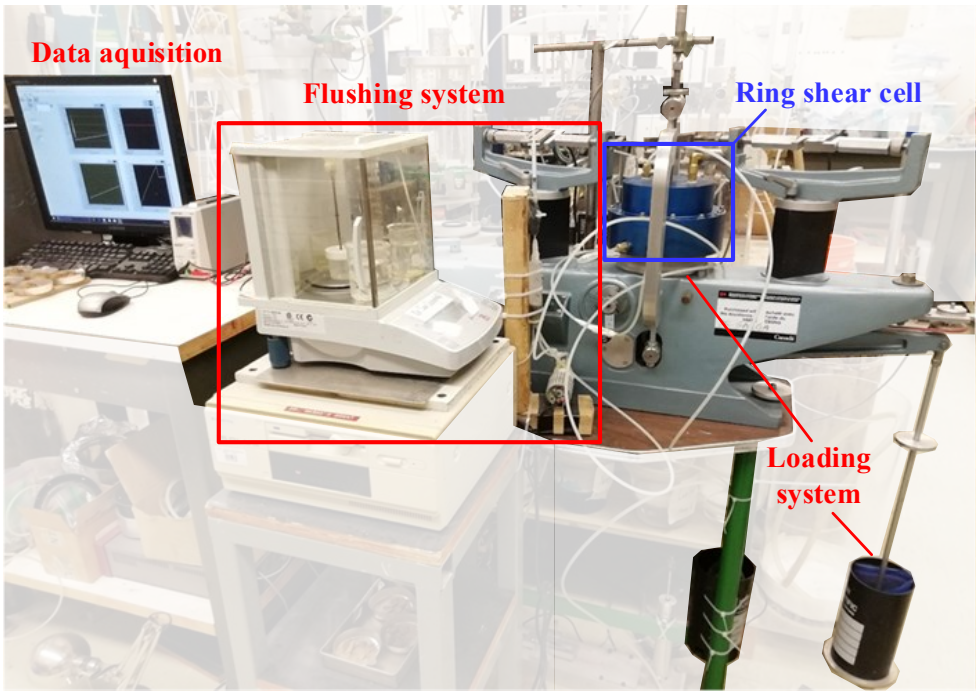

Figure 4.1 Modified suction-controlled ring shear apparatus

4.2.1 Loading system

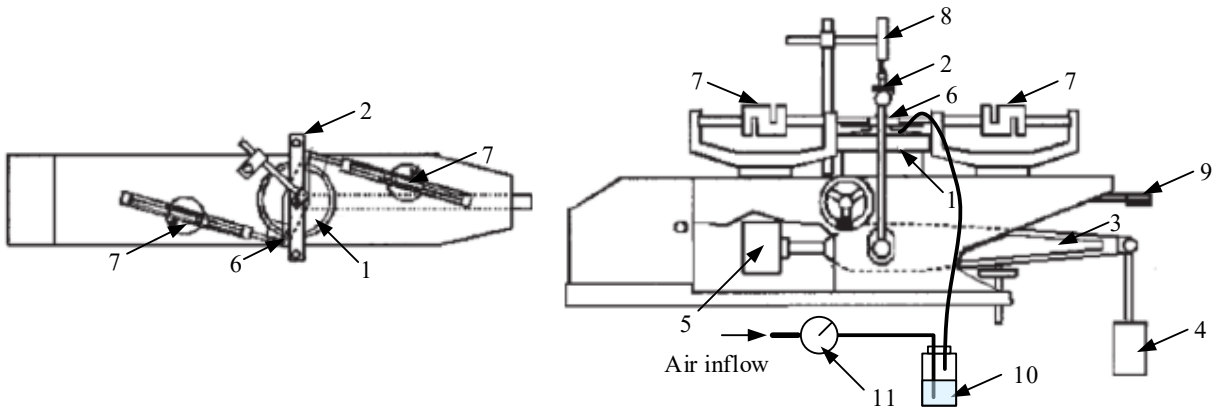

1 – Ring shear cell; 2 – Loading yoke; 3 – loading arm; 4 – Loading bucket; 5 – Counter weight; 6 – Torque arm; 7 – Torque load cell; 8 – LVDT; 9 – Rotary potentiometer; 10 – Wetting bottle; 11 – Gas pressure gauge

Figure 4.2 Schematic of normal load and torque application systems (modified after Garga and Infante Sedano 2002)

The conventional Bromhead ring shear apparatus was used to apply the normal load and torque to the specimen. As shown in Figure 4.2, the normal load was applied through the loading yoke by adding weight into the loading bucket which was magnified through the loading arm using leverage. The torque was applied by turning the ring shear cell clockwise with the torque arm being fixed.

A certain known value of air pressure should be applied in a closed ring shear cell where the unsaturated soil specimen was placed and tested. As shown in Figure 4.2, air passed through a bottle that was partially filled with water and connected to the ring shear cell. This approach facilitated wetting of the air entering the ring shear cell to significantly reduce evaporation of water from the test specimen.

4.2.2 Ring shear cell

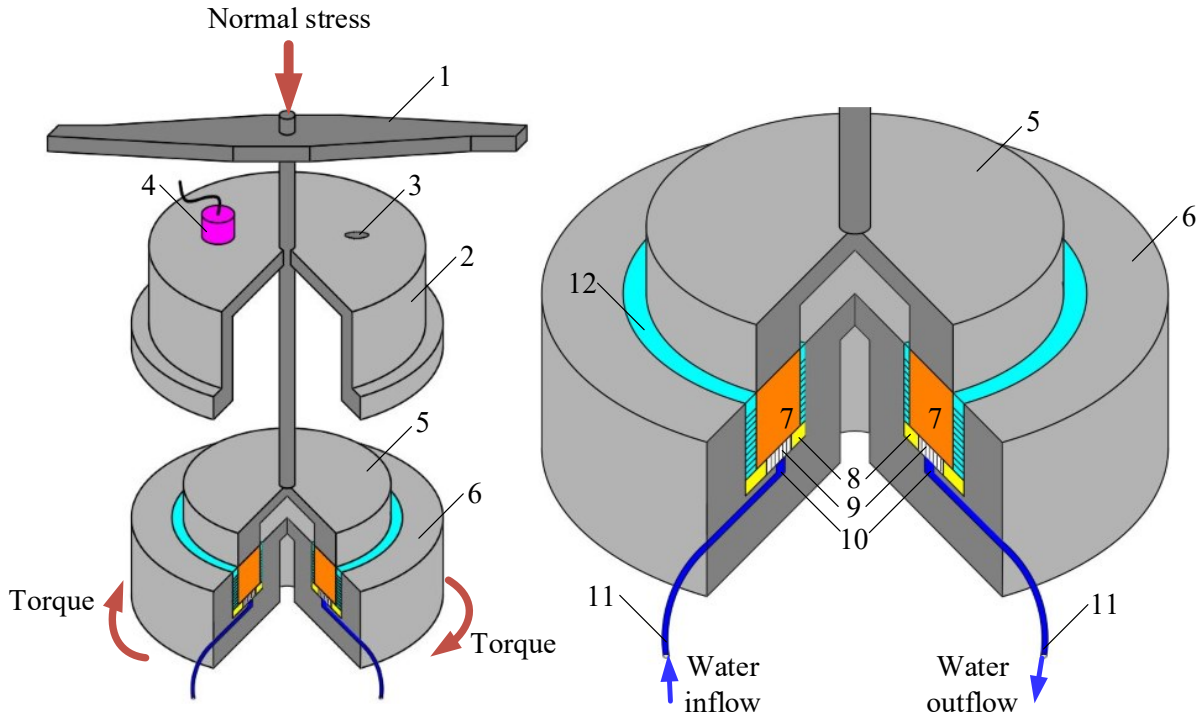

1 – Torque arm; 2 – Cell cover; 3 – Air intake; 4 – Air pressure transducer; 5 – Top platen; 6 – Cell base; 7 – Specimen; 8 – Bottom platen; 9 – Ceramic disk; 10 – Deairing groove; 11 – Tube; 12 – Confining rings

Figure 4.3 Schematic of ring shear cell

The conventional Bromhead ring shear cell has been modified to control matric suction in the test specimen extending the axis translation technique. This technique involves artificial elevation of pore air pressure while maintaining the pore water pressure at a measurable value. Consequently, the origin of reference for matric suction variable ('axis') is 'translated' from the condition of atmospheric air pressure and negative pore water pressure to the condition of the final air pressure in the cell and atmospheric water pressure (Lu and Likos 2004). This translation is accomplished by using a saturated high air-entry value ceramic disk to separate the water phase and air phase of the unsaturated soil. Figure 4.3 shows the schematic of the ring shear cell. The main components of the modified ring shear cell are introduced succinctly below. More comprehensive details are available in Infante Sedano (2006).

4.2.2.1 Cell base

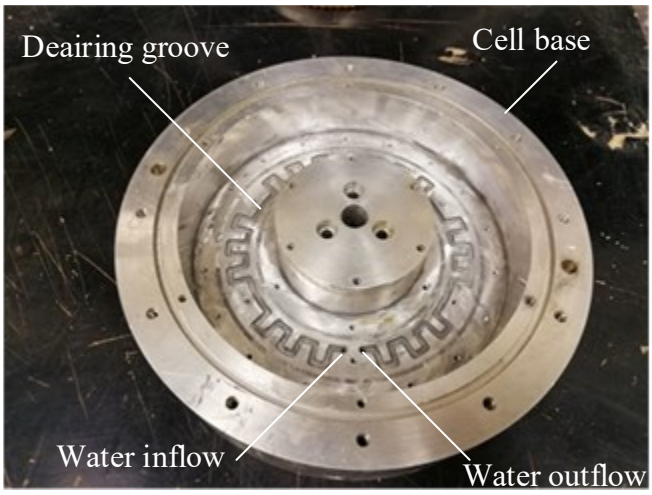

Figure 4.4 Deairing groove

A deairing groove (Figure 4.4) was machined on the cell base under the bottom platen. When the air pressure in the ring shear cell is higher than the atmospheric pressure, the air in the ring shear cell can dissolve into the pore water of the specimen and then cross the ceramic disks through the water phase. The dissolved air comes out from the water phase from the bottom of the ceramic disks due to relatively lower pressure and forms as air bubbles. If these air bubbles were not removed, they would significantly reduce or even break the continuity of the water phase between the ceramic disks and external reservoir. The volume of air bubbles would be treated as the volume of water drained out from the specimen; as a result, the water content of the test specimen would be underestimated. The deairing groove was used to collect the air bubbles below the ceramic disks and flowed them out by using the flushing system. This technique ensured that the system could be full of water during the testing period.

4.2.2.2 Bottom platen

The bottom platen consists of an aluminum ring that is embedded with 18 round high air-entry value ceramic disks of 14 mm dia and 7 mm height (Figure 4.5). The inner diameter of aluminum ring is 74.3 mm, the outer diameter is 150 mm, and the thickness is 8.9 mm. The air-entry value of the ceramic disks is 500 kPa. The bottom platen was placed under the specimen to separate the water phase and air phase for axis translation technique. Prior to performing tests, the ceramic disks should be saturated. Therefore, during tests, the water in the specimen, ceramic disks and

external reservoir were interconnected. Such a provision would ensure the pore water pressure in the specimen remained at atmospheric pressure. However, the air in the ring shear cell cannot flow through the ceramic disks. Thus, a differential pressure could be established between the pore air pressure (i.e., the air pressure in the ring shear cell) and pore water pressure (i.e., the atmospheric pressure), which is the matric suction.

The thickness of the ceramic disks (7 mm) is slightly less than the aluminum ring (8.9 mm). This design feature could increase the shearing resistance at the interface between the bottom platen and bottom surface of the specimen to make the slip surface occur within the specimen. The ceramic disks were fixed on the aluminum ring by using epoxy and following instructions as suggested by Power and Vanapalli (2010). The epoxy was applied in the gap between the ceramic disk and aluminum ring in three layers to ensure a good bonding. The bottom platen was fixed on the cell base by using screws.

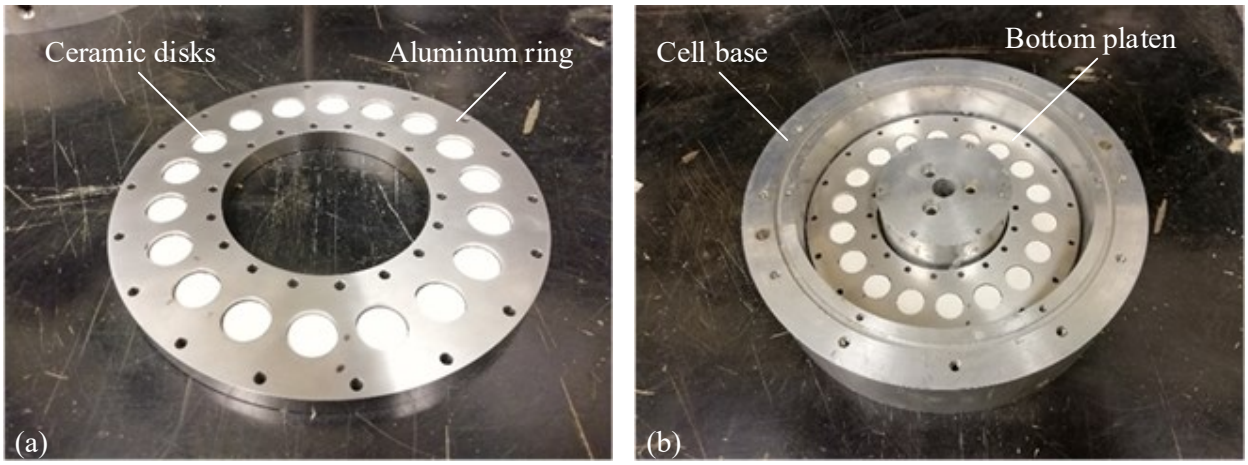

Figure 4.5 Bottom platen of ring shear cell: (a) bottom platen; (b) installation of bottom platen

4.2.2.3 Confining rings

The friction that arises from the annular specimen along the confining walls of the cell contributes to likely errors in the measurement of shear strength using the conventional Bromhead ring shear cell. For alleviating this limitation, two stacks of inner and outer confining rings were used to replace the rigid wall of the cell (Figures 4.6a and 4.6b) to reduce the friction. During ring shear tests, the top surface of the specimen was fixed by the top platen and the bottom surface of the

specimen was subjected to deformation together along with the cell base. In addition, the bottom confining rings were fixed on the cell base using screws (Figure 4.6c) to prevent the slipping between specimen and the bottom platen. Thus, the slip surface could occur at the interface between any two neighboring rings.

Each stack of confining rings consists of one top ring (the thickness is 6 mm) and six normal rings (the thickness is 2 mm). The inner and outer diameter of the inner confining rings is 72.86 mm and 92.18 mm. The inner and outer diameter of the outer confining rings is 130.10 mm and 149 mm. In other words, the inner and outer diameter of the specimen is 92.18 mm and 130.10 mm.

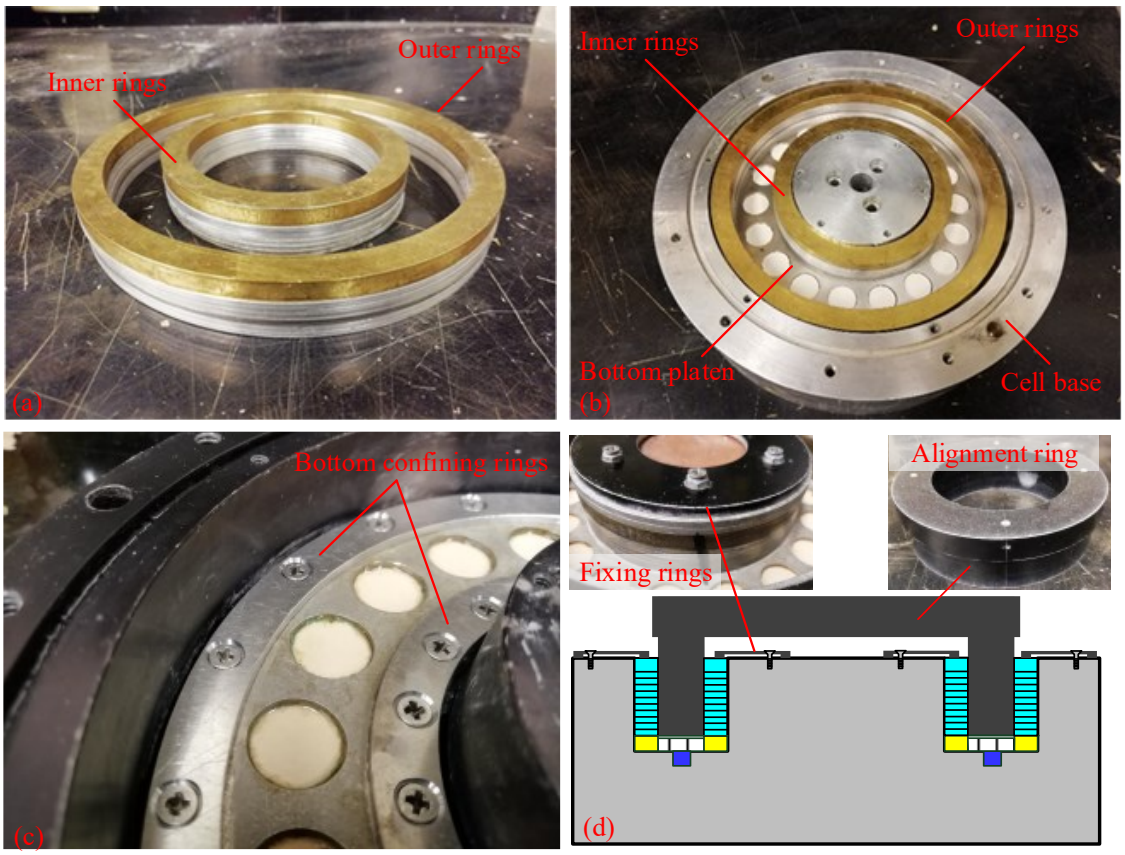

Figure 4.6 Confining rings of ring shear cell: (a) confining rings; (b) installation of confining rings; (c) bottom confining rings; (d) alignment of confining rings

A small quantity of vacuum grease was applied on the surface of the confining rings during the installation of the confining rings. The vacuum grease could seal the gap between the neighboring confining rings to prevent the extrusion of soils during shearing and it could reduce the friction

between the neighboring confining rings at the position of slip surface. In addition, an alignment ring matching the specimen dimensions (Figure 4.6d) was used to ensure the confining rings were perfectly centered. Two rings were fixed on the cell base using screws (Figure 4.6d) that facilitated in applying a pressure on the confining rings to ensure the confining rings were secured and did not move during compaction.

The confining rings were installed in the ring shear cell prior to compacting the specimen into the ring shear cell. A marking line was plotted on the confining rings and cell base (Figure 4.7). After shearing, the specimen at the position of the marking line would be removed carefully. Thus, the position where the neighboring confining rings have significant relative displacement could be determined and it could show the position of the slip surface of the specimen (Figure 4.7).

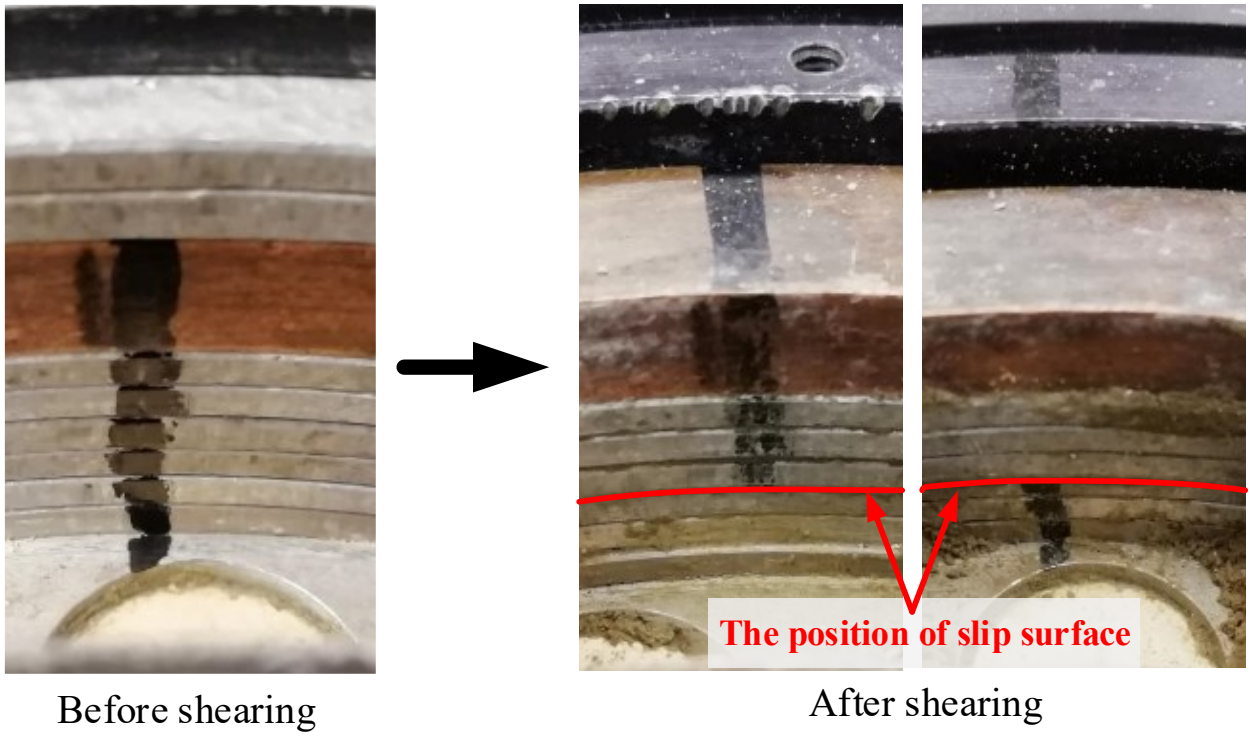

Figure 4.7 Determination of the position of slip surface

4.2.2.4 Top platen

During the ring shear test, the normal stress could be applied via the top platen on the top surface of the specimen. Firstly, a top platen with bronze vanes (Figure 4.8a) was used to conduct a series of ring shear tests on the saturated Indian Head till (IHT) specimens under low normal stress of 10

kPa, 25 kPa and 50 kPa. The experimental results showed that the slip surface sometimes happened at the interface between the top platen and the top surface of the specimen (Figure 4.8a). Such a behavior could be attributed to the vanes on the top platen that cannot penetrate into the specimen under a low net normal stress. In other words, the top platen and the specimen cannot touch tightly during tests. For this reason, the top platen was modifed by gluing coarse sands on the surface of the top platen (Figure 4.8b). This modification could increase the shearing resistance at the interface between the top platen and top surface of the specimen such that the slip surface could occur within the specimen. The experimental results showed that the top platen with coarse sands could work well for the tests under normal stress ≥ 50 kPa.

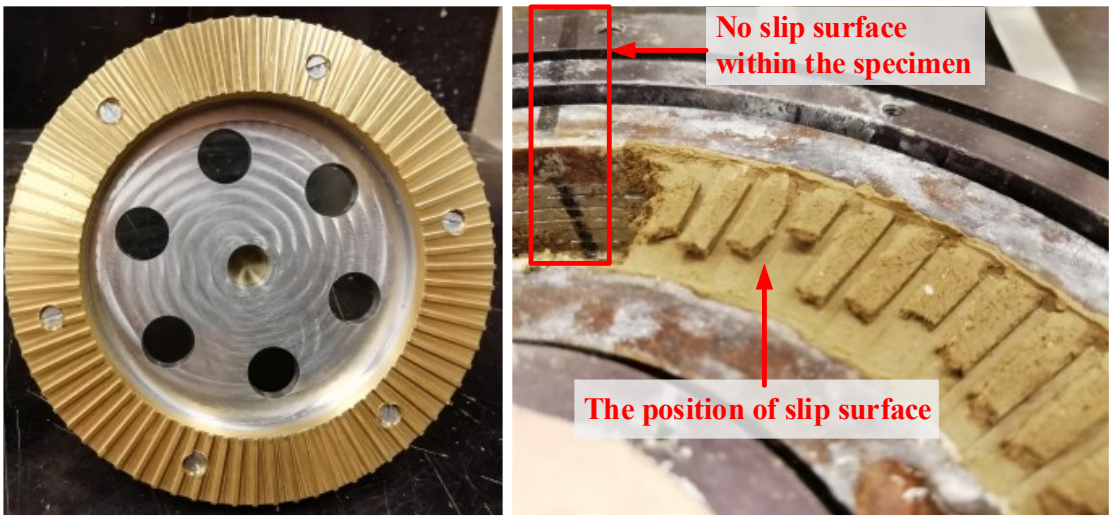

(a) Platen with bronze vanes

(b) Platen with coarse sand

Figure 4.8 Top platens: (a) top platen with bronze vanes; (b) top platen with coarse sand

4.2.2.5 Cell cover

As shown in Figure 4.9, a cell cover was designed on the cell base to create a closed environment. This system facilitated controlling the air pressure in the ring shear cell at a certain value higher than the atmospheric pressure. Two holes were machined on the cell cover. One of them was the air intake hole and the other was connected to an air pressure transducer to facilitate measurement of the air pressure in the ring shear cell directly during the tests.

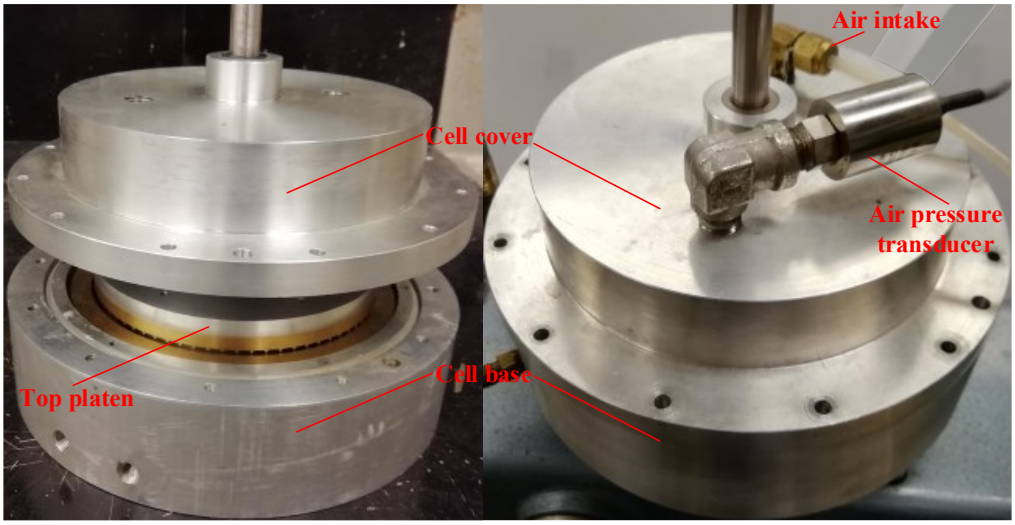

Figure 4.9 Cell cover of ring shear cell

4.2.3 Flushing system

As discussed in section 4.2.2, air bubbles might accumulate in the deairing groove, which would result in the discontinuity of water phase in the system and contribute to errors in the reliable measurement of water content. Therefore, a flushing system was designed to remove the air bubbles. In addition, the flushing system could also be used to measure the mass of water drained out from the specimen.

As shown in Figures 4.10a and 4.10b, the deairing groove was connected to an air trap using soft tubes. Then, the air trap was connected to an overflow jar placed on a precise balance with 0.001g accuracy. During tests, the system remained saturated with deaired water and the valve above the air trap remained closed. This ensured no variation in the water mass in the flushing system during tests. Thus, any water drained out from the test specimen pushed the water into air trap and then

the displaced water moved into the overflow jar. This means the decrement in the water mass in the specimen should be equal to the increment in the water mass in overflow jar.

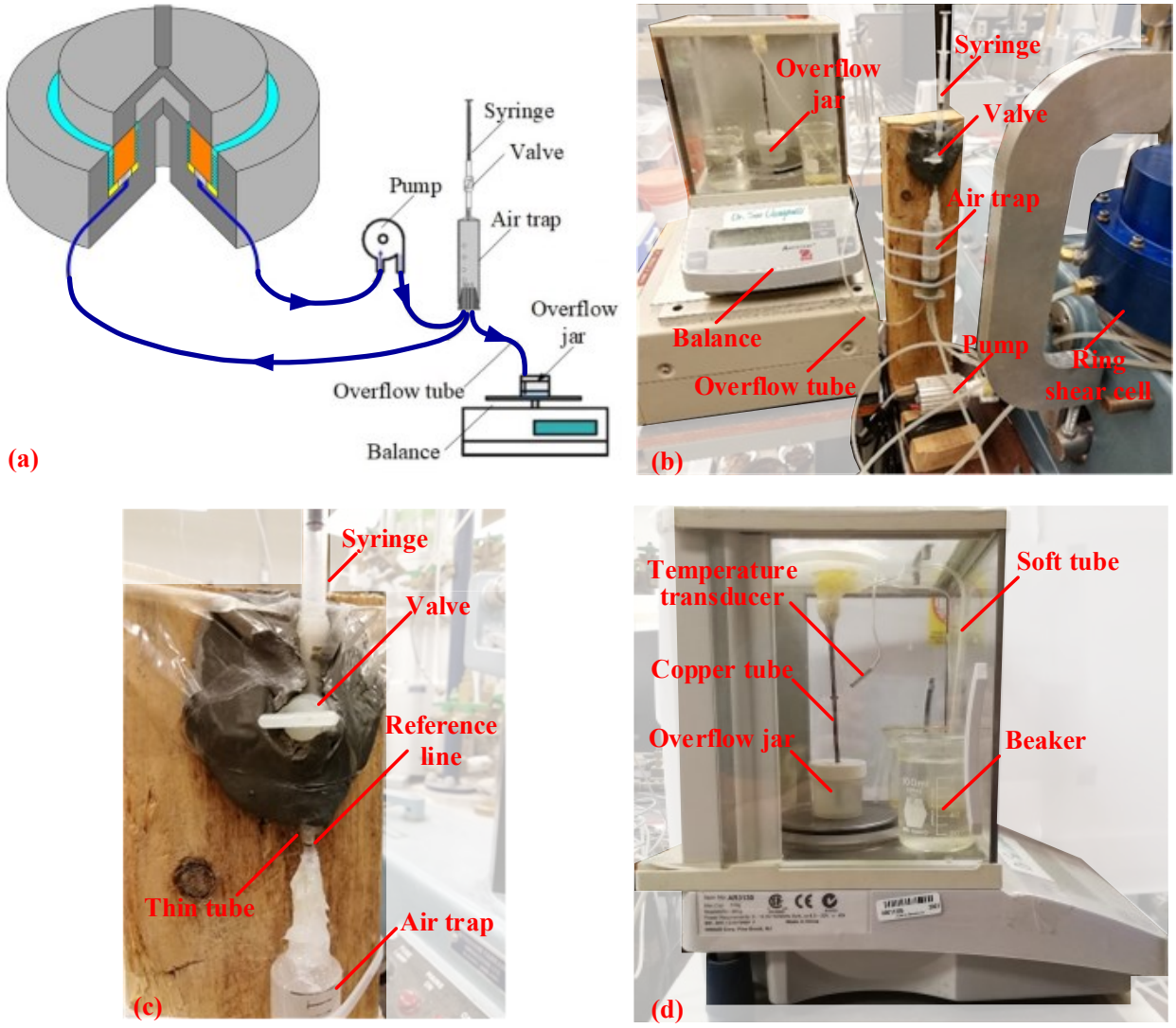

Figure 4.10 Flushing system: (a) diagram of the flushing system (modified after Infante Sedano et al. 2007); (b) picture of the flushing system; (c) air trap of the flushing system; (d) overflow tube and jar of the flushing system

During unsaturated tests, the pump was run at regular intervals to circulate the water between the deairing groove and the air trap. This technique facilitated flushing out the air bubbles in the deairing groove into the air trap. The flushing lasted until there were no air bubbles to come out from the deairing groove.

Figure 4.10c shows more details of the air trap. A thin plastic tube with 2 mm inner diameter was connected to the air trap. This means 1 mm variation in the height of water column in the thin tube is equivalent to 0.003 g variation in the water mass in the overflow jar. A black horizontal line was marked on the thin tube as a reference line. After flushing, the valve would be opened, and the collected air could be removed by the small syringe by adjusting the water level in the thin tube to the reference line. This design facilitated not only flushing out the air bubbles but also towards maintaining the mass of water in the system at a constant value during the tests and consequently avoiding errors in water content measurement.

The reading of the precise balance is sensitive to the variation in the mass of overflow jar. Any minor factor that was transmitted to the overflow jar through the overflow tube (e.g., the moment build-up at the junction between overflow tube and overflow jar, the tremor of overflow tube due to water flowing, the ambient changes and air movements, etc.) could cause unstable readings of the balance. The overflow tube was designed as shown in Figure 4.10d to reduce the influence of these factors. A small hole was made in the lid of the overflow jar. A rigid copper tube was inserted into the overflow jar through the hole in the lid. The diameter of the hole was slightly greater than the outer diameter of the copper tube. Thus, there was no direct touch between the copper tube and the overflow jar, which could avoid the influence of the overflow tube on the readings of the balance. A soft tube was used to connect the copper tube and the air trap. Both the copper tube and soft tube were fixed on the wall of the balance chamber.

The influence of evaporation cannot be alleviated from the overflow jar through the gap between the copper tube and the hole in the jar lid despite eliminating the influence of overflow tube on the readings of balance. Four beakers full of water were placed in the chamber to adjust the humidity in the chamber to reduce the evaporation. In addition, the chamber was sealed by using tape to create a relatively closed environment. The performance of this approach has been checked by measuring the evaporation rate from the overflow jar when the flushing system was empty. The measurement results are shown in Figure 4.11. These results suggest that the evaporation rate was relatively low at about 0.001g/hr.

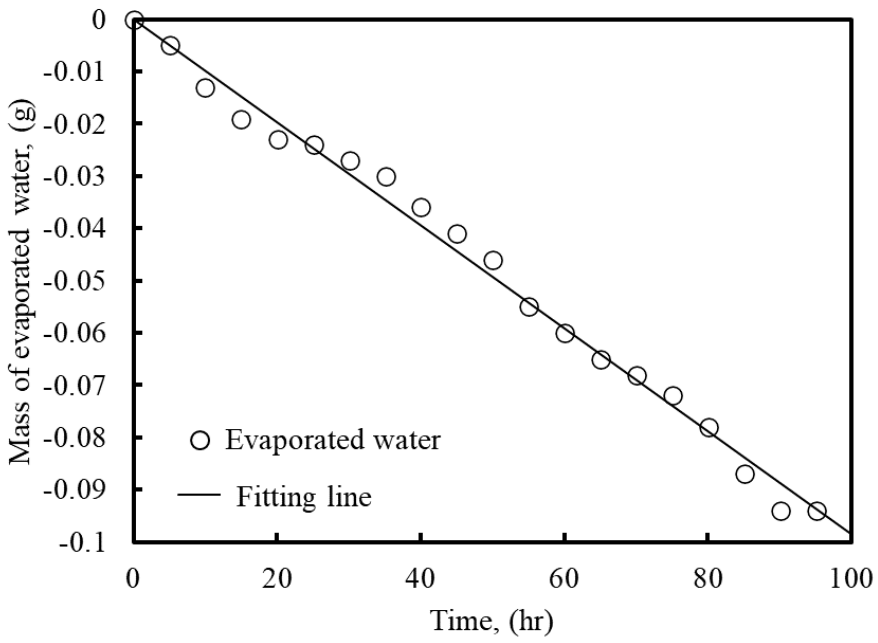

Figure 4.11 Evaporation rate from the overflow jar ('–' sign represents evaporation)

4.2.4 Measuring system and data acquisition

The measuring system consists of the following components:

(1) Two torque load cells (Artech 20210 Load cell, maximum capacity of 250 lbs) were used to monitor the torque applied on the specimen (see Figure 4.2). The shear stress sustained by the specimen could be calculated from the applied torque (Equation 4.1a). In addition, the normal stress on the specimen was assumed to be uniform in this study; thus, the total normal stress on the specimen could be calculated using Equation 4.1b.

$$\tau = \frac{3T}{2\pi\left(r_2^3 - r_1^3\right)} \tag{4.1a}$$

$$\sigma_n = \frac{F_n}{\pi\left(r_2^2 - r_1^2\right)} \tag{4.1b}$$

where τ is the shear stress in the specimen; σ_n is the total normal stress on the specimen; T is the applied torque; F_n is the normal force applied on the specimen top surface through the loading system; r_1 and r_2 is the inner and outer radius of the specimen.

(2) A rotary potentiometer (Nidec Copal JC40S potentiometer) was used to monitor the angular displacement of the ring shear cell with respect to the top platen (see Figure 4.2). Due to the angular shape of the specimen, the shear displacement changed along the radius of the specimen. For this reason, the shear displacement at the mean radius (Equation 4.2) was used to represent the shear displacement of the specimen.

$$\delta = 2\pi \frac{r_1 + r_2}{2} \frac{\theta}{360} \tag{4.2}$$

where δ is the shear displacement at the mean radius (unit: mm); θ is the angular displacement (unit: degree).

(3) A LVDT was used to monitor the vertical displacement of the specimen (see Figure 4.2). The void ratio of the specimen could be calculated from the height of the specimen and initial void ratio.

(4) An air pressure transducer was used to monitor the air pressure in the ring shear cell (see Figure 4.3). The magnitude of the matric suction is equal to the magnitude of air pressure since the pore water pressure remains at zero.

(5) A balance (Ohaus AR3130 balance, maximum capacity of 310 g with a readability sensitivity of 0.001g) was used to monitor the mass of water drained out from the specimen. The water content of the specimen could be calculated from the mass of drained water.

(6) A temperature transducer was installed in the balance chamber (Figure 4.10d) to measure the temperature during the tests. The reading of the temperature transducer was recorded by a camera hourly. The measured results showed the room temperature varied between 21 ºC and 23.5 ºC during the tests.

A data logger was used to collect the data from all the sensors and transferred the data to a computer. A software, LabView, was used to record and visualize the data in real time.

4.3 Test material

The soils used in the ring shear tests included a fine sand and Indian Head till (IHT). The physical and hydraulic properties of the tested soils have been measured and presented below.

4.3.1 Basic soil properties

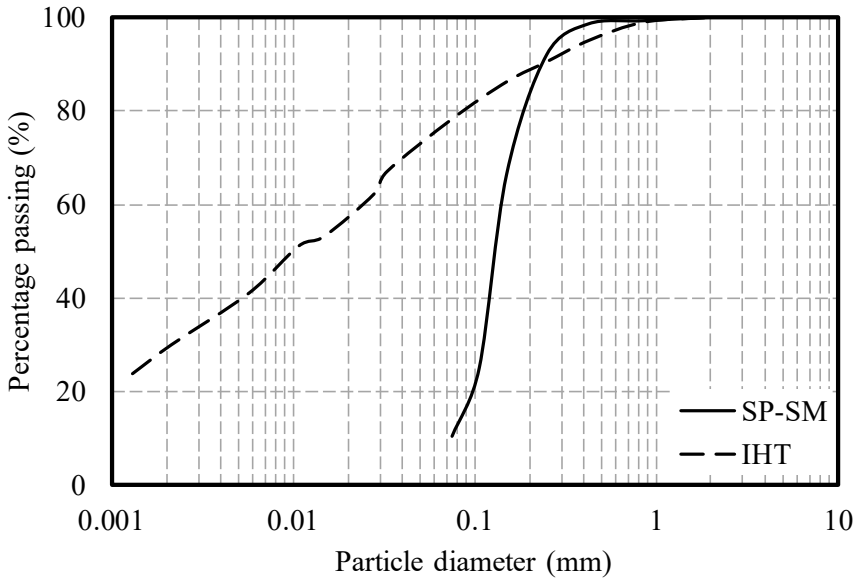

Figure 4.12 Grain size distribution of the tested soils

The specific gravity of the sand was determined as 2.75 according to ASTM D854–14. The grain size distribution of the sand was obtained by performing seive analysis test according to ASTM D6913–17. The grain size distribution curve was shown in Figure 4.12. This sand can be classified as poorly graded sand with silt (SP-SM) according to ASTM D2487–06.

The basic properties of the IHT have been measured and reported by Ren (2019). The specific gravity, plastic limit and liquid limit of the IHT are 2.72, 17% and 36%, respectively. The grain size distribution curve is shown in Figure 4.12. The IHT can be classified as lean clay (CL) according to ASTM D2487–06.

4.3.2 Static compaction

The specimens for the suction-controlled ring shear tests were prepared by static compaction. Therefore, a series of static compaction tests were conducted on the SP-SM and IHT specimens

with various water contents to study the static compaction behavior of the tested soils. The static compaction tests were conducted using the apparatus shown in Figure 4.13. The procedures of static compaction are summarized below.

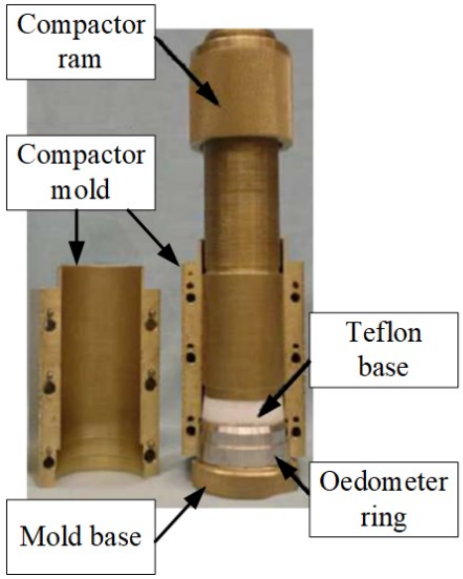

Figure 4.13 Apparatus for static compaction

(i) The soil was prepared by mixing the dry soil powder with an appropriate amount of distilled water. Then the prepared soil was placed into a plastic bag and left to stand for at least 24 hours to ensure moisture reaches equilibrium condition.

(ii) The mass of the oedometer ring and mold base should be weighed and recorded prior to compaction. Then, the apparatus for static compaction could be assembled by screws.

(iii) The prepared soil was placed loosely into the compactor mold. The amount of prepared soil placed into the mold should be estimated to ensure the final height of the compacted specimen can be slightly greater than that of an oedometer ring. Then, the compactor ram could be inserted into the compactor mold and an unconfined compression apparatus was used to apply pressure on the compactor ram. During the compaction, the compaction pressure was applied slowly until a maximum pressure of 375 kPa, which was applied for 1 minute.

(iv) After completion of compaction, the compactor mold was disassembled. The amount of soil that protruded from the oedometer ring should be removed carefully. Then, the mass of the mold

base and the oedometer ring containing the compacted specimen could be measured and recorded. Thus, the density of the compacted specimen could be calculated.

(v) The compacted specimen was removed from the oedometer ring to measure the water content of the specimen. The dry unit weight of the specimen could be calculated based on its bulk density, water content and specific gravity.

(vi) The compaction process was repeated for various soils prepared at different water contents. Eventually, a relationship between the dry unit weight and the water content of compacted specimen could be obtained.

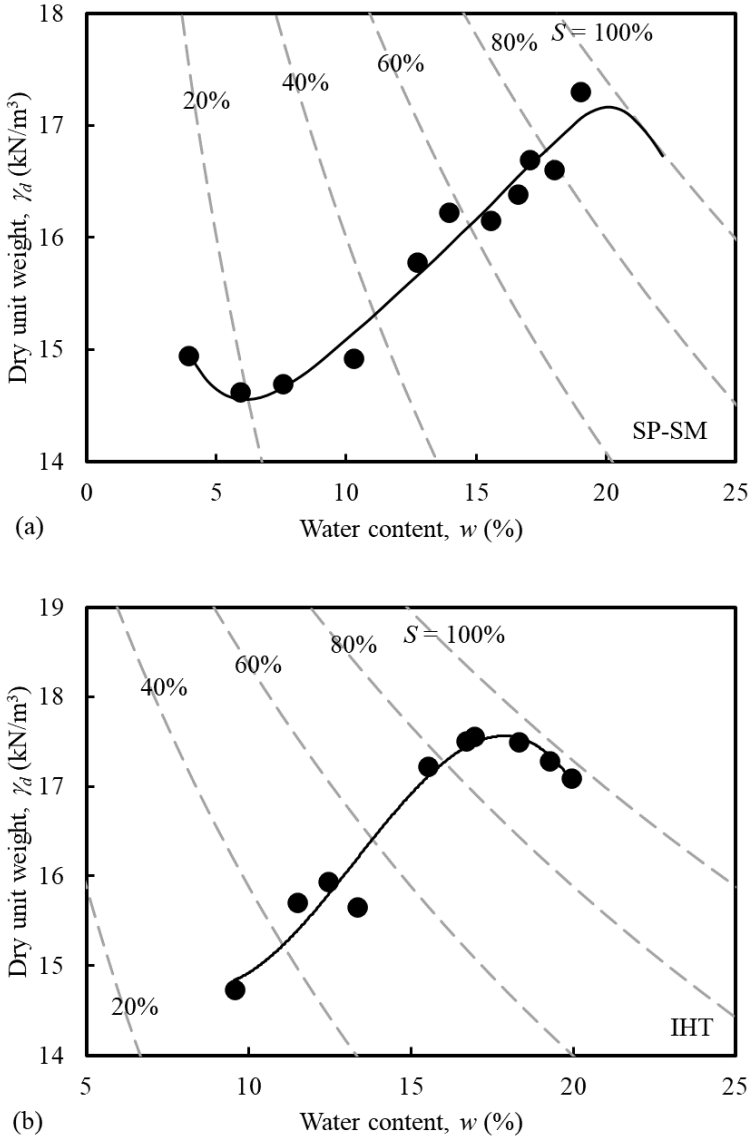

Figure 4.14 Static compaction curve of tested soils: (a) SP-SM; (b) IHT

Figure 4.14 shows the static compaction curves of the tested soils. At relatively low water contents, the dry unit weight of the SP-SM decreases with an increase in water content. As indicated by Singh (1984), this decrease may be due to the capillary tension which is not fully counteracted by the compactive effort and holds the particles in a loose state resisting compaction. After that, the unit weight will increase with increasing water content due to the reduction of effective pressure between soil particles by hydraulic pressure.

4.3.3 Soil-water characteristic curve (SWCC)

The SWCC of the SP-SM was measured by hanging column test. As shown in Figure 4.15, a saturated compacted specimen was placed on a ceramic disk in a sealed chamber. Below the ceramic disk, a groove was machined on the base of the chamber which facilitated movement of water and acted as a reservoir. The groove was connected to a measuring tube (the diameter is 6.47 mm) by using the outflow tube. The chamber was placed on a plate which could go up and down along the vertical slideway by using a pulley fixed on the roof. During tests, the system (i.e., the groove, the outflow tube and measuring tube) was full of water. When the chamber was elevated to a certain elevation, the suction could be calculated from the elevation difference between the specimen and the air-water interface in the measuring tube. The volume of water drained from the specimen could be calculated from the movement of the air-water interface in the measuring tube. The procedures of hanging column test are summarized below.

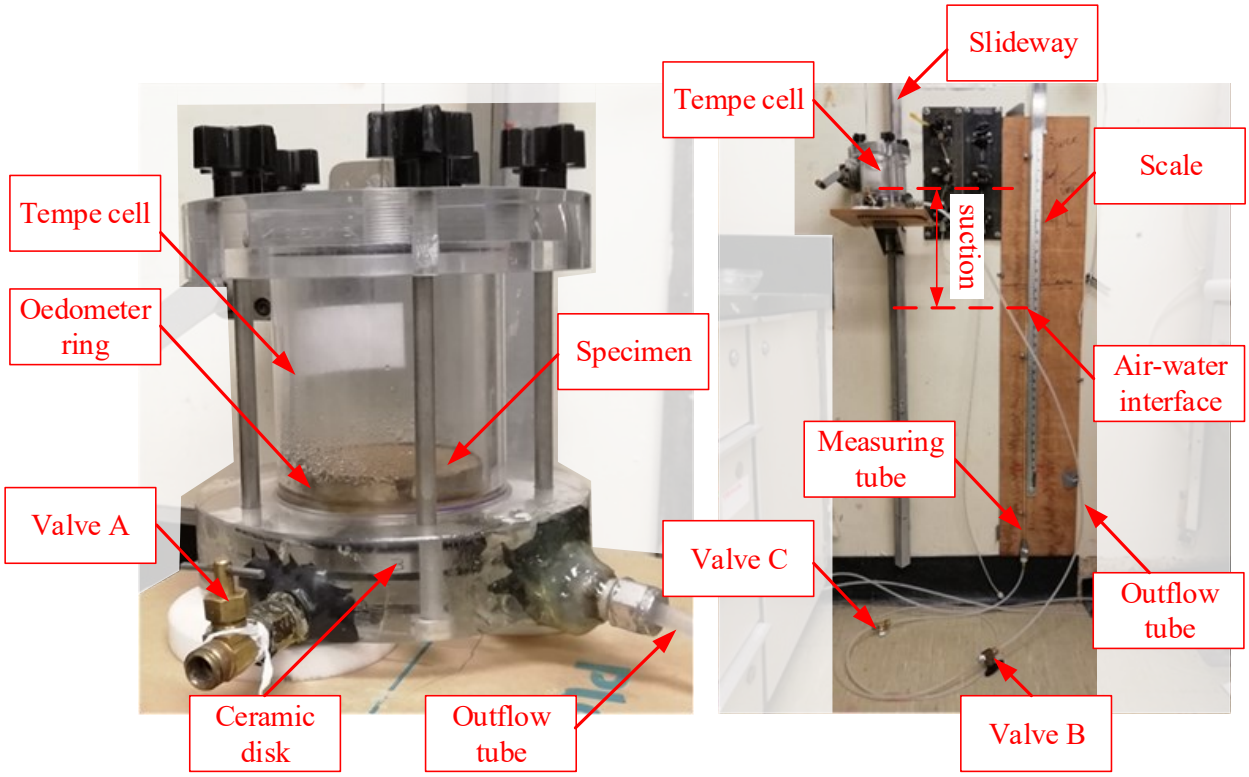

Figure 4.15 Hanging column apparatus

(i) The soil with 20% water content was prepared by mixing the dry soil powder with an amount of distilled water. The prepared soil was placed into a plastic bag and left to stand for at least 24 hours to ensure moisture reaches equilibrium condition.

(ii) The specimen was compacted statically following step ii through step iv in section 4.3.2. If the compacted specimen was lower than the oedometer ring, the height of the compacted specimen should be measured.

(iii) The ceramic disk should be saturated in advance by soaking in distilled water for at least 24 hours. Some distilled water was added into the chamber base to ensure the groove was full of water. The saturated ceramic disk was placed into the chamber base carefully to prevent the generation of air bubbles. Then, the specimen was placed on the ceramic disk and the chamber was assembled.

(iv) The assembled chamber was connected to the outflow tube with valve A, B and C closed. The system should be checked carefully; if there were air bubbles, valve A and B should be opened with valve C closed. A large syringe was used to add water into the system from valve A; thus, the

air bubbles could be flushed out into the measuring tube and finally go into the air. After flushing, valve A should be closed with valve B remaining open. If there was too much water in the measuring tube, valve C would be opened to remove the extra water in the measuring tube.

(v) In order to saturate the specimen, the chamber was lowered to the bottom of the slideway to ensure the specimen was lower than the air-water interface in the measuring tube. The specimen was considered saturated when water was observed on the top surface of the specimen. After saturation, the specimen was raised to the same elevation as the air-water interface in the measuring tube. The position of the specimen should be adjusted until the air-water interface in the measuring tube had no further movement and was at the same elevation as the midpoint of the specimen. Finally, this position of the specimen and air-water interface was recorded and treated as datum during tests.

(vi) The first increment of suction was applied by elevating the specimen. The first increment in suction should not exceed the air-entry value of the specimen. Thus, the first increment in the elevation of specimen was 50 mm which is equivalent to 0.5 kPa suction. The location of the air-water interface was monitored regularly until the movement of the air-water interface ceased for 24 hr. The locations of the specimen and the air-water interface with respect to the datum were recorded after ensuring equilibrium conditions.

(vii) The next increment in suction was applied using the same procedure as described in step vi. The increment in the elevation of specimen remained 50 mm. The air-entry value of the specimen was exceeded when the air-water interface went up after elevating the specimen. After that, the increment in elevation of specimen could be increased. This step was repeated until the specimen cannot be elevated any more.

(viii) The chamber was disassembled, and the specimen was retrieved. The mass of the specimen was measured. Then, the specimen was dried using an oven and the mass of the dried specimen was measured.

(ix) The SWCC could be determined based on the values of the suction and corresponding water contents. Figure 4.16 shows the measured SWCC of SP-SM.

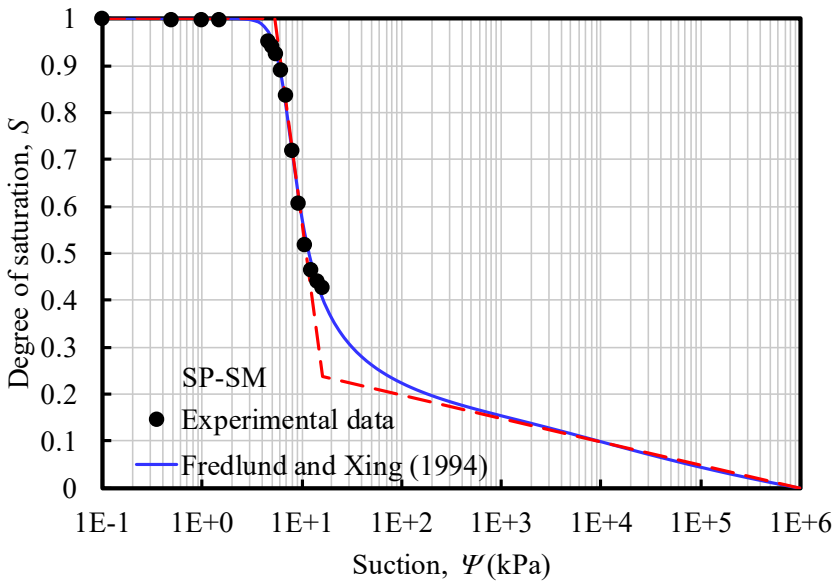

Figure 4.16 Soil-water characteristic curve of SP-SM

All the IHT specimens in this study were prepared with a water content of 15%, that is lower than the optimum water content based on the static compaction curve (i.e., 18%) (Figure 4.14b). Infante Sedano (2006) measured the SWCC of the IHT specimens which were statically compacted at an initial water content of 15% (Figure 4.17); thus, the experimental data generated by Infante Sedano (2006) were also used for interpreting the SWCC of the tested IHT soil in this study.

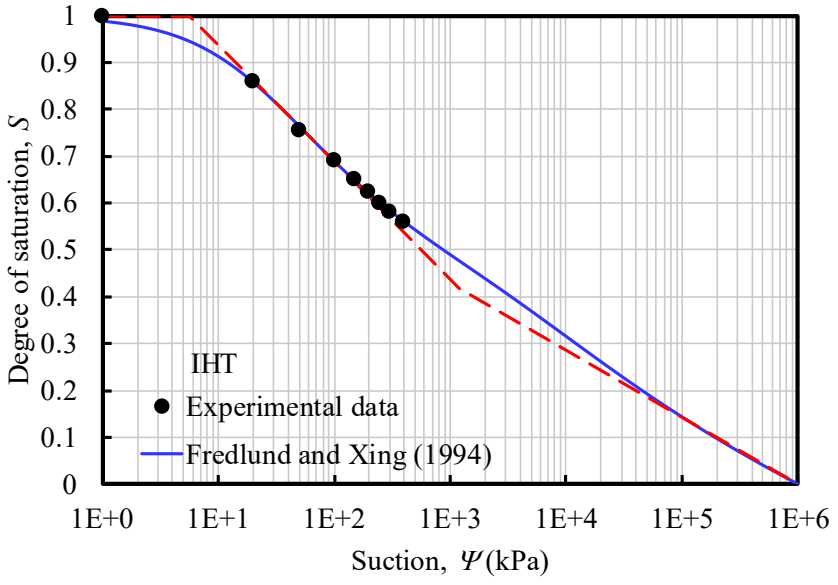

Figure 4.17 Soil-water characteristic curve of IHT (modified after Infante Sedano 2006)

4.4 Testing program and procedures

4.4.1 Testing program

The ring shear tests on SP-SM and IHT in this study were conducted under constant matric suction and net normal stress. The selected values of matric suction and net normal stress for SP-SM and IHT specimens are shown in Tables 4.1 and 4.2, respectively.

Table 4.1 Testing program of SP-SM

Test	σ_n (kPa)	u_a (kPa)	u_w (kPa)	$(\sigma_n - u_a)$ (kPa)	$(u_a - u_w)$ (kPa)	Stages of test
SP-SM1	10	0	0	10	0	Single stage
SP-SM2	25	0	0	25	0	Single stage
SP-SM3	50	0	0	50	0	Single stage
SP-SM4	15	2.5	0	12.5	2.5	Multistage
	30	2.5	0	27.5	2.5	
	55	2.5	0	52.5	2.5	
SP-SM5	25	7.5	0	17.5	7.5	Multistage
	40	7.5	0	32.5	7.5	
	65	7.5	0	57.5	7.5	
SP-SM6	30	10	0	20	10	Multistage
	45	10	0	35	10	
	70	10	0	60	10	

Table 4.2 Testing program of IHT

Test	σ_n (kPa)	u_a (kPa)	u_w (kPa)	$(\sigma_n - u_a)$ (kPa)	$(u_a - u_w)$ (kPa)	Stages of test
IHT1	50	0	0	50	0	Single stage
IHT2	100	0	0	100	0	Single stage
IHT3	150	0	0	150	0	Single stage
IHT4	100	25	0	75	25	Multistage
	150	25	0	125	25	
	200	25	0	175	25	
IHT5	250	100	0	150	100	Multistage
	300	100	0	200	100	
	350	100	0	250	100	
IHT6	550	250	0	300	250	Multistage
	600	250	0	350	250	
	650	250	0	400	250	
	750	250	0	500	250	

The selection of matric suction values was based on the SWCC. As shown in Figure 4.16, the air entry value, matric suction at inflection point and residual suction of SP-SM are equal to 5.30 kPa, 7.94 kPa, 15.95 kPa, respectively. Thus, 2.5 kPa, 7.5 kPa and 10 kPa were selected, which are within boundary effect zone, primary transition zone and secondary transition zone of the SWCC, respectively. Several low net normal stresses (i.e., 10 kPa – 60 kPa) were selected considering most of engineering problems associated with unsaturated soils occur within a shallow depth under the ground surface.

As shown in Figure 4.17, the air entry value, the air entry value, matric suction at inflection point and residual suction of IHT are equal to 5.67 kPa, 50.12 kPa, 1194.52 kPa. Thus, 25 kPa, 100 kPa and 250 kPa were selected, which are within primary transition zone and secondary transition zone of the SWCC. Several ring shear tests on saturated IHT specimens were conducted under a low net normal stress of 10 kPa and 25 kPa. However, the slip surface always happened at the interface between the top surface of specimen and the top platen. For this reason, several net normal stress higher than 50 kPa were selected for the ring shear tests on IHT specimens.

For saturated specimens, single stage tests were conducted to capture full stress-strain relationships under different normal stress. The ring shear tests on unsaturated soil specimens, however, are always time consuming. Some researchers (Vaunat et al. 2006; Vaunat et al. 2007; Hoyos et al. 2014) have shown the residual shear strength of unsaturated soils is independent on the pre-shearing history experienced by the soil. Therefore, multistage tests were conducted on the unsaturated soil specimens to shorten the testing period. The procedures of the single stage and multistage tests will be discussed in the following sections.

4.4.2 Specimen preparation

All the specimens for ring shear tests were compacted using the soil described in section 4.3. The soil was prepared by mixing the dry soil powder with an appropriate amount of distilled water. The prepared soil was placed into a plastic bag for at least 24 hours to ensure moisture reaches equilibrium condition. The SP-SM soil was prepared with water content of 18%. Thus, the corresponding dry unit weight of the statically compacted SP-SM specimens is equal to 16.5 kN/m^3 (Figure 4.14a) and the mass of one specimen is 236.50 g. The IHT soil was prepared with water

content of 15%. Thus, the corresponding dry unit weight of the statically compacted IHT specimens is equal to 16.77 kN/m^3 (Figure 4.14b) and the mass of one specimen is 241.87 g.

The ceramic disks on the bottom platen were saturated using deaired water by connecting a water reservoir to the inflow and outflow holes on the ring shear cell base, prior to compacting the specimen. The deaired water could flow from the water reservoir to the deairing groove on the cell base and then flow into the ring shear cell through the ceramic disks. A pressure of 20 kPa was applied in the water reservoir to accelerate the saturation process.

After saturation of ceramic disks, the specimens were statically compacted into the ring shear cell. The compaction apparatus for ring shear test specimen is shown in Figure 4.18. After placing the prepared soil for testing into the ring shear cell, the alignment ring, which has similar dimensions with the specimen, was inserted into the ring shear cell. The compactor ram was placed on the alignment ring to transfer the compaction pressure. The protruded part of the compactor ram is consistent with the central hole of the compactor ring to avoid eccentric loading.

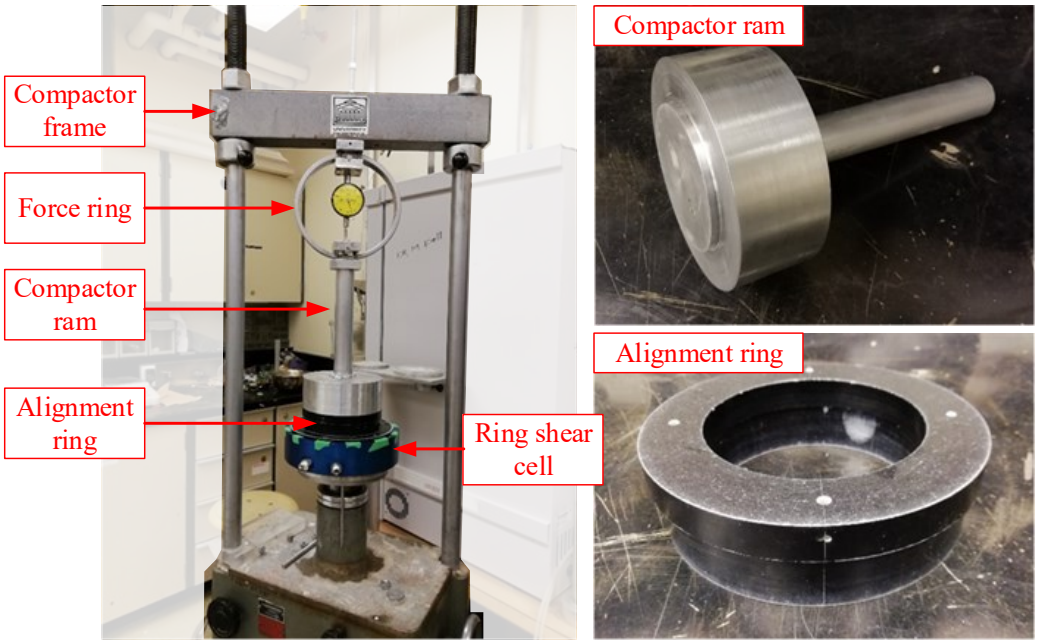

Figure 4.18 Compaction apparatus for ring shear testing specimen

The SP-SM specimens were compacted in three layers. In order to prevent the interface between two layers from being at the same level with the interface between two confining rings, the thickness of three layers after compaction were selected as 7 mm, 7 mm and 4 mm respectively.

Extending the same preparation technique, the IHT specimens were compacted in six layers each of which had a thickness of 3 mm. For the compaction of each layer, the compaction pressure was applied slowly until a maximum pressure of 375 kPa was applied, which was then maintained for 1 minute. After compacting each layer, the surface of the compacted layer was scarified to prevent the slip surface from occurring at the interface between two layers during shearing.

After compaction of the specimen, the ring shear cell was installed on the ring shear frame. The top platen was placed on the specimen and the cell cover was installed but not fixed on the ring shear cell to avoid evaporation from the specimen. The water reservoir was connected again to the ring shear cell and a pressure of 20 kPa was applied in the water reservoir to saturate the specimen. The specimen was considered saturated when there was water extruding on the surface of the specimen.

4.4.3 Suction equilibrium stage

For shortening the testing period, the suction equilibrium stage of one unsaturated soil specimen was conducted at the same time with the previous ring shear test. For example, when the ring shear test IHT3 was being conducted, the suction equilibrium stage of the specimen for the test IHT4 was also conducted at the same time. Similarly, when the ring shear test IHT4 was being conducted, the suction equilibrium stage of the unsaturated specimen for the test IHT5 was conducted at the same time.

For this purpose, three ring shear cells (shown as Figure 4.3) have been machined and a separate apparatus for desaturation was used (Figure 4.19). Therefore, at the same time with the ring shear test on one specimen, another specimen was prepared using a different ring shear cell and suction equilibrium was achieved using the apparatus for desaturation for the next ring shear test. During suction equilibrium stage, the predetermined air pressure was applied, while no net normal stress was applied. The air pressure applied in the ring shear cell was measured by an air pressure gauge and controlled by an air pressure valve. A flushing system (including the pump, air trap, tube indicator and soft tubes) was designed to remove the air bubbles accumulating in the deairing groove every 24 hours. The suction equilibrium was considered achieved when the height of water column in the tube indicator did not change any more.

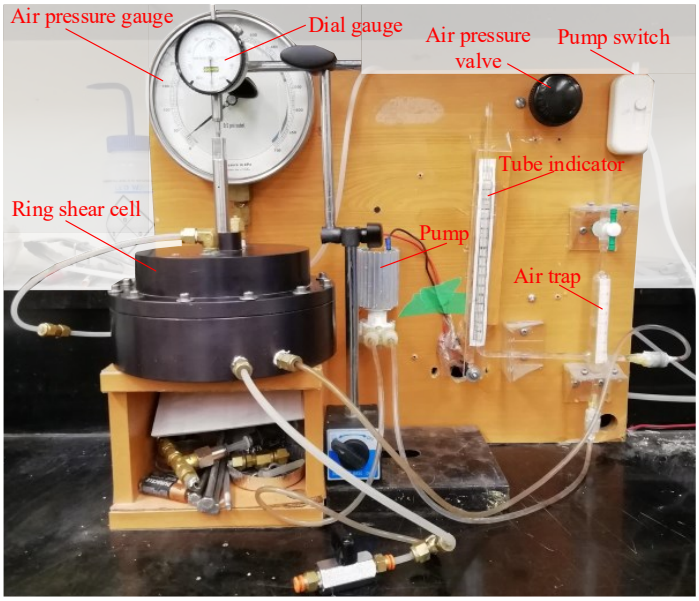

Figure 4.19 Apparatus for desaturation of specimens

4.4.4 Consolidation stage

For the tests on saturated specimens, the ring shear cell was installed on the ring shear frame after the saturation of the specimen. Then, the pre-determined normal stress (shown in Tables 4.1 and 4.2) was applied on the specimen. The specimen was considered to have achieved equilibrium condition when there was no further change in the vertical displacement.

For the tests on unsaturated specimens, the ring shear cell was installed on the ring shear frame after the unsaturated specimen reached suction equilibrium under the predetermined air pressure following the procedures in section 4.4.3. Then, the pre-determined air pressure was applied in the ring shear cell and the first stage net normal stress was applied on the specimen (shown in Tables 4.1 and 4.2). The vertical displacement and mass of water in the overflow jar were monitored in real time. The specimen was considered to reach equilibrium condition when there was no further change in the vertical displacement and water mass drained from the specimen. During the consolidation stage, the system was flushed every 24 hours to remove the air bubbles accumulating in the deairing groove.

4.4.5 Shearing stage

After the consolidation stage, the ring shear cell was turned clockwise to shear the specimen. All the ring shear tests were conducted under constant net normal stress and matric suction at a rotational speed of 0.024 °/min, which is equivalent to a horizontal displacement rate of 0.048 mm/min. This shearing speed is similar to most ring shear tests on unsaturated soils (Infante Sedano 2006; Velosa 2011; Hossain 2013). The specimens were sheared to a shear displacement of 100 mm in each stage.

For multistage tests on unsaturated specimens, after completion of the first-stage shearing, the shear stress was unloaded. The next level of normal stress was applied by adding more weights in the loading bucket, while the air pressure remained unchanged. The specimen was assumed to have reached equilibrium condition when there was no further change in vertical displacement and there was no more water mass that drained from the specimen. Then, the specimen was sheared again to a 100 mm shear displacement. Throughout the shearing stage, the system was flushed at 24 hours intervals to remove the air bubbles that accumulated in the deairing groove.

Each of multistage suction-controlled ring shear tests typically needed around 10 to 12 weeks for completion.

4.5 Corrections

4.5.1 Corrections to water mass versus time curve

As discussed above, the infiltrated air accumulating in the deairing groove was flushed out at set intervals during the testing period. After flushing, the air bubbles collected in the air trap were removed using the small syringe, which could cause a sudden decrease in the readings of the water mass in the overflow jar. Therefore, a correction is required to create a continuous line of the water mass readings without the influence of infiltrated air.

In addition, the evaporation, occurring in the balance chamber and ring shear cell, could also influence the water mass readings. Firstly, the water in the overflow jar could evaporate through the gap between the copper tube and the hole on the lid (see section 4.2.3). For this reason, the balance chamber was sealed by tapes and four beakers filled with water were placed in the chamber

to adjust the humidity. Secondly, air leakage happened during the testing period through the holes on the cell base (Figure 4.4) and the gaps at the joints between different components. The air leakage led to a continuous flow of air into the ring shear cell to keep a constant air pressure, which caused the evaporation from the specimen. The holes on the cell base were sealed using silicone to limit the air leakage. A bushing was used to seal the gap between the cell cover and torque rod. The thread seal tape was used for each connector. A wetting bottle was used to wet the air flowing into the ring shear cell (Figure 4.2). Despite these prevention measures, the influence of evaporation on the measured readings cannot be eliminated completely. Therefore, a correction is required to the water mass readings to remove the influence of evaporation.

Figure 4.20a illustrates the approach for correcting the water mass versus time curve. In this figure, the line with solid circles represents the original data obtained from experiments. The air bubbles are flushed between point 2 and point 3. The correction to the water mass readings for air infiltration and evaporation can be conducted as follows:

(i) Before correction, a continuous line (i.e., 1′ – 2′ – 3′ in Figure 4.20a) should be obtained from the original data. For this purpose, the increase rate of water mass from 2′ to 3′ is assumed to be equal to that from 1 to 2 as shown below:

$$\frac{m_{w,3'} - m_{w,2}}{t_3 - t_2} = \frac{m_{w,2} - m_{w,1}}{t_2 - t_1} \tag{4.3}$$

where t is the time; m_w is the water mass reading; i and i' represent the number of the points on original line and continuous line.

(ii) Correction for infiltration: It is assumed that the infiltration of air through the ceramic disks happens at a fixed rate during the period between two successive flushing. Thus, the infiltration rate, R_{inf}, can be defined as the ratio of the reduction in water mass reading after flushing to the time between two successive flushing. The continuous line in step (i) can be corrected by using Equation 4.4 to obtain the corrected line for air infiltration (i.e., 1″ – 2″ – 3″ in Figure 4.20a).

$$m_{w,i''} = m_{w,(i-1)''} + \left(\frac{m_{w,i'} - m_{w,(i-1)'}}{t_{i'} - t_{i'-1}} - R_{\inf} \right) \left(t_{i'} - t_{(i-1)'} \right), \quad R_{\inf} = \frac{m_{w2} - m_{w3}}{t_3 - t_0} \tag{4.4}$$

where i'' is the number of points on the corrected line for infiltration.

(iii) Correction for evaporation: It is assumed that the evaporation happens at a fixed rate throughout one ring shear test (including equilibrium and shearing stage). The evaporation rate, R_{evp}, can be determined from the water mass versus time curve of the equilibrium stage that has been corrected for infiltration. As shown in Figure 4.20b, at the later stage of the equilibrium, the water mass versus time curve exhibits a linear decrease which can be attributed to the evaporation. Thus, the slope of the linear part of the water mass versus time curve at the later stage of the equilibrium can be used as the evaporation rate. The same evaporation rate is also used to correct the water mass versus time curve at the shearing stage of the same ring shear test. The continuous line in step (i) can be corrected by using Equation 4.5 to obtain the corrected line for both the infiltration and evaporation.

$$m_{w,i'''} = m_{w,(i-1)'''} + \left(\frac{m_{w,i'} - m_{w,(i-1)'}}{t_{i'} - t_{i'-1}} - R_{\inf} + R_{evp} \right) \left(t_{i'} - t_{(i-1)'} \right) \tag{4.5}$$

where i''' is the number of points on the corrected line for evaporation.

Figure 4.20b can serve as an example of the corrections to the water mass versus time curve of suction-controlled ring shear tests. This figure shows the variation of water mass readings during the equilibrium stage of the ring shear test SP-SM6 under (u_a - u_w) = 10 kPa and (σ_n – u_a) = 20 kPa. A total of 300 hours was required for achieving equilibrium stage.

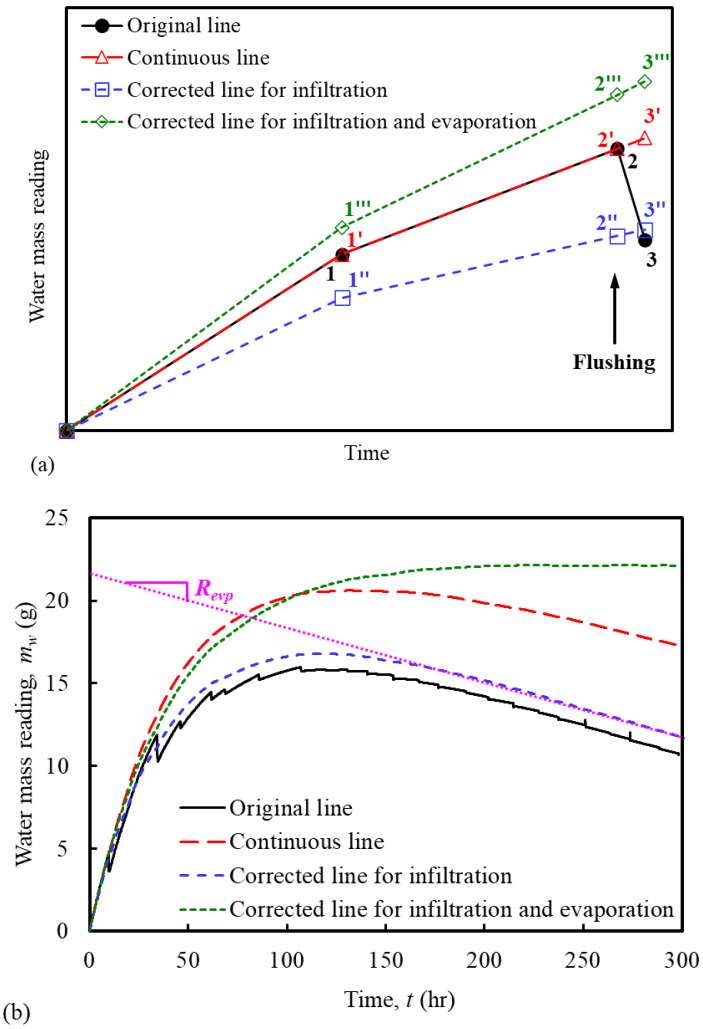

Figure 4.20 Corrections to water mass versus time curve: (a) schematic for corrections; (b) evaporation rate (equilibrium stage of SP-SM6 under (u_a - u_w) = 10 kPa and (σ_n – u_a) = 20 kPa)

4.5.2 Corrections to shear stress versus shear displacement curve under large shear deformation

Figure 4.21 shows the typical shear stress-shear displacement (τ – δ) curves and vertical displacement-shear displacement (δ_v – δ) curves of suction-controlled ring shear tests. It can be found the shear stress increases again at large shear displacement after it has been relatively constant. The variation in shear stress was also associated with a further decrease in the height of the specimen at large shear displacement. The shear strength of specimens in drained tests is

typically dependent on the soil behavior in the shear zone of the specimen. The behavior of soils on either side of the shear zone does not influence the shear strength of specimens in drained tests.

As suggested by Fredlund et al. (1978), the shear strength of unsaturated soils consists of three parts (Equation 2.1; i.e., $c'' + (\sigma_n - u_a)\tan\phi^a + (u_a - u_w)\tan\phi^b$). c'' is typically zero under large shear deformation after critical or residual state is reached. $(\sigma_n - u_a)$ and $(u_a - u_w)$ are constant in drained condition. Therefore, the increase in shear stress under large shear deformation may possibly be due to the increase in ϕ^a and ϕ^b of soils in shear zone. However, ϕ^a of soils in shear zone is reduced due to the reorientation of clayey particles under large shear deformation. ϕ^a of soils cannot increase again after the completion of reorientation of particles. The specimen is compressed to a relatively steady state after the shear displacement of 50 mm (Figure 4.21a). Thus, it is not reasonable that the specimen would be compressed again with further shearing while the net normal stress and the matric suction remain constant. In other words, only minor volume change in shear zone may likely occur under large shear deformation. The water content of soils in shear zone is typically reduced due to the rupture of water menisci under continuous shearing. Therefore, ϕ^b of soils in shear zone that is related to the degree of saturation (wG_s/e) would decrease under large shear deformation. Due to these reasons, a further decrease in shear stress should be expected under large shear deformation (e.g., from 50 mm to 100 mm shear displacement in Figure 4.21a). This means the increase in shear stress under large shear deformation in the suction-controlled ring shear tests with constant net normal stress and matric suction may be associated with measurement error rather than the material behavior.

This phenomenon can mainly be attributed to the extrusion of the soil sheared to a large displacement. As shown in Figure 4.22, when the specimen was sheared to a large displacement, the soil would be extruded from the gap between two adjacent confining rings at the position of the slip plane. Despite the application of vacuum grease on the surface of rings for sealing the gaps, the extrusion of soils cannot be avoided completely. In addition, during the long testing time (around 10 weeks for one multistage test on unsaturated specimen), mold was generated on the surface of the confining rings at the position of the slip plane (Figure 4.22), which could also increase the friction between the two rings. Due to these reasons, the measurement of the shear stress and the vertical displacement of specimens sheared at large shear displacement was influenced; thus, it is hard to exactly determine the residual shear strength and the void ratio at

residual state of unsaturated specimens from the experimental curves. Similar problems caused by the extrusion of soils were also widely observed in other ring shear tests on saturated and unsaturated soils (Bishop et al. 1971; Stark and Vettel 1992; Meehan et al. 2007; Velosa 2011).

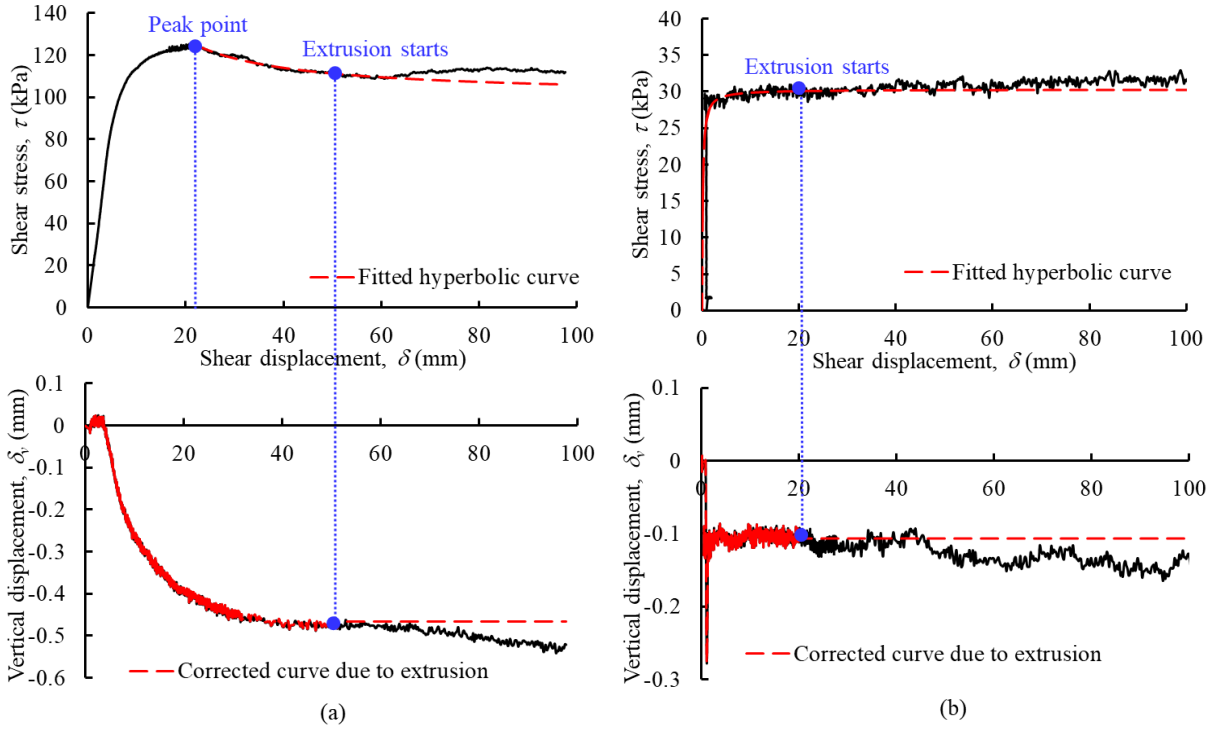

Figure 4.21 Corrections to the shear stress-shear displacement curves: (a) strain-softening curve (IHT5: $(u_a - u_w)$ = 100 kPa, $(\sigma_n - u_a)$ = 150 kPa); (b) strain-hardening curve (SP-SM5: $(u_a - u_w)$ = 7.5 kPa, $(\sigma_n - u_a)$ = 57.5 kPa). The negative value of vertical displacement represents compression.

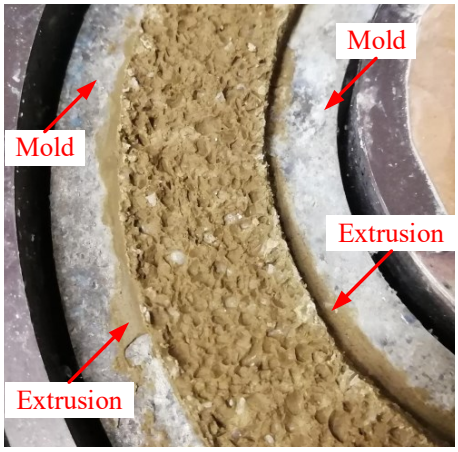

Figure 4.22 Extrusion of soils sheared to a large displacement and mold on confining rings during suction-controlled ring shear tests

An approximate method is proposed to determine the residual shear strength and the void ratio at residual state of unsaturated soils based on the experimental curves, for alleviating the influence of the extrusion of soils and the generation of mold. It is assumed that, for the $\tau - \delta$ curve exhibiting a peak point (Figure 4.21a), the post-peak curve can be approximated by a hyperbolic curve expressed as Equation 4.6. For the $\tau - \delta$ curve exhibiting no peak point (Figure 4.21b), the entire curve can be approximated by a hyperbolic curve expressed as Equation 4.7. Thus, the residual shear strength can be defined as the asymptotic value of the corresponding hyperbolic curve at infinite shear displacement.

$$\frac{\tau_p - \tau}{\tau_p} = \frac{\left(\frac{\delta - \delta_p}{\delta_p}\right)}{a + b\left(\frac{\delta - \delta_p}{\delta_p}\right)} \tag{4.6}$$

$$\tau = \frac{\delta}{a + b\delta} \tag{4.7}$$

where τ is the shear stress; δ is the shear displacement; τ_p and δ_p is the peak shear stress and its corresponding displacement on the $\tau - \delta$ curve; a and b are fitting parameters.

The fitting parameters (i.e., a and b) can be obtained by best-fitting the part of experimental $\tau - \delta$ curve before significant extrusion happens. The initiation of extrusion can be determined based on two criteria: (i) the shear stress starts increasing after remaining relatively constant value and (ii) the measured height of specimen starts decreasing after remaining relatively constant value. It is also assumed that the change of the vertical displacement after the initiation of extrusion is attributed to the extrusion instead of the volume change of the specimen; in other words, the void ratio of the specimen will not change any more after the extrusion starts.

Figure 4.21 can serve as an example of the corrections to the $\tau - \delta$ curve and the $\delta_v - \delta$ curve of suction-controlled ring shear tests. In Figure 4.21a, the extrusion is assumed to start at the shear

displacement of 50mm. Thus, a best-fitted hyperbolic curve can be obtained to correct the $\tau - \delta$ curve by best-fitting the experimental $\tau - \delta$ curve between the peak point and the displacement of 50 mm using Equation 4.6. In addition, the vertical displacement is assumed to be constant after the displacement of 50 mm. In Figure 4.21b, the extrusion is assumed to start at the shear displacement of 20mm. Thus, a best-fitted hyperbolic curve can be obtained to correct the $\tau - \delta$ curve by best-fitting the experimental $\tau - \delta$ curve prior to the displacement of 20 mm using Equation 4.7. In addition, the vertical displacement is assumed to be constant after the displacement of 20 mm.

4.5.3 Corrections to void ratio versus time curve during consolidation stage

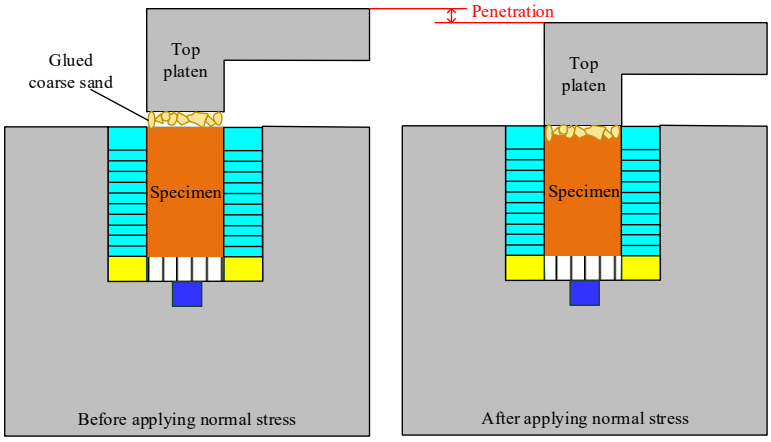

Figure 4.23 Penetration of the coarse sand glued on the top platen into the specimen

As discussed in section 4.2.2, the coarse-grained sands were glued on the top platen to increase the shearing resistance at the interface between the top platen and top surface of the specimen. Due to this reason, when the net normal stress was applied on the specimen, the coarse-grained sands would penetrate into the specimen (Figure 4.23). This could contribute to an increase in the vertical displacement of the specimen. The increase in the vertical displacment due to the penetration could result in an overestimation of the volume change of the specimen during consolidation. For this reason, the void ratio versus time curve during consolidation stage should be corrected by removing the vertical displacment due to the penetration.

Figure 4.24a shows a measured void ratio versus logarithmic time ($e - \log(t)$) curve and water ratio versus logarithmic time ($e_w - \log(t)$) curve during consolidation stage (IHT4: $(u_a - u_w)$ = 25 kPa,

($\sigma_n - u_a$) = 75 kPa). Four stages of the e – log(t) curve can be found from Figure 4.24a. In stage I, e decreases with log(t) at a increasing rate within a very short time period, while e_w does not change. In stage II, e decreases almost linearly with log(t) at a high rate, while e_w does not change. In stage III, e decreases almost linearly with log(t) at a low rate, while e_w decreases gradually. In stage IV, e and e_w do not change any more with time.

By comparing the e – log(t) curve and e_w – log(t) curve, it can be found that (i) the vertical displacement of the unsaturated specimen in stage III can be attributed to the consolidation associated with the drainage of pore water; (ii) the vertical displacement of the unsaturated specimen in stage I and II can be attributed to the the consolidation associated with drainage of pore air and the peneration of coarse-grained sands on top platen. It is difficult to distinguish the vertical displacement caused by the consolidation associated with the drainage of pore air and the vertical displacement caused by the penetration. Thus, an assumption is made to approximate the vertical displacement caused by the penetration. It is assumed that, similar to the e – log(t) curve during the consolidation associated with pore water drainage, the e – log(t) curve during the consolidation associated with pore air drainage exhibits a linear behavior. For this reason, the vertical displacement of the unsaturated specimen in stage II is assumed to be attributed to the consodiation associated with the pore air drainage. The vertical displacement of the unsaturated specimen in stage I is assumed to be attributed to the peneration of coarse-grained sands on top platen. The measured e – log(t) curve can be corrected by removing the vertical displacement caused by the penetration, which is shown in Figure 4.24b.

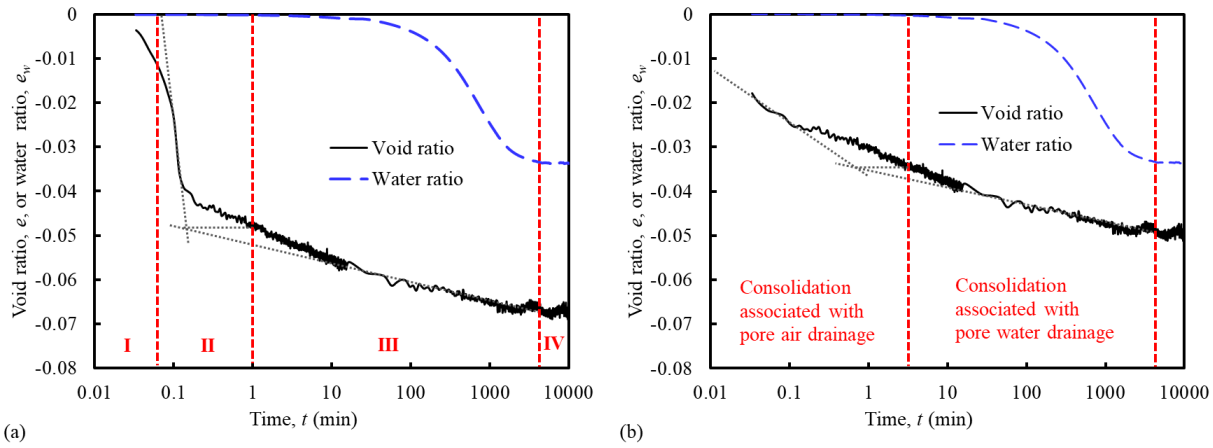

Figure 4.24 Corrections to the void ratio versus time curve during consolidation: (a) measured curves; (b) corrected curves

4.6 Summary

This chapter introduces the modified suction-controlled ring shear apparatus based on the axis translation technique developed by Infante Sedano et al. (2007). The main modifications on the ring shear cell include: (i) a groove machined on the cell base to collect air bubbles accumulating below the ceramic disks, (ii) a bottom plate with high air-entry value ceramic disks to separate the water and air phase, (iii) two stacks of confining rings used as the confining wall of the specimen to remove the friction between the confining wall and the specimen, (iv) a cell cove added to create a closed environment. In addition, a flushing system was designed to remove the air bubbles accumulating below the ceramic disks and measure the mass of water drained from or absorbed into the specimen.

Two sets of suction-controlled ring shear tests were designed for two different unsaturated soils, including a poorly graded sand with silt (SP-SM) and the Indian Head till (IHT), using the introduced suction-controlled ring shear apparatus. The properties of the test materials (including the basic physical properties, static compaction curve and the soil water characteristic curve) were measured and decribed. All the ring shear tests on the SP-SM and IHT soil were conducted under constant matric suction and net normal stress. The multistage tests were used for the unsaturated specimens to shorten the testing period. The procedures of the suction-controlled multistage ring sehar tests were described in detail in this chapter.

The modified suction-controlled ring shear apparatus still has several limitations (e.g., the extrusion of soils during shearing, the evaporation of water, etc.) which can result in the errors in the measurements of the shear stress, volume change and water content of the specimens. Therefore, the correction methods are introduced for the corrections of the water mass versus time curve, the shear stress/vertical displacement versus shear displacement curve and the void ratio versus time curve, respectively.

4.7 References

ASTM. 2014. Designation: D854–14. Standard test methods for specific gravity of soil solids by water pycnometer. D854. West Conshohocken, PA.

ASTM. 2017. Designation: D6913/D6913M−17. Standard Test Methods for Particle-Size Distribution (Gradation) of Soils Using Sieve Analysis. West Conshohocken, PA.

ASTM. 2006. Designation: D2487–06. Standard practice for classification of soils for engineering purposes (unified soil classification system). West Conshohocken, PA.

Bishop, A. W., Green, G. E., Garga, V. K., Andresen, A., and Brown, J. D. 1971. A new ring shear apparatus and its application to the measurement of residual strength. Géotechnique, 21(4): 273-328.

Cai, G., Han, B., Asreazad, S., Liu, C., Zhou, A., Li, J., and Zhao, C. 2022. Experimental study on critical state behavior of unsaturated silty sand under constant matric suctions. Géotechnique, 1-67.

Cui, Y. J., and Delage, P. 1996. Yielding and plastic behaviour of an unsaturated compacted silt. Géotechnique, 46 (2): 291-311.

Derbyshire, E., Dijkstra, T. A., Smalley, I. J., and Li, Y. 1994. Failure mechanisms in loess and the effects of moisture content changes on remoulded strength. Quaternary International, 24: 5-15.

Dijkstra, T. A., Rogers, C. D., Smalley, I. J., Derbyshire, E., Li, Y. J., and Meng, X. M. 1994. The loess of north-central China: geotechnical properties and their relation to slope stability. Engineering Geology, 36(3-4): 153-71.

Estabragh, A. R., and Javadi, A. A. 2008. Critical state for overconsolidated unsaturated silty soil. Canadian Geotechnical Journal, 45(3): 408-20.

Fan, X., Xu, Q., Scaringi, G., Li, S., and Peng, D. 2017. A chemo-mechanical insight into the failure mechanism of frequently occurred landslides in the Loess Plateau, Gansu Province, China. Engineering Geology, 228: 337-45.

Garga, V. K., and Infante Sedano, J. 2002. Steady state strength of sands in a constant volume ring shear apparatus. Geotechnical Testing Journal, 25(4): 414-421.

Hossain, J. (2013). Geohazard potential of rainfall induced slope failure on expansive clay. Ph. D. Thesis, University of Texas at Arlington, Arlington, US.

Hossain, M. A., and Yin, J. H. 2010. Behavior of a compacted completely decomposed granite soil from suction controlled direct shear tests. Journal of Geotechnical and Geoenvironmental Engineering, 136(1): 189-98.

Hoyos, L. R., Velosa, C. L., and Puppala, A. J. 2011. A servo/suction-controlled ring shear apparatus for unsaturated soils: Development, performance, and preliminary results. Geotechnical Testing Journal, 34(5): 413-23.

Hoyos, L. R., Velosa, C. L., and Puppala, A. J. 2014. Residual shear strength of unsaturated soils via suction-controlled ring shear testing. Engineering Geology, 172: 1-11.

Infante Sedano, J. A. 2006. A modified ring shear test device for testing hydro-mechanical behavior of saturated soils. Ph.D. thesis, University of Ottawa, Ottawa, Canada.

Infante Sedano, J. A., Vanapalli, S. K. and Garga, V.K. 2007. Modified ring shear apparatus for unsaturated soils testing. Geotechnical Testing Journal, 30(1): 39–47.

Infante Sedano, J. A., and Vanapalli, S. 2011. Experimental investigation of the relationship between the critical state shear strength of unsaturated soils and the soil-water characteristic curve. International Journal of Geotechnical Engineering, 5(1): 1-8.

Lian, B., Peng, J., Wang, X., and Huang, Q. 2020. Moisture content effect on the ring shear characteristics of slip zone loess at high shearing rates. Bulletin of Engineering Geology and the Environment, 79(2): 999-1008.

Lu N. and Likos W.J. 2004. Unsaturated soil mechanics, Wiley, New York, NY, USA.

Maquaire, O., Malet, J. P., Remaıtre, A., Locat, J., Klotz, S., and Guillon, J. 2003. Instability conditions of marly hillslopes: towards landsliding or gullying? The case of the Barcelonnette Basin, South East France. Engineering Geology, 70(1-2): 109-30.

Meehan, C. L., Brandon, T. L., and Duncan, J. M. 2007. Measuring drained residual strengths in the Bromhead ring shear. Geotechnical Testing Journal, 30(6), 466-473.

Merchán, V., Romero, E., and Vaunat, J. 2011. An adapted ring shear apparatus for testing partly saturated soils in the high suction range. Geotechnical Testing Journal, 34(5): 433-44.

Patil, U. D., Puppala, A. J., Hoyos, L. R., and Pedarla, A. 2017. Modeling critical-state shear strength behavior of compacted silty sand via suction-controlled triaxial testing. Engineering Geology, 231: 21-33.

Postill, H., Dixon, N., Fowmes, G., El-Hamalawi, A., and Take, W. A. 2020. Modelling seasonal ratcheting and progressive failure in clay slopes: a validation. Canadian Geotechnical Journal, 57(9): 1265-79.

Power, K. C., and Vanapalli, S. K. 2010. Modified null pressure plate apparatus for measurement of matric suction. Geotechnical Testing Journal, 33(4): 335-341.

Qi, S., and Vanapalli, S. K. 2016. Influence of swelling behavior on the stability of an infinite unsaturated expansive soil slope. Computers and Geotechnics, 76: 154-69.

Ren, J. 2019. Interpretation of the frozen soils behavior extending the mechanics of unsaturated soils. Ph.D. thesis, University of Ottawa, Ottawa, Canada.

Romero, E., Vaunat, J., and Merchán, V. 2014. Suction effects on the residual shear strength of clays. Journal of Geo-Engineering Sciences, 2(1-2): 17-37.

Singh, A., Singh, A., and Pummia, B. C. 1984. Soil Mechanics and Foundations. D Nonfand Book House.

Stark, T. D., and Vettel, J. J. 1992. Bromhead ring shear test procedure. Geotechnical Testing Journal, 15(1), 24-32.

Take, W. A., and Bolton, M. D. 2011. Seasonal ratcheting and softening in clay slopes, leading to first-time failure. Géotechnique, 61(9): 757-69.

Tarantino, A., and Tombolato, S. 2005. Coupling of hydraulic and mechanical behaviour in unsaturated compacted clay. Géotechnique, 55(4): 307-17.

Toll, D. G. 1990. A framework for unsaturated soil behaviour. Géotechnique, 40(1): 31-44.

Vanapalli, S. K., Fredlund, D. G., Pufahl, D. E., and Clifton, A. W. 1996. Model for the prediction of shear strength with respect to soil suction. Canadian Geotechnical Journal, 33(3): 379-92.

Vaunat, J., Amador, C., Romero, E., and Djeran-Maigre, I. 2006. Residual strength of a low plasticity clay at high suctions. In Unsaturated Soils 2006, 1279-1289.

Vaunat, J., Merchán, V., Romero, E., and Pineda, J. 2007. Residual strength of clays at high suctions. In Theoretical and Numerical Unsaturated Soil Mechanics, 151-163. Springer, Berlin, Heidelberg.

Velosa, C. L. 2011. Unsaturated soil behavior under large deformations using a fully servo/suction-controlled ring shear apparatus. Ph. D. Thesis, University of Texas at Arlington, Alington, US.

Wheeler, S. J., and Sivakumar, V. 1995. An elasto-plastic critical state framework for unsaturated soil. Géotechnique, 45(1): 35-53.

CHAPTER 5 EXPERIMENTAL RESULTS OF SUCTION-CONTROLLED RING SHEAR TESTS

5.1 Introduction

Several geo-structures in unsaturated soils undergo large shear deformation prior to reaching the failure condition. The shear strength typically reduces from a peak value to a residual value with an increase in the shear deformation of several unsaturated soils. Thus, the behaviors of the geo-structures in unsaturated soils undergoing large shear deformation will be influenced by the strain-softening behavior of unsaturated soils under large shear deformation. The factor of safety of such geo-structures will gradually but significantly decrease over a long period with the development of the shear deformation. For this reason, it is crucial for the reliable analysis and design of geo-structures in unsaturated soils to understand the shear strength behavior of unsaturated soils during strain-softening associated with large shear deformations.

To date, however, there are only limited experimental studies on the behaviors of unsaturated soils in suction-controlled state under large shear deformation. Infante Sedano and Vanapalli (2011), Hoyos et al. (2014) and Heredia (2015) studied the behaviors of unsaturated soils under large shear deformation within low suction range (lower than 500 kPa) by using the axis-translation technique to control the matric suction. Vaunat et al. (2006), Vaunat et al. (2007), Merchán et al. (2008) and Romero et al. (2014) studied the behaviors of unsaturated soils under large shear deformation within high suction range (higher than 10 MPa) by using the vapor equilibrium technique to control the total suction. All the studies showed the suction can significantly contribute to the residual shear strength of unsaturated soils. These investigation studies also highlight that suction can enhance the brittleness and dilatancy of the unsaturated soils. In addition, these studies also showed the residual shear strength of unsaturated soils is independent of the history specific structure caused by various factors (e.g., the initial water content, the suction history, and the pre-shearing history). Despite these valuable findings, the experimental data about the behaviors of unsaturated soils in suction-controlled state under large shear deformation is still limited and far from conclusive.

In this study, a series of suction-controlled ring shear tests were conducted on two unsaturated soils (the IHT and SP-SM soil) following the multistage tests summarized in Chapter 4. The variations of the shear stress, void ratio, and water ratio of the IHT and SP-SM specimens during shearing stage were presented in this chapter. The behaviors of different unsaturated soils in suction-controlled state under large shear displacement (100 mm) were discussed. The envelopes of the residual shear strength were presented with respect to the net normal stress and matric suction, respectively. The influence of the matric suction and net normal stress on the residual shear strength and residual friction angle with respect to the net normal stress and the matric suction (ϕ_r^a and ϕ_r^b) were analyzed. The experimental results of the residual shear strength, ϕ_r^a and ϕ_r^b were compared with the predicted results of three models proposed for the critical shear strength of unsaturated soils. Finally, the void ratio, water ratio and degree of saturation of the IHT soil sheared to the residual state were discussed.

5.2 Unsaturated soil behaviors under suction-controlled ring shear testing

5.2.1 IHT soil

Figure 5.1 shows the variation of shear stress, void ratio and water ratio of saturated IHT specimens with shear displacement. The three saturated IHT specimens were sheared in single stage under different effective normal stress. The variation of void ratio and water ratio were calculated from the variation of vertical displacement measured by LVDT and the variation of water mass in overflow jar measured by a balance. The shear stress-shear displacement and void ratio-shear displacement curves were corrected following the approach discussed in section 4.5.2 considering the extrusion. The corrected curves were presented in Figure 5.1 using continous dash lines.

Figure 5.1a shows, for all the three saturated specimens, the shear stress increases initially with the shear displacement and then decreases gradually to the residual shear strength after the peak state is reached. Bishop et al. (1971) and Lupini et al. (1981) attributed the reduction in shear strength of saturated soils under large shear displacement into the localized dilation inside the shear band and the reorientation of platy clay particles adjacent to the sliding surface. As shown in Figure 5.1b, the three saturated specimens exhibit compressive behavior. For this reason, the gradual decrease in shear stress with shear displacement after the peak state can be attributed to the reorientation of the clay particles of the IHT soil.

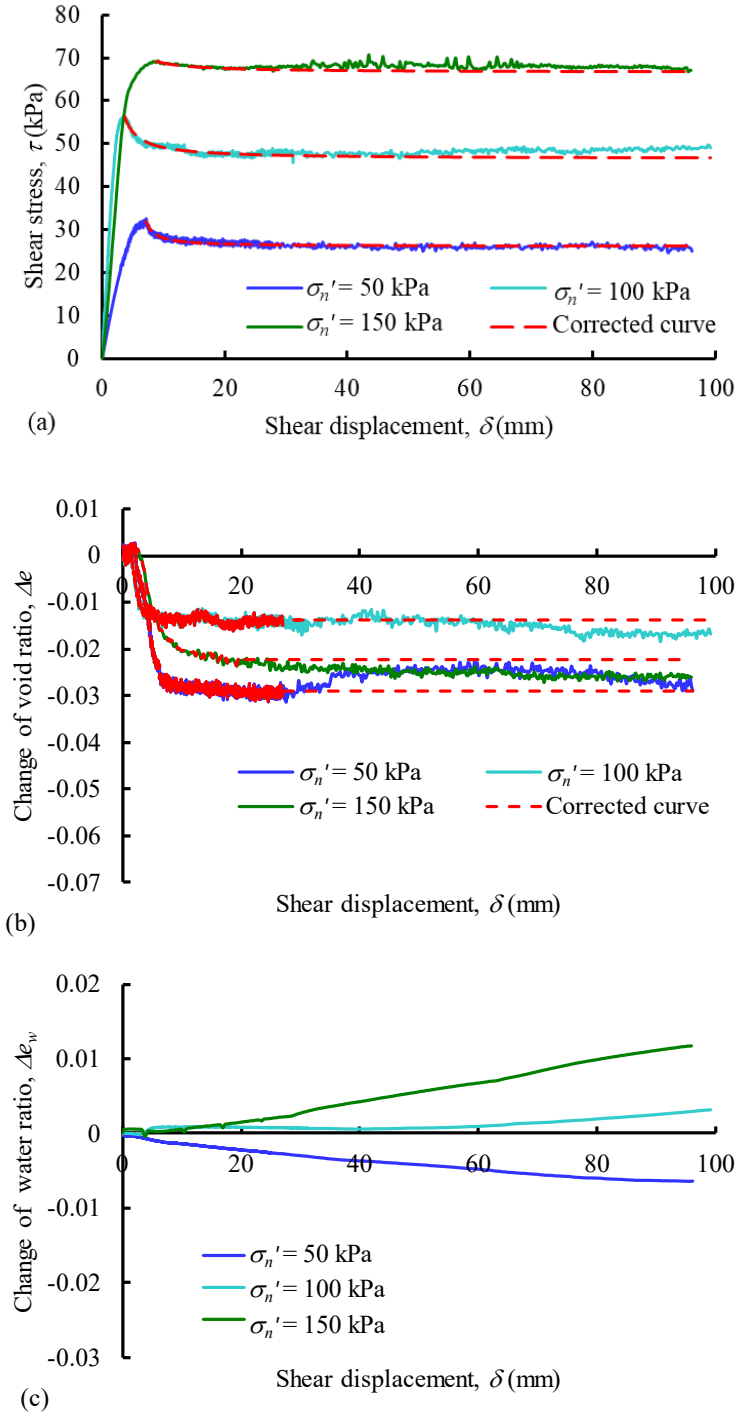

Figure 5.1 Experimental results of single stage IHT1 – IHT3 tests under saturated condition and σ_n' = 50, 100 and 150 kPa

Figure 5.1b shows all the three saturated specimens exhibit compression under the shear displacement of 100 mm. However, the specimen under low effective normal stress (σ_n' = 50 kPa) exhibits more compression, whereas a less compression would be expected for a lower effective normal stress. This can be attributed to the difference of the initial void ratio of the saturated speicmens (Figure 5.2). All the IHT specimens used in this study were prepared by statically compacting the soil powders with a water content of 15% under 375 kPa vertical pressure. By using this preparation technique, it is hard to ensure every compacted specimen has the same void ratio. The as-compacted void ratio can be calculated by measuring the height of the compacted specimen. In addition, it is assumed that the void ratio of the specimens after saturation is equal to the as-compacted void ratio. Therefore, the void ratio of the speicmens before consolidation can be presented in Figure 5.2 (i.e., the hollow shapes). During consolidatin, the void ratio of saturated specimens will decrease following the straight dash lines with similar slopes in Figure 5.2 that can be treated as the swelling lines of the tested soil. Then, after shearing, the void ratio will decrease to the corresponding value on the residual state line. From Figure 5.2, it can be found that the specimen used for IHT1 test (i.e., σ_n' = 50 kPa) has a greater void ratio before the consolidation. This makes the specimen exhibit more compression during shearing.

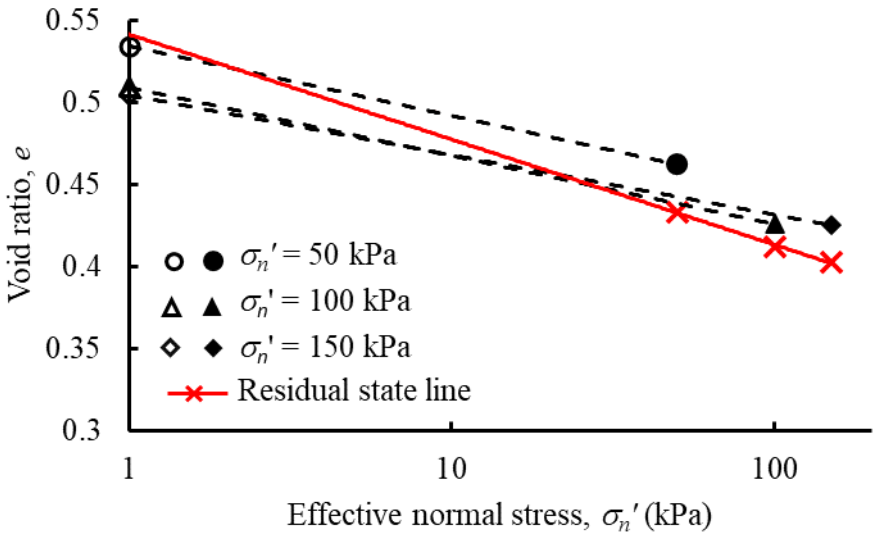

Figure 5.2 Change of void ratio of saturated IHT specimens during consolidation stage (hollow shapes represent the void ratios before consolidation; solid shapes represent the void ratios after consolidation)

Figure 5.1c presents the variation of the water ratio $e_w = wG_s$, where w is the water content and G_s is the specific gravity, during shearing. It can be found that the variation of e_w is not consistent with the variation of e. For the specimen under σ_n' = 50 kPa, e_w decreases with the shear displacement, but the decrease of e_w is smaller than the decrease of e. For the specimens under σ_n' = 100 and 150 kPa, e_w increases with the shear displacement, while e decreases with shear displacement. Such a trend in results suggests that the specimens may not have reached the degree of saturation of 100% prior to shearing. In this study, all the compacted specimens were saturated by percolating water through the specimens from bottom to top under 20 kPa pressure. This process typically takes 4 days. However, as suggested by Leroueil and Hight (2013), the degree of saturation after submergence is typically not at a degree of saturation of 100% but rather at a degree of saturation close to that at the optimum (i.e., 80% for the studied IHT soil). For this reason, the degree of saturations of specimens keep increasing during consolidation and shearing stage in the IHT1 – IHT3 tests. In addition, in unsaturated tests, a certain air pressure was applied in the ring shear cell; thus, the drained water can only flow through the ceramic disk into the overflow jar. However, in saturated tests, no air pressure was applied in the ring shear cell; thus, some pore water may be drained into the gaps in ring shear cell, which cannot be measured by the overflow jar. This phenomenon can also influence the measurement of the mass of the drained water in the saturated tests.

Figure 5.3 shows the typical shear zone of the saturated IHT specimen in IHT3 test (σ_n' = 150 kPa). The IHT soil exhibit the 'transitional mode' of residual shear strength described by Lupini et al. (1981). In the transitional mode, the specimen is not separated on the shear zone. Discontinuous sliding shear surfaces and pockets of soil behaving in the turbulent mode are both contained within a thick shear zone.

Figure 5.3 Typical shear zone of saturated IHT specimen (IHT3 test, σ_n' = 150 kPa)

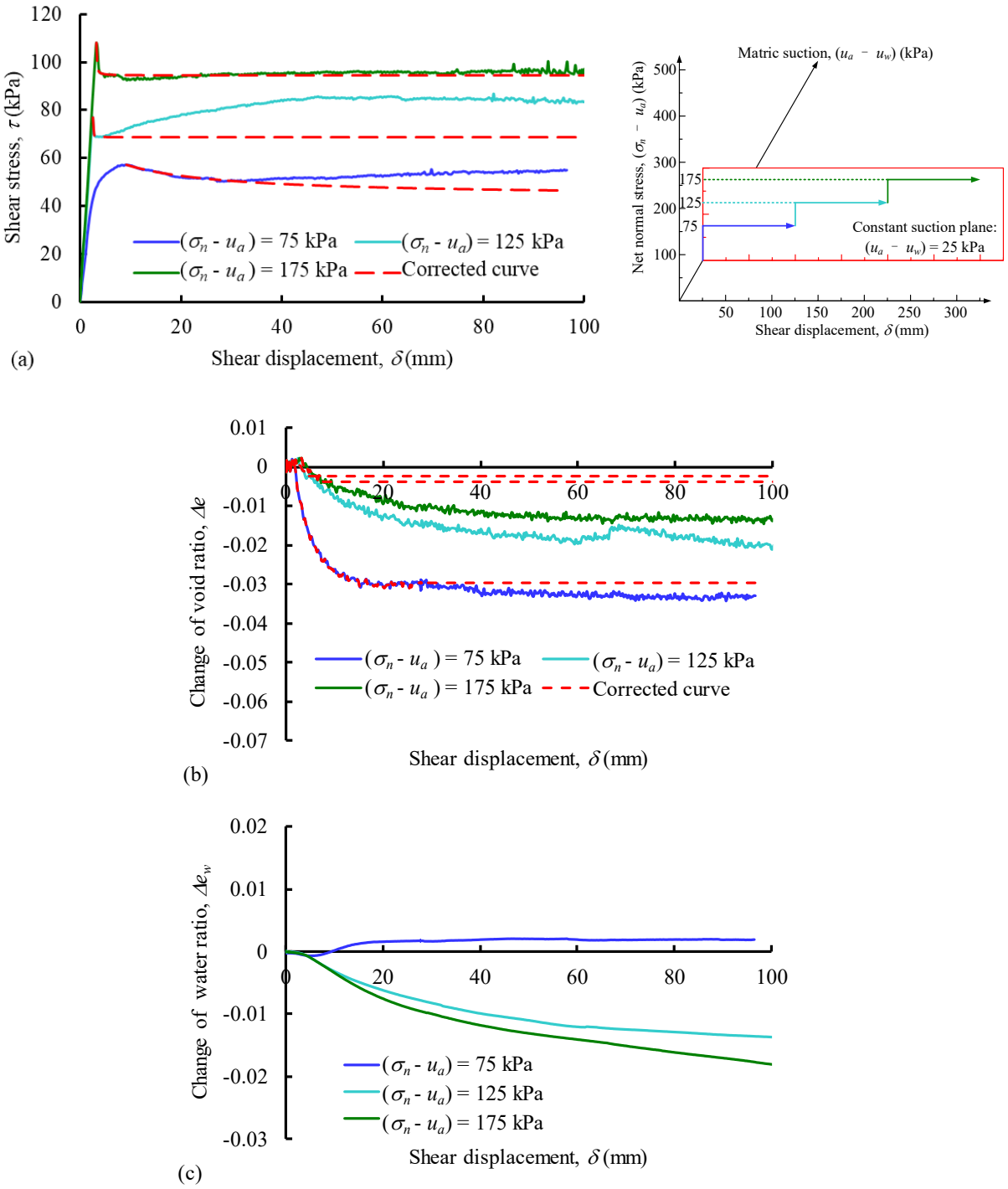

Figure 5.4 Experimental results of multistage IHT4 test under ($u_a - u_w$) = 25 kPa and ($\sigma_n - u_a$) = 75, 125 and 175 kPa

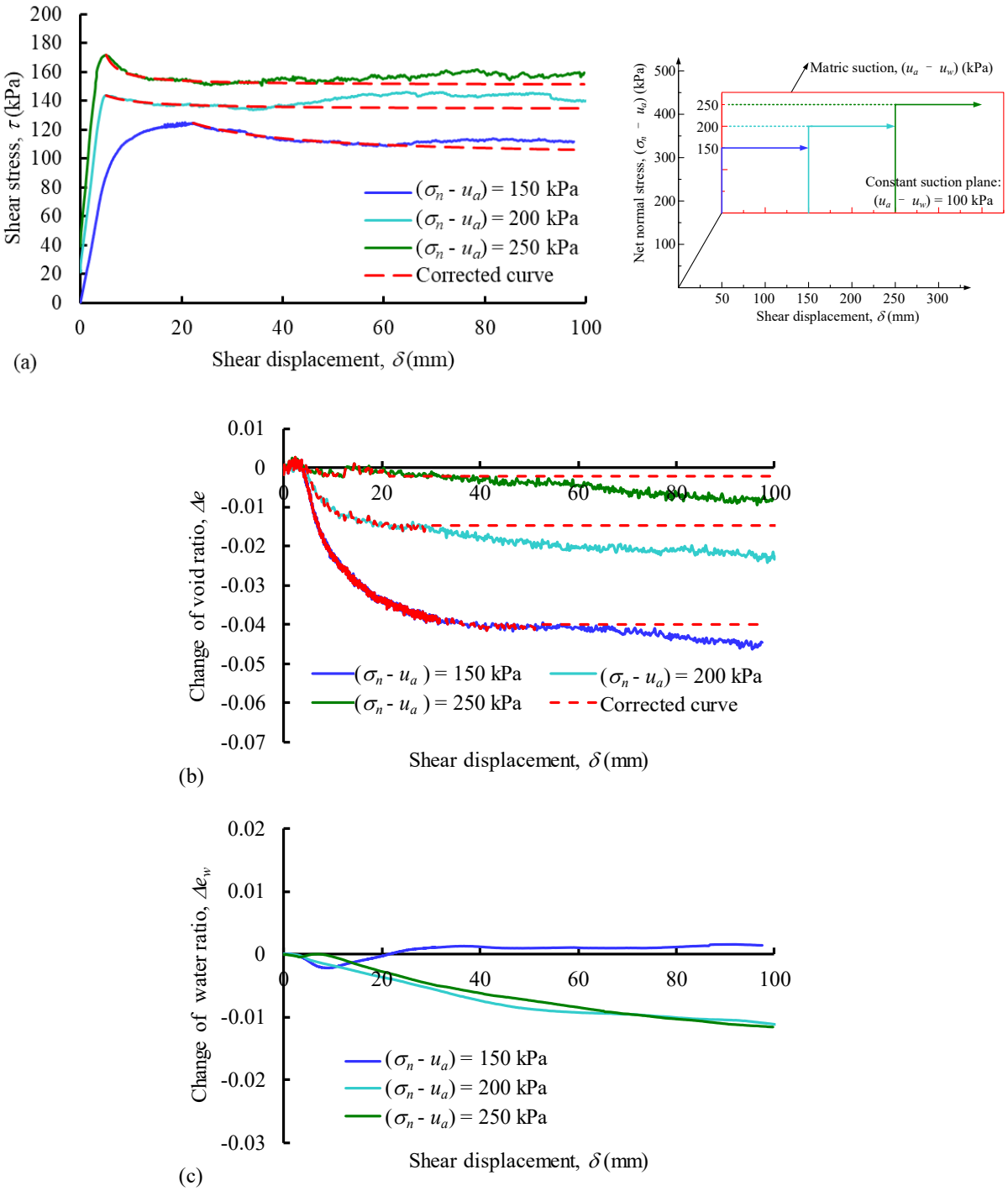

Figure 5.5 Experimental results of multistage IHT5 test under ($u_a - u_w$) = 100 kPa and ($\sigma_n - u_a$) = 150, 200 and 250 kPa

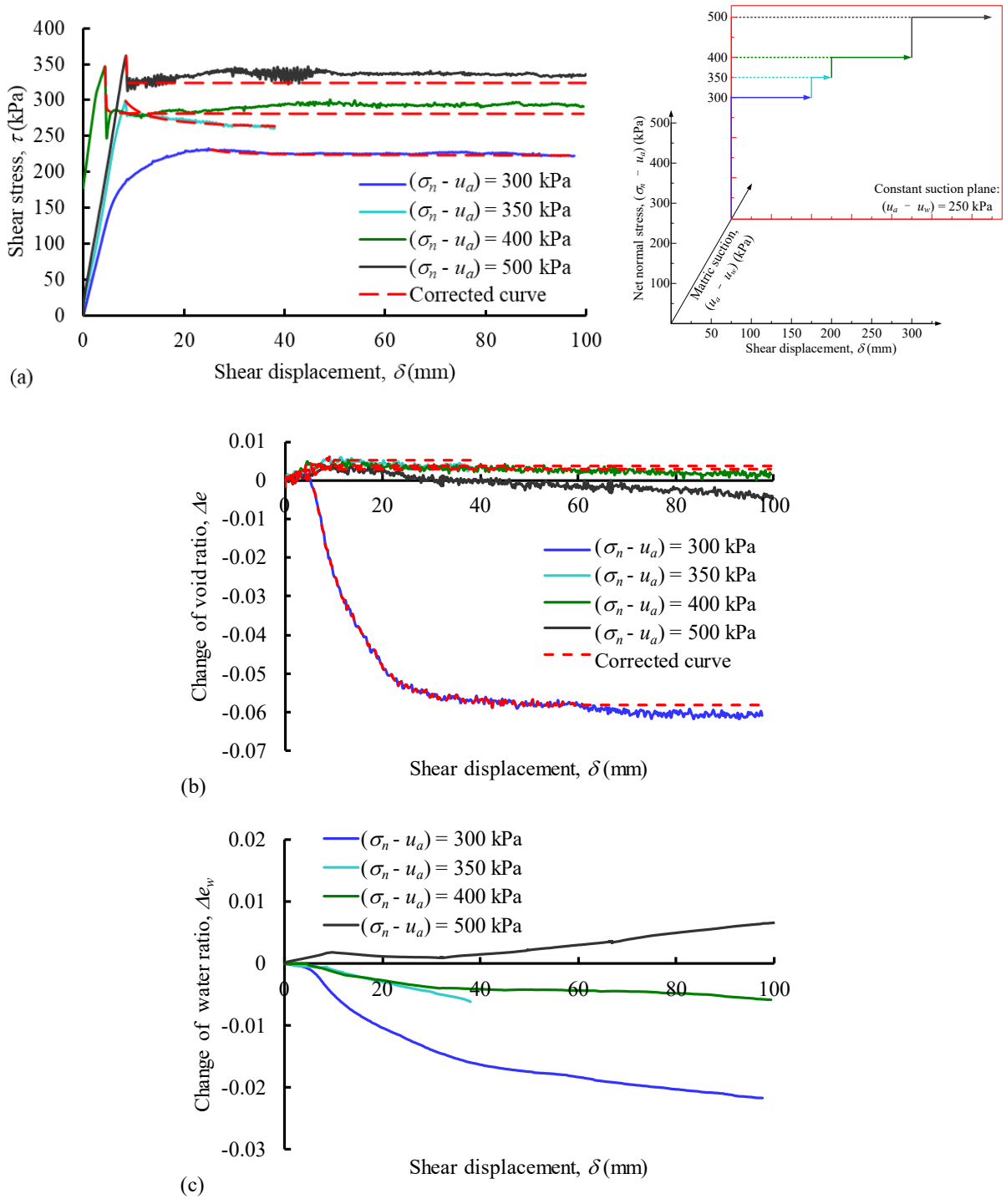

Figure 5.6 Experimental results of multistage IHT6 test under ($u_a - u_w$) = 250 kPa and ($\sigma_n - u_a$) = 300, 350, 400 and 500 kPa

Figures 5.4, 5.5 and 5.6 summarize the variation of shear stress, void ratio and water ratio of unsaturated IHT specimens during suction-controlled multistage ring shear tests under constant matric suction, $(u_a - u_w)$ = 25, 100, 250 kPa (i.e., IHT4 – IHT6), respectively. The loading path of the three tests are also presented in Figures 5.4a, 5.5a and 5.6a. As shown in Figure 5.4a and Figure 5.6a, in the IHT4 and IHT6 test, the net normal stress was increased to the next level directly after each of shearing stages. However, as shown in Figure 5.5a, in the IHT5 test, the net normal stress was removed for a short time and then was increased to the next level after each of shearing stages. It can be found, for each of the multistage tests, the residual shear strength increases with the net normal stress. The matric suction can also contribute to the residual shear strength of unsaturated IHT soil.

Figures 5.4a, 5.5a and 5.6a show all the shear stress – shear displacement curves exhibit peak point. However, since the IHT4 – IHT6 tests are multistage tests, only the peak point of the shear stress – shear displacement curve of the first shearing stage can represent the real peak shear strength of the unsaturated IHT soil. Figures 5.4b, 5.5b and 5.6b show the specimens exhibit compressive behavior at the first shearing stage. This is attributed to the fact that the specimen with higher matric suction also has a higher net normal stress; thus, no dilative behavior was observed at the first shearing stage of the unsaturated specimens. For this reason, the reduction in shear strength of unsaturated specimens during the first shearing stage can be attributed to the reorientation of the clay particles and the loss of water menisci area in shear zone.

Figure 5.4a shows the shear strength is reduced suddenly after the peak point at the second and third shearing stages of IHT4 test ($(u_a - u_w)$ = 25 kPa). Figure 5.7a shows the position of the shear zones at three shearing stages of IHT4 test. All the shear zones were created at the same position between the first and second confining rings. As suggested by Velosa (2011), the apparent peak may be attributed to the effort required initially to reorient the particles/aggregates in the direction of shearing under the new net normal stress state, and/or the aging effects occurred during the first shearing stage, which is similar with the behavior of saturated materials. In addition, for the unsaturated soils, the ruptured water menisci in shear zone due to continuous shearing can be recovered during the consolidation stage under new net normal stress. This may also contribute to the apparent peak in multistage ring shear tests.

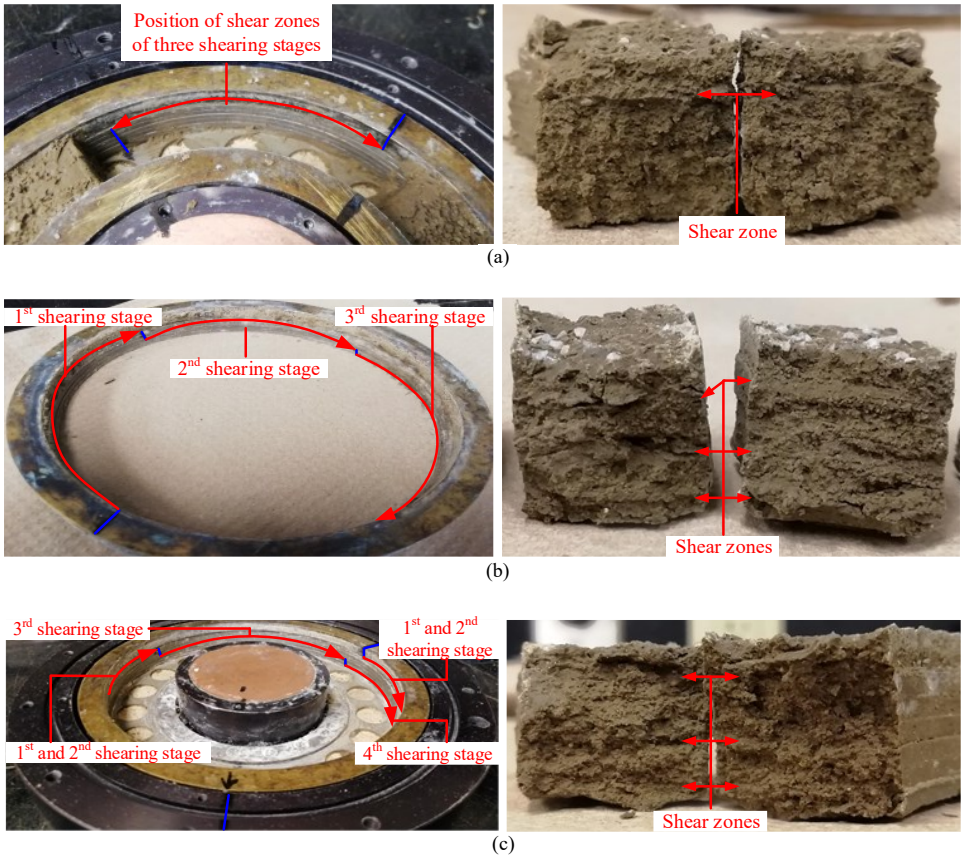

Figure 5.7 Positions of the shear zones of the unsaturated IHT specimens: (a) IHT4 test under ($u_a - u_w$) = 25 kPa; (b) IHT5 test under ($u_a - u_w$) = 100 kPa; (c) IHT6 test under ($u_a - u_w$) = 250 kPa

Figure 5.5a shows the shear strength is reduced gradually after peak point at the second and third shearing stages of IHT5 test (($u_a - u_w$) = 100 kPa). Figure 5.7b shows the position of the shear zones at three shearing stages of IHT5 test. It can be found the shear zones in different shearing stages occurred at different positions. This means the strain-softening behavior at the second and third shearing stages should be attributed to the creation of a new shear zone, where the compression (Figure 5.5b) and reorientation of partiles/aggregates occurred.

Figure 5.6a shows the shear strength is reduced suddenly at the second, third and fourth shearing stages of IHT6 test (($u_a - u_w$) = 250 kPa). Figure 5.7b shows the position of the shear zones at four shearing stages of IHT6 test. The shear zones of the first and second shearing stage occurred at the same position between the first and second confining rings. The shear zones of the third and fourth shearing stage occurred at different positions. Therefore, the apparent peak at the second shearing

stage can be attributed to the modification of the soil structure in shear zone, the ageing effects, and the recovery of water menisci. The strain-softening behavior at the third and fourth shearing stages can be attributed to the creation of new shear zones, where the dilation (Figure 5.6b) and reorientation of partiles/aggregates occurred.

5.2.2 SP-SM soil

Figure 5.8 shows the variation of shear stress, void ratio and water ratio of saturated SP-SM specimens with shear displacement. The three saturated SP-SM specimens were sheared in single stage under different effective normal stress (σ_n' = 10, 25 and 50 kPa). The corrected curves using the approach discussed in section 4.5.2 considering the extrusion were presented in Figure 5.8 as continuous dash lines.

Figure 5.8a shows the SP-SM1 specimen exhibit a slight strain-softening behavior, while the SP-SM2 and SP-SM3 specimens exhibit significant strain-softening behavior. The SP-SM soil mainly consists of sand grains (89.59%), which means no reorientation of soil particles occur near the sliding surface; thus, the strain-softening behavior can be attributed to the localized dilation inside the shear band. Figure 5.8b shows the SP-SM1 specimen dilates slightly and then compresses as the shear displacement increases. The SP-SM2 and SP-SM3 specimens exhibit significant dilation. This is consistent with the strain-softening behavior shown in Figure 5.8a.

Generally, more dilation is expected for a specimen under lower effective normal stress. However, Figure 5.8b shows the SP-SM1 specimen (σ_n' = 10 kPa) has less dilation in comparison to the specimen under σ_n' = 25 and 50 kPa. This may be also attributed to the difference of the initial void ratio of the speicmens caused by the errors during static compaction, which has been discussed in section 5.2.1. In other words, the specimen used in SP-SM1 test has a larger as-compacted void ratio than the specimens in SP-SM2 and SP-SM3 tests, which results in less dilation in SP-SM1 test. Unfortunately, the initial heights of the compacted SP-SM specimens were not measured; thus, the initial void ratio of the compacted specimens cannot be obtained.

Figure 5.8c shows small change in water ratio during shearing. It is because the pore water may be drained into the gaps in ring shear cell in saturated tests where no additional air pressure was

applied in the shear cell. Thus, the change of water mass in the specimens cannot be measured by the overflow jar.

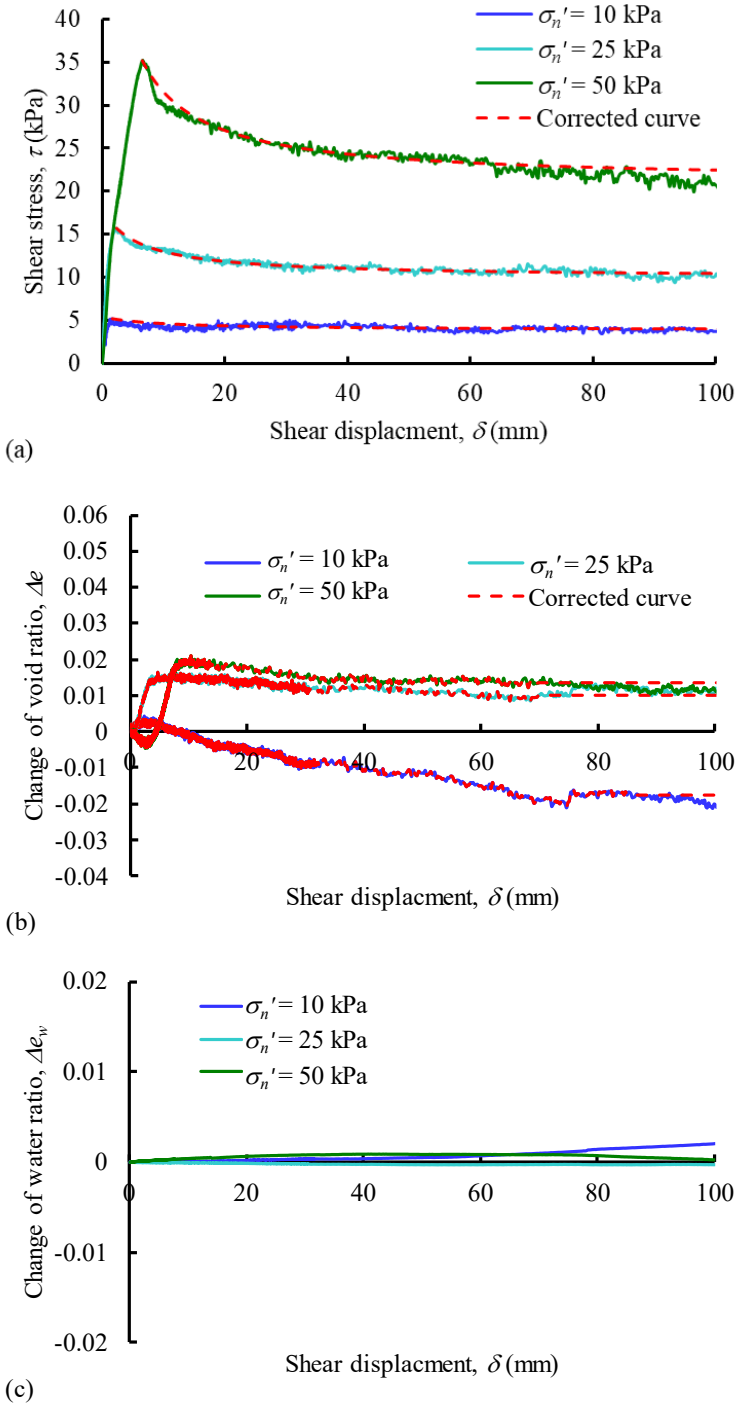

Figure 5.8 Experimental results of single stage SP-SM1 – SP-SM3 tests under saturated condition and σ_n' = 10, 25 and 50 kPa

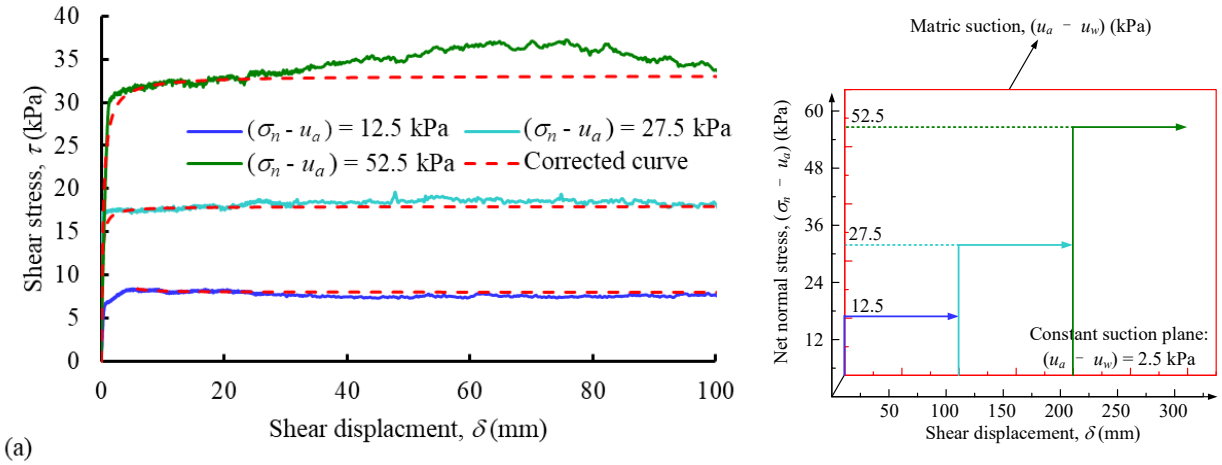

(a)

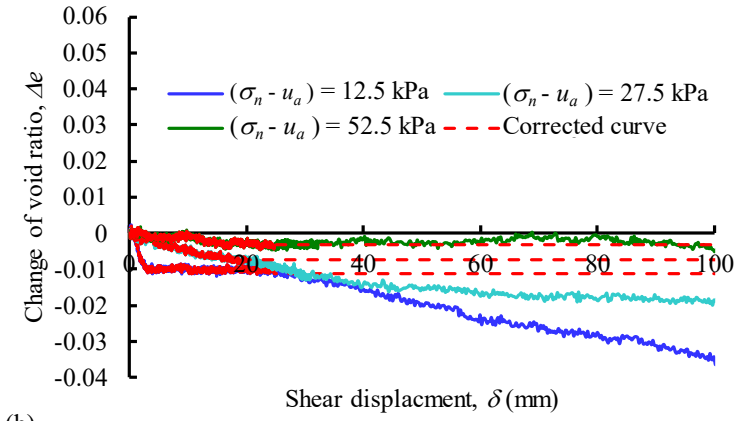

(b)

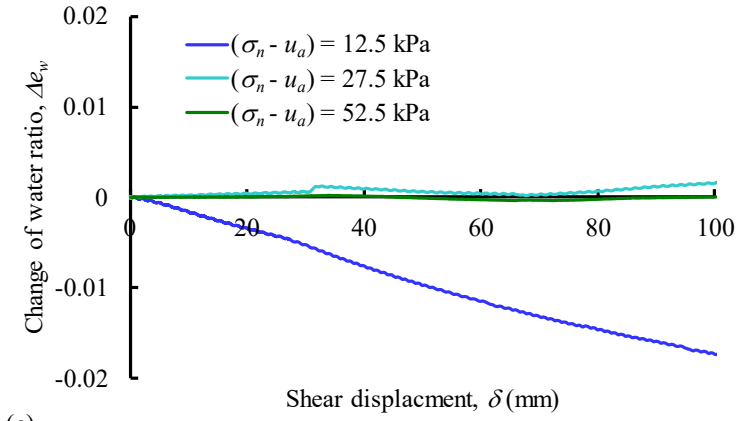

(c)

Figure 5.9 Experimental results of multistage SP-SM4 test under ($u_a - u_w$) = 2.5 kPa and ($\sigma_n - u_a$) = 12.5, 27.5 and 52.5 kPa

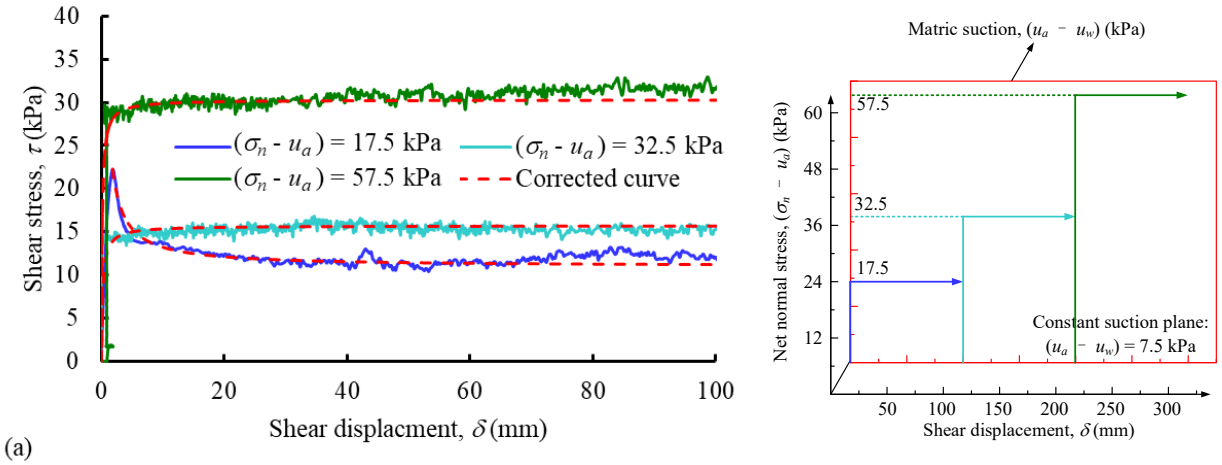

(a)

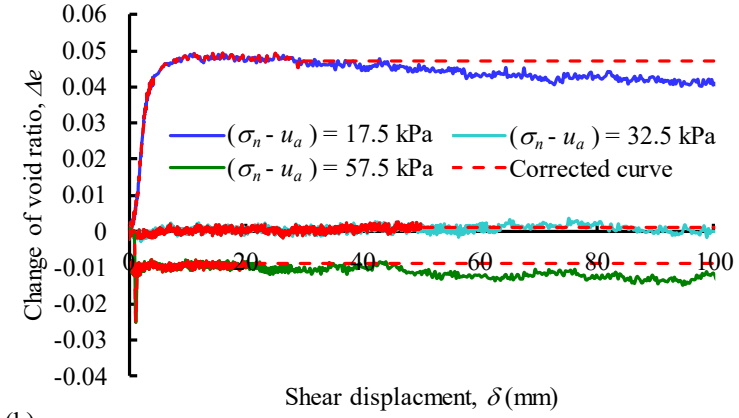

(b)

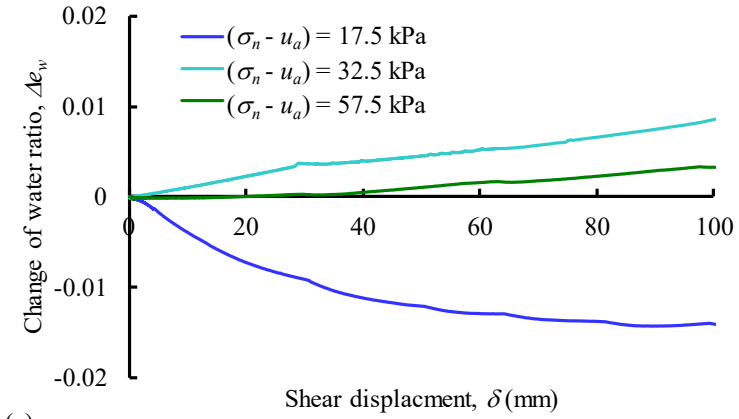

(c)

Figure 5.10 Experimental results of multistage SP-SM5 test under ($u_a - u_w$) = 7.5 kPa and ($\sigma_n - u_a$) = 17.5, 32.5 and 57.5 kPa

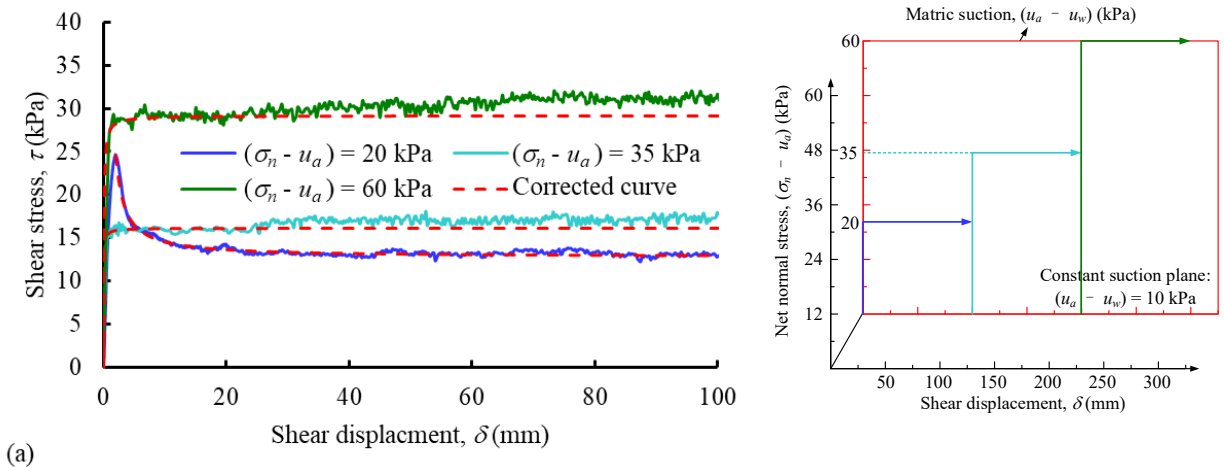

(a)

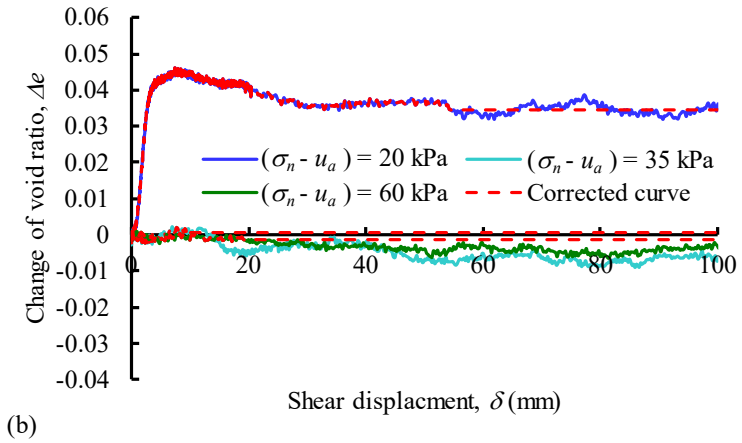

(b)

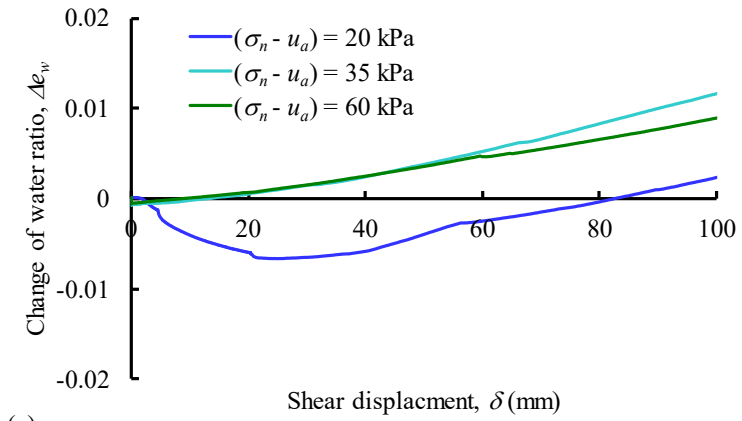

(c)

Figure 5.11 Experimental results of multistage SP-SM6 test under ($u_a - u_w$) = 10 kPa and ($\sigma_n - u_a$) = 20, 35 and 60 kPa

Figures 5.9, 5.10 and 5.11 summarize the variation of shear stress, void ratio and water ratio of unsaturated SP-SM specimens during suction-controlled multistage ring shear tests under constant matric suction, ($u_a - u_w$) = 2.5, 7.5, 10 kPa (i.e., SP-SM4 – SP-SM6), respectively. The loading

path of the three tests are also presented in Figures 5.9a, 5.10a and 5.11a. As shown in Figures 5.9a, 5.10a and 5.11a, in the three multistage tests (i.e., SP-SM4 – SP-SM6), the net normal stress was removed for a short time and then was increased to the next level after each of shearing stages. The results from these studies suggest that for each of the multistage tests, the residual shear strength increases with the net normal stress. The matric suction can also contribute to the residual shear strength of unsaturated SP-SM soil.

Figures 5.9a, 5.10a and 5.11a show only the shear stress – shear displacement curve of the first shearing stage exhibit peak state. Figure 5.12 summarize the experimental results of the first shearing stage of the unsaturated SP-SM soil. The net normal stresses of the three tests are 12.5, 17.5 and 20 kPa, which are much lower than the compaction pressure (375 kPa). It can be found the shear stress – shear displacement curve of the SP-SM4 test under $(u_a - u_w)$ = 2.5 kPa exhibit slight strain-softening behavior, while the the shear stress – shear displacement curves of the SP-SM5 test under $(u_a - u_w)$ = 7.5 kPa and the SP-SM6 test under $(u_a - u_w)$ = 10 kPa exhibit significant strain-softening behavior. This phenonemon is consistent with the volume change behavior (Figure 5.12b); i.e., the SP-SM4 specimen under $(u_a - u_w)$ = 2.5 kPa exhibit compressive behavior, while the SP-SM5 specimen under $(u_a - u_w)$ = 7.5 kPa and the SP-SM6 specimen under $(u_a - u_w)$ = 10 kPa exhibit significant dilative behavior. This means the strain-softening behavior of the SP-SM soil can be mainly attributed to the localized dilation inside the shear band. In addition, the matric suction can enhance the dilative and the strain-softening behavior of the unsaturated SP-SM soil.

Figures 5.9a, 5.10a and 5.11a show the shear stress – shear displacement curves of the SP-SM4 – SP-SM6 tests exhibit hardening behavior at the second and third shearing stage. In addition, Figures 5.9b, 5.10b and 5.11b show the SP-SM4 – SP-SM6 specimens exhibit slight compression at the second and third shearing stage. Such a behavior suggests the effect of net normal stress on the residual shear strength of the SP-SM soil in multistage tests is due to the reduction of the void ratio in shear zone, rather than to the modification of the soil structure in shear zone. This is different in comparison to the IHT soil results from multistage tests which needs to reorient the particles/aggregates to reach the new residual state under the new net normal stress.

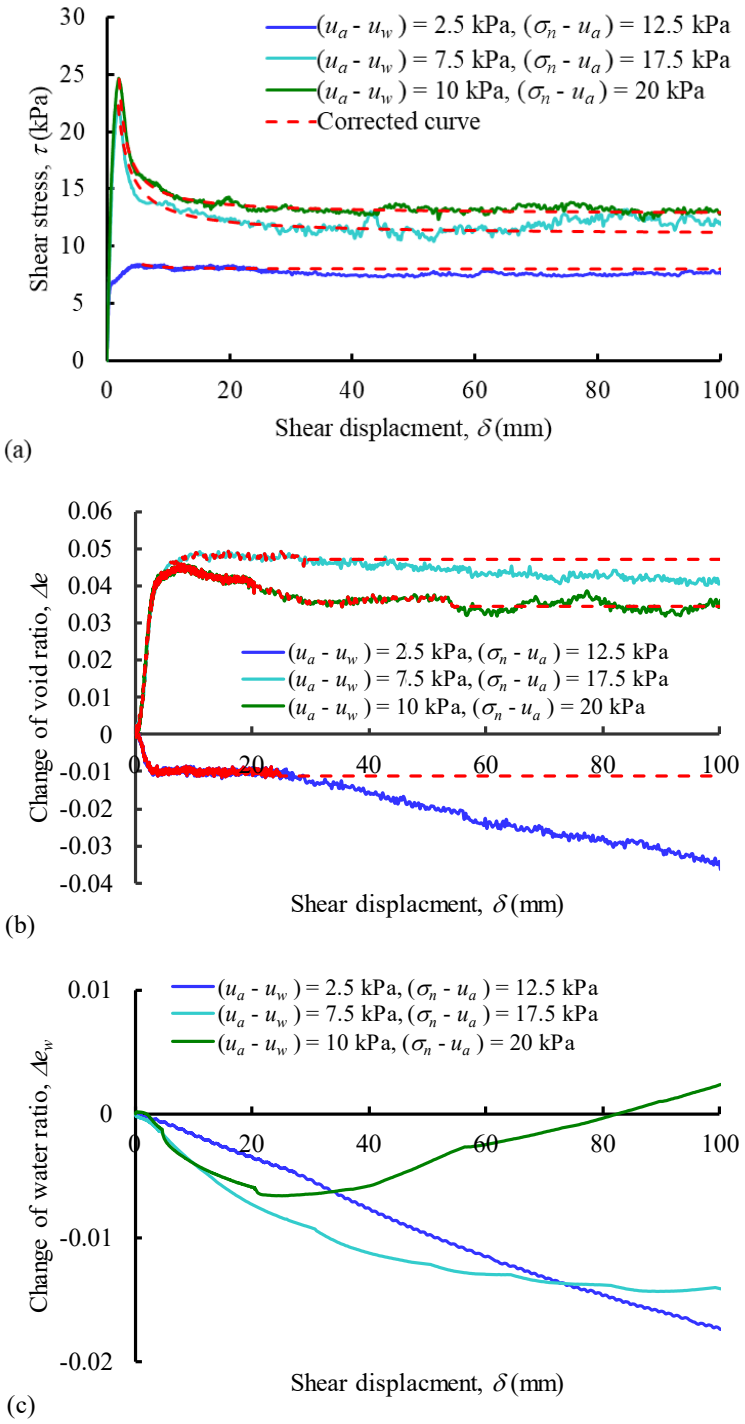

Figure 5.12 Experimental results of the first shearing stage of the unsaturated SP-SM soil

5.3 Residual shear strength envelopes of unsaturated soils

Fredlund et al. (1978) extended the Mohr-Coulomb shear strength criterion of saturated soils in terms of two independent stress state variables, $(u_a - u_w)$ and $(\sigma_n - u_a)$, to unsaturated soil

mechanics. This equation can be modified to interpret the residual shear strength of unsaturated soils as below:

$$\tau_r = c_r' + (\sigma_n - u_a)\tan(\phi_r^a) + (u_a - u_w)\tan(\phi_r^b) \quad (5.1)$$

where c_r' is the effective residual cohesion of the soil in saturated condition, which typically is equal to 0; ϕ_r^a is the residual friction angle with respect to net normal stress; ϕ_r^b is the residual friction angle with respect to matric suction; $(\sigma_n - u_a)$ is the net normal stress; $(u_a - u_w)$ is the matric suction.

5.3.1 IHT soil

Figure 5.13a shows the envelopes of the residual shear strength of the IHT soil with respect to the net normal stress. The relationship between the residual shear strength and the net normal stress is linear at any matric suction state. For this reason, the envelopes of the residual shear strength with respect to net normal stress can be fitted by using the equation below.

$$\tau_r = c_{r,a} + (\sigma_n - u_a)\tan(\phi_r^a) \quad (5.2)$$

where $c_{r,a} = c_r' + (u_a - u_w)\tan(\phi_r^b)$ is the apparent residual cohesion.

The linear envelopes with corresponding values of ϕ_r^a under different matric suctions are presented in Figure 5.13a. The coefficient of determintaion, R^2, values for the linear envelopes range between 0.96 and 1. It can be found that the matric suction has a significant influence on the behavior of residual shear strength envelopes. For the IHT soil in saturated condition, $c_{r,a} = c_r' = 0$. The value of $c_{r,a}$ increases significantly with an increase in the matric suction. In addition, $\tan(\phi_r^a)$ also varies with matric suction instead of being constant.

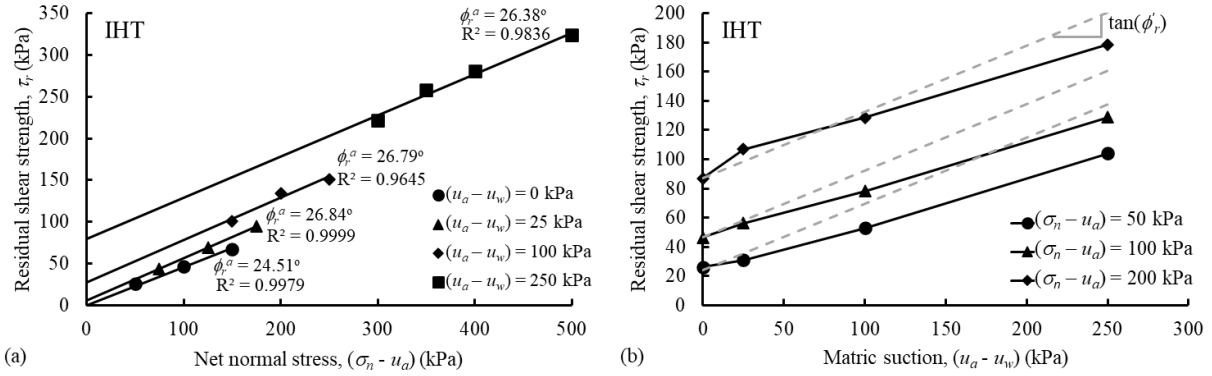

Figure 5.13 Envelopes of residual shear strength of the IHT soil: (a) envelopes with respect to the net normal stress; (b) envelopes with respect to the matric suction (estimated using the linear fitting relationhips in (a))

Figure 5.14a presents the variation of tan(ϕ_r^a) with the matric suction of the IHT soil. It can be found the values of ϕ_r^a of unsaturated soils are higher than the value of the effctive residual friction angle of saturated soils (ϕ_r'). tan(ϕ_r^a) increases with increasing matric suction when the matric suction is lower than 50 kPa. However, after the matric suction exceeds 50 kPa, tan(ϕ_r^a) decreases slightly with increasing matric suction. This phenominon may be explained by the postulation of Toll and Ong (2003) that was proposed to interpret the behavior of unsaturated soils at critical state. When matric suction is in a relatively low range (i.e., 0 – 50 kPa for the studied IHT soil), the local degree of saturation in shear zone is relatively high and the higher matric suction can increase the granularity and stiffness of aggregates of soil particles, which can contribute to a higher ϕ_r^a. However, when matric suction is in a relatively high range (i.e., higher than 50 kPa for the studied IHT soil), the local degree of saturation in shear zone is relatively low; thus, the aggregates will break down due to the lower degree of saturation, which can contribute to a lower ϕ_r^a.

Figure 5.14b presents the variation of $c_{r,a}$ with the matric suction of the IHT soil. The relationship between $c_{r,a}$ and the matric suction appears to be linear. The slope of the linear relationship is lower than the value of tan(ϕ_r'). In other words, the value of ϕ_r^b is a constant lower than ϕ_r' and independent of the matric suction.

Figure 5.13b shows the envelopes of the residual shear strength of the IHT soil with respect to the matric suction. In the suction-controlled ring shear tests, the residual shear strength were not

measured under the same net nomral stress (Figure 5.13a). For this reason, the residual shear strength under the same net normal stress shown in Figure 5.13b were obtained by calculations using the linear fitting equations (Equation 5.2) in Figure 5.13a. For the net normal stress of 50 kPa, the residual shear strength increases with the matric suction linearly. For the net normal stress of 200 kPa, the residual shear strength increases with the matric suction non-linearly; in other words, the increase rate at $(u_a - u_w) > 25$ kPa is lower than the increase rate at $(u_a - u_w) < 25$ kPa. In addition, the initial increasing rate of the residual shear strength increases with net normal stress; for the net normal stress of 200 kPa, the initial increasing rate is higher than $\tan(\phi_r')$. This phenomenon can be attributed to the variation of $\tan(\phi_r^a)$ with matric suction. At a low net normal stress, the variation of $\tan(\phi_r^a)$ cannot significantly influence the residual shear strength; however, at a high net normal stress, the variation of $\tan(\phi_r^a)$ can have significant influence on the residual shear strength.

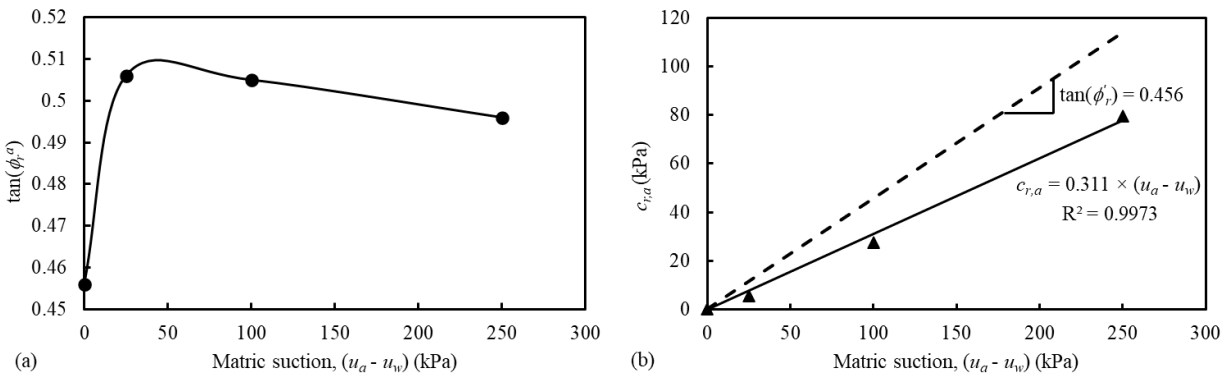

Figure 5.14 Variation of $\tan(\phi_r^a)$ and $c_{r,a}$ with matric suction of the IHT soil: (a) variation of $\tan(\phi_r^a)$; (b) variation of $c_{r,a}$

5.3.2 SP-SM soil

Figure 5.15a shows the envelopes of the residual shear strength of the SP-SM soil with respect to the net normal stress. The relationship between the residual shear strength and the net normal stress is linear at any matric suction state. Thus, the residual shear strength envelopes of the SP-SM soil can also be fitted by using Equation 5.2. The linear envelopes with the corresponding values of the R^2 and ϕ_r^a are presented in Figure 5.15a. It can be found $c_{r,a} = c_r' = 0$ for the SP-SM soil in saturated condition. $c_{r,a}$ increases with the matric suction. The matric suction has a significant influence on the value of ϕ_r^a.

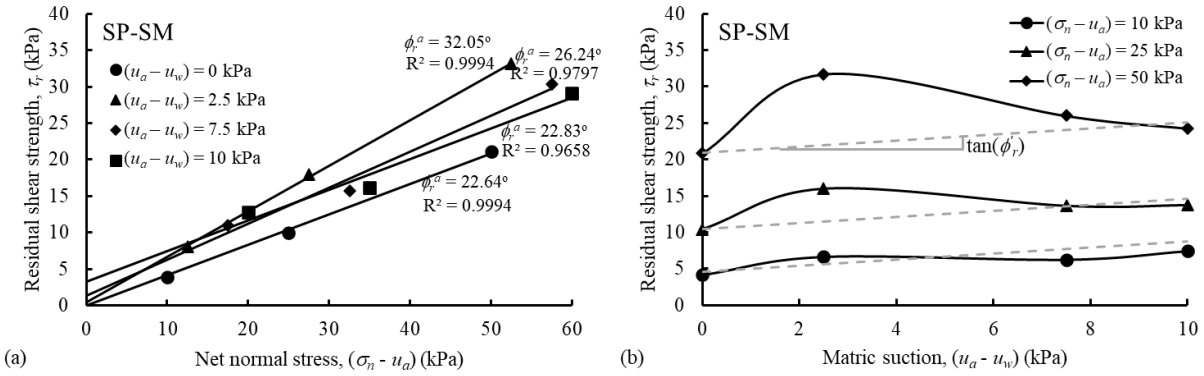

Figure 5.15 Envelopes of residual shear strength of the SP-SM soil: (a) envelopes with respect to the net normal stress; (b) envelopes with respect to the matric suction (estimated using the linear fitting relationhips in (a))

Figure 5.16a presents the variation of tan(ϕ_r^a) with the matric suction of the SP-SM soil. Similar with the IHT soil, tan(ϕ_r^a) of the SP-SM soil increases with the matric suction at first and then decreases when the matric suction exceeds a certain value (e.g., 2.5 kPa for the studied SP-SM soil). However, in comparison to the IHT soil, the variaton of tan(ϕ_r^a) of the SP-SM soil is more obvious. At the matric suction 10 kPa, tan(ϕ_r^a) decreases to the value equal to tan(ϕ_r'). This may indicate that the matric suction will not influence the tan(ϕ_r^a) of the SP-SM soil after the matric suction is greater than 10 kPa. However, no experimental data is provided for the matric suction greater than 10 kPa in this research.

Figure 5.16b presents the variation of $c_{r,a}$ with the matric suction of the SP-SM soil. The linear correlation between the $c_{r,a}$ and the matric suction for the SP-SM is not as good as the IHT soil. However, R^2 is still as high as 0.93 for the SP-SM. This means the value of ϕ_r^b of the SP-SM soil can also be assumed as a constant lower than ϕ_r' and independent of the matric suction.

Figure 5.15b shows the envelopes of the residual shear strength of the SP-SM soil with respect to the matric suction. As discussed in section 5.3.1, the residual shear strength under the same net normal stress shown in Figure 5.15b were obtained by calculations using the linear fitting equations (Equation 5.2) in Figure 5.15a. For the net normal stress of 10 kPa, the residual shear strength increases with the matric suction; after the matric suction exceeds 2.5 kPa, the variation of the residual shear strength with the matric suction is not obvious. For the net normal stress of 50 kPa, the residual shear strength increases with the matric suction; after the matric suction

exceeds 2.5 kPa, the residual shear strength decreases significantly with the matric suction. In addition, the initial increasing rate of the residual shear strength is higher than the value of tan(ϕ_r'). This means, in the studied suction-controlled ring shear tests on the SP-SM soil, the variation of the residual shear strength with the matric suction is significantly influenced by the variation of tan(ϕ_r^a).

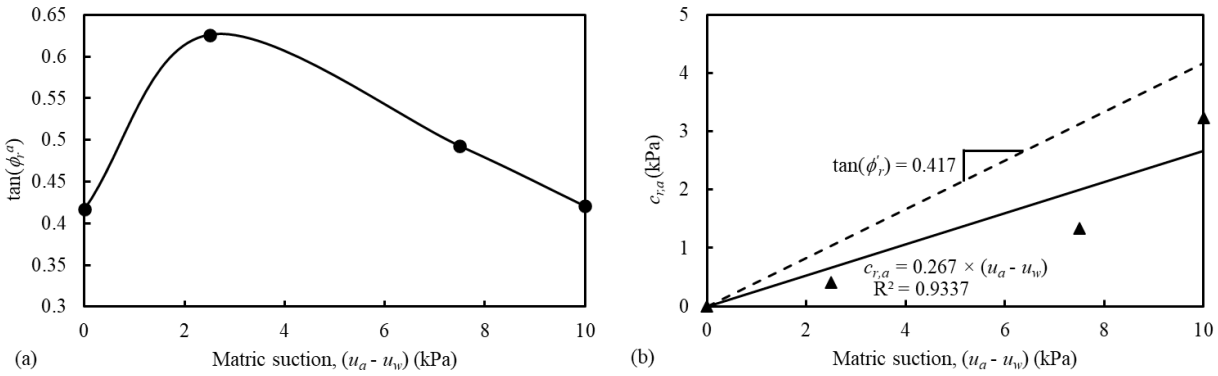

Figure 5.16 Variation of tan(ϕ_r^a) and $c_{r,a}$ with matric suction of the SP-SM soil: (a) variation of tan(ϕ_r^a); (b) variation of $c_{r,a}$

5.3.3 Comparisons between experimental data and prediction models

Three models proposed for the critical shear strength of unsaturated soils were used for the prediction of the ϕ_r^a, ϕ_r^b and the residual shear strength of the studied IHT and SP-SM soil. These three models were discussed in Chapter 2, that include the Sun et al. (2000) model (Equation 2.8), Toll and Ong (2003) model (Equation 2.9) and the modified Gallipoli et al. (2008) model (Equation 2.10). These three models were selected because they can consider the variation of the friction angle with respect to the net normal stress (ϕ^a) with the matric suction.

Figures 5.17 and 5.18 compare the experimental results and the predicted results of the three selected prediction models for the IHT and SP-SM soil, respectively. ϕ_r^b can be defined as tan(ϕ_r^b) = ($c_{r,a} - c_r'$)/($u_a - u_w$). The values of $c_{r,a}$ and ϕ_r^a were determined by fitting the residual shear strength envelopes with respect to net mean stress using Equation 5.2 (Figures 5.13a and 5.15a). Figure 5.17b shows the three prediction models (Equations 2.8 – 2.10) can predict the residual shear strength of the IHT soil well. However, Equations 2.8 and 2.10 under predict tan(ϕ_r^a) of the IHT soil and over predict tan(ϕ_r^b) of the IHT soil (Figure 5.17a). Equation 2.9 can capture the

variation of ϕ_r^a with the matric suction, but it cannot predict the ϕ_r^b well (Figure 5.17a). Figure 5.18 shows the three prediction models (Equations 2.8 – 2.10) cannot well predict the ϕ_r^a, ϕ_r^b and the residual shear strength of the SP-SM soil.

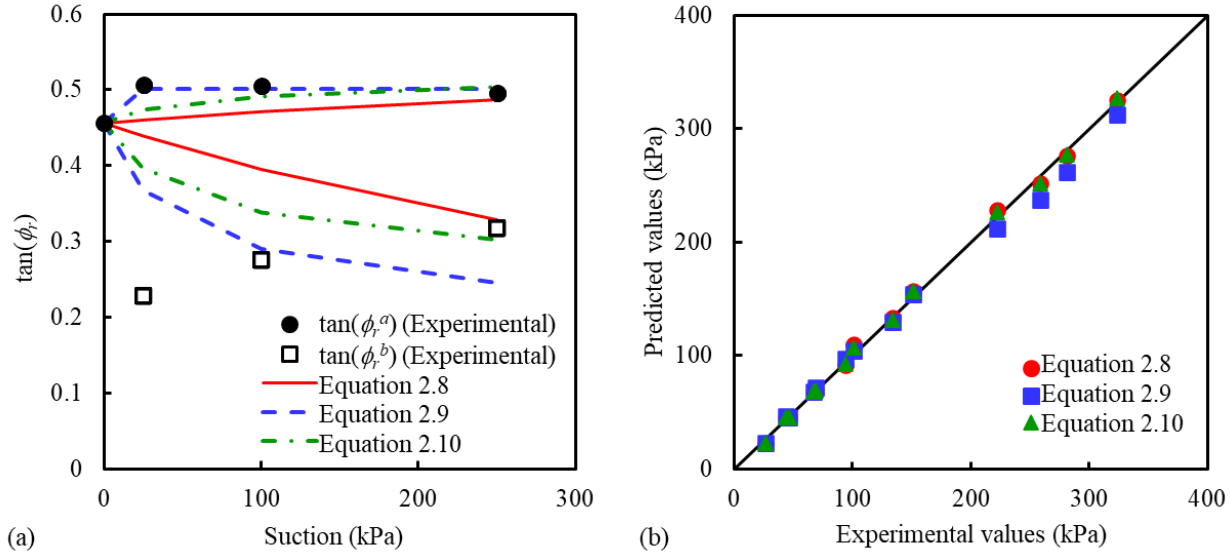

Figure 5.17 Comparisons between the experimental and predicted results of the residual shear strength of the IHT soil: (a) comparisons for tan(ϕ_r^a) and tan(ϕ_r^b); (b) comparisons for the residual shear strength

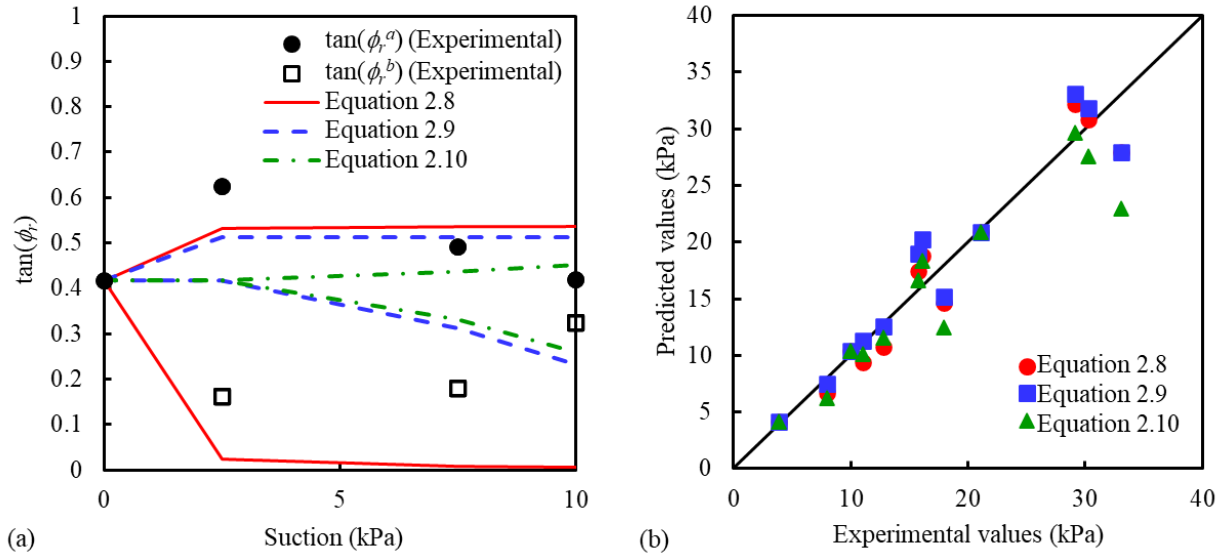

Figure 5.18 Comparisons between the experimental and predicted results of the residual shear strength of the SP-SM soil: (a) comparisons for tan(ϕ_r^a) and tan(ϕ_r^b); (b) comparisons for the residual shear strength

The limitations with respect to the performance of the three models may be attributed to the fact that the variation of ϕ_r^a cannot be captured well by the three models. As shown in Figures 5.17a and 5.18a, the three models can only predict the monotone increase of ϕ_r^a with the matric suction; however, the ϕ_r^a of the studied unsaturated soils increases first and then decreases with the matric suction. For the IHT soil, the decrease of ϕ_r^a is slight; thus, Equation 2.9 can still capture the variation of ϕ_r^a. However, for the SP-SM soil, the decrese of ϕ_r^a is significant; thus, none of the three models can capture the variation of ϕ_r^a. In addition, in Equations 2.9 and 2.10, ϕ^b is assumed to decrease from ϕ' with decreasing degree of saturation; thus, the value of ϕ^b is close to the value of ϕ' within low suction range. However, the experimental data show the value of ϕ_r^b is obviously lower than the value of ϕ_r' within low suction range.

The comparisons shown in Figures 5.17 and 5.18 suggest that the prediction models proposed for the critical shear strength of unsaturated soils have limitations in the prediction of the residual shear strength of the studied unsaturated soils. It is necessary to develop models for the prediction of the residual shear strength of the unsaturated soils that can well capture the variation of ϕ_r^a and ϕ_r^b with the matric suction, respectively.

5.4 Volume change behavior of the IHT soil sheared to the residual state

The void ratio, water ratio and the degree of saturation of the unsaturated soils sheared to the residual state will be discussed in this section. Unfortunately, the initial height of the compacted SP-SM specimens was not measured; thus, the void ratio and the degree of saturation of the specimens sheared to the residual state cannot be calculated accurately. For this reason, only the experimental results of the IHT tests were studied in this section. In addition, during the multistage IHT5 test under ($u_a - u_w$) = 100 kPa, the normal stress was removed for a short time and then was applied again after the first stage and second stage shearing. The variations of the height of the IHT5 specimen due to the rebound and recompression during this process were not measured. In other words, the void ratio and the degree of saturation of the specimens sheared to the residual

state at the second and third stage cannot be determined. For this reason, only the experimental results at the first stage (($u_a - u_w$) = 100 kPa and ($\sigma_n - u_a$) = 150 kPa) were presented for the multistage IHT5 test.

Figure 5.19 shows the relationship between the void ratio of the IHT soil sheared to the residual state and the logarithm of the net normal stress for each value of matric suction. In the ring shear tests, the measurements of the vertical displacement of specimens were usually influenced by the extrusion of the soils during the shearing stage and the penetration of the coarse sands on the top platen during the consolidation stage. Thus, the measured specimen height cannot be used directly as an indicator of specimen void ratio change. Some corrections must be conducted as discussed in section 4.5. The corrected values of the void ratio were presented in Figure 5.19 to represent the void ratio at residual state.

It can be found that the relationship between the residual void ratio and the logarithm of the net normal stress is linear at any matric suction state, which can be fitted by using the equation below. These linear relationships can be identified as the residual state lines.

$$e_r = \Gamma_r + \psi_r \ln\left(\sigma_n - u_a\right) \tag{5.3}$$

where Γ_r and ψ_r is the intercept and slope of the residual state line in the e–ln($\sigma_n - u_a$) plane.

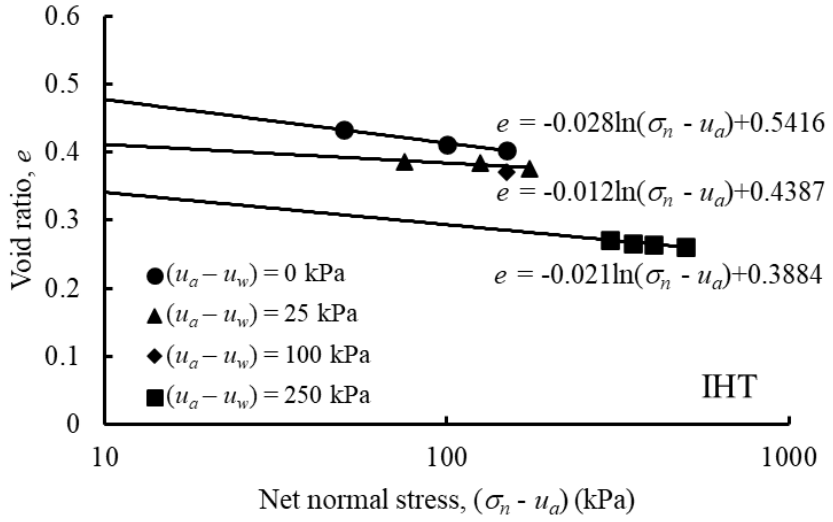

Figure 5.19 Void ratio of the IHT soil sheared to the residual state

Figure 5.20 presents the variation of Γ_r and ψ_r with the matric suction of the IHT soil. The values of Γ_r and ψ_r of unsaturated IHT specimens is lower than the values of the saturated specimens. Γ_r decreases monotonously with increasing matric suction. ψ_r decreases first and then increases with increasing matric suction.

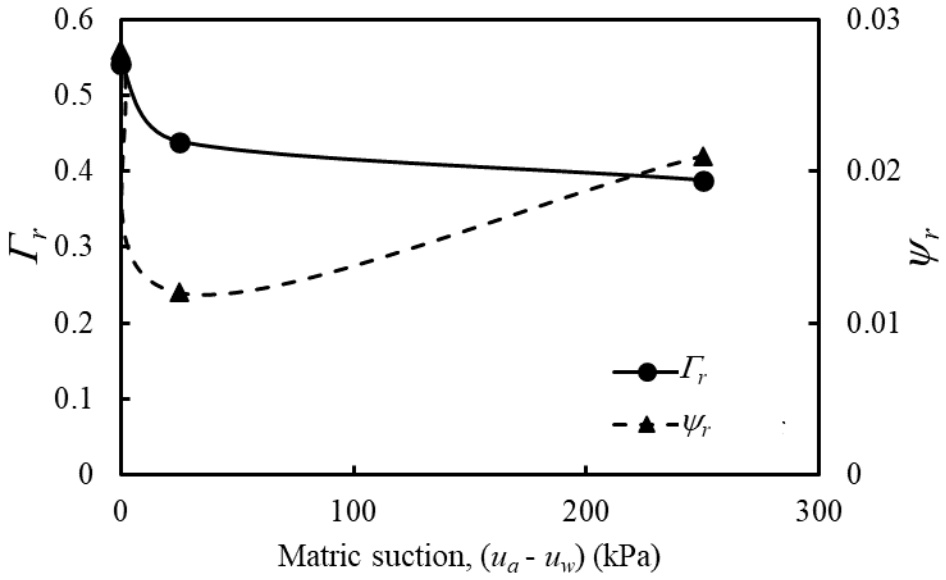

Figure 5.20 Variation of Γ_r and ψ_r with the matric suction of the IHT soil

Figure 5.21 shows the relationship between the water ratio of the IHT soil sheared to the residual state and the logarithm of the net normal stress for each value of matric suction. Figures 5.1, 5.4, 5.5 and 5.6 show, in some ring shear tests, the water ratio was still changing at the end of the shearing stage. This means, in some ring shear tests, the water ratio did not reach the real residual value at the end of the tests even when the shear displacement reaches 100 mm. For this reason, the data in Figure 5.21 are just the water ratio at the end of each of shearing stages which are used to approximately represent the water ratio at the residual state.

It can be found that the relationship between the residual water ratio and the logarithm of the net normal stress is linear at any matric suction state, which can be fitted by using the equation below.

$$e_{w,r} = \Gamma_{w,r} + \psi_{w,r} \ln\left(\sigma_n - u_a\right) \tag{5.4}$$

where $\Gamma_{w,r}$ and $\psi_{w,r}$ is the intercept and slope of the residual state line in the e_w–$\ln(\sigma_n - u_a)$ plane.

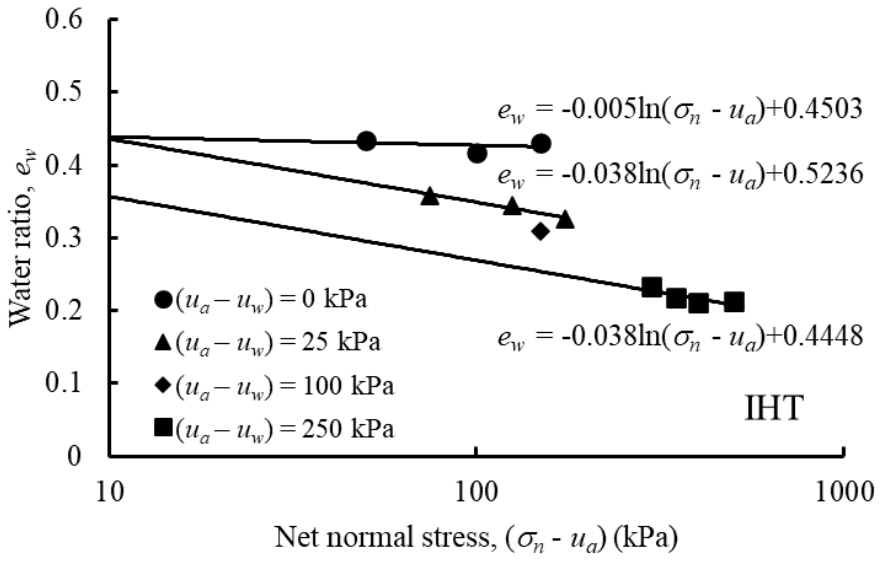

Figure 5.21 Water ratio of the IHT soil sheared to the residual state

Figure 5.22 presents the variation of $\Gamma_{w,r}$ and $\psi_{w,r}$ with the matric suction of the IHT soil. $\Gamma_{w,r}$ increases first with increasing matric suction and then decreases to the value equal to the $\Gamma_{w,r}$ of the saturated soil. $\psi_{w,r}$ of unsaturated soils is significantly higher than $\psi_{w,r}$ of saturated soils. However, the values of $\psi_{w,r}$ are almost same at ($u_a - u_w$) = 25 kPa and 250 kPa.

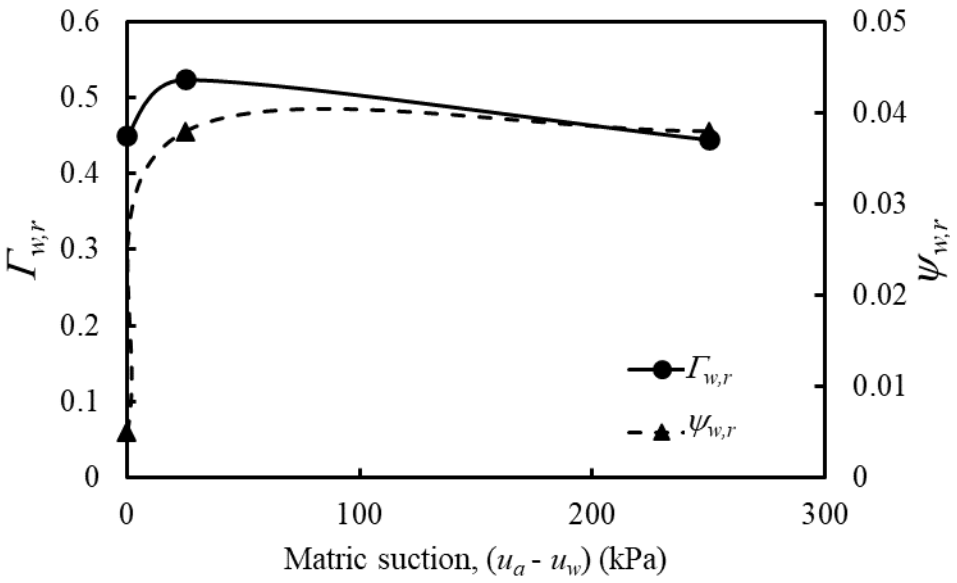

Figure 5.22 Variation of $\Gamma_{w,r}$ and $\psi_{w,r}$ with the matric suction

Figure 5.23 shows the variation of the SWCC of the IHT soil during the multistage suction-controlled ring shear tests. It can be found the degree of saturation at different matric suctions increases after the first consolidation stage in comparison to the corresponding values on the conventional SWCC that was measured under no net normal stress (i.e., the short dash continuous line in Figure 5.23). After shearing, the degree of saturation at different matric suctions further increases in comparison to the corresponding values after the first consolidation stage. The SWCC of the studied IHT soil after being sheared to the displacement of 100 mm were obtained by fitting the experimental data of the suction-controlled ring shear tests using Fredlund and Xing (1994) model (i.e., the solid line in Figure 5.23). This SWCC is close to the SWCC after ring shear tests measured by Infante Sedano and Vanapalli (2011) using a similar IHT soil (i.e., the long dash line in Figure 5.23).

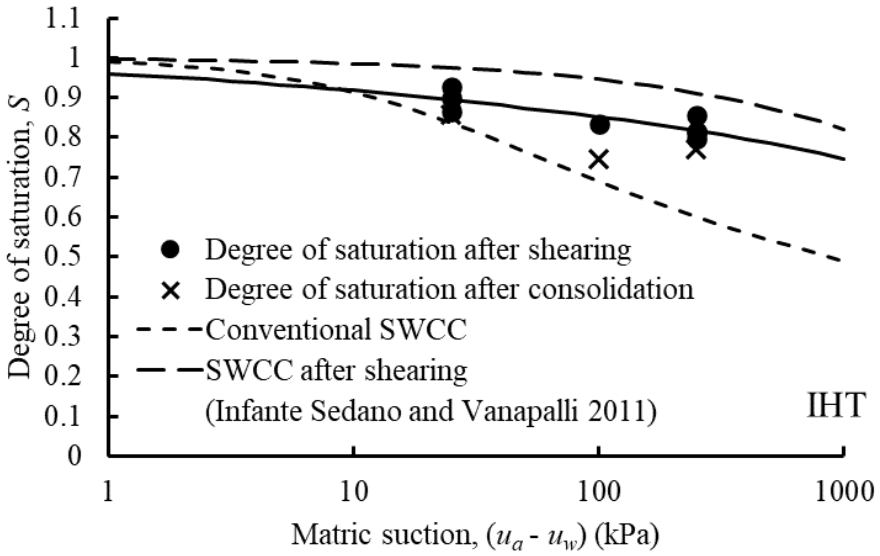

Figure 5.23 Degree of saturation of the IHT soil sheared to the residual state

5.5 Summary

The experimental results of a series of suction-controlled ring shear tests on the IHT and SP-SM soil described in Chapter 4 were presented in this chapter, including: (i) the variations of the shear stress, void ratio and water ratio of the IHT and SP-SM soil during multistage suction-controlled ring shear tests (the maximum shear displacement reached 100 mm); (ii) the envelopes of the residual shear strength of the IHT and SP-SM soil with respect to the net normal stress and matric

suction; (iii) the void ratio, water ratio and degree of saturation of the IHT soil sheared to the residual state.

The experimental results of the unsaturated IHT soil show that, for the first shearing stage of the three multistage tests on unsaturated soils, the shear stress – shear displacement curves exhibit strain-softening behavior, which are associated with compression of specimens. Thus, the reduction in shear strength of unsaturated specimens at first shearing stage can be attributed to the reorientation of the clay particles and the loss of water menisci area in shear zone. For the subsequent shearing stages of the three multistage tests on unsaturated IHT soils, the shear stress – shear displacement curves exhibit apparent peak point. If the shear zones occurred at the same position during the multistage shearings, the apparent peak point in subsequent shearing stages can be attributed to the effort required initially to reorient the particles/aggregates in the direction of shearing under the new net normal stress state. If the shear zones occurred at different positions during the multistage shearings, the apparent peak point in subsequent shearing stages can be attributed to the creation of the new shear zone.

The experimental results of the unsaturated SP-SM soil show that, for the first shearing stage of the three multistage tests on unsaturated soils, the shear stress – shear displacement curves exhibit strain-softening behavior. The increase in matric suction can enhance the brittleness of the unsaturated specimens and make the volume change transfer from compression to dilaiton. The strain-softening behavior of the SP-SM soil can be mainly attributed to the localized dilation inside the shear band. For the subsequent shearing stages of the three multistage tests on unsaturated soils, the shear stress – shear displacement curves exhibit hardening behavior, which are associated with slight compresion of the specimens. This may indicate the effect of net normal stress on the residual shear strength of the SP-SM soil is due to the reduction of the void ratio in shear zone. This is different in comparison to the IHT tests where the change in net normal stress can result in modification of the soil structure in shear zone.

For the IHT soil, the envelope of the residual shear strength with respect to the net normal stress is linear at any matric suction state. The effetive residual cohesion of the saturated IHT soil is equal to 0. The value of the residual friction angle with respect to the net normal stress (ϕ_r^a) increases first with matric suction and then decreases slightly after the matric suction exceeds 50 kPa. The

apparent residual cohesion increases linearly with matric suction, which means the residual friction angle with respect to the matric suction (ϕ_r^b) can be treated as a constant lower than ϕ_r' and independent of the matric suction.

For the SP-SM soil, the envelope of the residual shear strength with respect to the net normal stress is linear at any matric suction state. The effetive residual cohesion of the saturated IHT soil is equal to 0. The value of ϕ_r^a increases first with matric suction and then decreases obviously after the matric suction exceeds 2.5 kPa. ϕ_r^b can be treated as a constant lower than ϕ_r' and independent of the matric suction.

The prediction models proposed for the critical shear strength of unsaturated soils cannot capture well the variation of ϕ_r^a and ϕ_r^b of the studied unsaturated soils. Thus, it is necessary to develop models for the prediction of the residual shear strength of the unsaturated soils that can well capture the variation of ϕ_r^a and ϕ_r^b with the matric suction, respectively.

For the IHT soil, the relationship between the residual void ratio (or the residual water ratio) and the logarithm of the net normal stress is linear at any matric suction state. The compression of the specimen during consolidation and shearing stages can contribute to the increase in the degree of saturation of the unsaturated IHT specimens. As a result, the degree of saturation of the specimens sheared to the residual state is higher than the corresponding values on the conventional SWCC that was measured under no net normal stress.

5.6 References

Bishop, A. W., Green, G. E., Garga, V. K., Andresen, A., and Brown, J. D. 1971. A new ring shear apparatus and its application to the measurement of residual strength. Géotechnique, 21(4): 273-328.

Fredlund, D. G., Morgenstern, N. R., and Widger, R. A. 1978. The shear strength of unsaturated soils. Canadian geotechnical journal, 15(3): 313-321.

Fredlund, D. G., and Xing, A. 1994. Equations for the soil-water characteristic curve. Canadian geotechnical journal, 31(4): 521-532.

Gallipoli, D., Gens, A., Chen, G., and D'Onza, F. 2008. Modelling unsaturated soil behavior during normal consolidation and at critical state. Computers and Geotechnics, 35(6): 825-834.

Heredia, J. E. Y. 2015. Thermo-hydro-mechanical behavior of unsaturated clayey soils via thermo/suction-controlled ring shear testing. Ph. D. Thesis, University of Texas at Arlington, Alington, US.

Hoyos, L. R., Velosa, C. L., and Puppala, A. J. 2014. Residual shear strength of unsaturated soils via suction-controlled ring shear testing. Engineering Geology, 172: 1-11.

Infante Sedano, J. A., and Vanapalli, S. K. 2011. Experimental investigation of the relationship between the critical state shear strength of unsaturated soils and the soil-water characteristic curve. International Journal of Geotechnical Engineering, 5(1): 1-8.

Leroueil, S., and Hight, D. W. 2013. Compacted soils: From physics to hydraulic and mechanical behaviour. Advances in unsaturated soils, 41-59.

Lupini, J. F., Skinner, A. E., and Vaughan, P. R. 1981. The drained residual strength of cohesive soils. Géotechnique, 31(2): 181-213.

Merchán, V., Vaunat, J., Romero, E., and Meca, T. 2008. Experimental study of the influence of suction on the residual friction angle of clays. In proceedings of the First European Conference on Unsaturated Soils, 423-428. CRC Press.

Romero, E., Vaunat, J., and Merchán, V. 2014. Suction effects on the residual shear strength of clays. Journal of Geo-Engineering Sciences, 2(1-2): 17-37.

Sun, D. A., Matsouka, H., Yao, Y. P., and Ichihara, W. 2000. An elasto-plastic model for unsaturated soil in three-dimensional stresses. Soils and foundations, 40(3), 17-28.

Toll, D. G., and Ong, B. H. 2003. Critical-state parameters for an unsaturated residual sandy clay. Géotechnique, 53(1): 93-103.

Vaunat, J., Amador, C., Romero, E., and Djeran-Maigre, I. 2006. Residual strength of a low plasticity clay at high suctions. In Unsaturated Soils 2006, 1279-1289.

Vaunat, J., Merchán, V., Romero, E., and Pineda, J. 2007. Residual strength of clays at high suctions. In Theoretical and Numerical Unsaturated Soil Mechanics, 151-163. Springer, Berlin, Heidelberg.

Velosa, C. L. 2011. Unsaturated soil behavior under large deformations using a fully servo/suction-controlled ring shear apparatus. Ph. D. Thesis, University of Texas at Arlington, Alington, US.

CHAPTER 6 MODEL FOR THE PREDICTION OF RESIDUAL SHEAR STRENGTH OF UNSATURATED SOILS[3]

6.1 Introduction

The shear strength of the unsaturated clayey soils can reduce significantly from a peak value (i.e., peak shear strength, PSS) to a constant low value (i.e., residual shear strength, RSS) when they undergo large shear deformation. This is due to the reorientation of platy clay particles in the shear surface and the loss of suction contribution towards shear strength. In addition, the unsaturated sandy soils can also exhibit a reduction in shear strength due to the loss of water menisci area within the shear band during shearing. Several studies (Hoyos et al. 2014) suggest unsaturated sandy soils can attain residual condition at a relatively small shear deformation. Due to this behavior, the factor of safety of geo-structures in unsaturated soils reduces gradually with the progressive development of large shear deformation. The RSS of unsaturated soils is a crucial parameter that influences the mechanical behaviors of the geo-structures in unsaturated soils undergoing large shear deformation (Qi and Vanapalli 2016; Yang and Vanapalli 2019; Postill et al. 2021). For this reason, a model for predicting the RSS for a wide range of unsaturated soils comprising coarse- to fine-grained soils can be of interest for the geotechnical engineers in the design of geo-structures in unsaturated soils that undergo large shear deformation.

Several models have been proposed for predicting the PSS and critical shear strength (CSS) of unsaturated soils, which have been reviewed by Vanapalli (2009) and Sheng et al. (2011). However, these models are not suitable for the prediction of the RSS of unsaturated soils, since they are proposed based on the experimental studies using suction-controlled triaxial and direct shear tests that can only provide data for limited shear deformation. To-date, a few prediction models (Infante Sedano and Vanapalli 2011; Romero et al. 2014) were proposed for RSS of unsaturated soils. Infante Sedano and Vanapalli (2011) proposed a prediction model for the RSS of unsaturated soils based on two independent stress state variables (i.e., net normal stress and matric suction) by

[3] The contents presented in this chapter are from a manuscript: **Yang, X.,** and Vanapalli, S. K. 2022. Model for the prediction of residual shear strength of unsaturated soils. (Under peer review with a Journal)

extending an approach proposed for predicting the PSS by Vanapalli et al. (1996) that requires the information of the effective shear strength parameters, SWCC and a fitting parameter. This model performs well for the experimental results that constitute two multistage ring shear tests performed by Infante Sedano and Vanapalli (2011) on unsaturated IHT specimens. Romero et al. (2014) proposed another model based on the total normal stress (σ_n) and total suction (Ψ) by assuming a linear relationship between the residual stress ratio (τ_r/σ_n) and the effective suction (i.e., the product of total suction, Ψ and degree of saturation, S). This model was tested for the suction-controlled ring shear tests via vapor equilibrium technique on several unsaturated clayey soils; thus, it is suitable for the unsaturated soils under high suction range.

In this chapter, a model is proposed for the prediction of the RSS for a wide range of unsaturated soils comprising coarse- to fine-grained soils. The model is formulated based on the experimental studies of the RSS of various unsaturated soils using suction-controlled ring shear tests based only on the axis-translation technique, where the suction change in unsaturated soils is typically associated with liquid phase flow. For this purpose, five sets of experimental data of suction-controlled ring shear tests were analyzed, including two sets of tests on unsaturated SP-SM and IHT soil from this study and three sets of tests on unsaturated SM, SC-SM and CH soil collected from the literature. The capability of the proposed model is validated for predicting the RSS, apparent residual cohesion ($c_{r,a}$) and the residual friction angle with respect to net normal stress (ϕ_r^a) of the five studied unsaturated soils.

6.2 Investigated soils

In recent years, several suction-controlled ring shear tests based on the axis-translation technique have been reported in the literature (Infante Sedano and Vanapalli 2011, Hoyos et al. 2014; Heredia 2015) for different unsaturated soils. The suction-controlled ring shear tests of Infante Sedano and Vanapalli (2011) were conducted under a fixed net normal stress; in other words, the behaviors of ϕ_r^a cannot be analyzed in this set of data. For this reason, another three sets of suction-controlled ring shear data on SM, SC-SM and CH (Hoyos et al. 2014; Heredia 2015) were selected for study. These three sets of data collected from the literature and the two sets of data obtained in this study were used for the development of a prediction model of the RSS that can be used for a wide range

of unsaturated soils comprising coarse- to fine-grained soils. The information of these investigated materials and corresponding testing programs are summarized in Table 6.1.

Figure 6.1a summarizes the SWCC of studied non-plastic soils. The matric suction values applied in the tests on SM (Hoyos et al. 2014) are higher than the suction at inflection point (Figure 6.1a). Therefore, the RSS behavior of non-plastic soil for matric suction values lower than the inflection point cannot be studied based on this set of experimental data. Thus, the set of suction-controlled ring shear tests on SP-SM conducted in this study considers the matric suctions lower than the inflection point (Figure 6.1a). Figure 6.1b summarizes the SWCC of studied plastic soils. The SC-CM has a I_p = 6.2 (Hoyos et al. 2014), while the CH has a I_p = 38 (Heredia 2015). The set of suction-controlled ring shear tests on IHT with I_p = 19 conducted in this study fills up the gap between SC-SM and CH (Figure 6.1b).

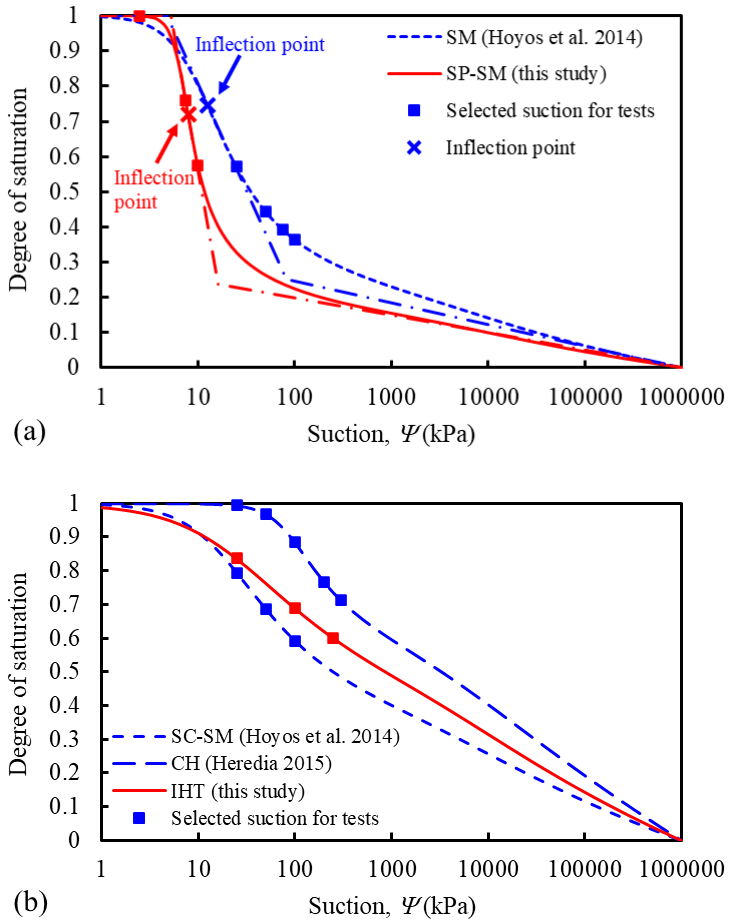

Figure 6.1 Soil-water characteristic curves of studied materials: (a) non-plastic soils; (b) plastic soils

Table 6.1 Properties of soils along with testing program details

	SP-SM (This study)	IHT (This study)	SM (Hoyos et al. 2014)	SC-SM (Hoyos et al. 2014)	CH (Heredia 2015)
Sand (%)	89.59	28	83.6	60	-
Silt (%)	10.41	42	9.8	34.05	-
Clay (%)		30	6.6	5.95	-
Liquid limit (%)	-	36	-	26.4	67
Plastic limit (%)	-	17	-	20.2	29
Plasticity index (%)	-	19	-	6.2	38
Specific gravity	2.75	2.72	2.68	2.71	2.7
Maximum dry density, $\gamma_{d,max}$ (g/cm^3)	1.75 (Static compaction)	1.79 (Static compaction)	1.84 (Standard Proctor compaction)	1.33 (Standard Proctor compaction)	-
Optimum water content (%)	20 (Static compaction)	18 (Static compaction)	10.5 (Standard Proctor compaction)	26 (Standard Proctor compaction)	-
Initial water content of specimens (%)	18	15	Corresponding to suction value slightly less than target suction according to SWCC	Corresponding to suction value slightly less than target suction according to SWCC	-
Specimen preparation technique	Static compaction (375 kPa vertical stress)	Static compaction (375 kPa vertical stress)	Static compaction (to a dry unit weight of 95% of the corresponding $\gamma_{d,max}$)	Static compaction (to a dry unit weight of 95% of the corresponding $\gamma_{d,max}$)	-
Consolidated drained ring shear tests on saturated specimens	σ_n = 10, 25, 50 kPa (single-stage tests)	σ_n = 50, 100, 150 kPa (single-stage tests)	σ_n = 25, 50, 100 kPa (multistage tests)	σ_n = 25, 50, 75, 100, 200 kPa (multistage tests)	-
Consolidated drained ring shear tests on unsaturated specimens	$(u_a - u_w)$ = 2.5, 7.5, 10 kPa (multistage tests)	$(u_a - u_w)$ = 25, 100, 250 kPa (multistage tests)	$(u_a - u_w)$ = 25, 50, 75, 100 kPa (multistage tests)	$(u_a - u_w)$ = 25, 50, 100 kPa (multistage tests)	$(u_a - u_w)$ = 25, 50, 100, 200, 300 kPa (single-stage tests)
Shearing rate (deg/min)	0.024	0.024	0.023	0.023	0.023

6.3 Envelopes of residual shear strength of unsaturated soils

The values of RSS for all the five sets of experimental data investigated in this chapter were determined using the approximate method proposed in section 4.5.2. The RSS values for the five sets of suction-controlled ring shear tests are presented in Figure 6.2. The envelopes of RSS of unsaturated soils with respect to net normal stress were well fitted by using a linear function expressed as Equation 6.1.

$$\tau_r = c_{r,a} + (\sigma_n - u_a)\tan\phi_r^a \tag{6.1}$$

where τ_r is the residual shear strength; $(\sigma_n - u_a)$ is net normal stress; $c_{r,a}$ is the apparent residual cohesion; ϕ_r^a is the residual friction angle with respect to net normal stress.

The linear envelopes with corresponding values of ϕ_r^a are presented in Figure 6.2 for the five sets of tests, respectively. It can be found that the matric suction has a significant influence on the behavior of RSS envelopes for different unsaturated soils. For all the five unsaturated soils, $c_{r,a}$ increases significantly with matric suction and $\tan(\phi_r^a)$ also varies with matric suction instead of being constant.

The variation of the values of $\tan(\phi_r^a) - \tan(\phi_r')$ with the degree of saturation are summarized in Figure 6.3 for the five sets of experimental data (i.e., solid circles in Figure 6.3). During desaturation, the value of $\tan(\phi_r^a)$ typically increases at first and then decreases to $\tan(\phi_r')$ with decreasing degree of saturation. These results suggest that higher matric suction values can contribute to a greater $\tan(\phi_r^a)$ when the degree of saturation is relatively large. However, when the degree of saturation is relatively small, $\tan(\phi_r^a)$ decreases gradually with desaturation. In other words, $\tan(\phi_r^a)$ is influenced by the combined effect of matric suction and degree of saturation.

This observation is not consistent with the published research about the PSS and CSS of unsaturated soils (Vanapalli et al. 1996; Wang et al. 2002; Tarantino and Tombolato 2005). These studies showed that, for PSS or CSS, $\tan(\phi^a)$ should be at a constant equal $\tan(\phi')$ independent of the matric suction and degree of saturation. However, there are also several other studies showing the variation of $\tan(\phi^a)$ with matric suction for PSS or CSS (Escario and Saez 1986; Delage and

Graham 1995; Maatouk et al. 1995; Toll and Ong 2003; Estabragh and Javadi 2008; Sivakumar et al. 2010).

Toll and Ong (2003) proposed an explanation for the variation of tan(ϕ^a) for CSS of unsaturated compacted fine-grained soils based on the aggregation structure. As well known, the soil particles of compacted fine-grained soils are aggregated during compaction. In unsaturated condition, the aggregation can be maintained during shearing due to the shear strength provided by suction and can act as large individual particles. Toll and Ong (2003) suggested that, when the pore water is drained out from inter-aggregate pores, suction contributes to a high tan(ϕ^a) due to an increase in the granularity and rigidity of the aggregates. However, when the pore water is drained out from intra-aggregate pores, tan(ϕ^a) decreases with suction as the aggregates break down. Romero et al. (2014) also suggested that the effective suction can contribute to a high total residual friction angle of unsaturated soils due to an increase in the stiffness of the soil/aggregates during desaturation. This means the variation of residual friction angle of unsaturated soils can also be attributed to the aggregation structure even though the specimen has been sheared to residual state.

For this reason, the postulations of Toll and Ong (2003) and Romero et al. (2014) about the aggregation structure can be extended to interpret the variation of tan(ϕ_r^a) with matric suction in this study. During the initial stage of desaturation, where the degree of saturation is high and matric suction is low, the aggregates will be destroyed under large shear displacement and the specimen exhibits a small tan(ϕ_r^a) that is close to tan(ϕ_r'). With the specimen desaturation, the higher matric suction can increase the granularity and stiffness of aggregates. More granular and stiff aggregates can be maintained even at large shear displacement. Such a behavior can contribute to a higher tan(ϕ_r^a). However, as the desaturation continues, the large aggregates start to break down due to low degree of saturation despite a higher stiffness caused by higher matric suction. This results in a decrease in tan(ϕ_r^a).

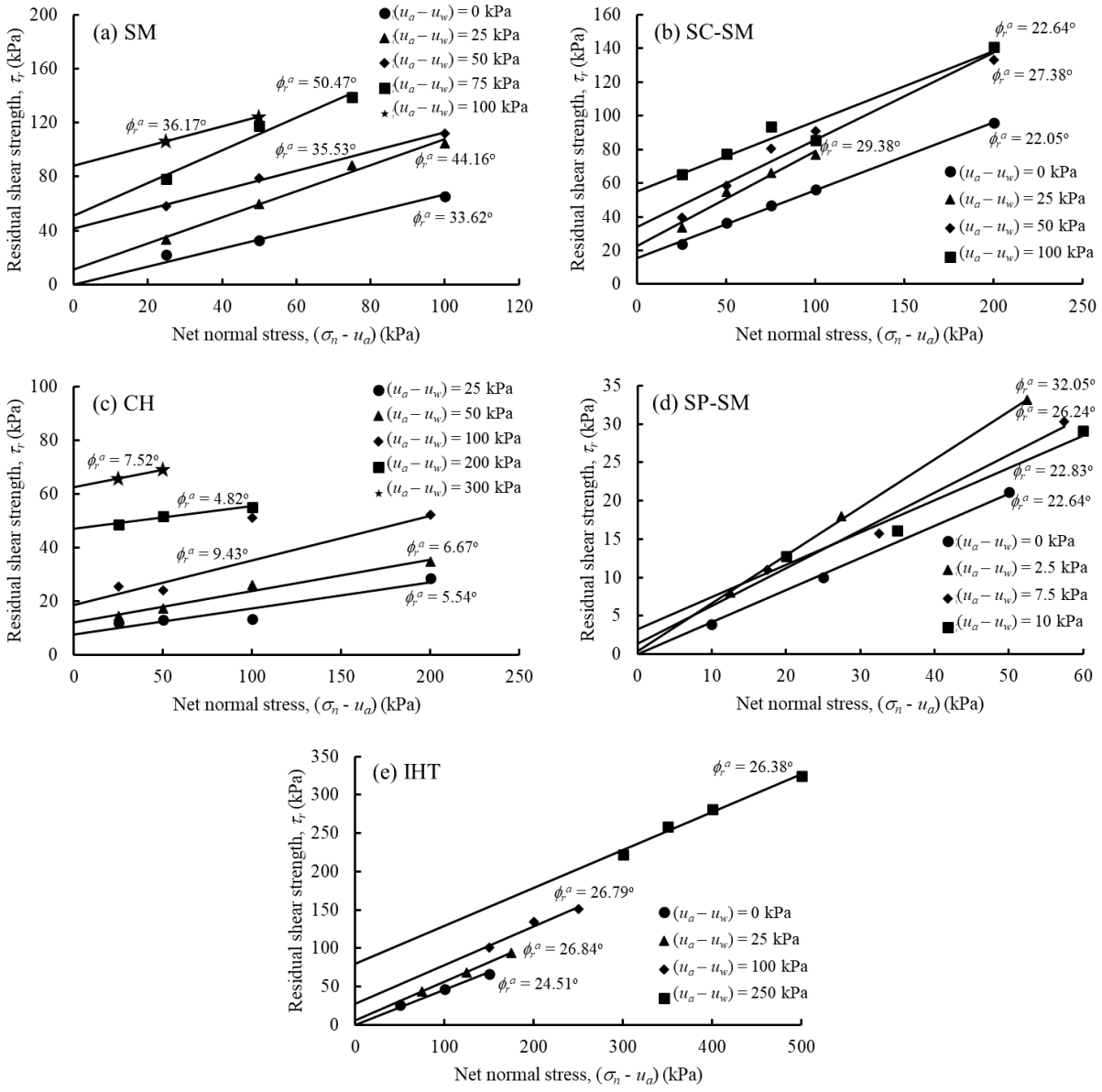

Figure 6.2 Envelopes of residual shear strength with respect to net normal stress: (a) SM (Hoyos et al. 2014); (b) SC-SM (Hoyos et al. 2014); (c) CH (Heredia 2015); (d) SP-SM (this study); (e) IHT (this study)

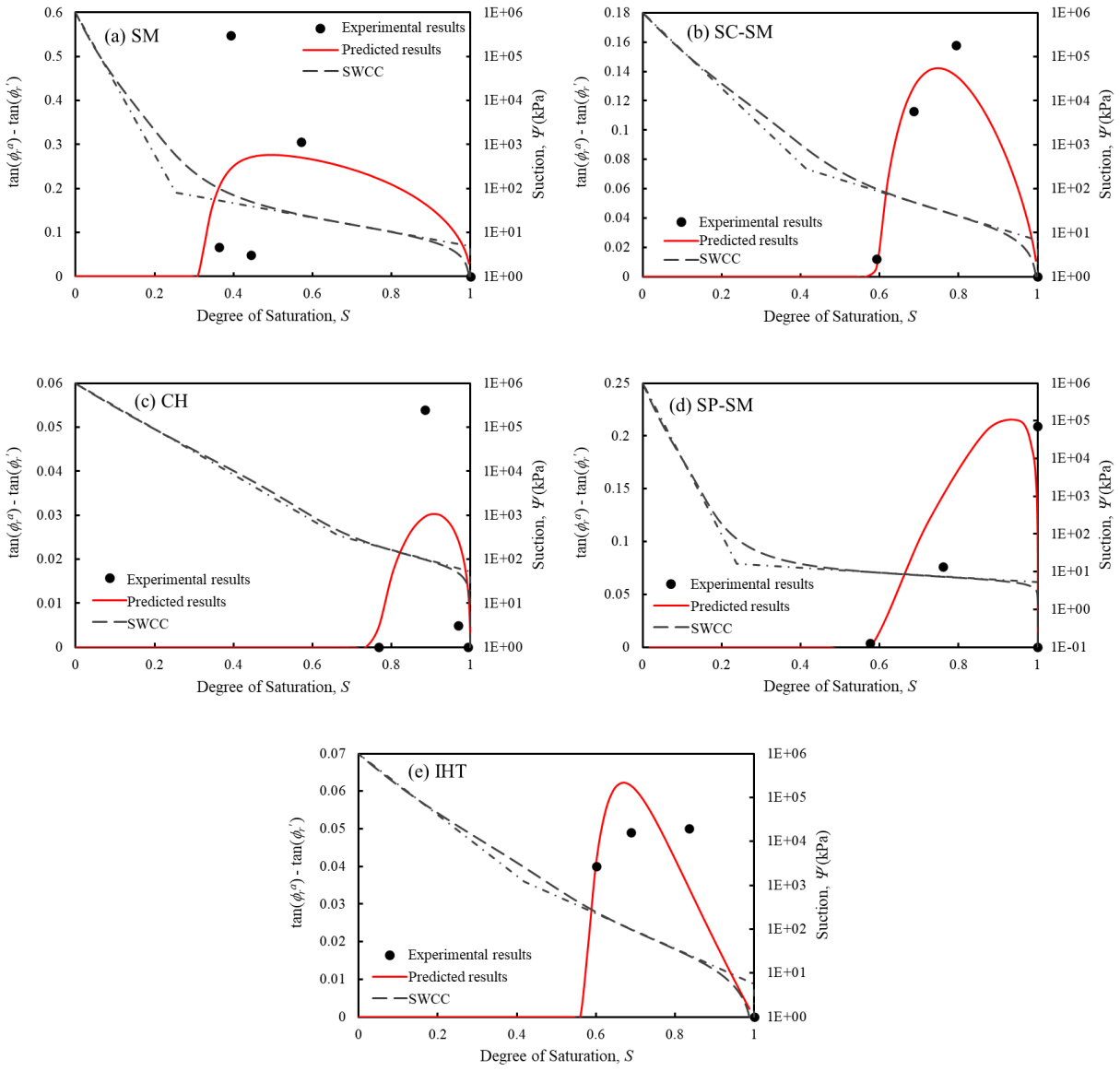

Figure 6.3 Variation of tan(ϕ_r^a) with degree of saturation and corresponding SWCC: (a) SM (Hoyos et al. 2014); (b) SC-SM (Hoyos et al. 2014); (c) CH (Heredia 2015); (d) SP-SM (this study); (e) IHT (this study)

6.4 Model for the prediction of residual shear strength of unsaturated soils

6.4.1 Prediction of residual friction angle with respect to net normal stress, $\tan(\phi_r^a)$

In this study, a linear relationship is assumed between $\tan(\phi_r^a) - \tan(\phi_r')$ and $(u_a - u_w) f(S)$ for the prediction of $\tan(\phi_r^a)$ taking account the combined effect of matric suction and degree of saturation. $f(S)$ represents the contribution of matric suction towards the mechanical behavior of unsaturated soils, which is typically related to the degree of saturation (Alonso et al. 2010; Lu et al. 2010; Romero et al. 2014).

The experimental results used in the present study are developed based on axis-translation technique for the unsaturated soils that are within boundary and transition zone (i.e., $S > S_r$). In between these zones the mechanical behavior of unsaturated soils is mainly influenced by the capillary water existing as water menisci among soil particles or aggregates. Therefore, the concept of effective degree of saturation, $(S - S_r)/(1 - S_r)$, (Vanapalli et al. 1996; Tarantino and Tombolato 2005; Alonso et al. 2010; Lu et al. 2010) can be extended to determine the $f(S)$. Several studies (Vanapalli et al. 1998; Lu et al. 2010) suggested the pore water mainly existed as adsorbed water in the soils in the residual zone (i.e., $S < S_r$) where water is transferred through the thin film of adsorbed water or by transfer in the vapor phase. Thus, S_r can be used to represent the volume of adsorbed water.

When an unsaturated specimen is sheared to a large displacement, a part of capillary water within the shear band will be lost due to the generation of large voids caused by local dilation and the rupture of water menisci caused by continuous movement and rotation of soil particles/aggregates. The lost capillary water within the shear band cannot influence the RSS of unsaturated soils. In other words, for the unsaturated soils sheared to residual state, the volume of the lost capillary water due to shearing (represented by S_L) should be removed from the calculation of the effective degree of saturation.

For this reason, the contribution of matric suction to the magnitude of $\tan(\phi_r^a)$ (i.e., $f(S)$) should be represented by the ratio of the remainder volume of capillary water that is in shear band when the specimen is sheared to residual state $(S - S_L - S_r)$ to the total available volume of capillary water

$(1 - S_r)$. Thus, the assumed linear relationship between $\tan(\phi_r^a) - \tan(\phi_r')$ and $(u_a - u_w)f(S)$ can be expressed as Equation 6.2a.

Typically, no capillary water will be lost within the shear band during shearing in saturated condition, while more capillary water will be lost within the shear band during shearing under higher matric suction. In other words, the value of S_L is inversely proportional to the degree of saturation. Such a behavior can be attributed to a greater dilation under higher matric suction, which means there can be a generation of larger voids within the shear band and lower water retention capability. In addition, in a specimen at higher matric suction, more capillary water exists as meniscus water that will rupture easily due to shearing and less capillary water exists as bulk water. Thus, Equation 6.2b is proposed to describe S_L.

$$\tan\left(\phi_r^a\right) = \tan\left(\phi_r'\right) + \alpha_R\left(u_a - u_w\right)\frac{S - S_L - S_r}{1 - S_r} \tag{6.2a}$$

$$S_L = \beta_R\left(1 - \frac{S - S_r}{1 - S_r}\right) \tag{6.2b}$$

where $(u_a - u_w)$ is matric suction; ϕ_r' is effective residual friction angle; S is degree of saturation; S_r is the residual degree of saturation on SWCC; S_L is the loss of degree of saturation in shear band caused by large shear displacement; α_R and β_R are fitting parameters.

The best-fitted curves for the relationship between $\tan(\phi_r^a) - \tan(\phi_r')$ and S using Equation 6.2 are presented in Figure 6.3 (i.e., continuous solid line) for the five sets of experimental data, respectively. It can be found Equation 6.2 can predict $\tan(\phi_r^a)$ when $S > (S_L + S_r)$. However, when $S < (S_L + S_r)$, the value of $\tan(\phi_r^a)$ is assumed to be $\tan(\phi_r')$. The experimental data of suction-controlled ring shear tests based on axis-translation technique are still limited to show the influence of matric suction on $\tan(\phi_r^a)$ when $S < (S_L + S_r)$. On the other hand, the experimental data of suction-controlled ring shear tests based on vapor equilibrium technique (Romero et al. 2014) indicated that total suction can contribute to the total residual friction angle of unsaturated soils even when $S < S_r$. Therefore, Equation 6.2 can only be used to predict $\tan(\phi_r^a)$ for the suction range where $S > (S_L + S_r)$. As for the predictions of $\tan(\phi_r^a)$ when $S < (S_L + S_r)$, more studies are still required.

6.4.2 Prediction of apparent residual cohesion, $c_{r,a}$

The RSS of unsaturated soils due to suction ($\tau_{r,s}$) is defined as the difference between the apparent residual cohesion of unsaturated soil and the effective residual cohesion of saturated soil, i.e., $\tau_{r,s} = c_{r,a} - c_r'$. The values of $c_{r,a}$ can be obtained from the fitted linear envelopes (Equation 6.1) shown in Figure 6.2. Figure 6.4 summarized the relationships between $\tau_{r,s}$ and $(u_a - u_w)$ for the five sets of experimental data. It can be found the relationship between $\tau_{r,s}$ and $(u_a - u_w)$ can be well fitted by using linear functions with, coefficients of determination, R^2 = 0.934 to 0.997. Thus, $c_{r,a}$ can be predicted by using the equation as below.

$$c_{r,a} = c_r' + (u_a - u_w)\tan\phi_r^b \tag{6.3}$$

where c_r' is effective residual cohesion; ϕ_r^b is the residual friction angle with respect to matric suction, which is a constant.

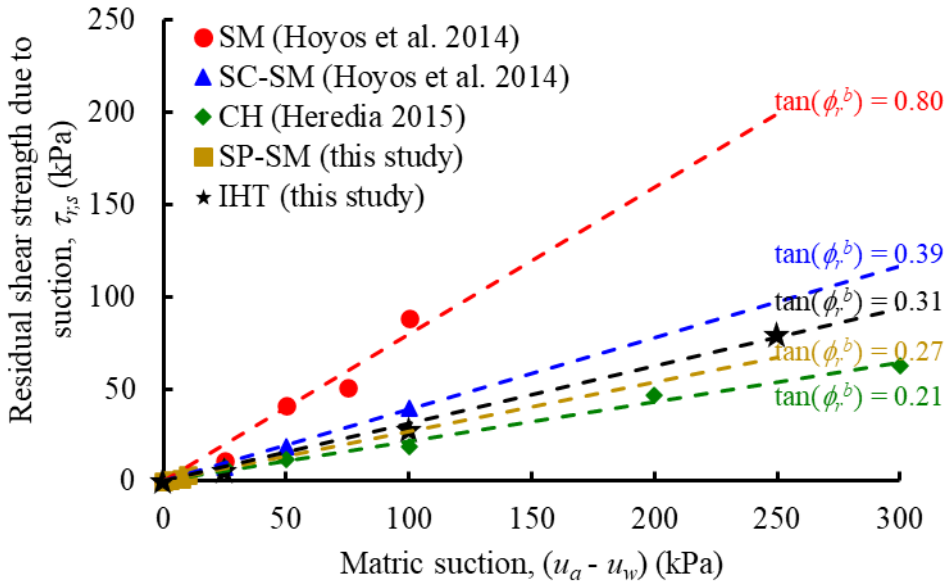

Figure 6.4 Relationship between the residual shear strength due to suction and the matric suction of studied soils

6.4.3 Formulation of the prediction model for RSS of unsaturated soils

A model for predicting the RSS of unsaturated soils can be formulated by combining Equations 6.1 – 6.3, which is shown below.

$$\tau_r = c_r' + (\sigma_n - u_a)\left[\tan\phi_r' + \alpha_R (u_a - u_w)\frac{S - \beta_R \dfrac{1-S}{1-S_r} - S_r}{1-S_r}\right] + (u_a - u_w)\tan\phi_r^b \qquad (6.4)$$

In Equation 6.4, the saturated RSS parameters (c_r' and ϕ_r') can be determined by using drained ring shear tests on saturated specimens. S_r can be determined from the SWCC. The values of α_R and β_R can be determined by best-fitting the relationship between $\tan(\phi_r^a)$ and $(u_a - u_w)$ obtained from suction-controlled ring shear tests using Equation 6.2. The values of ϕ_r^b can be determined by best-fitting the relationship between $c_{r,a}$ and $(u_a - u_w)$ obtained from suction-controlled ring shear tests using Equation 6.3.

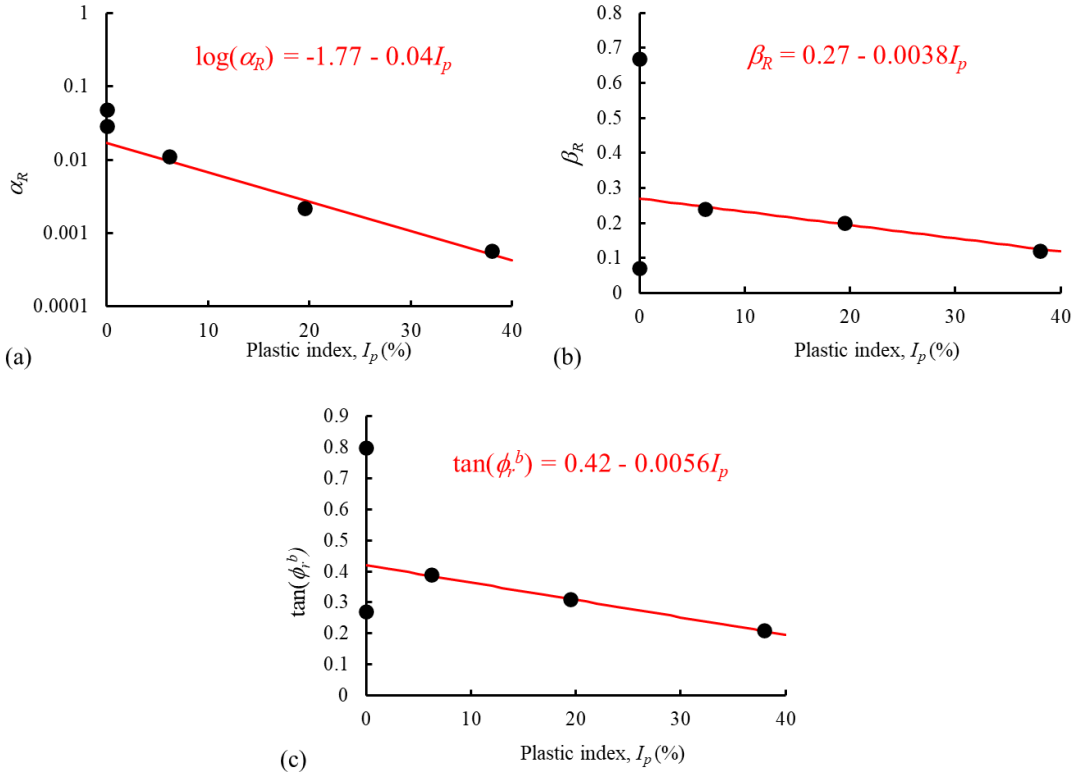

Figure 6.5 Relationship between fitting parameters in the proposed RSS prediction model and the plastic index: (a) α_R; (b) β_R; (c) $\tan(\phi_r^b)$

The relationships between the three fitting parameters (α_R, β_R and ϕ_r^b) and plastic index (I_p) are summarized in Figure 6.5. A good linear relationship can be found for the $\log(\alpha_R) - I_p$ relationship, $\beta_R - I_p$ relationship and $\tan(\phi_r^b) - I_p$ relationship, respectively, for the three plastic soils (i.e., SC-SM, IHT and CH). The corresponding equations for the three relationships are also presented in Figure 6.5. However, the data points of the two non-plastic soils (i.e., SM and SP-SM) do not fall on the linear relationships for the three plastic soils. Such a behavior may be attributed to the mechanical behaviors of non-plastic soils are not significantly dependent on the plastic index. Thus, more studies are still required to build reliable relationships between the fitting parameters (α_R, β_R and ϕ_r^b) and physical parameters of soils. Despite these errors, an approximate approach that can be extended for all soils can still be formulated as below by substituting the equations in Figure 6.5 into Equation 6.4.

$$\tau_r = c_r' + (\sigma_n - u_a)\left[\tan\phi_r' + 10^{(-1.77-0.04I_p)}(u_a - u_w)\frac{S - (0.27 - 0.0038I_p)\frac{1-S}{1-S_r} - S_r}{1-S_r}\right] + (u_a - u_w)(0.42 - 0.0056I_p) \quad (6.5)$$

Figure 6.6 compares the predicted RSS envelopes with respect to matric suction using Equations 6.4 and 6.5 with the experimental results for the five sets of experimental data discussed in this research. In the suction-controlled ring shear tests on the SP-SM and IHT soil, the residual shear strength were not measured under the same net nomral stress (Figures 6.2d and 6.2e). For this reason, the residual shear strength under the same net normal stress shown in Figure 6.6 were obtained by calculations using the linear fitting equations (Equation 6.1) in Figure 6.2. The prediction results based on two prediction models (Equations 2.8 and 2.9) proposed for the critical shear strength of unsaturated soils considering the variation of $\tan(\phi^a)$ were also presented in Figure 6.6 for providing comparisons.

Figure 6.7 compares the predicted values of $\tan(\phi_r^a)$, $c_{r,a}$, and RSS using Equations 6.4 and 6.5 with the experimental values. As discussed in the previous section, Equations 6.4 and 6.5 are invalid at some data points where S was less than $(S_L + S_r)$. Thus, only the experimental and predicted results within the suction range where $S > (S_L + S_r)$ were presented in Figures 6.6 and 6.7. For example, in Figure 6.6a, only the predicted envelopes within $(u_a - u_w) < 50$ kPa were presented.

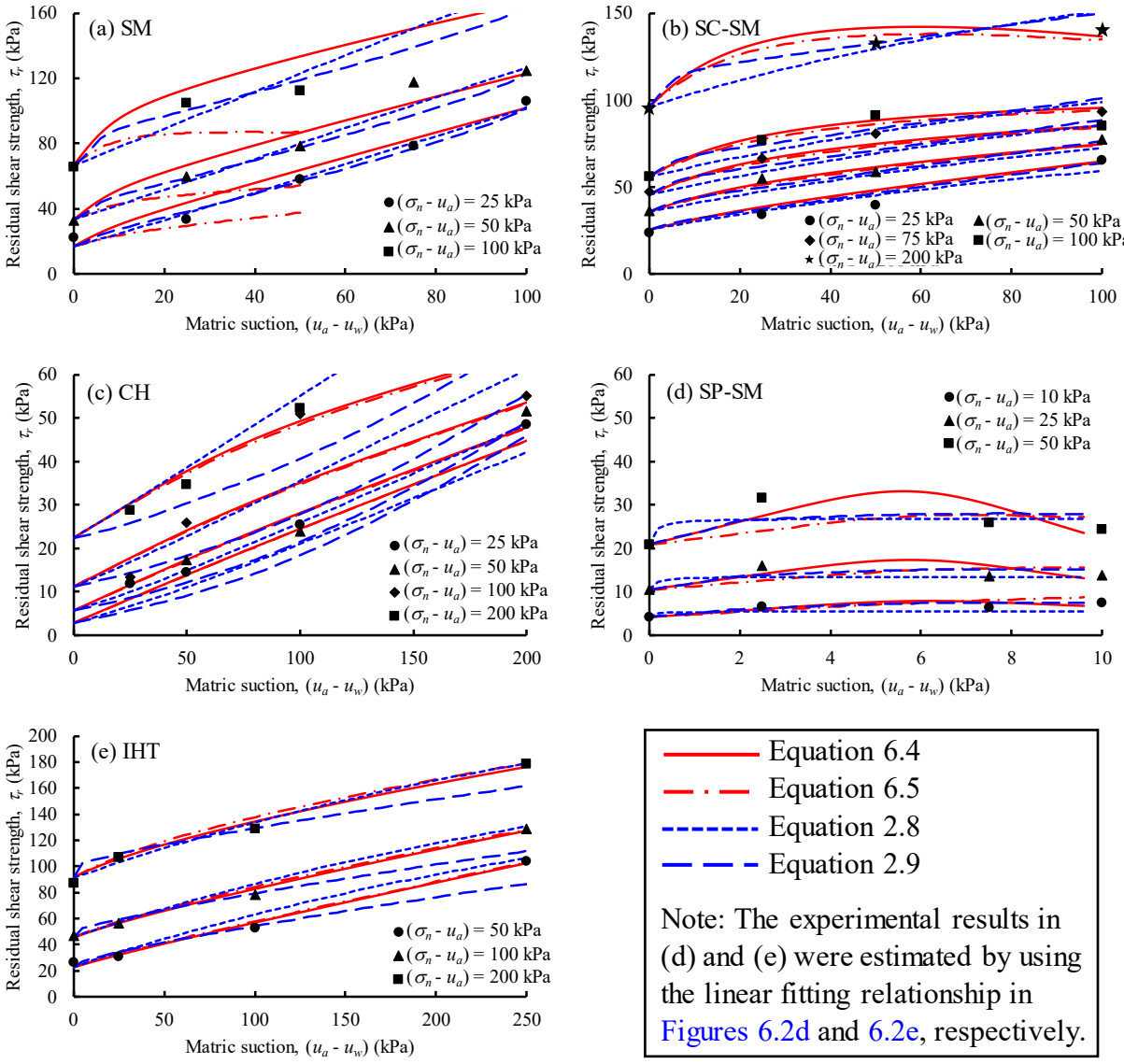

Figure 6.6 Comparison between the experimental and predicted results of residual shear strength envelopes: (a) SM (Hoyos et al. 2014); (b) SC-SM (Hoyos et al. 2014); (c) CH (Heredia 2015); (d) SP-SM (this study); (e) IHT (this study)

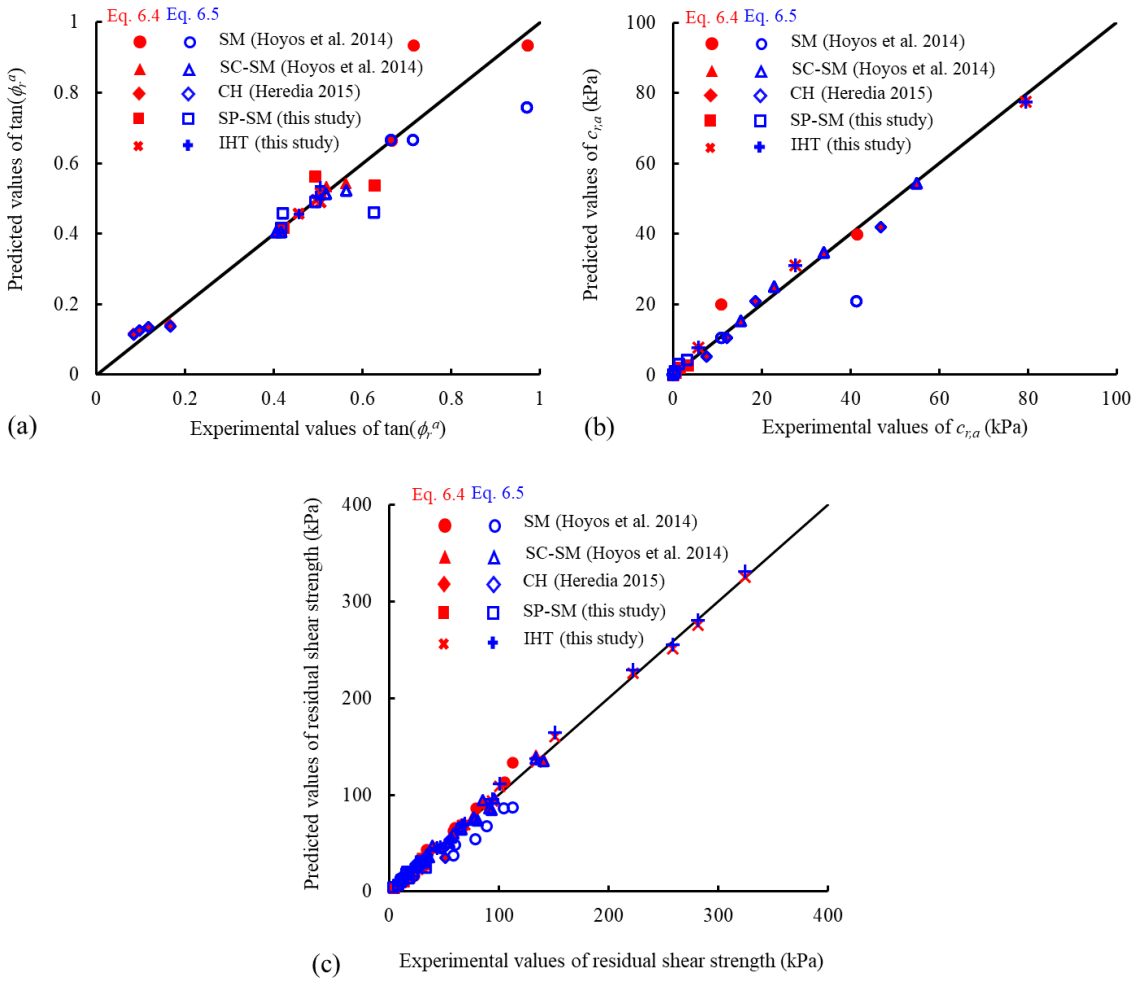

Figure 6.7 Comparison between experimental and predicted values: (a) tan(ϕ_r^a) values; (b) $c_{r,a}$ values; (c) residual shear strength values

The comparison studies suggest that the prediction models proposed for the critical shear strength of unsaturated soils are not suitable for predicting the residual sheaer strength of unaturated soils. The experimental RSS envelope flatten more with increasing matric suction than the predicted results of Equation 2.8 for the five datasets. In other words, Equation 2.8 overestimated the contribution of matric suction to RSS of unsaturated soils. Equation 2.9 performs well for some datasets (e.g., SM); however, it did not provide resonable predictions of RSS for other datasets (e.g., CH).

The best-fitting approach (Equation 6.4) can provide reasonable prediction for the values of tan(ϕ_r^a), $c_{r,a}$, and RSS of unsaturated soils. However, this approach includes three fitting parameters (α_R, β_R and ϕ_r^b) that needs to be determined by best-fitting experimental results of

suction-controlled ring shear tests. The predicted results of the approximate approach (Equation 6.5) are also reasonable for the studied plastic unsaturated soils; however, its performance is not as good as that of Equation 6.4 for the studied non-plastic unsaturated soils. However, the errors can be acceptable considering no fitting parameters are required for this approach. Equation 6.5 only includes four basic parameters of soils (i.e., c_r', ϕ_r', S_r and I_p) that can be determined using conventional geotechnical laboratory tests.

6.4.4 Parametric study

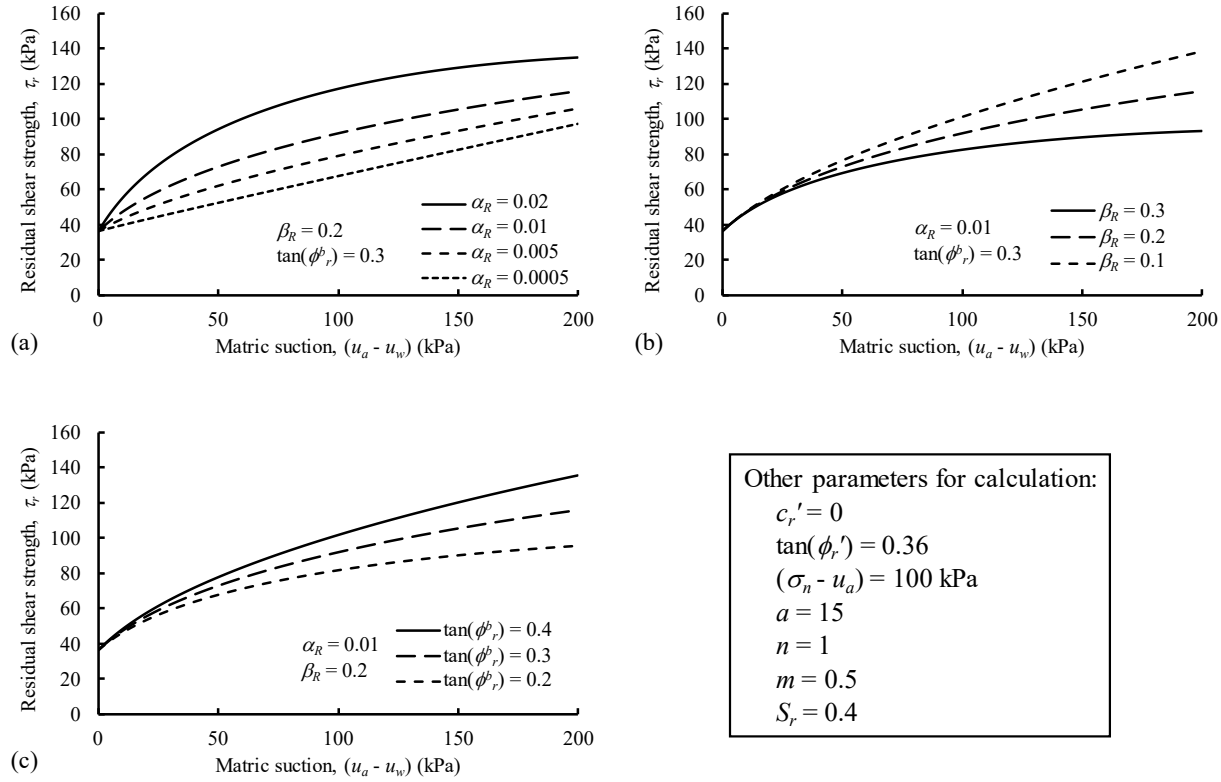

Figure 6.8 Influence of parameters (α_R, β_R and ϕ_r^b) on the predicted RSS envelope with respect to matric suction: (a) influence of α_R; (b) influence of β_R; (c) influence of $\tan(\phi_r^b)$

Figure 6.8 shows the influence of the three parameters (α_R, β_R and ϕ_r^b) in Equation 6.4 on the predicted RSS envelope with respect to matric suction. The selection of values of α_R, β_R and ϕ_r^b for parametric studies are based on the value ranges shown in Figure 6.5.

Figure 6.8a suggests the RSS envelope is a curved line when α_R = 0.02 and it gradually changes to a straight line with decreasing α_R. α_R can significantly influence the initial slope of RSS envelope within the low suction range. α_R controls the enhancement of $\tan(\phi_r^a)$ caused by suction. The lower plastic soil typically has higher α_R value (Figure 6.5a); thus, the enhancement of $\tan(\phi_r^a)$ caused by suction is more significant within low suction range. In other words, the RSS envelope of low plastic soils tend to exhibit curved envelope. This is consistent with the experimental observations (Figures 6.3 and 6.6). In addition, the influence of α_R can be magnified by net normal stress. For this reason, the influence of α_R is more significant when net normal stress is higher.

Figure 6.8b suggests β_R does not have influence on the initial slope of RSS envelope. However, the RSS envelope flattens more with increasing matric suction when β_R is higher. β_R controls the volume of lost capillary water due to shearing. A higher value of β_R means more loss of capillary water during shearing. As a result, the contribution of suction to RSS is reduced more significantly (i.e., the RSS envelope flattens more) when β_R is higher.

Figure 6.8c suggests the influence of $\tan(\phi_r^b)$ is similar with the influence of β_R. $\tan(\phi_r^b)$ has a minor influence on the initial slope of RSS envelope. That is because the value of $\tan(\phi_r^b)$ typically varies within a relatively small range for different soils (Figure 6.5c). The RSS envelope flattens more with an increase in the matric suction when $\tan(\phi_r^b)$ is lower.

6.5 Summary

A model is proposed in this chapter for the prediction of the RSS for a wide range of unsaturated soils comprising coarse- to fine-grained soils. In addition to the two sets of data obtained in this study (i.e., SP-SM and IHT), another three sets of experimental data (i.e., SM, SC-SM and CH) of suction-controlled ring shear tests based on axis-translation technique were collected from the literature in the development of the prediction model.

Based on the five sets of experimental data, the behavior of the RSS of unsaturated soils were discussed. It can be found that the envelops of RSS of unsaturated soils with respect to net normal stress are linear. The apparent residual cohesion ($c_{r,a}$) increases significantly with matric suction. Reasonably good linear relationship between $c_{r,a}$ and matric suction ($u_a - u_w$) were observed for

all the five sets of data. The residual friction angle with respect to net normal stress (ϕ_r^a) varies with matric suction instead of being constant. During desaturation, the value of $\tan(\phi_r^a)$ typically increases at first and then decreases to $\tan(\phi_r')$ with decreasing degree of saturation. In other words, $\tan(\phi_r^a)$ is influenced by the combined effect of matric suction and degree of saturation.

Based on the five sets of experimental data, a model is formulated, and two approaches (Equations 6.4 and 6.5) are provided to predict the RSS of unsaturated soils. The parameters involved in the proposed model include: (i) effective residual shear strength parameters (c_r' and ϕ_r') that can be determined by using drained ring shear tests on saturated specimens, (ii) residual degree of saturation (S_r) that can be determined from SWCC, and (iii) fitting parameters (α_R, β_R and ϕ_r^b). In the first approach (Equation 6.4), the three fitting parameters need to be determined by best-fitting experimental results of suction-controlled ring shear tests. This approach can provide reasonable predictions for ϕ_r^a, $c_{r,a}$, and RSS of various unsaturated soils. In the second approach (Equation 6.5), the three fitting parameters are related to the plastic index (I_p). Thus, this approach only includes four basic parameters of soils (i.e., c_r', ϕ_r', S_r and I_p) that can be determined using conventional geotechnical laboratory tests. The second approach provides reasonable predictions for ϕ_r^a, $c_{r,a}$, and RSS of the studied plastic unsaturated soils; however, its performance is not as good as that of the first approach for the studied non-plastic unsaturated soils.

The proposed model (Equations 6.4 and 6.5) is only valid for the suction range where $S > (S_L + S_r)$, where S_r is the residual degree of saturation on SWCC, and S_L is the loss of degree of saturation within shear band caused by large shear displacement (Equation 6.2b).

6.6 References

Alonso, E. E., Pereira, J. M., Vaunat, J. and Olivella, S. 2010. A microstructurally based effective stress for unsaturated soils. Géotechnique, 60(12): 913-925.

Delage, P. and Graham, J. 1995. Mechanical behaviour of unsaturated soils: understanding the behaviour of unsaturated soils requires reliable concept models. In Proceedings of 1st International Conference on Unsaturated Soils, 1223-1256. Rotterdam: Balkema.

Escario, V. and Saez, J. 1986. The shear strength of partly saturated soils. Géotechnique, 36(3): 453-456.

Estabragh, A. R. and Javadi, A. A. 2008. Critical state for overconsolidated unsaturated silty soil. Canadian Geotechnical Journal, 45(3): 408-420.

Heredia, J. E. Y. 2015. Thermo-hydro-mechanical behavior of unsaturated clayey soils via thermo/suction-controlled ring shear testing. Ph.D. dissertation, Arlington, US: University of Texas at Arlington.

Hoyos, L. R., Velosa, C. L. and Puppala, A. J. 2014. Residual shear strength of unsaturated soils via suction-controlled ring shear testing. Engineering Geology, 172: 1-11.

Infante Sedano, J. A. and Vanapalli, S. 2011. Experimental investigation of the relationship between the critical state shear strength of unsaturated soils and the soil-water characteristic curve. International Journal of Geotechnical Engineering, 5(1): 1-8.

Lu, N., Godt, J. W. and Wu, D. T. 2010. A closed-form Equation for effective stress in unsaturated soil. Water Resources Research, 46(5): W05515.

Maatouk, A., Leroueil, S. and La Rochelle, P. 1995. Yielding and critical state of a collapsible unsaturated silty soil. Géotechnique, 45(3): 465-477.

Postill, H., Helm, P. R., Dixon, N., Glendinning, S., Smethurst, J. A., Rouainia, M., Briggs, K. M., El-Hamalawi, A. and Blake, A.P. 2021. Forecasting the long-term deterioration of a cut slope in high-plasticity clay using a numerical model. Engineering Geology, 280: 105912.

Qi, S. and Vanapalli, S. K. 2016. Influence of swelling behaviour on the stability of an infinite unsaturated expansive soil slope. Computers and Geotechnics, 76: 154-169.

Romero, E., Vaunat, J. and Merchán, V. 2014. Suction effects on the residual shear strength of clays. Journal of Geo-Engineering Sciences, 2(1-2): 17-37.

Sheng, D., Zhou, A. and Fredlund, D. G. 2011. Shear strength criteria for unsaturated soils. Geotechnical and Geological Engineering, 29(2): 145-159.

Sivakumar, V., Sivakumar, R., Boyd, J. and Mackinnon, P. 2010. Mechanical behaviour of unsaturated kaolin (with isotropic and anisotropic stress history). Part 2: performance under shear loading. Géotechnique, 60(8): 595-609.

Tarantino, A. and Tombolato, S. 2005. Coupling of hydraulic and mechanical behaviour in unsaturated compacted clay. Géotechnique, 55(4): 307-317.

Toll, D. G. and Ong, B. H. 2003. Critical-state parameters for an unsaturated residual sandy clay. Géotechnique, 53(1): 93-103.

Vanapalli, S. K., Fredlund, D. G., Pufahl, D. E. and Clifton, A. W. 1996. Model for the prediction of shear strength with respect to soil suction. Canadian Geotechnical Journal, 33(3): 379-392.

Vanapalli, S. K., Sillers, W. S. and Fredlund, M. D. 1998. The meaning and relevance of residual state to unsaturated soils. In 51st Canadian Geotechnical Conference, 4-7. Alberta, Canada: Edmonton.

Vanapalli, S. K. 2009. Shear strength of unsaturated soils and its applications in geotechnical engineering practice. In Proceeding of 4th Asia-Pacific Conference on Unsaturated Soils, 579-598. New Castle, Australia.

Wang, Q., Pufahl, D. E. and Fredlund, D. G. 2002. A study of critical state on an unsaturated silty soil. Canadian Geotechnical Journal, 39(1): 213-218.

Yang, X. and Vanapalli, S. K. (2019). Slope stability analyses of outang landslide based on the peak and residual shear strength behaviour. Advanced Engineering Sciences, 51(4): 55-68.

CHAPTER 7 SLOPE STABILITY ANALYSES OF OUTANG LANDSLIDE BASED ON THE PEAK AND RESIDUAL SHEAR STRENGTH BEHAVIOR[4]

7.1 Introduction

There are limited case studies in the literature that provide detailed information with respect to the large deformations in unsaturated soil slopes prior to reaching failure conditions (Widger and Fredlund 1979; Ng et al. 2003; Kovacevic et al. 2001; Nyambayo et al. 2004; Take and Bolton 2011). The shear strength of the soils in such slopes typically drops from the peak shear strength (PSS) to the residual shear strength (RSS) due to the strain-softening behavior. Therefore, the RSS and the strain-softening behavior must be considered for the rational analysis and design of the slopes that undergo large deformation prior to reaching failure conditions. The importance of RSS of soil in the long-term stability analysis of fine-grained soils is widely accepted and used in the analyses of progressive failure of saturated soil slopes (Skempton 1964; Potts et al. 1990; Potts et al. 1997; Leroueil 2001; Gens and Alonso 2006). More recently, Qi and Vanapalli (2016) highlighted the importance of RSS in slope stability analysis of unsaturated slopes.

Geotechnical engineers understand the importance of RSS in the slope stability analysis of both saturated and unsaturated soils. However, research studies related to the application of the RSS concepts in the analyses of unsaturated soils slope are limited in comparison to saturated soils. Most current research studies related to the stability analyses of unsaturated soils focus on the slope failure caused by rainfall infiltration. In such cases, typically a saturated zone is formed in the shallow layer of the slope due to the infiltration of rainwater. A shallow landslide tends to occur in the saturated zone that forms due to loss in matric suction. This means the dominant factor controlling slope stability remains to be the saturated shear strength parameters.

This chapter introduces a deep-seated reactivated Outang landslide near Three Gorges Dam in China caused by the combined influence of rainfall infiltration and the Yangtze River water level

[4] The contents presented in this chapter are published as a journal article: **Yang, X.**, and Vanapalli, S. K. 2019. Slope stability analyses of Outang landslide based on the peak and residual shear strength behavior. Advanced Engineering Sciences, 51(4): 55-68. DOI: 10.15961/j.jsuese.201900273.

variation at the slope toe. Laboratory experiments and site investigations related to this case study from the literature are summarized. A slope stability analysis is undertaken using commercial software Geoslope based on the PSS and the RSS parameters. The influence of rainfall infiltration and Yangtze River water level variation on the factor of safety (FOS) has been investigated and summarized. Due to the limitations of the commercial software, studies of advanced programing are required for incorporating the prediction model for RSS of unsaturated soils proposed in Chapter 6 into slope stability analysis. However, it is out of the scope of this thesis. For this reason, only a conventional shear strength equation that has been incorporated in the software was used for the slope stability analysis. This method is not consistent with the proposed approach in predicting the magnitudes of RSS of unsaturated soils. However, the results summarized in this Chapter can highlight the significance of RSS of unsaturated soils in slope stability analysis based on the differences between FOS values determined based on PSS and RSS.

7.2 Site investigation studies

7.2.1 Study area

The investigated Outang landslide (Dai 2016) is in Anping, Fengjie, China, which is on the south bank of the Yangtze River. It is about 177 km away from the Three Gorges Dam. The annual mean temperature and mean precipitation are 16.3 ℃ and 1147.9 mm, respectively. The total annual precipitation is 1636.3 mm. However, 70% of total annual precipitation occurs between the months of May and September. The Yangtze River flows in front of the slope toe, as shown in Figure 7.1. The water level of Yangtze River in the study area can be regulated by the Three Gorges Reservoir floodgates. The Yangtze River water is typically limited to 145 m for flood control from mid-June to the end of September (i.e., rainy season); however, it varies between 145 m and 175 m during other months.

7.2.2 Description of Outang landslide

The total length of Outang sliding mass is 1800 m with an average thickness of 50.8 m. The average gradient of the slope surface is 1:25. The relative difference in elevation between the slope crest and toe is about 600 m. Dai (2016) studied the slip surface of the Outang landslide and indicated three weak zones (shown as R1, R2 and R3 in Figure 7.1) which are sandwiched between the

sliding mass and bedrock. The sliding mass moved along these weak zones when the landslide occurred. The landslide had three stages which are described below:

(i) The first-stage landslide occurred from the midpoint of the slope to the toe of the slope. The length of the sliding mass is about 880 m and the width is about 1100 m. The average thickness is 70.3 m. The sliding mass moved along the R3 weak zone. It is parallel to the bedrock with an inclination between 18° and 25°. In the zone near leading edge, the slip surface is approximately circular. The toe slides out below the water level of the Yangtze River with an inclination between -15° and 5°.

(ii) The second-stage landslide is 440 m long, 650 m wide and the average thickness is 32.3 m. The sliding mass also moved along the R3 weak zone with an inclination between 25° and 27°. The toe slides out over the trailing edge of the first-stage landslide with an inclination between -12° and 4°.

(iii) The third-stage landslide is 640 m long, 830 m wide with an average thickness of 27.2 m. The sliding mass moved along the R1 weak zone with an inclination between 20° and 25°. The toe slides out almost horizontally over the trailing edge of the second-stage landslide.

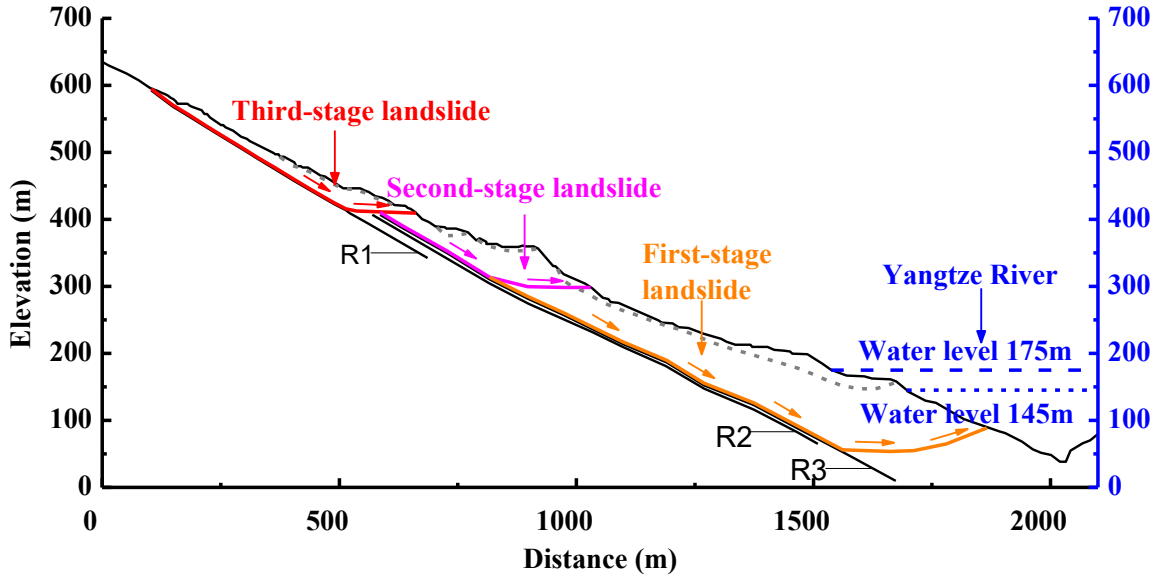

Figure 7.1 Typical cross section of the Outang landslide (modified after Dai 2016)

The site investigation studies showed that the three stage landslides occurred about thousands of years ago in sequence. However, since the Three Gorges Reservoir began to store water in 2003, the behaviors of the old Outang landslide were influenced significantly. Large displacements of the sliding masses and more than 106 cracks on the ground were observed (Dai 2006). Most cracks were observed in the first-stage sliding mass, especially during 2008 and 2009. The second-stage sliding mass was relatively stable. Settlements of the road and cracks of the ground were observed in the third-stage sliding mass every year during the rainy season, since then. These results and observations suggest that the old Outang landslide has been reactivated, locally. This may be attributed to the influence of intense rainfall and significant variation of the Yangtze River water level.

7.2.3 Soil properties

The site investigation studies have shown that the Outang sliding mass mainly consists of silty clay mixed with gravels and broken rock. The surface layer of sliding mass is the silty clay with gravels, the thickness of which is about 3-20m. Underlying the surface layer, there is a 10-85m thick broken rock layer mainly including sandstone, siltstone and claystone. Three weak zones were sandwiched between the Outang sliding mass and bedrock. Only the two weak zones (i.e., R1 and R3) along which the sliding mass moved were studied. R3 is a clay layer with thickness of 40 – 70 cm. R1 is claystone layer with thickness of 10 – 35 cm.

Several undisturbed samples were collected from the Outang sliding mass and weak zones. The degree of saturation of the collected natural samples was around 89.53%. A series of consolidated undrained direct shear tests were conducted on both the natural and the saturated soil samples of R1 and R3. A series of quick undrained direct shear tests were conducted on the natural and saturated soil samples of silty clay. The physical and mechanical properties of the soils are summarized in Tables 7.1 and 7.2.

The shear strength properties of natural (i.e., unsaturated) and saturated specimens suggested that the shear strength of natural specimens reduced when they were saturated (see R1 for example). The peak cohesion, c_p, decreased by 27.86% and the peak internal friction angle, ϕ_p, decreased by 32.78%. The RSS parameters, c_r and ϕ_r, decreased by 14.83% and 26.36% respectively. This can be attributed to the reduction in matric suction associated with an increase in the S_r. Unfortunately,

the matric suction of the natural samples collected from the test site were not measured by Dai (2016).

Table 7.2 summarizes the strain-softening characteristic behavior from this slope. For example, the cohesion and angle of internal friction for peak and residual conditions decreased by 34.66% and 21.49%, respectively for saturated R1 specimens. In addition, for the unsaturated R1 specimen, the soil cohesion decreased by 44.66% and the angle of internal friction decreased by 28.33% under large deformation. This means the reduction in shear strength from peak to residual conditions (i.e., brittleness) under unsaturated soil conditions is greater than that of the saturated soil.

Table 7.1 Physical properties of soils (summarized from Dai 2016)

	Plasticity index	Liquid index	Coefficient of permeability ($\times 10^{-7}$ cm/s)	Specific gravity	Natural specimen (Unsaturated)		Saturated specimen	
					w (%)	ρ (kg/m^3)	w (%)	ρ (kg/m^3)
Silty clay with gravels	12.3	-0.02	53.01	-	0.05	2040	21.63	2070
R3 (CL)	11.1	0.17	55.95	2.70	19.48	2070	20.51	2080
R1 (CL)	10.7	0.15	24.80	2.71	18.00	2007	19.80	2100

Table 7.2 Shear strength parameters of soils (summarized from Dai 2016)

	Natural specimen (Unsaturated)				Saturated specimen			
	c_p (kPa)	ϕ_p (°)	c_r (kPa)	ϕ_r (°)	c_p (kPa)	ϕ_p (°)	c_r (kPa)	ϕ_r (°)
silty clay with gravels	45.9	14.6	27.0	11.3	34.7	12.4	21.6	9.2
R3	36.6	14.7	27.8	11.5	30.0	12.5	24.2	9.3
R1	52.4	18.0	29.0	12.9	37.8	12.1	24.7	9.5

7.2.4 Yangtze River water level and rainfall data

The rainfall data along with the variation of Yangtze River water level in the slope are summarized in Figure 7.2. From this figure, it can be observed that the precipitation varied periodically. The precipitation was relatively high from May to September, which is the rainy season period. However, it decreased significantly after this period and reached a minimum value between January and March. The water level of Yangtze River reduced from 175 m to 145 m from May to

September as a flood control measure during the peak period of rainfall. However, between January and March, Yangtze River water level increased gradually and reached 175 m. Dai (2016) measured the accumulated displacement of the ground surface using GPS. Two typical variation curves of the accumulated displacement with time are also shown in Figure 7.2. Both the monitor points were located in the third-stage landslide.

The accumulated displacements increased even between January and March in 2013 and 2014 when the precipitation rate was very low. This may be attributed to the decrease in the Yangtze River water level which resulted in a greater seepage force downward the slope. In addition, the fluctuations of Yangtze River water level were similar from May to September in 2012 and 2013. The accumulated displacement however increased significantly during this period in 2012 in comparison to 2013. These displacements were consistent with the precipitation rates in 2012 and 2013; it can be seen from Figure 7.2 the precipitation rate in 2013 was lower than that in 2012. This means the variation of increase rate of accumulated displacement is also influenced by the variation of average precipitation rate. Therefore, it is reasonable to conclude that the increase in accumulated displacement of the third-stage sliding mass was influenced by both the water level variation and the heavy precipitation.

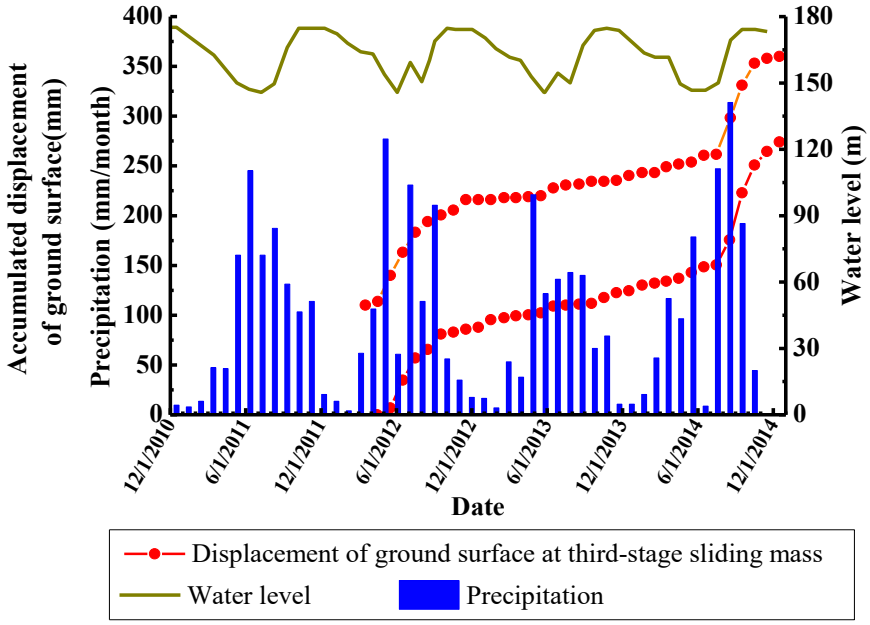

Figure 7.2 Variation of the Yangtze River water level, precipitation, and accumulated displacement of ground surface (modified after Dai 2016)

7.3 Slope stability analyses

7.3.1 Schematic of slope in numerical modelling

Numerical modelling was conducted using the commercial software GeoStudio to study the stability of this slope based on the PSS and the RSS parameters. The schematic of the investigated slope is shown in Figure 7.3 highlighting several key details. The mixed quad and triangle elements were used to generate the mesh. The approximate global element size was 30 m.

However, in order to build the numerical model, some assumptions have been introduced. Firstly, the surface of the slope is simplified. Only the main variations of gradient were introduced into the numerical model. Some minor variations of gradient were not considered. Secondly, for R1 and R3, only the part overlapping with the slip surface are presented in the numerical model. The thickness of R1 and R3 are set as 0.5 m. Lastly, the three landslides that have occurred in a sequence were considered to occur at the same time. This means the soils above the slip surface was considered to be sliding mass as a whole.

The seepage and slope stability analysis were conducted considering three different scenarios, which included: (i) the influence of precipitation with Yangtze River water level at constant value of 175 m; (ii) the influence of decrease in Yangtze River water level from 175 m to 145 m; (iii) considering the combination influence of precipitation and decrease in Yangtze River water level.

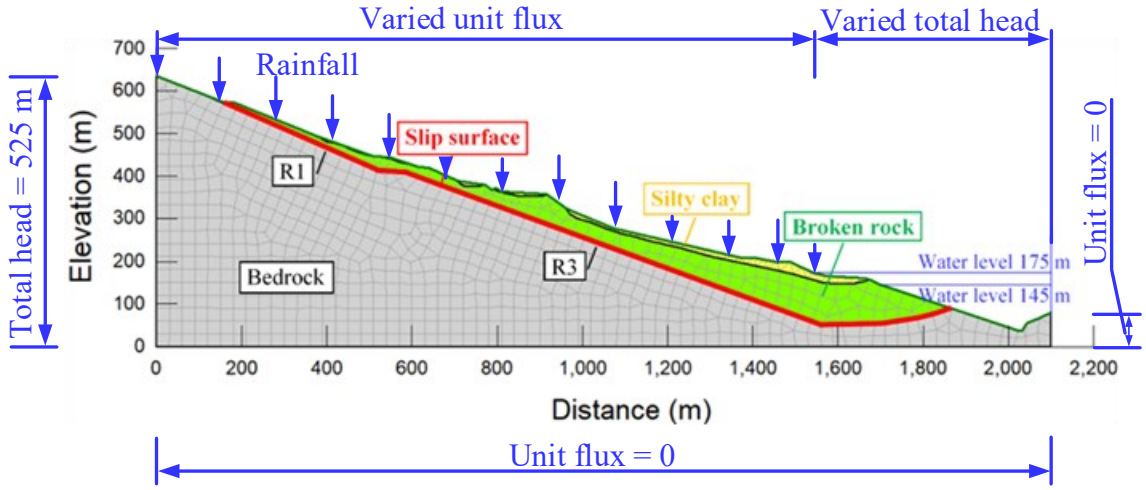

Figure 7.3 Schematic of the slope used in the numerical modelling

7.3.2 Procedures of numerical analyses

Numerical analyses involved four steps, which are summarized below:

(1) *Steady-state seepage analysis*: A steady-state seepage analysis was conducted with a constant total head on the left boundary and the slope surface below the Yangtze River water level. The initial pore water pressures can be simulated in the slope under no precipitation and variation of water level.

(2) *Transient seepage analysis*: In each scenario, a specific type of boundary conditions was applied on the surface of the slope to model the precipitation and variation of water level. Then, a transient seepage analysis was conducted to calculate the pore water pressures in the slope at different times based on the initial pore water pressures obtained in Step (1).

(3) *Slope stability analysis*: In each scenario, a series of values of FOS can be calculated using the Morgenstern-Price method and PSS parameters based on the obtained pore water pressures at different times calculated in Step (2). Therefore, the variation of the FOS calculated using PSS (FOS_P) with time can be obtained for each scenario.

(4) *Slope stability analysis*: Step (3) can be repeated replacing PSS parameters with the RSS parameters. The variation of the FOS calculated using RSS (FOS_R) with time can be obtained for the three different scenarios.

7.3.3 Boundary conditions

As shown in Figure 7.3, a no flow boundary condition was applied on the right and bottom boundaries, i.e., the unit flux q was assumed to equal zero. As suggested by Dai (2016), a constant total head at 525 m was applied on the left boundary in this numerical model. In the steady-state seepage analysis, a constant total head of 175 m was applied on the slope surface below the elevation of 175 m.

Since the precipitation and water level varied periodically (Figure 7.2), only a representative period of one year (Feb 2012 – Feb 2013) was selected for the study. The shear strength decreased during the wet season of this year due to precipitation, while the seepage force increased during this period due to the decrease in water level. These two factors can accelerate slope failure; as a result, the

wet (i.e., mostly the rainy) season is the most vulnerable period. For this reason, only the wet period from Feb 2012 – Sep 2012 was studied in this research. In other words, a transient seepage analysis was conducted for a duration of 7 months.

The precipitation and water level variations have been simplified as shown in Figure 7.4. In the transient seepage analysis, a varied unit flux with time was applied on the slope surface above the elevation of 175 m to simulate the rainfall precipitation (Figure 7.3). The unit flux was defined as a function of the elapsed time. Initially, the unit flux was zero and then it increased linearly to 240 mm/month after 3 months. Finally, it was constant at 240 mm/month from the 3rd to the 7th month. A varied total head with time was applied on the slope surface below the elevation of 175 m to simulate the variation of water level (Figure 7.3). Initially, the total head was 175 m and then it decreased linearly to 145 m after 3 months. Finally, it was constant at 145 m during the following 4 months (i.e., from May to September).

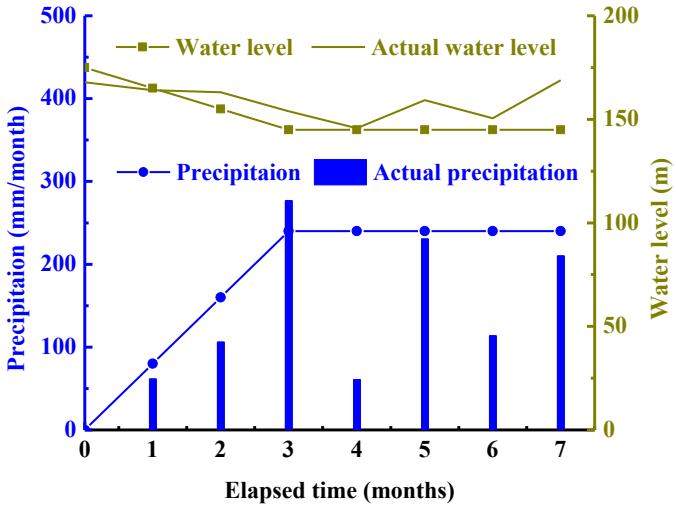

Figure 7.4 Variation of actual and assumed values of precipitation and Yangtze River water level used in the numerical model (Feb 2012 – Sep 2012)

By default, when the total head was lower than the elevation, the boundary condition was set as no flow boundary (i.e., total flux is equal to zero). This is not consistent with the actual boundary condition. For an actual slope, once the water level decreased, the constant total head boundary on the exposed slope surface should be replaced by a rainfall infiltration boundary. However, in this numerical model the rainfall infiltration was neglected on this part of surface between the elevation of 175 m and 145 m. In this model, the slip surface was seated at a depth of more than 100 m in

the zone near the river. The numerical results suggested that the 7-month rainfall infiltration could only create a saturated zone within a shallow layer (about 3 m below the surface).

7.3.4 Material properties

Five different types of materials were used in this numerical model, including R1, R3, silty clay, broken rock and bedrock respectively (Figure 7.3). The Mohr-Coulomb model was used for all those materials. Since effective shear strength parameters were not provided by Dai (2016), the PSS and RSS shown in Table 7.2 were used for R1, R3 and silty clay. The parameters of the R1 and R3 were derived from consolidated undrained direct shear test results. The parameters of silty clay were obtained from quick undrained direct shear test results. This approach will underestimate the magnitudes of the factor of safety (FOS). However, the trends in the variation of FOS would be similar when shear strength is reduced from the peak value to residual value. The influence of residual state can still be analyzed by comparing the FOS calculated using peak and residual shear strength, in spite of not using the effective shear strength parameters in this study. The saturated unit weight values of different materials are summarized in Table 7.1.

Dai (2016) did not provide experimental results about the shear strength parameters of the broken rock and bedrock and the hydraulic behaviors of all the five materials. However, Dai (2016) conducted a numerical modelling study of the landslide. In the numerical models, the hydraulic and mechanical properties of those materials were suggested based on experimental results. The properties of similar materials in Three Gorges Dam region were used as a reference. Back calculations were also used to determine the parameters based on the ground water table and slope surface displacement measurements. Therefore, in this research, the PSS parameters of broken rock and bedrock and the SWCC and permeability functions of these five materials were collected from the numerical studies reported by Dai (2016).

The RSS parameters were not provided for the broken rock and bedrock by Dai (2016). The slip surface only passed through the R1 and R3 weak zones. This means the FOS was controlled by the shear strength parameters of R1 and R3. The shear strength of broken rock and bedrock did not influence the FOS significantly. Therefore, the RSS parameters of those two materials were assumed equal to the corresponding peak values. The peak and residual shear strength parameters of broken rock and bedrock were given in Table 7.3.

Table 7.3 Shear strength parameters in numerical model

	c'_p (kPa)	ϕ'_p (°)	c'_r(kPa)	ϕ'_r (°)
Broken rock	70	16.2	70	16.5
Bedrock	700	42	700	42

The same SWCC and permeability functions were used for the R1 and R3 since they are both clays. The equation proposed by Fredlund and Xing (1994) was used to fit the SWCC. The parameter related to residual suction C_r can be selected as 3000 kPa, as suggested by Vanapalli et al. (1996). The approach proposed by Vanapalli et al. (1998) was used to determine the residual volumetric water content. The SWCC parameters of the five materials are given out in Table 7.4. The permeability functions of the five materials are presented in Figure 7.5.

Table 7.4 Parameters of SWCC

	a	n	m	θ_s	θ_r
Silty clay with gravels	10.65	1.40	0.81	0.32	0.059
Broken rock	9.12	1.73	0.76	0.27	0.051
R1 and R3	9.07	1.53	0.59	0.30	0.094
Bedrock	9.81	1.46	0.70	0.05	0.012

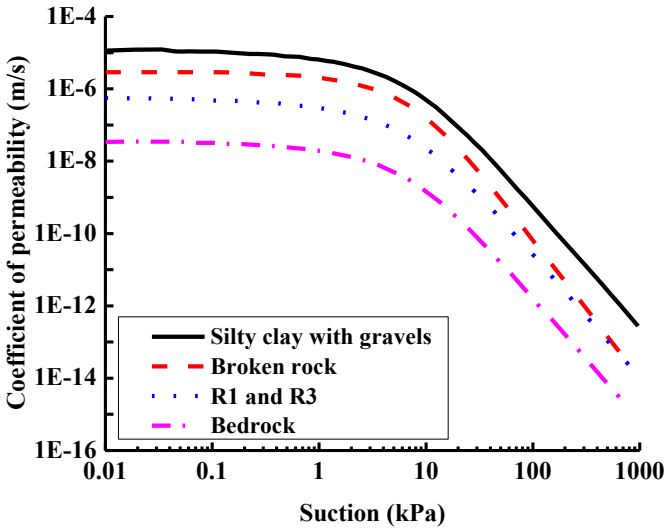

Figure 7.5 Coefficient of permeability functions for different materials (modified after Dai 2016)

The PSS of those materials under unsaturated condition can be predicted using the second approach proposed by Vanapalli (1996). This approach has been used as an add-in equation in the Geo-slope. Only four parameters (c_r', ϕ_r', θ_s and θ_r) are required to be used as input parameters in the software. PSS can be calculated automatically at each node. It is convenient to perform calculations using this equation in Geo-slope.

The prediction models for residual shear strength of unsaturated soils are very limited. The apparent SWCC of sheared specimen were not provided by Dai (2016). For this reason, the approach proposed by Infante Sedano and Vanapalli (2011) cannot be used. In addition, the approach proposed by Romero et al. (2014) was used for high suction range, which cannot be used in this model. The prediction model described in Chapter 6 can only be applied within the suction range where $S > (S_L + S_r)$. This means, for the R1 (I_p = 10.7) and R3 (I_p = 11.1), this model is valid when suction is lower than 80 kPa. However, numerical simulations of seepage analysis showed that the suction at some points in the slope can reach as high as 800 kPa. Thus, the prediction model proposed in Chapter 6 cannot be used in this case study. Since there is a lack of prediction model that can be used for RSS of unsaturated soils, an equation with the same form of the second approach proposed by Vanapalli (1996) was used to approximate the RSS of unsaturated soils, which can be expressed as:

$$\tau = c_r' + (\sigma_n - u_a)\tan\phi_r' + (u_a - u_w)\frac{\theta - \theta_r}{\theta_s - \theta_r}\tan\phi_r' \tag{7.1}$$

7.3.5 Slip surface and FOS

The Morgenstern-Price method was used to calculate the FOS. The half-sine function was selected as the interslice force function. The slip surface was specified manually before the slope stability analysis, which is shown in Figure 7.3. In Morgenstern-Price method, two independent FOS equations were used; one with respect to moment equilibrium, F_m, and the other with respect to horizontal force equilibrium, F_f (Geoslope 2012). These equations can be expressed as:

$$F_m = \frac{\sum (c'\beta R + NR\tan\phi' - u_w\beta R\frac{\theta - \theta_r}{\theta_s - \theta_r}\tan\phi')}{\sum Wx - \sum Nf + \sum Aa} \tag{7.2}$$

$$F_f = \frac{\sum (c'\beta + N\tan\phi' - u_w\beta\frac{\theta-\theta_r}{\theta_s-\theta_r}\tan\phi')\cos\alpha}{\sum N\sin\alpha + \sum A} \tag{7.3}$$

$$N = \frac{W + (X_R - X_L) - \frac{[c'\beta\sin\alpha + u_w\beta\sin\alpha\tan\phi^b]}{F}}{\cos\alpha + \frac{\sin\alpha\tan\phi'}{F}} \tag{7.4}$$

where N is the total normal force on the base of the slice; s is matric suction; W is the total weight of a slice; A is the resultant external water forces; X is the vertical interslice shear forces and the L and R subscripts designate the left and right sides of the slice; β, R, x, f, e, a is geometric parameters; α is the angle between the tangent to the center of the base of each slice and the horizontal.

In SLOPE/W, the seepage force is considered by using the concept of boundary water forces and total weight (Geoslope 2012). This means no seepage forces were applied internal to the sliding mass. Instead, boundary water forces A_R and A_L were applied on the rear and front boundaries of the slip surface.

From Equations 7.2 – 7.4, it can be found that the resistance force included the shear strength on slip surface and the driving force included W and A. All the three parameters are influenced by the hydraulic/climatic conditions. W is determined by unit weight of each slice, which is a function of volumetric water content. The shear strength on slip surface is dependent on the matric suction. A is determined by the difference between the water levels at the rear and front part of the slope. Therefore, the variation in FOS caused by the change of hydraulic/climatic conditions was controlled by the shear strength on slip surface, total weight of the slice and the water forces.

7.4 Analyses results

7.4.1 Scenario 1: Influence of precipitation

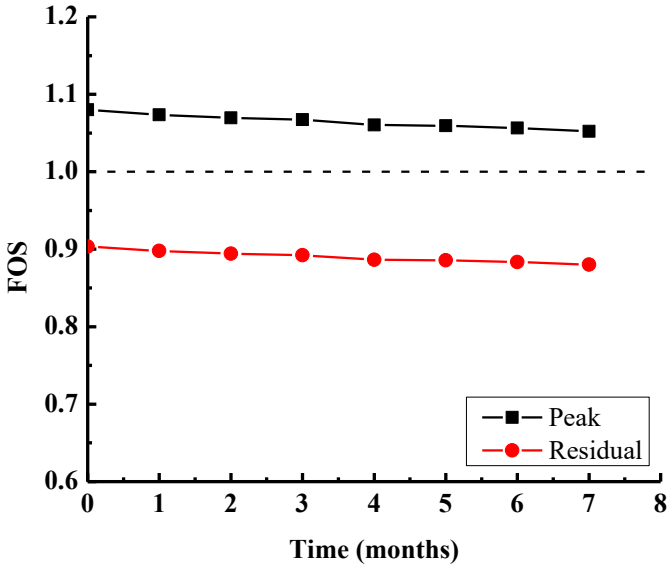

Figure 7.6 Variation of FOS with time taking account of rainfall infiltration

Figure 7.6 presents the variation of FOS with time considering the influence of rainfall infiltration when the water level is at 175 m. The FOS decreased linearly with time when only the influence of rainfall infiltration is considered. The total reduction in both FOS_P and FOS_R was relatively small despite 7-months precipitation period.

The reduction in FOS due to rainfall infiltration can be explained in terms of the shear strength on slip surface and the total weight of the sliding mass. Figure 7.7 shows the pore water profile along the slip surface at different times (shown in Figure 7.4). It can be found under initial condition, only the slip surface going through R1 and the connection part between R1 and R3 were in the unsaturated zone. The remainder part of the slip surface was in the saturated zone. During precipitation, two saturated zones were formed through which the slip surface passed. The first one was formed at the top of the slip surface in R1. The formation of this slip surface can be attributed to the soil layer above the bedrock is thin at this zone (shown in Figure 7.8). The infiltrated rainfall can saturate the R1 and sliding mass within a short time. The second saturated zone was formed at the connection between R1 and R3. In this zone, the bedrock is almost horizontal (shown in Figure 7.8). Therefore, the infiltrated rainfall cannot flow downwards along

the slope. Consequently, the infiltrated rainfall accumulated above the bedrock and saturated the soils. Once the saturated zones are formed, the shear strength of the slip surface passing through these zones reduced due to loss of matric suction. In addition, the volumetric water content of the sliding mass increased during precipitation. As a result, the total weight of the sliding mass increased. Therefore, under the influence of precipitation, the resistance on the slip surface reduced, while the driving force, W, increased. Consequently, the FOS decreased.

However, when matric suction is high, the volumetric water content is low. Thus, the shear strength contribution due to matric suction is relatively small in comparison with the shear strength due to normal stress. Furthermore, the shear strength on most part of the slip surface was not influenced by the precipitation since they were saturated throughout. In other words, the phreatic line was not influenced by the precipitation. Such a behavior may be attributed to the thick soil layer (i.e., average thickness is about 50 m) through which only limited amount of rainfall water can infiltrate into the shallow depth. Therefore, reduction in FOS caused by decrease in matric suction and increase in total weight was not significant.

By comparing the FOS_P and FOS_R, it can be found that the FOS_P was greater than 1; however, the FOS_R was less than 1. The FOS decreased by about 16 % from peak to residual value. Such a behavior can be attributed to lower values of c_r' and ϕ_r' in comparison to c_p' and ϕ_p'. At residual state, the soils can only provide a low resistance on the slip surface to prevent the shear deformation.

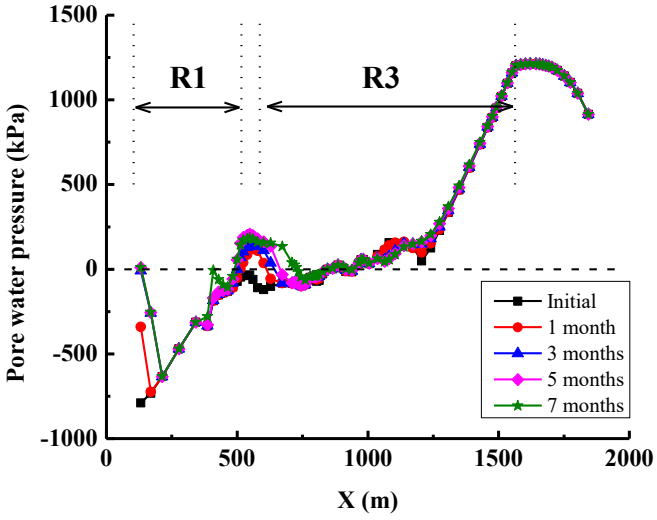

Figure 7.7 Pore water pressure profiles along slip surface taking account of rainfall infiltration

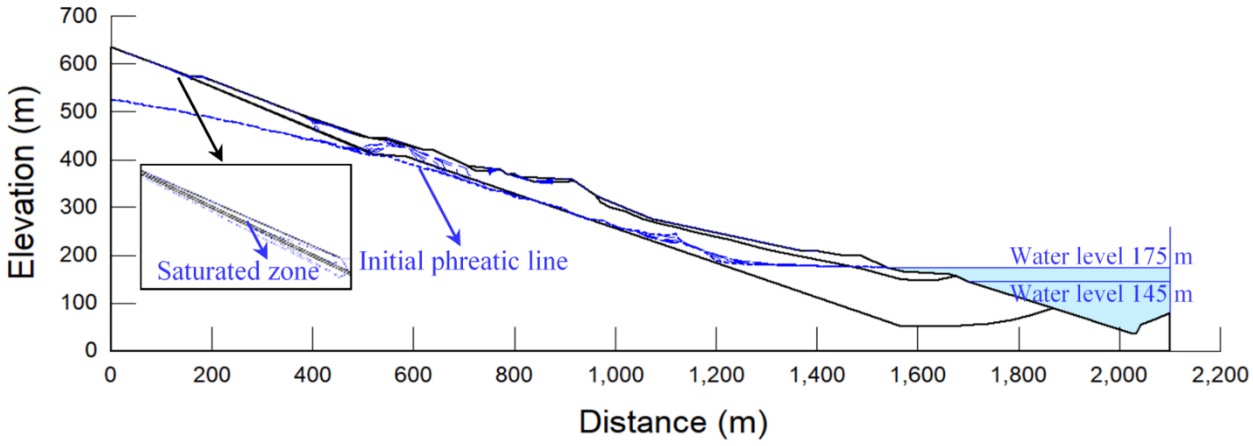

Figure 7.8 Development of the phreatic line in the Outang landslide during precipitation

7.4.2 Scenario 2: Influence of Yangtze River water level variation

Figure 7.9 presents the variation of FOS with time considering only decrease in water level. The FOS decreased rapidly and linearly with time within the first three months. By the third month, both FOS_P and FOS_R have decreased by 5.5%. From the third to the seventh month, both FOS_P and FOS_R increased slightly by 0.65%.

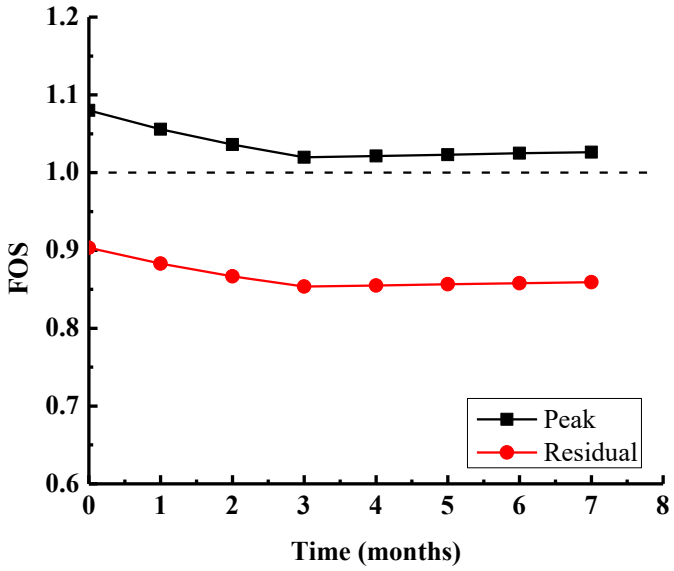

Figure 7.9 Variation of FOS with time considering Yangtze River water level variation

Figure 7.10 shows the pore water pressure profiles along the slip surface at different times (shown in Figure 7.4). It can be found that only the pore water pressure on the circular part of the slip surface was influenced by the water level variation. The pore water pressure and volumetric water content were not influenced by the variation in water level for most part of the slope. This means the shear strength on the slip surface and total weight of sliding mass were not influenced significantly by the water level variation. Therefore, the reduction in FOS can be mainly attributed to the increase in the total water force caused by the decrease in water level.

After three months, the water level decreased to the minimum value and was constant. Due to this reason, the water force was constant after three months. However, the FOS increased slightly during this period. The small increase in FOS from the third to the seventh month can be attributed to the lowering of the phreatic line. Despite the constant water level, the phreatic line in the zone near the river continued moving downwards (Figure 7.11). Due to this reason, there was a decrease in volumetric water content of the sliding mass above the phreatic line near the river. As a result, the total weight of this part of sliding mass decreased and contributed to a relatively small increase in the FOS.

In addition, the FOS_P was still greater than 1, while the FOS_R was lower than 1. In both scenarios (i.e., 1 and 2) where only rainfall infiltration and water level variations are considered, the FOS_R was 16% lower than the FOS_P.

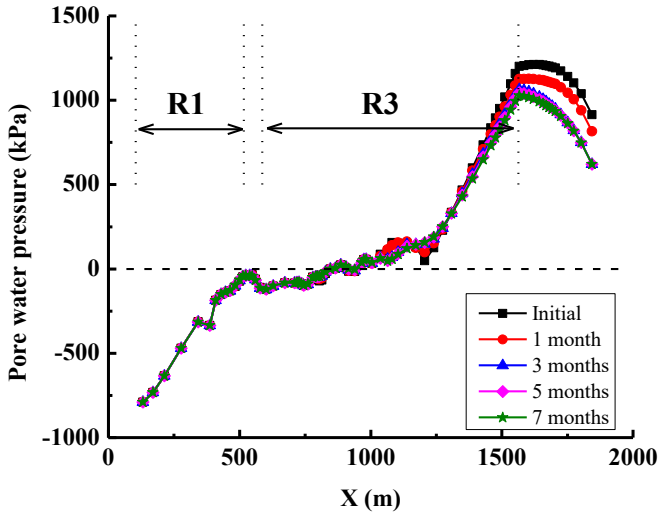

Figure 7.10 Pore water pressure profiles along Outang landslide slip surface considering water level variation

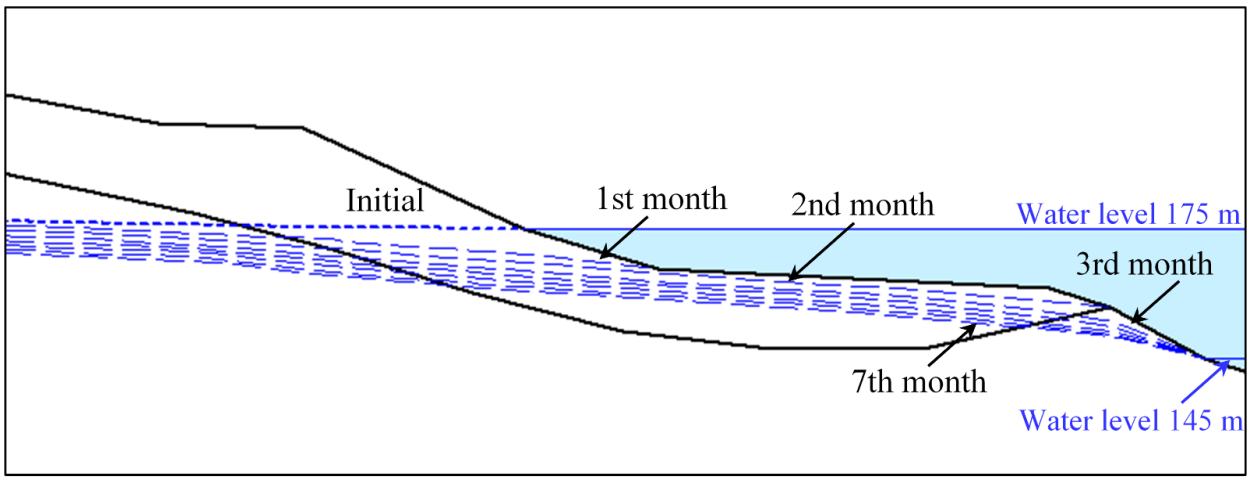

Figure 7.11 Development of the phreatic line during water level variation in the Yangtze River

7.4.3 Scenario 3: Combined influence of precipitation and water level variation

Figure 7.12 presents the variation of FOS with time considering combined influence of both precipitation and decrease in the Yangtze River water level. The FOS decreased linearly with time at a relatively faster rate within the first three months. By the third month, both FOS_P and FOS_R have decreased by 6.6%. After that, FOS decreased relatively at a slower rate with time. From the third to the seventh month, FOS decreased by 0.66%.

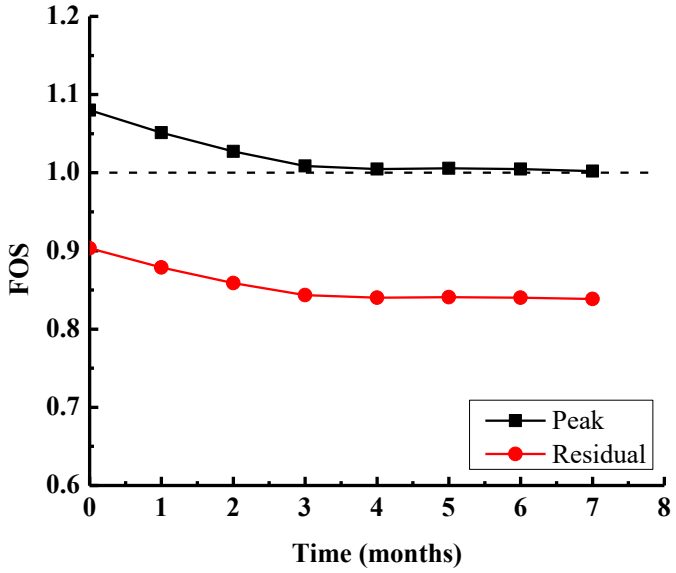

Figure 7.12 Variation of FOS with time considering the combined influence of precipitation and Yangtze River water level variation

The reduction in FOS can be attributed to the different mechanisms described in the previous two sections. Firstly, precipitation contributed to saturated zones in the rear part of the slope (Figure 7.13). This resulted in matric suction decrease on the slip surface and increase in total weight of sliding mass. Secondly, the decrease in water level leads to an increase in the total water force. Within the first three months, the reduction in FOS caused by Yangtze River water level decrease was greater than that caused by precipitation. Therefore, the decrease in Yangtze River water level was the dominant factor, which contributed to a reduction in the FOS. The influence of precipitation however is secondary. After the third month, the water level was constant with a lowest value and the precipitation was constant at a maximum value (shown in Figure 7.4). The FOS continued to decrease at a slower rate due to the influence of rainfall infiltration.

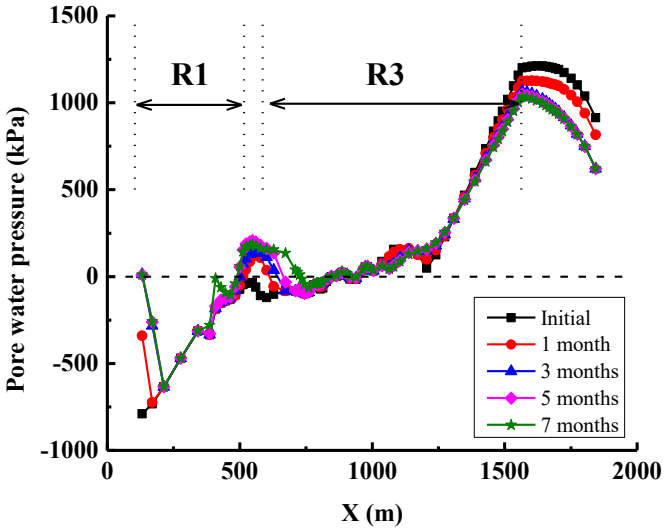

Figure 7.13 Pore water pressure profiles along slip surface considering the combined effect of precipitation and Yangtze River water level variation

The FOS_R was lower than the FOS_P during the seven months. Despite a decrease in FOS_P with time under the influence of precipitation and Yangtze River water level variation, it was greater than 1 throughout the 7 months period. The shear strength parameters used in these analyses were derived from consolidated undrained direct tests. The values of FOS can be greater than the current values if the effective shear strength parameters were used. In other words, the slope would be stable throughout the 7 months if the PSS was used in the analysis. These results however are inconsistent with the in-situ slope behavior because of a significantly large displacement that has occurred between the third and seventh month (Figure 7.2). The FOS was overrated due to the use

of PSS throughout the slope, which is a limiting scenario. In other words, the RSS should be considered in the slope stability analysis for reliably modeling the slope behavior.

However, using the RSS throughout the slope is another limiting scenario, which contributes to a lower FOS. Typically, the deformations within a slope are not uniform. In some parts where the deformation is large, the RSS parameters should be used. The PSS however should be used if the deformation is relatively small. In other words, the variation of shear strength parameters associated with the magnitude of deformation should be established from experimental results. In the present study, a limit equilibrium method was used in the numerical analyses. This approach cannot consider the influence of deformation behavior on the shear strength. For this reason, the RSS was extended for the entire slope. The calculated FOS of the slope would be somewhere between the FOS_P and the FOS_R from such an analysis, which is more realistic. Initially, when there was no deformation, the real FOS was equal to FOS_P. During the wet season, the combined effect of rainfall infiltration and Yangtze River water level variation contributes to a decrease in the FOS. In addition, the shear strength in some parts of the slope starts reducing from PSS to RSS due to an increase in the deformation; thus, the FOS deviates from the FOS_p and approaches to FOS_R.

7.5 Summary

In this chapter, reactivated Outang landslide near the Three Gorges Dam in China was revisited and analyzed. The landslide was activated by the combined influence of rainfall infiltration and Yangtze River water level variation during recent years (Figure 7.2). The results of laboratory experiments and field measurements were used to analyze the failure mechanism associated with this landslide. A series of slope stability analyses were conducted using Geoslope based on the peak shear strength (PSS) and the residual shear strength (RSS) parameters. The following conclusions can be drawn from this study:

(1) The site investigations suggested that the heavy precipitation and Yangtze River water level decrease contributed to the reactivation of the sliding mass of an old landslide along the weak zones sandwiched between sliding mass and bedrock.

(2) For the soils in the sliding zones, the RSS parameters were significantly lower than the peak values. The reduction in shear strength from peak to residual state under unsaturated soil condition was greater than that of saturated soil.

(3) The water infiltration associated with the prolonged period of rainfall can reduce the FOS of the slope. The FOS reduction, however, is small. This can be attributed to the generation of two saturated zones at the rear part of the slope, which contributes to a decrease in the shear strength. However, the extent of saturated zones was still limited.

(4) The decrease in Yangtze River water level can decrease the FOS of the slope. However, after Yangtze River water level reached the lowest value, FOS was relatively constant. This can be mainly attributed to the increase in the total water force caused by the decrease in Yangtze River water level.

(5) Despite the variations in hydraulic/climatic conditions, FOS decreased by 16%, when the PSS parameters were replaced with the RSS values. If PSS were used in the analysis, the slope would still be stable even under the combined influence of precipitation and Yangtze River water level decrease, which is inconsistent with the field observations. Therefore, the RSS should be considered in the slope stability analysis for reliably modelling the slope behaviors taking account strain softening.

The results of the present study are useful for the geotechnical engineers as they highlight the role of residual shear strength behavior in the slope stability of unsaturated soils. However, more rigorous studies are required to investigate the Outang landslide using the prediction model for RSS of unsaturated soils developed in Chapter 6.

7.6 References

Dai. Z. 2016. Study on the deformation and failure mechanism of Outang landslide in the Three Gorges Reservoir Region, China. Ph.D. thesis, Chang'an University, Xi'an, China (in Chinese).

Fredlund, D. G., Morgenstern, N. R., and Widger, R. A. 1978. The shear strength of unsaturated soils. Canadian geotechnical journal, 15(3): 313-321.

Fredlund, D. G., and Xing, A. 1994. Equations for the soil-water characteristic curve. Canadian geotechnical journal, 31(4): 521-532.

GeoSlope International Ltd. 2012. Stability modeling with SLOPE/W: an engineering methodology. Calgary: GEO-SLOPE International Ltd.

Hoyos, L. R., Velosa, C. L., and Puppala, A. J. 2014. Residual shear strength of unsaturated soils via suction-controlled ring shear testing. Engineering Geology, 172: 1-11.
Infante Sedano, J. A. and Vanapalli, S. 2011. Experimental investigation of the relationship between the critical state shear strength of unsaturated soils and the soil-water characteristic curve. International Journal of Geotechnical Engineering, 5(1): 1-8.
Locat, A., Jostad, H.P. and Leroueil, S., 2013. Numerical modeling of progressive failure and its implications for spreads in sensitive clays. Canadian Geotechnical Journal, 50(9): 961-978.
Lupini, J. F., Skinner, A. E., and Vaughan, P. R. 1981. The drained residual strength of cohesive soils. Géotechnique, 31(2): 181-213.
Merchán, V., Romero, E., and Vaunat, J. 2011. An adapted ring shear apparatus for testing partly saturated soils in the high suction range. Geotechnical Testing Journal, 34(5): 433-444.
Patil, U. D., Puppala, A. J., Hoyos, L. R., and Pedarla, A. 2017. Modeling critical-state shear strength behavior of compacted silty sand via suction-controlled triaxial testing. Engineering Geology, 231: 21-33.
Potts, D. M., Kovacevic, N., and Vaughan, P. R. 1997. Delayed collapse of cut slopes in stiff clay. Géotechnique, 47(5): 953-982.
Qi, S., and Vanapalli, S. K. 2016. Influence of swelling behavior on the stability of an infinite unsaturated expansive soil slope. Computers and Geotechnics, 76: 154-169.
Romero, E., Vaunat, J. and Merchán, V. 2014. Suction effects on the residual shear strength of clays. Journal of Geo-Engineering Sciences, 2(1-2): 17-37.
Skempton, A. W. 1964. Long-term stability of clay slopes. Géotechnique, 14(2): 77-102.
Skempton, A. W. 1985. Residual strength of clays in landslides, folded strata and the laboratory. Géotechnique, 35(1): 3-18.
Stark, T. D., and Eid, H. T. 1994. Drained residual strength of cohesive soils. Journal of Geotechnical Engineering, 120(5): 856-871.
Vanapalli, S. K., Fredlund, D. G., Pufahl, D. E., and Clifton, A. W. 1996. Model for the prediction of shear strength with respect to soil suction. Canadian Geotechnical Journal, 33(3): 379-392.
Vanapalli, S. K., Sillers, W. S., and Fredlund, M. D. 1998. The meaning and relevance of residual state to unsaturated soils. In 51st Canadian Geotechnical Conference, 4-7.
Vaunat, J., Amador, C., Romero, E., and Djeran-Maigre, I. 2006. Residual strength of a low plasticity clay at high suctions. In Unsaturated Soils 2006, 1279-1289.
Widger, R. A., and Fredlund, D. G. 1979. Stability of swelling clay embankments. Canadian Geotechnical Journal, 16(1): 140-151.

CHAPTER 8 SUMMARY AND CONCLUSIONS

8.1 Summary

The unsaturated soils typically exhibit strain-softening behavior under large shear deformation, characterized by a stress-strain response in which the shear stress increases rapidly with limited shear strain to a peak value and then drops to a residual value gradually with further increase in shear strain. A variety of geo-structures associated with unsaturated soils typically undergo large progressive shear deformation prior to reaching the failure condition due to the influence of environmental factors (e.g., rainfall infiltration, wetting-drying cycles, etc.). Therefore, the shear strength of soils in sliding zones typically reduces from a peak to a residual value with the progressive development of large shear deformation, while the shear strength of soils in other zones are still at the peak level. For this reason, the shear strength behavior of unsaturated soils during strain-softening is crucial for rational analyses and design of geo-structures undergoing large shear deformation. Significant advances have been made during the last thirty years to understand and model the strain-softening behavior of unsaturated soils within a relatively small shear deformation based on the direct/triaxial shear apparatuses. However, the studies under large shear deformation based on the suction-controlled ring shear apparatus are limited. Therefore, more investigations are still required to provide a comprehensive understanding of the shear strength behavior of unsaturated soils during strain-softening under large shear deformation.

In this thesis, a variety of studies about the strain-softening behavior of unsaturated soils published in the last thirty years are reviewed to investigate the physical mechanisms and modelling methods of the strain-softening behavior and the peak, critical and residual shear strength of unsaturated soils. A simple disturbed state concept (DSC)-based model is proposed for the prediction of the strain-softening stress-strain relationship of unsaturated soils. In addition, two sets of suction-controlled ring shear tests are conducted on unsaturated SP-SM and IHT soils, respectively, to investigate the shearing behaviors of unsaturated soils under large shear deformation. Based on the observations in suction-controlled ring shear tests, a model is proposed for the prediction of the residual shear strength for a wide range of unsaturated soils comprising coarse- to fine-grained soils. Major conclusions drawn from this research are summarized below.

(1) Physical mechanisms and modelling methods of the strain-softening behavior of unsaturated soils

The strain-softening of unsaturated soils associated with the dilation can be attributed to two key factors: (i) the destruction of the original structure of soil particles/aggregates inside the shear band due to the rolling of soil particles, which is similar to the behavior of saturated soils, and (ii) the local loss of water menisci area inside the shear band caused by the rupture of the water menisci due to the movements of soil particles/aggregates and the lower water retention capability due to the generation of the large voids. In addition, the strain-softening of unsaturated soils under large shear deformation is associated with the reorientation of the clay particles/aggregates.

Various prediction models have been proposed for the peak and critical shear strength of unsaturated soils, in the literature. In these models, $\tan\phi^b$ which is the frictional parameter associated with suction contribution typically decreases nonlinearly with an increase in suction which can be interpreted in terms of the area of free capillary water existing as water menisci among soil particles or aggregates. However, $\tan\phi^a$ can be constant, increase or decrease with suction. This may be attributed to the aggregation fabric, particularly for unsaturated fine-grained soils. Three prediction models from the literature that considers the variation of $\tan\phi^a$ with suction can well predict the magnitudes of critical shear strength of unsaturated soils; however, the model based on two independent stress state variables is more flexible that can provide a better prediction for the variations of $\tan\phi^a$ and $\tan\phi^b$ with respect to suction. In addition, the models proposed for the critical shear strength of unsaturated soils are not suitable for the prediction of the residual shear strength of unsaturated soils.

The conventional Cam-clay-type models can capture the main features of the behaviors observed in unsaturated soils; however, they are limited in reproducing the strain-softening behavior. The bounding surface plasticity (BSP) models are powerful for simulating various behaviors of unsaturated soils; however, they are complex as they are based on advanced soil plasticity concepts that typically require more parameters. The DSC approach can also overcome several limitations of the conventional Cam-clay-type models; additionally, it does not require advanced soil plasticity concepts and is based on simpler concepts in comparison to BSP. However, the DSC models cannot provide a comprehensive physical interpretation of the material response because it is

formulated based on several assumptions on the relative intact and fully adjusted states and disturbance function.

(2) Model for predicting the strain-softening stress-strain relationship of unsaturated soils

A model is proposed based on the disturbed state concept (DSC) to predict the variation of shear stress during strain-softening process for a wide range of unsaturated soils taking account of the influence of stress state variables; namely, net minor principal stress and matric suction. The parameters involved in the proposed model include: (i) saturated soil parameters (i.e., K_E, n_E, K_M, n_M, m_p, M_p, m_c and M_c) that can be determined by conventional laboratory shearing tests, (ii) SWCC parameters (a, n, m and S_r) that can be determined by conventional pressure plate tests, (iii) fitting parameters (i.e., α_E, β_E, α_M, β_M, κ_p, κ_c and R_f) that can be determined by back-calculating a few typical experimental results of suction-controlled shearing tests on unsaturated soil specimens.

The proposed model is validated using five sets of experimental data for SM, CL, ML, expansive clay, and residual clayey soil. The results show the proposed model can provide a reasonable prediction for the strain-softening stress-strain relationship of a wide range of unsaturated soils varying from coarse- to fine-grained soils. Comprehensive error analysis based on the index of agreement (δ) suggests that the error in predicting the stress-strain relationship using the proposed model is sensitive to the degree of accuracy of predicting peak shear strength.

(3) Unsaturated soil behaviors under suction-controlled ring shear testing

The suction-controlled ring shear tests on unsaturated specimens in this research are conducted in multi stages under constant matric suction. In the first shearing stage of unsaturated IHT soil, the shear stress – shear displacement curves exhibit strain-softening behavior, which are associated with compression of specimens. The reduction in shear strength can be attributed to the reorientation of the clay particles and the loss of water menisci area in the shear zone. In the subsequent shearing stages of unsaturated IHT soil, the shear stress – shear displacement curves exhibit apparent peak point. If the shear zones occurred at the same position during the multistage shearings, the apparent peak point in subsequent shearing stages can be attributed to the effort required initially to reorient the particles/aggregates under the new net normal stress state. If the

shear zones occurred at different positions during the multistage shearings, the apparent peak point in subsequent shearing stages can be attributed to the creation of the new shear zone.

In the first shearing stage of the unsaturated SP-SM soil, the shear stress – shear displacement curves exhibit strain-softening behavior. The matric suction can enhance the brittleness of the unaturated specimens and make the volume change transfer from compression to dilaiton. The strain-softening behavior of the SP-SM soil can be mainly attributed to the localized dilation inside the shear band. For the subsequent shearing stages of the unsaturated SP-SM soil, the shear stress – shear displacement curves exhibit hardening behavior, which are associated with slight compresion of the specimens. This may indicate the effect of net normal stress on the residual shear strength of the SP-SM soil is due to the reduction of the void ratio in shear zone. This is different in comparison to the IHT soil results from multistage tests which needs to reorient the particles/aggregates to reach the new residual state under the new net normal stress.

The envelopes of the residual shear strength of the unsaturated SP-SM and IHT soil exhibit similar behaviors. The envelope of the residual shear strength with respect to the net normal stress is typically linear for any matric suction range. The effective residual cohesion (c_r') is equal to 0. The value of the residual friction angle with respect to the net normal stress (ϕ_r^a) increases first with matric suction and then decreases. The apparent residual cohesion ($c_{r,a}$) increases linearly with matric suction, which means the residual friction angle with respect to the matric suction (ϕ_r^b) can be treated as a constant lower than ϕ_r' and independent of the matric suction.

(4) Model for predicting the residual shear strength of unsaturated soils

A model is formulated, and two approaches are provided to predict the residual shear strength for a wide range of unsaturated soils comprising coarse- to fine-grained soils. The parameters involved in the proposed model include: (i) effective residual shear strength parameters (c_r' and ϕ_r') that can be determined by using drained ring shear tests on saturated specimens, (ii) residual degree of saturation (S_r) that can be determined from the soil water characteristic curve, and (iii) fitting parameters (α_R, β_R and ϕ_r^b).

In the first approach, the three fitting parameters are determined by best-fitting experimental results of suction-controlled ring shear tests. This approach can provide reasonable predictions for

ϕ_r^a, $c_{r,a}$, and residual shear strength of various unsaturated soils. In the second approach, the three fitting parameters are related to the plasticity index (I_p); thus, only four basic parameters (i.e., c_r', ϕ_r', S_r and I_p) are included in this approach. The second approach provides reasonable predictions for ϕ_r^a, $c_{r,a}$, and residual shear strength of the studied plastic unsaturated soils; however, its performance for the studied non-plastic unsaturated soils is not as good as that of the first approach.

8.2 Suggestions for future research

(1) The studies based on suction-controlled ring shear tests on unsaturated soils are still limited in comparison to the studies based on suction-controlled direct/triaxial shear tests. For this reason, the investigations on the shearing behaviors of unsaturated soils under large shear deformation are rather limited and may be far from conclusive. The prediction model for the residual shear strength of unsaturated soils is formulated based on a limited database. Therefore, more experimental studies based on the suction-controlled ring shear tests on various unsaturated soils are recommended to provide more data for the investigations of the shear strength behavior of unsaturated soils under large shear deformation.

(2) Several suction-controlled ring shear apparatuses have been developed based on the axis-translation technique and the vapor equilibrium technique, respectively. However, these apparatuses still have limitations which can influence the measurement of parameters during tests; for example, the soils may extrude during shearing, the water content in the testing system may change due to the evaporation or condensation, and the mold may be generated during a long-time test. For this reason, an improvement of the testing apparatus and optimization of testing procedures are recommended to produce more reliable experimental data.

(3) The proposed DSC-based model for the strain-softening stress-strain relationship of unsaturated soils can only predict the variation of shear strength of unsaturated soils with the shear deformation. This model should be incorporated into an elastoplastic constitutive model of unsaturated soils to solve the boundary value problems. For this reason, a simple DSC-based elastoplastic constitutive model is recommended to be developed for the unsaturated soils that can consider the strain-softening behavior. The numerical modelling programs that can implement the DSC-based constitutive model should be developed for engineering practice applications.